

CONTROLLED AND EXPLOSIVE SILICIDATION OF
METAL / AMORPHOUS-SILICON MULTILAYER THIN FILMS

by

LAWRENCE ALFRED CLEVINGER

B.S. Materials Engineering, University of California, Los Angeles
(1984)

Submitted to the Department of Materials Science and Engineering
in Partial Fulfillment of
the Requirements for the Degree of

DOCTOR OF PHILOSOPHY

at the

Massachusetts Institute of Technology

September 1989

© Massachusetts Institute of Technology. All rights reserved

Signature of Author _____
Department of Materials Science and Engineering
August 11, 1989

Certified by _____
Carl V. Thompson
Associate Professor, Electronic Materials
Thesis Supervisor

Accepted by _____
Linn W. Hobbs
Chairman, Departmental Committee on Graduate Studies



CONTROLLED AND EXPLOSIVE SILICIDATION OF METAL / AMORPHOUS-SILICON MULTILAYER THIN FILMS

by

LAWRENCE ALFRED CLEVINGER

Submitted to the Department of Materials Science and Engineering
on August 11, 1989 in partial fulfillment of the requirements for the
Degree of Doctor of Philosophy

Abstract

Metal silicides are used as diffusion barriers at metal/silicon contacts and as low resistivity gate materials in integrated circuits. We have undertaken a quantitative investigation of the fundamental aspects of amorphous and crystalline silicide phase formation in metal/amorphous-silicon multilayer thin films. Controlled and explosive silicidation has been studied in nickel/amorphous-silicon, vanadium/amorphous-silicon and titanium/amorphous-silicon multilayer thin films using differential scanning calorimetry (DSC), transmission electron microscopy, thin film X-ray diffraction, high speed optical pyrometry and photography, and thermodynamic and kinetic modeling. The multilayer films were deposited using electron-beam evaporation onto unheated substrates, and had metal to silicon atomic concentration ratios of 2 to 1 or 1 to 2 for nickel/amorphous-silicon and 1 to 2 for the vanadium/amorphous-silicon and titanium/amorphous-silicon multilayer thin films.

The as-deposited films were found to have a thin metastable amorphous-silicide phase between the metal and the amorphous silicon layers. Thermodynamic analysis demonstrated that the existence of the metastable amorphous silicide was only possible when there were nucleation barriers to the formation of the stable crystalline silicides. Upon heating, the amorphous-silicide thickened before the crystalline silicide phase formed. Cross-sectional transmission electron microscopy, combined with isothermal and constant-scan-rate kinetic analysis indicated that nucleation barriers also controlled the formation of the crystalline silicides. The formation temperatures of the crystalline silicides did not vary with modulation period while the temperatures required for growth increased with increasing modulation period. Both isothermal and constant-scan-rate kinetic modeling and analysis were done to determine the activation energies and pre-exponential coefficients for the formation of amorphous and crystalline silicide phases.

Explosive silicidation could be initiated in all free-standing thin films, while a larger number of layers and greater total film thickness were required for explosive silicidation to occur in films on substrates. Explosive silicidation occurs when the rate of heat generation at the various reacting

interfaces exceeds the rate of heat dissipation to the surrounding environment. Explosive silicidation reaction fronts propagated very rapidly and resulted in the formation of stable crystalline silicide phases. For nickel/amorphous-silicon multilayer films on substrates, high speed photography and optical pyrometry was used to determine the velocity and temperature of the reaction front to be approximately 25 m/sec and 1500 K respectively.

Thesis Supervisor: Dr. Carl V. Thompson
Title: Associate Professor, Electronic Materials

Acknowledgments

During my five years at MIT, I have interacted with and been helped with specific problems by too many people to list in a few short paragraphs. I sincerely hope that all those who I have worked with will know of my respect and lasting appreciation.

I would first like to thank International Business Machines Corporation for providing the financial support for this research. Without their backing this work would not have been even attempted. I also appreciate the help of the technical staff of the MIT Submicron Structures Laboratory, especially Professor H.I. Smith, J. Carter, M. Porter, D. Roan and T. McClure, in the deposition of most of the thin films used in this research. I sincerely appreciate all their support and hard work.

I have interacted on a professional level with numerous students over the years. A partial list includes J. Floro, B. Park, K. Barmack, J. Elmer, Y.S. Kim, W. Furdanowicz, T. Ference, A. Judas, J. Olson, K. Coffey and T. Piccone. Thank you all for your help and insight into materials science that made me achieve most of my original research goals.

I would also like to thank Dr. K.N. Tu and Professors A.L. Greer, F. Spaepen, R. Cammarata, M. Grujicic and U. Gosele for helpful comments and critical reviews of most of this thesis. I would especially like to thank Professor R.R. deAvillez, a MIT visiting scientist who worked with me during the last year of my thesis research. Our interactions produced several significant results in the understanding of thin film reactions.

I am also indebted to my thesis committee, Professors S.M. Allen, D.A. Rudman and C.V. Thompson for their efforts and comments towards

this thesis. I especially want to thank my thesis advisor, Professor C.V. Thompson, for first allowing me the freedom to pursue exciting materials science issues in thin film reactions, and second for helping with intuitive insight towards my understanding of the large amount of data, results, and theories obtained.

Most importantly, I am grateful to my wife Leigh Anne. For five years, she has tolerated the ups and downs of a husband going through an MIT graduate education. I could not have done any of this thesis without her. Thanks Babe, now its time to get on with the rest of our lives.

Table of Contents

	<u>Page</u>
Title Page	1
Abstract	i
Acknowledgments	2
Table of Contents	4
Listing of Figures	9

Chapter

1	Introduction.....	17
	1.1 Silicides in Integrated Circuits.....	17
	1.2 Objective and Outline of Thesis	20
	1.3 Intermetallic Phase Selection in Thin Film Reactions.....	25
	1.4 References	31
2	Literature Review	32
	2.1 Controlled Silicidation -- Silicide Phase Formation Sequence.....	32
	2.2 Reaction Kinetics	34
	2.3 Thermodynamics of Intermetallic Phase Formation.....	37
	2.4 Structural Transitions in Amorphous-Silicon Thin Films.....	37
	2.5 Explosive Silicidation.....	38
	2.6 References	39
3	Experimental Procedures and Analysis.....	43
	3.1 Experimental Methods Used	43
	3.1.1 Deposition of Thin films.....	43

3.1.2	Calorimetry.....	46
3.1.3	Transmission Electron Microscopy.....	47
3.1.4	X-ray Diffraction.....	49
3.1.5	High Speed Pyrometry/Photography.....	49
3.2	Analysis of Calorimetric Data	51
3.2.1	Activation Energies.....	51
3.2.2	The Analysis of Nucleation Controlled Versus Growth Controlled Phase Selection in Thin Film Reactions Using Calorimetric Techniques	54
3.3	References	57
4	Controlled Silicidation of Nickel/Amorphous-Silicon Multilayer Thin Films with Atomic Concentration Ratios of 2 Ni Atoms to 1 Si Atom.....	59
4.1	Introduction.....	59
4.2	Phase Formation Sequence Upon Heating Nickel/Amorphous-Silicon Thin Films with Atomic Concentration Ratios of 2 Ni Atoms to 1 Si Atoms.....	60
4.3	Activation Energy of Silicide Formation in Nickel/Amorphous-Silicon Multilayer Thin Films with Atomic Concentration Ratios of 2 Ni Atoms to 1 Si Atom	69
4.4	Effect of Layer Thickness on the Reaction Kinetics of Nickel/Amorphous-Silicon Multilayer Films.....	72
4.5	Determination of Whether Nucleation and Growth or Growth Alone Controls Phase Selection in Nickel/Amorphous- Silicon Thin Film Reactions	76
4.6	Comments on Nucleation Energies of Silicide Phases.....	98

4.7	Conclusion for Controlled Silicidation of Nickel/Amorphous-Silicon Thin Film Reactions With Atomic Concentration Ratios of 2 Ni Atoms to 1 Si Atom	103
4.8	References	104
5	Controlled Silicidation of Vanadium/Amorphous-Silicon Multilayer Thin Films.....	106
5.1	Introduction.....	106
5.2	Reaction Kinetics.....	106
5.3	Determination of the Mechanism that Controls Silicide Phase Selection in Vanadium/Amorphous-Silicon Reactions.....	108
5.3.1	Results	110
5.3.2	Discussion	116
5.4	Conclusions	130
5.5	References	131
6	Controlled Silicidation of Titanium/Amorphous-Silicon Multilayer Thin Films with Atomic Concentration Ratios of 1 Ti Atom to 2 Si Atoms.....	132
6.1	Introauction.....	132
6.2	Phase Formation Sequence and Kinetics of Titanium/Amorphous-Silicon Reactions.....	133
6.2.1	Results	133
6.2.2	Discussion	148
6.3	Conclusion.....	155
6.4	References	156
7	Thermodynamics of Amorphous and Crystalline Intermetallic Phase Formation in Thin Films.....	158
7.1	Introduction.....	158

7.2	Formation of an Amorphous-Intermetallic Phase	159
7.3	Simultaneous Growth of an Amorphous and Crystalline Intermetallic Phase	167
7.4	Thermodynamic Driving Forces for Crystalline Intermetallic Formation.....	174
7.5	Conclusion.....	184
7.6	References	185
8	Structural Transitions in Electron-Beam Evaporated Amorphous-Silicon Thin Films.....	187
8.1	Introduction.....	187
8.2	Results and Discussion.....	187
8.3	Conclusion.....	195
8.4	References	195
9	Explosive Silicidation.....	197
9.1	Introduction.....	197
9.2	Experimental Determination of Reaction Front Velocities and Temperatures Along with the Microstructures of the Crystalline Silicide Formed	198
9.3	Comparison of Measured Explosive Silicidation Temperatures to Predicted Values.....	206
9.4	Conclusion.....	210
9.5	References	211
10	Summary and Future Work.....	213
Appendix A.	Controlled Silicidation of Nickel/Amorphous- Silicon Multilayer Films With Atomic Concentration Ratios of 1 Ni Atoms to 2 Si Atoms	219
A.1	Phase Formation Sequence and Reaction Kinetics	219

A.2	Effect of Modulation Period.....	221
A.3	References	223
Appendix B.	Modeling of the Double Peak Structure in Constant-Scan-Rate Calorimetric Data for the Formation and Growth of a Crystalline Silicide Phase.....	224
B.1	Ni ₂ Si Formation and Growth.....	224
B.2	VSi ₂ Formation and Growth.....	226
B.3	References	227
Appendix C	Thermodynamic Data.....	228
C.1.	Liquid and bcc Vanadium.....	228
C.2.	Liquid and fcc Nickel and Liquid, fcc, Amorphous and Diamond Cubic Silicon ..	229
C.3	Gibbs and Excess Gibbs Energies of Nickel/Silicon and Vanadium/Silicon Solutions.....	230
C.4	Gibbs Energies of Crystalline Vanadium Silicides	231
C.5	Gibbs Energies of Crystalline Nickel Silicides.....	231
C.6	References	232
Appendix D	Calculation of the Temperature of Explosive Silicidation of Nickel/Amorphous-Silicon Multilayer Thin Films with an Atomic Concentration Ratio of 2 Ni to 1 Si.....	234
D.1	Analysis	234
D.2	References	236

List of Figures

<u>Figure Number</u>	<u>Page</u>
Chapter 1	17
Figure 1 Cross-sectional view of a Metal Oxide Semiconductor Field Effect Transistor.....	18
Figure 2 Gibbs free energy versus composition diagram for an idealized A/B system with two thermodynamically stable intermetallic phases A_xB and A_yB . The common tangents define $C_{A_yB/B}$, C_{A_yB/A_xB} , C_{A_xB/A_yB} , and $C_{A_xB/A}$	28
Figure 3 Gibbs free energy versus composition diagram for an idealized A/B system with two intermetallics, thermodynamically stable A_xB and thermodynamically metastable A_yB . The common tangents define $C_{A_yB/B}$, C_{A_yB/A_xB} , C_{A_xB/A_yB} , and $C_{A_xB/A}$	29
Chapter 2	32
No Figures	
Chapter 3	43
Figure 1 Schematic illustration of the experimental configuration for high-speed photography and temperature measurements.	50
Chapter 4	59
Figure 1 Constant-heating-rate differential scanning calorimeter traces for nickel/amorphous-silicon multilayer films with atomic concentration ratios of 2 Ni to 1 Si and modulation periods of 14, 25, 50 and 100 nm.....	61
Figure 2 Bright field transmission electron microscope image of an as-deposited nickel/amorphous-silicon multilayer thin film.	63
Figure 3 Bright field transmission electron microscope image of the multilayer film of figure 2 which has been heated at 20 K/min to 460 K and quenched to room temperature.	64
Figure 4 Bright field transmission electron microscope image of the multilayer film of figure 2 which has been heated at 20 K/min to 490 K and quenched to room temperature.	65

Figure 5	Bright field transmission electron microscope image of the multilayer film of figure 2 which has been heated at 20 K/min to 535 K and quenched to room temperature.	66
Figure 6	Constant-heating-rate DSC traces for multilayer films with atomic concentration ratios of 2 Ni atoms to 1 Si atom and with a modulation period of a 100 nm. Each curve corresponds to a different scan rate.	70
Figure 7	Plot of $\ln(H/T_p^2)$ versus $1/T_p$ for the data of figure 6.	71
Figure 8	The relationship between the peak temperature T_p for Ni ₂ Si one-dimensional growth in figure 1 and the modulation period λ as indicated by equation 7.	75
Figure 9	Gibbs free energy versus composition diagram for the nickel/silicon system at a temperature of 350 K. The crystalline silicides are distinguished by "O"	78
Figure 10	Gibbs free energy versus composition curve for the nickel/silicon system at a temperature of 350 K considering only fcc nickel, amorphous-nickel-silicide, amorphous-silicon and crystalline Ni ₂ Si.	81
Figure 11	Same as figure 9, except that we have assumed that nucleation barriers prevent the formation of the crystalline silicides.	83
Figure 12	Nickel composition versus distance across one modulation period of a nickel/amorphous-silicon multilayer film heated to 535 K.	84
Figure 13	Gibbs free energy versus composition diagram for the nickel/silicon system at a temperature of 650 K considering only fcc nickel, amorphous-nickel-silicide, amorphous-silicon and Ni ₂ Si.	86
Figure 14	Calorimetric data at a scan rate of 20 K/min for a 100 nm modulation period multilayer film.	87
Figure 15	Constant-scan-rate calorimetric data for a 100 nm modulation period multilayer film plotted along with predicted calorimetric data (dashed line) derived from equation 5.	90
Figure 16a	Isothermal differential scanning calorimetry trace for a nickel/amorphous-silicon multilayer film annealed at 420 K.	92

Figure 16b Isothermal differential scanning calorimetry trace for the nickel/amorphous-silicon film of figure 16a annealed at 455 K.....	93
Figure 17a Theoretical isothermal calorimetry curve for simple one-dimensional growth (or thickening) of a silicide, without nucleation.....	96
Figure 17b Theoretical isothermal calorimetry curve for nucleation and growth of a silicide.....	97
Figure 18 Ideal lense shaped silicide nucleus forming at the nickel/amorphous-silicon interface.....	101
Chapter 5.....	106
Figure 1 DSC traces for multilayer films with atomic concentration ratios 1 V to 2 Si, with a modulation period of 50 nm and with a total film thickness of 250 nm. Each curve corresponds to a different scan rate.....	107
Figure 2 Plot of $\ln(H/T_p^2)$ vs $(1/T_p)$ for the data in figure 1 where H is the heating rate and T_p is the peak temperature.....	109
Figure 3 Constant-heating-rate differential scanning calorimeter traces for vanadium/amorphous-silicon multilayer films with atomic concentration ratios of 1 V atom to 2 Si atoms and modulation periods of 14 and 50 nm.....	111
Figure 4 Dark field transmission electron micrograph (using the (110) vanadium polycrystalline diffraction ring) of a vanadium/amorphous-silicon multilayer film which has been heated at 20 K/min to 758 K and quenched to room temperature.....	113
Figure 5 Dark field transmission electron micrograph (using the (110) vanadium and (1121) VSi_2 diffraction rings) of a vanadium/amorphous-silicon multilayer film which has been heated at 20 K/min to 783 K and quenched to room temperature.....	114
Figure 6 Dark field transmission electron micrograph (using the (110) vanadium and (1121) VSi_2 diffraction rings) of a vanadium/amorphous-silicon multilayer film which has been heated at 20 K/min to 808 K and quenched to room temperature.....	115
Figure 7 Isothermal differential calorimetry trace for a vanadium/amorphous-silicon multilayer film annealed at 750 K. The modulation period of the film was 14 nm.....	117

Figure 8	Gibbs free energy versus composition diagram for the vanadium/silicon system at a temperature of 750 K. The crystalline silicides are distinguished by the symbol "O".	118
Figure 9	Same diagram as figure 6, except that we have assumed that nucleation barriers prevent the formation of the crystalline silicides. Common tangents are drawn in for bcc vanadium (a), amorphous-vanadium-silicide (b) and amorphous-silicon.	120
Figure 10	Morphology for the idealized case of phase X forming at an A/B interface for (a) nucleation controlled formation and (b) growth controlled formation.	122
Figure 11	Constant-scan-rate calorimetric data for a 50 nm modulation period multilayer film plotted with predicted calorimetric data (dashed line) derived from equation 3.	125
Figure 12a	Theoretical isothermal calorimetry curve for nucleation and growth of a silicide.	128
Figure 12b	Theoretical isothermal calorimetry curve for simple one-dimensional growth of a silicide without nucleation.	129
Chapter 6		132
Figure 1	DSC traces for heating rates of 2.5, 5, 10, 20, 40 K/min for titanium/amorphous-silicon multilayer thin films with a modulation period of 30 nm and an atomic concentration ratio of 1 Ti atom to 2 Si atoms.	134
Figure 2	Bright field transmission electron microscope image of an as-deposited titanium/amorphous-silicon multilayer thin film.	135
Figure 3	Bright field transmission electron microscope image of a titanium/amorphous-silicon multilayer thin film heated to 670 K.	136
Figure 4	DSC trace for a titanium/amorphous-silicon multilayer film with a modulation period of 30 nm and an atomic concentration ratio of 1 Ti atom to 2 Si atoms heated at 20 K/min to 700 K.	138
Figure 5	Bright field transmission electron microscope image of a titanium/amorphous-silicon multilayer thin film heated to 790 K.	139

Figure 6	Bright field transmission electron microscope image of a titanium/amorphous-silicon multilayer thin film heated to 860 K.	140
Figure 7	Bright field transmission electron microscope image of a titanium/amorphous-silicon multilayer thin film heated to 900 K.	141
Figure 8a	Auger composition profiles of an as deposited titanium/amorphous-silicon multilayer thin film with a modulation period of 30 nm and an atomic concentration ratio of 1 Ti atom to 2 Si atoms.	144
Figure 8b	Auger composition profiles of a titanium/amorphous-silicon multilayer thin film with a modulation period of 30 nm and an atomic concentration ratio of 1 Ti atom to 2 Si atoms heated at 20 K/min to 790 K.	145
Figure 8c	Auger composition profiles of a titanium/amorphous-silicon multilayer thin film with a modulation period of 30 nm and an atomic concentration ratio of 1 Ti atom to 2 Si atoms heated at 20 K/min to 860 K.	146
Figure 9	Plot of $\ln(H/T_p^2)$ versus $1/T_p$ for the data for peak 2 of figure 1.	147
Figure 10	Chemical diffusivity determined from the amorphous-titanium-silicide growth data reported by Holloway, as a function of temperature.....	151
Figure 11	DSC trace for a titanium/amorphous-silicon multilayer thin film with a modulation period of 30 nm and an atomic concentration ratio of 1 Ti atom to 2 Si atoms, heated at 20 K/min to 790 K.....	153
Chapter 7	158
Figure 1	Gibbs free energy versus composition diagram for an idealized A-B system. Dashed lines are common tangents for the A solution, crystalline intermetallics A_xB and AB_y and the B solution.....	160
Figure 2	Same as figure 1 except that we have assumed that kinetic barriers prevent the formation of the crystalline intermetallics. Common tangents are drawn between the A solution, the amorphous-intermetallic phase and the B solution.	162

- Figure 3a Gibbs free energy versus composition diagram for the nickel/silicon system at a temperature of 400 K. The crystalline nickel silicides are indicated by "O"s.....163
- Figure 3b Gibbs free energy versus composition diagram for the vanadium/silicon system at a temperature of 750 K. The crystalline vanadium silicides are indicated by "O"s.....164
- Figure 4a Same as figure 3a, with the assumption that nucleation barriers prevent the formation of the crystalline nickel silicides. Common tangents are drawn for fcc nickel (a), amorphous-nickel-silicide (b) and amorphous-silicon.....165
- Figure 4b Same as figure 3b with the assumption that kinetic nucleation barriers prevent the formation of the crystalline vanadium silicides. Common tangents are drawn for bcc vanadium (a), amorphous-vanadium-silicide (b) and amorphous-silicon.....166
- Figure 5 Same as figure 2 with the common tangents between the amorphous-intermetallic phase and A and the amorphous-intermetallic phase and B extended to intersect the Gibbs free energy axes. These common tangents divide the diagram into six regions.....169
- Figure 6 Same as figure 2 with a crystalline intermetallic A_xB , that has formed at the A/amorphous-intermetallic interface. The A_xB crystalline intermetallic has a free energy located in region 4 of figure 5.170
- Figure 7 Same as figure 2 , with a crystalline intermetallic A_xB that has formed at the amorphous-intermetallic/B interface. The A_xB crystalline intermetallic has a free energy located in region 6 of figure 5.....172
- Figure 8 Gibbs free energy versus composition diagram at 650 K for the nickel/silicon system considering only fcc nickel, amorphous-nickel-silicide, Ni_2Si and amorphous-silicon.173
- Figure 9 Gibbs free energy versus composition diagram at 750 K for the vanadium/silicon system considering only bcc vanadium. amorphous-vanadium-silicide, VSi_2 and amorphous-silicon.....175
- Figure 10 Gibbs free energy versus composition diagram for an idealized A-B system demonstrating how the driving force ΔG_v , for crystalline A_xB formation from a arbitrary solution is calculated.177

Figure 11a	Driving force for crystalline nickel silicide formation at 400 K from fcc nickel as a function of composition of the nickel.....	180
Figure 11b	Driving force for crystalline nickel silicide formation at 400 K from amorphous-nickel-silicide as a function of composition of the amorphous-nickel-silicide.....	181
Figure 11c	Driving force for crystalline vanadium silicide formation at 750 K from amorphous-vanadium-silicide as a function of the composition of the amorphous-vanadium-silicide.	182
Chapter 8	187
Figure 1	Differential scanning calorimetry traces for amorphous-silicon films prepared by electron beam evaporation with two different deposition rates.....	188
Figure 2	Differential scanning calorimeter traces for consecutive temperature scans from 330 to 750 K of an amorphous-silicon film deposited at 0.2 nm/min.....	190
Figure 3a	Transmission electron micrograph and diffraction pattern (insert) of an amorphous-silicon film deposited at 0.2 nm/min, at room temperature.....	191
Figure 3b	Transmission electron micrograph and diffraction pattern (insert) of an amorphous-silicon film deposited at 0.2 nm/min, at room temperature, after being heated at 20 K/min from 330 to 750 K and quenched at 320 K/min.	192
Chapter 9	197
Figure 1	High speed temperature measurements for explosive silicidation occurring in a nickel/amorphous-silicon multilayer film with an atomic concentration ratio of 2 Ni atoms to 1 Si atom.....	199
Figure 2	High-speed video output showing the explosive silicidation front (bright band) at 12 different times, 1/12 of a millisecond apart. This film was made in the same way as described in figure 1. The indicated front velocity was 23 m/sec.	200
Figure 3	Explosive reaction front velocities versus modulation period and total film thickness for 2 Ni to 1 Si multilayer thin films.....	202
Figure 4a	Plan view transmission electron micrograph of an as-deposited of 2 Ni to 1 Si multilayer thin film with	

modulation period of 14 nm and a total film thicknesses of 70 nm.	203
Figure 4b Plan view transmission electron micrograph of an 2 Ni to 1 Si multilayer thin film with modulation period of 14 nm and a total film thicknesses of 70 nm which has been explosively reacted to form Ni ₂ Si.....	204
Figure 4c Plan view transmission electron micrograph of an 2 Ni to 1 Si multilayer thin film with modulation period of 14 nm and a total film thicknesses of 70 nm which has been thermally annealed to form Ni ₂ Si.....	205
Chapter 10.....	213
No Figures	
Appendix A.....	219
Figure 1 Constant-heating-rate DSC traces for multilayer films with atomic concentration ratios of 1 Ni atom to 2 Si atoms and with a modulation period of 95 nm. Each curve corresponds to a different scan rate.....	220
Figure 2 Constant-heating-rate DSC traces for nickel/amorphous-silicon multilayer films with atomic concentration ratios of 1 Ni atoms to 2 Si atom and modulation periods of 116.2, 95.2, 58.1 and 33.0 nm.....	222
Appendix B	224
No Figures	
Appendix C	228
No Figures	
Appendix D	234
No Figures	

1 Introduction

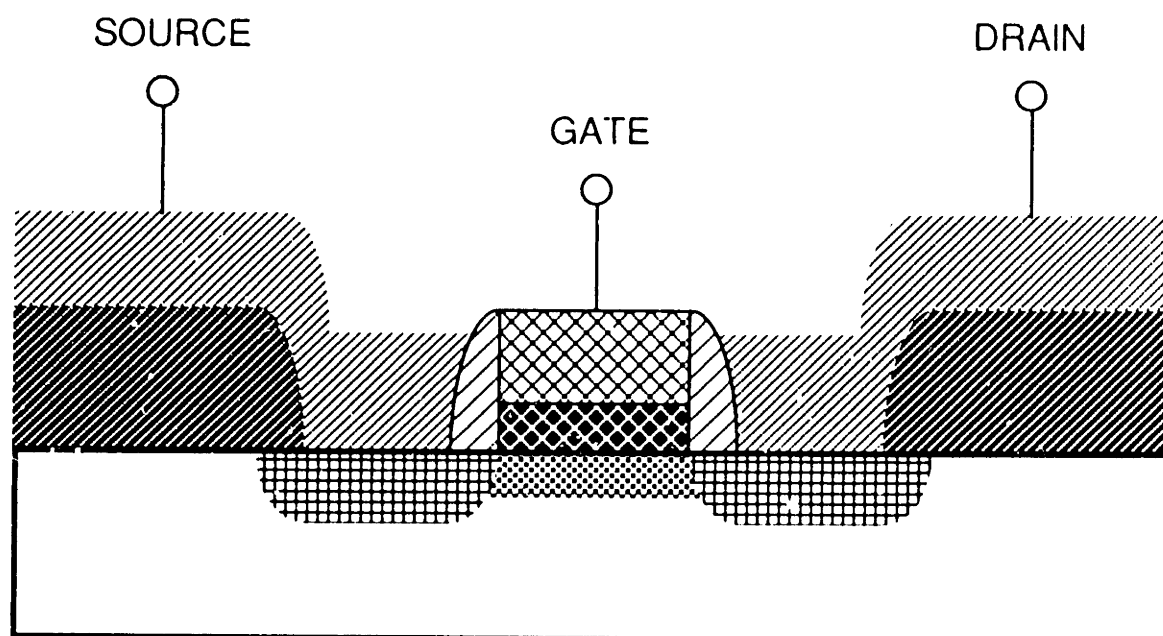
1.1 Silicides in Integrated Circuits

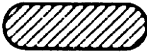






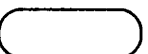
Since the development of the first transistor in 1947,¹ scientists in the field of microelectronics have used a wide variety of materials to create innovative devices and computer systems. The desire to achieve high speed performance in these systems has led to the development of bipolar and metal oxide semiconductor (MOS) integrated circuits with micron and submicron device dimensions. In order to build these devices, researchers began to investigate new classes of interconnect materials called silicides, which have all the required properties (low resistivity, long term reliability) for high performance in very small devices.²

One type of device is a MOS field effect transistor (MOSFET). A cross-sectional view of a MOSFET is shown in figure 1. In this device, the current between the source and the drain is modulated by the voltage applied to the gate. Major factors limiting the speed and reliability of this device are the resistance of the source, gate and drain interconnects and the integrity of the metal/SiO₂ and metal/silicon interfaces.^{3,4}

Since the early 1970's doped polycrystalline silicon has been used as a gate material and aluminum has been used for source and drain contacts to the silicon substrate. The use of these materials had several advantages. The doped polycrystalline silicon was easily deposited by chemical vapor deposition techniques, it did not degrade the underlying gate oxide, and it could be oxidized to form a passivating layer on top of the gate. Aluminum source and drain interconnects were easily deposited by electron beam

Figure 1 Cross-sectional view of a Metal Oxide Semiconductor Field Effect Transistor.



	Al		poly-Si
	SiO ₂		Gate SiO ₂
	n+		Spacer SiO ₂
	p+		Silicon

evaporation or sputtering, and they typically had a low resistivity ($\approx 3 \mu\Omega\text{-cm}$).⁵

However, as device sizes have shrunk down to micron and submicron dimensions in the early 1980's, two major problems have become apparent with doped polycrystalline silicon gates and aluminum source and drain contacts. First, the resistivity of doped polycrystalline silicon is typically 500 to 1000 $\mu\Omega\text{-cm}$.⁶ This is too high for optimum device performance in micron and submicron dimensions. Second, silicon has a high solubility in aluminum at elevated temperatures, which leads to interdiffusion of the two elements during device manufacture. This interdiffusion causes voids (called spikes) to be formed in the silicon substrate at the aluminum/silicon interface which can short-circuit the n⁺/p junctions shown in figure 1 and cause failure of the device.⁷

To address these problems, researchers have sought a gate material with a lower resistivity than doped polycrystalline silicon, and source and drain contact materials with a resistivity comparable to that of aluminum but without the spiking problem apparent in aluminum/silicon interconnections. One solution was to use intermetallic compounds called metal silicides in these applications.⁸ These metal silicides are intermetallic phases formed by a reaction between metal and silicon. For gate materials, these metal silicides are usually transition metal silicides and they have all the advantages of doped polycrystalline silicon (easy deposition, good thermal stability) with a resistivity that is typically a factor of 50 to 100 times lower than doped polycrystalline silicon.² For source and drain contacts, both transition and near noble metal silicides have been used as thin diffusion barriers between the aluminum interconnect layer and the silicon transistor.² This structure preserves the advantages of the

lower resistivity aluminum interconnects and at the same time prevents the interdiffusion of silicon into aluminum which can cause device failure.

These metal silicide layers are typically a few hundred to several thousand angstroms thick in submicron devices. They can be prepared by a variety of techniques such as the recrystallization of an amorphous-metal-silicide alloy deposited by co-evaporation of metal and silicon, chemical vapor deposition of crystalline metal silicide, and solid state reaction of a thin film of a metal with a silicon thin film or crystalline silicon substrate.

For this thesis, we have investigated amorphous and crystalline silicide formation from reactions between metal and amorphous-silicon thin films with nickel, vanadium or titanium as the chosen metal. The thin films were prepared as multilayer films with alternating layers of metal and amorphous-silicon. This allowed for the observation of the same reaction occurring at many reacting interfaces, which enabled us to study the early stages of amorphous and crystalline silicide nucleation and growth.

1.2 Objective and Outline of Thesis

The purpose of this thesis is to perform a quantitative study of the fundamental aspects of controlled and explosive silicidation in metal/amorphous-silicon multilayer films. Controlled silicidation is the formation of amorphous and crystalline silicide phases by a solid state reaction, at a predetermined annealing temperature T , between metal and amorphous-silicon. Explosive silicidation is the formation of a crystalline silicide phase by the self-propagating explosive reaction of a

metal/amorphous-silicon multilayer thin film. This work focuses on four main areas: first, the demonstration of the use of calorimetry in combination with other techniques to obtain kinetic information on amorphous and crystalline silicide phase formation and structural transitions in amorphous materials; second, the use of calorimetric techniques to determine that nucleation and growth as opposed to growth alone control phase selection in thin film reactions; third, a discussion of the thermodynamics of amorphous phase formation and nucleation of crystalline silicide phases as a function of atomic composition; and fourth, an investigation of explosive silicidation in metal/amorphous-silicon multilayer thin films.

In section 1.3, we present an overview of the atomic mechanisms that can control intermetallic phase selection in a thin film reaction. Chapter 2 presents a literature review of past research on silicide reactions while in chapter 3 we present an overview of the experimental methods used in this thesis. Chapter 4 focuses on controlled silicidation of nickel/amorphous-silicon multilayer films with atomic concentration ratios of 2 Ni atoms to 1 Si atom. It was with nickel/amorphous-silicon reactions that we first tested the concept of using calorimetry, cross-sectional transmission and scanning transmission electron microscopy, and X-ray diffraction to investigate the thermodynamics and kinetics of silicide reactions. We begin this chapter by determining the amorphous and crystalline silicide phase formation sequence as a function of the modulation period upon heating a nickel/amorphous-silicon thin film. We then proceed to discuss how reaction kinetics of the silicide phases formed by heating can be determined with calorimetric analysis. We next discuss the kinetic modeling of increasing peak temperatures with increasing modulation periods for

silicide growth reactions in constant-heating-rate calorimetric data. We next show how thermodynamic modeling and isothermal and constant-heating-rate calorimetry can be used to demonstrate that nucleation controls amorphous and crystalline phase selection in nickel/amorphous-silicon thin film reactions. Finally, we discuss the implication of nucleation controlled phase selection on the nucleation surface energies of the silicide phases.

In chapter 5, we use the knowledge gained from investigating nickel/amorphous-silicon reactions to examine vanadium/amorphous-silicon multilayer thin film reactions. We begin by determining activation energies for crystalline vanadium silicide formation using calorimetric analysis. We then show that the first silicide phase to form from a vanadium/amorphous-silicon reaction is metastable amorphous-vanadium-silicide. Finally we demonstrate that thermodynamic modeling, isothermal and constant-heating-rate calorimetry, and cross-sectional transmission electron microscopy indicate that nucleation controls amorphous and crystalline vanadium silicide phase selection.

In chapter 6 titanium/amorphous-silicon thin film reactions are discussed. These reactions were studied with the same techniques that were used to investigate the controlled silicidation of vanadium/amorphous-silicon and nickel/amorphous-silicon thin films. Titanium/amorphous-silicon reactions are similar to vanadium/amorphous-silicon and nickel/amorphous-silicon reactions in two ways. First, the first silicide phase to form at the titanium/amorphous-silicon interface is metastable amorphous-titanium-silicide, and second, the activation energies for crystalline silicide formation are easily determined with calorimetric analysis. Titanium/amorphous-silicon

reactions are different from vanadium/amorphous-silicon and nickel/amorphous-silicon reactions in that there is calorimetric evidence of densification and/or compositional homogenization occurring within the amorphous-titanium-silicide phase upon heating which was not seen in the other systems.

In chapter 7, we discuss the thermodynamics of amorphous and crystalline intermetallic phase formation in thin film reactions. The examples used in this chapter are from nickel/amorphous-silicon and vanadium/amorphous-silicon thin film reactions. In this section, we discuss the thermodynamic conditions for amorphous phase formation and for the simultaneous growth of an amorphous and crystalline intermetallic phase. We also discuss how the driving force for crystalline intermetallic formation depends on the interface at which the intermetallic forms, the layer in which the intermetallic forms and the composition of the layer where the intermetallic nucleates.

In chapter 8 structural transitions in pure amorphous-silicon thin films are discussed. In chapter 6, we presented calorimetric evidence of structural transitions occurring in amorphous-titanium-silicide layers, and we wanted to find out if these transitions also occurred in pure amorphous-silicon thin films. In this work, we determined that both exothermic and endothermic transitions occurred in amorphous-silicon film upon heating. We attributed exothermic transitions to bond angle relaxations and endothermic transitions to structural homogenization of the amorphous-silicon structure.

Next, in chapter 9 we discuss explosive silicidation of metal/amorphous-silicon multilayer thin films. We show how the reaction front velocity, temperature and the resulting crystalline silicide

microstructure are interrelated. Explosive silicidation occurred in nickel/amorphous-silicon, vanadium/amorphous-silicon and titanium/amorphous-silicon thin films. However, in this chapter we only focus on nickel/amorphous-silicon thin film explosive reactions.

In chapter 10, we discuss our conclusions and potential future work. The work described in this thesis has contributed to a broader quantitative understanding of thin film reactions, especially in the areas of nucleation controlled silicide formation, amorphous silicide formation and growth, structural changes in amorphous materials, thermodynamic analysis of thin film reactions and explosive silicidation. However, there are also many avenues open for future work which should provide an even deeper understanding of the fundamental mechanisms of thin film interactions.

Finally in appendices A through D, we discuss various aspects of our work which did not fit into the organizational structure of chapters 4 through 9. In appendix A, we discuss the controlled silicidation of nickel/amorphous-silicon multilayer thin films with atomic concentration ratios of 1 Ni atom to 2 Si atoms. This section is similar to chapter 4 where we discussed the controlled silicidation of nickel/amorphous-silicon multilayer films with atomic concentration ratios of 2 Ni atoms to 1 Si atom. In appendix B, we present a detailed discussion of a model that is used to predict the shape of the constant-heating-rate calorimetric data for Ni_2Si formation and growth in chapter 4 section 5 and VSi_2 formation and growth chapter 5 section 3. In appendix C, we present thermodynamic data that we used to calculate the Gibbs free energy versus composition diagrams used in chapters 4,5 and 7. Finally in appendix D, we present a detailed calculation of the expected reaction front temperature for the explosive silicidation of a nickel/amorphous-silicon multilayer thin film with an

atomic concentration ratio of 2 Ni atoms to 1 Si atom. In chapter 9 this calculated temperature is compared to the experimentally determined temperature.

1.3 Intermetallic Phase Selection in Thin Film Reactions

One of the main goals of our research was to determine the atomic mechanisms that control intermetallic phase selection in a thin film reactions. This problem has been discussed by scientists for many years and two different models for this mechanism have been proposed, which we will call the nucleation control model and the growth control model. In the nucleation control model, the intermetallic phase that forms first from a thin film reaction is the phase with the highest nucleation rate.⁸ In the growth control model, nucleation is assumed not to be the rate limiting step and the intermetallic phase that forms from a thin film reaction is the phase that grows the fastest.⁹ To illustrate how these two models could control phase selection in a thin film reaction, consider a bilayer thin film of an A layer and a B layer in which one of two intermetallics A_xB or A_yB could form at the A/B interface.

If phase selection in this system is nucleation controlled, then the intermetallic that does form at the interface is the one with the highest nucleation rate. This nucleation rate, I , can be approximated by:¹⁰

$$I = N v_o \exp\left(\frac{\Delta G_a + \Delta G^*}{kT}\right) \quad (1)$$

where N is the nucleation site density, v_0 is an atomic jump frequency, ΔG_a is an activation energy for atomic migration and ΔG^* is the free energy barrier to nucleation of the intermetallic. ΔG^* can be expressed as:¹¹

$$\Delta G^* = \frac{16\pi}{3} \frac{(\Delta\sigma)^3}{(\Delta G_v)^2} \quad (2)$$

where ΔG_v is the thermodynamic driving force for nucleation (discussed in chapter 7) and $\Delta\sigma$ is the "nucleation surface energy" for heterogeneous nucleation¹² (discussed in section 4.6 for nickel/amorphous-silicon reactions).

If intermetallic formation at the A/B interface is controlled by growth mechanisms, then the intermetallic phase that forms first at this interface (A_xB or A_yB) is the phase that has the largest positive growth rate. Following the analysis of Gosele and Tu,⁹ the growth rates for A_yB and A_xB phases can be expressed as:

$$\frac{dX_{A_yB}}{dt} = (A3)(j_{A_yB}) - (A4)(j_{A_xB}) \quad (3)$$

$$\frac{dX_{A_xB}}{dt} = (A5)(j_{A_xB}) - (A6)(j_{A_yB}) \quad (4)$$

where A_i 's are positive constants which depend on the stoichiometric ratios of the intermetallic phases and j_{A_yB} and j_{A_xB} are the atomic fluxes through each layer which can be expressed as:

$$j_{A_yB} = \frac{(\Delta C_{A_yB}^{eq})(K_{A_yB})}{1 + (X_{A_yB})(K_{A_yB}) / (\tilde{D}_{A_yB})} \quad (5)$$

$$j_{A_x B} = \frac{(\Delta C_{A_x B}^{eq})(K_{A_x B})}{1 + (X_{A_x B})(K_{A_x B}) / (\tilde{D}_{A_x B})} \quad (6)$$

In equations 5 and 6, $X_{A_y B}$ and $X_{A_x B}$ are the thicknesses of the $A_y B$ and the $A_x B$ intermetallic layers, $K_{A_y B}$ and $K_{A_x B}$ are the interface reaction coefficients for either $A_y B$ or $A_x B$, and $\tilde{D}_{A_y B}$ and $\tilde{D}_{A_x B}$ are the diffusivity of the $A_x B$ or $A_y B$ intermetallic phases. $\Delta C_{A_y B}^{eq}$ and $\Delta C_{A_x B}^{eq}$ can be expressed as:

$$\Delta C_{A_y B}^{eq} = C_{A_y B / B} - C_{A_y B / A_x B} \quad (7)$$

$$\Delta C_{A_x B}^{eq} = C_{A_x B / A_y B} - C_{A_x B / A} \quad (8)$$

where $C_{A_y B / B}$, $C_{A_y B / A_x B}$, $C_{A_x B / A_y B}$, and $C_{A_x B / A}$ are defined in figures 2 and 3 for the possible formation at the A/B interface of either thermodynamically stable $A_x B$ or $A_y B$ (figure 2), or for the possible formation at the A/B interface of either thermodynamically stable $A_x B$ or thermodynamically metastable $A_y B$ (figure 3).

For the case where both $A_y B$ and $A_x B$ are thermodynamically stable, figure 2 and equations 3 through 7 predict that $\Delta C_{A_y B}^{eq}$, $\Delta C_{A_x B}^{eq}$, $j_{A_y B}$ and $j_{A_x B}$ are all positive. The $A_y B$ intermetallic will form first at the A/B interface if the constants A3 through A6 and the fluxes $j_{A_y B}$ and $j_{A_x B}$ have combined in equations 3 and 4 such that $\frac{dX_{A_y B}}{dt} > 0$ and $\frac{dX_{A_y B}}{dt} \gg \frac{dX_{A_x B}}{dt}$. This is a possible model for determining phase selection in a thin film reaction when all the possible intermetallic phases are thermodynamically stable.

Figure 2 Gibbs free energy versus composition diagram for an idealized A/B system with two thermodynamically stable intermetallic phases A_xB and A_yB . The common tangents define $C_{A_yB/B}$, C_{A_yB/A_xB} , C_{A_xB/A_yB} , and $C_{A_xB/A}$.

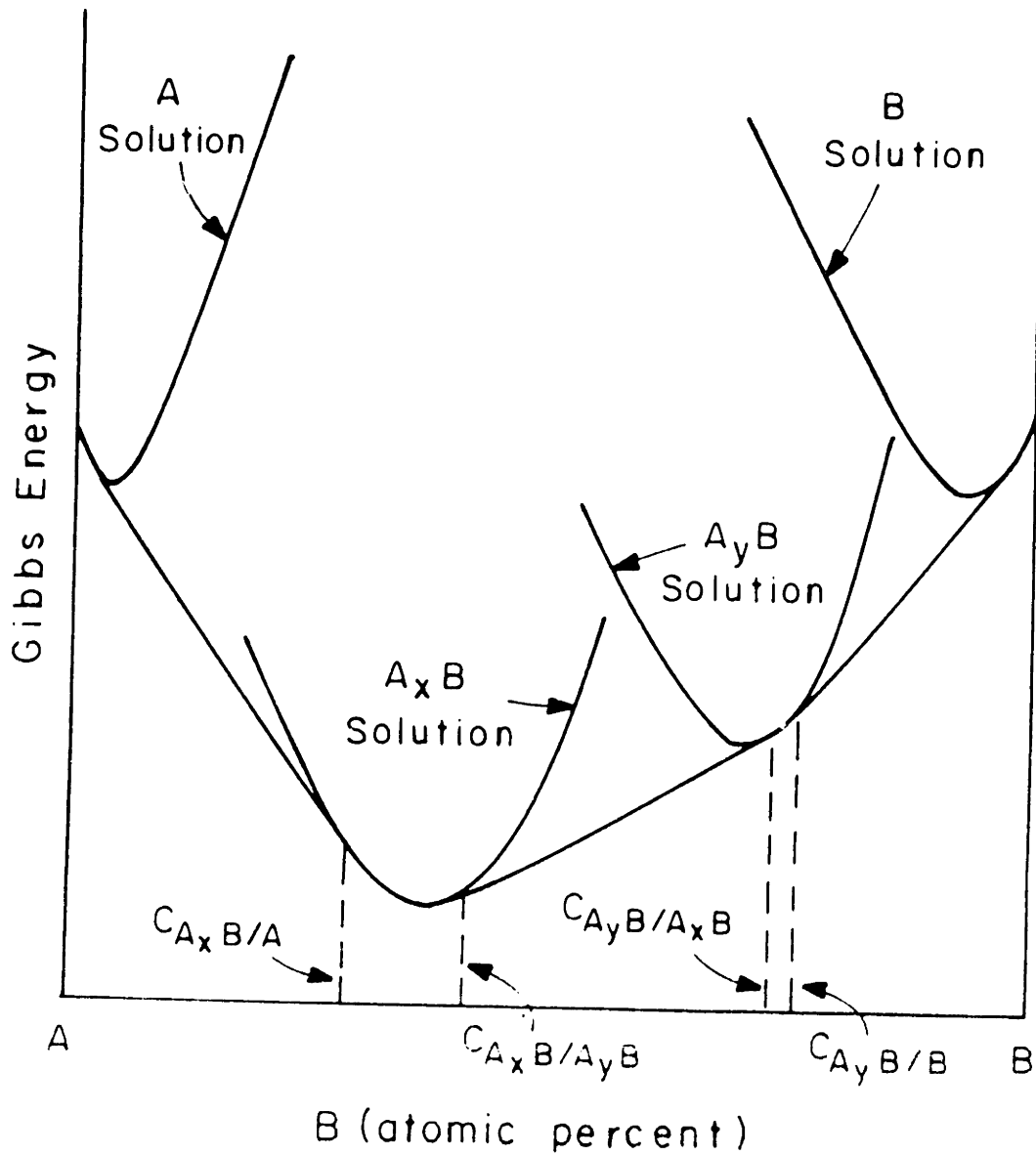
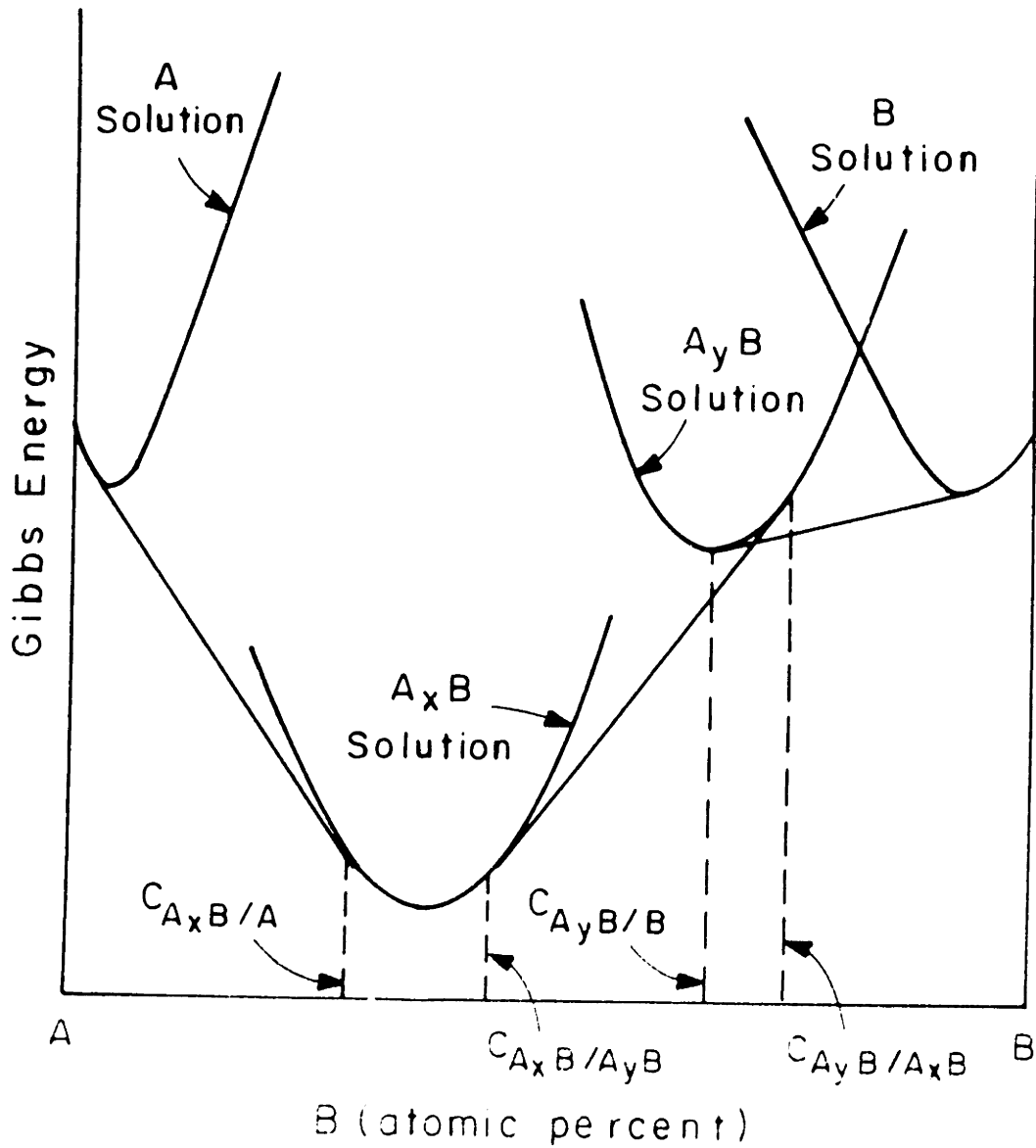


Figure 3 Gibbs free energy versus composition diagram for an idealized A/B system with two intermetallics, thermodynamically stable A_xB and thermodynamically metastable A_yB . The common tangents define $C_{A_yB/B}$, C_{A_yB/A_xB} , C_{A_xB/A_yB} , and $C_{A_xB/A}$.



However, now consider the case where A_yB is thermodynamically metastable and A_xB is thermodynamically stable as shown in figure 3. From this figure and equations 5 and 6, $\Delta C_{A_yB}^{eq}$ is always negative for metastable A_yB formation when competing against A_xB . This implies by equations 3 through 8 that A_yB would always have a negative growth rate and A_xB would have a positive growth rate. Thus by a growth controlled model for intermetallic phase formation, thermodynamically stable A_xB would be the first intermetallic phase to form at the A/B interface and thermodynamically metastable A_yB would never form.

In this research, we discuss metal/amorphous-silicon reactions with nickel, vanadium or titanium as the chosen metal. For each of these systems, a thermodynamically metastable amorphous-metal-silicide phase is the first phase to form at the metal/amorphous-silicon interface. The analysis presented above for growth controlled phase selection indicates that by this model, an amorphous-metal-silicide phase should never form at the metal/amorphous-silicon interface, which is contrary to experimental observations presented in this thesis and by other authors. This strongly suggests that phase selection in these thin film reactions is not determined by kinetic growth barriers at the metal/amorphous silicon interface. Rather, as discussed for nickel/amorphous silicon reactions (chapter 4) and vanadium/amorphous silicon reactions (chapter 5) phase selection in metal/amorphous silicon is determined by the nucleation controlled kinetics presented in equations 1 and 2.

1.4 References

1. S. Sze, Physics of Semiconductor Devices, Wiley, New York (1981)
2. S.P. Muraka, Silicides for VLSI Applications, Academic, Orlando (1983)
3. K.C. Saraswat and F. Mahammadani, IEEE Trans. Electron. Dev., ED 29, 645 (1982)
4. A.K. Sinha, J.A. Cooper and H.J. Levinstein, IEEE Electron. Dev. Lett., EDL 3, 90 (1982)
5. S. Ghandi, VLSI Fabrication Principles, Wiley, New York (1983)
6. F.C. Eversteyn and B.H. Put, J. Electrochem. Soc., 120, 106 (1973)
7. G.L. Schnoble and R.S. Keen, Proc. IEEE, 57, 1570 (1971)
8. F. M. d'Heurle, J. Mater. Res., 3, 167 (1988)
9. U. Gosele and K.N. Tu, J. Appl. Phys., 53, 3252 (1982)
10. J.W. Christen, The Theory of Transformations in Metals and Alloys, Pergamon, Oxford (1965), first edition
11. W.C. Johnson, C.L. White, P.E. Marth, P.K. Rut, S.M. Tuominen, K.D. Wade, K.C. Russel and H.I. Aaronson, Met. Trans. A, 6A, 911 (1970)
12. M. Nathan J. Appl. Phys., 63, 5539 (1988)
13. L.A. Clevenger, C.V. Thompson, A.Judas and K.N. Tu, First MRS International Meeting on Advanced Materials, 10, 431 (1989)
14. K. Holloway and R. Sinclair, J. Appl. Phys., 61, 1359 (1987)

2 Literature Review

2.1 Controlled Silicidation – Silicide Phase Formation Sequence

In the past, most researchers have studied the formation of a crystalline silicide phase at a metal/silicon interface by a combination of cross-sectional transmission electron microscopy for structured analysis, thin film X-ray diffraction for phase identification and Rutherford Backscattering for silicide thickness measurements.¹ In particular, the phase formation sequence for nickel/silicon reactions has been investigated by Tu et al.,² Olowolafe et al.,³ Nathan,⁴ Ma et al.⁵ and Clevenger et al.⁶⁻⁹ The phase formation sequence for vanadium/silicon reactions has been determined by Tu et al.,¹⁰ Krautle et al.,¹¹ Psaras et al.,¹² Clevenger et al.,⁹ Nathan,¹³ Oya et al.¹⁴ and Moto et al.¹⁵ Finally, the phase formation sequence for titanium/silicon reactions was determined by Hung et al.,¹⁶ Holloway et al.,¹⁷ Raaijmakers et al.,¹⁸ Butz et al.,¹⁹ and Rubloff et al.²⁰

Nickel/silicon reactions were first studied by Tu et al.² They studied the reaction between a thin polycrystalline nickel film and a crystalline silicon wafer and determined that the first silicide phase to form was crystalline Ni₂Si at the nickel/crystalline-silicon interface. Later work by Olowolafe et al.³ confirmed Tu's results and determined the next phase to form after Ni₂Si was crystalline NiSi at the Ni₂Si/crystalline-silicon interface.

More recent work with nickel/amorphous-silicon thin film reactions has shown that the first silicide phase to form at the nickel/amorphous-silicon interface is amorphous-nickel-silicide.^{4,6-9,21} It has been shown

that this phase usually forms during deposition and that it will grow upon heating. Clevenger et al. has shown that the first crystalline silicide phase to form in nickel/amorphous-silicon reactions is Ni_2Si at the nickel/amorphous-nickel-silicide interface followed by NiSi at the Ni_2Si /amorphous-nickel-silicide interface.⁸ Finally, Ma et al.⁵ and Clevenger et al.⁹ have recently shown that after crystalline Ni_2Si forms at the nickel/amorphous-nickel-silicide interface, both crystalline Ni_2Si and amorphous-nickel-silicide grow simultaneously.

Vanadium/silicon reactions were first studied by Tu et al.¹⁰ They determined that the first silicide phase to form from a reaction between a polycrystalline vanadium thin film and a single crystal silicon wafer was crystalline VSi_2 . Later work by Krautle et al.¹¹ confirmed Tu's results. Nathan¹³ then showed that the first silicide phase to form from a vanadium/amorphous-silicon reaction was an amorphous-vanadium-silicide. Recently, Psaras et al.¹² and Clevenger et al.⁸ have determined that the first crystalline silicide phase to form from a vanadium/amorphous-silicon reaction was VSi_2 .

Titanium/silicon reactions have been studied extensively due to the applications of equilibrium C-54 TiSi_2 as a low resistivity gate material and as a source and drain diffusion barrier in MOS devices.²² Beyers and Sinclair²³ originally determined that the first crystalline silicide phase to form from a thin polycrystalline titanium film/single crystal silicon reaction was metastable C-49 TiSi_2 . They also determined that heating to elevated temperatures would cause the C-49 TiSi_2 to transform in equilibrium C-54 TiSi_2 . Titanium/amorphous-silicon reactions were first studied by Hung et al.¹⁶ They determined that the first crystalline silicide phase to form from these reactions was TiSi_2 . However, they did not

mention what type of TiSi_2 (C-49 or C-54) they observed. Later work by Holloway et al.¹⁷ and Raaijmakers et al.¹⁸ demonstrated that the first silicide phase to form from a titanium/amorphous-silicon reaction was amorphous-titanium-silicide. This amorphous-titanium-silicide was found to grow to several hundred angstroms in thickness before a crystalline titanium silicide phase would form.

2.2 Reaction Kinetics

In the past, most researchers have studied the reaction kinetics of crystalline silicide formation at a metal/silicon interface using a technique called Rutherford Backscattering.^{1,22} With this technique a metal film is deposited on a silicon wafer and then annealed to form a crystalline layer between the metal film and the wafer. The thickness of the layer is then inferred from measuring the intensity as a function of energy of He^+ ions which have been backscattered from the wafer surface.²⁴ With this technique, the growth rate of a crystalline silicide as a function of time and temperature of anneal can be measured.²⁴ If the growth is interface limited the interface reaction coefficient can be determined by:²⁵

$$\frac{dx}{dt} = K \quad (1)$$

where $\frac{dx}{dt}$ is the growth rate of the layer, and K the interface reaction coefficient. If the growth is diffusion limited, a diffusion coefficient can be determined by:²⁵

$$\frac{dx}{dt} = \frac{D}{x} \quad (2)$$

where D is the diffusion coefficient and x is the thickness of the silicide layer. Activation energies and pre-exponential coefficients can then be derived by measuring K or D as a function of temperature and using the following equations:

$$\ln K = \ln K_0 - \frac{Q}{kT} \quad (3)$$

for interface limited growth and

$$\ln D = \ln D_0 - \frac{Q}{kT} \quad (4)$$

for diffusion limited growth. There are many examples in the literature over the last 15 years of activation energies and pre-exponential coefficients for silicide growth which have been determined using equations 3 and 4.^{1,22,26}

For nickel/silicon reactions Tu et al.² was the first to use equation 4 to determine an activation energy of 1.5 ± 0.1 eV for the growth of Ni_2Si between a polycrystalline nickel film and a single crystal silicon wafer. Later Olowolafe et al.³ confirmed this result and also determine that the activation energy for NiSi growth at the Ni_2Si /crystalline silicon interface was 1.5 eV. For nickel/amorphous-silicon reactions, Clevenger et al.⁶⁻⁹ has recently determined with calorimetric techniques that the activation energy for Ni_2Si or NiSi growth is 1.5 ± 0.1 eV.

Tu et al.¹⁰ was the first to determine an activation energy for VSi_2 growth from a reaction between a thin polycrystalline vanadium film and a

single crystal silicon wafer. They suggested that the growth of VSi_2 was diffusion controlled with an activation energy of 2.9 eV. Later, Krautle et al.¹¹ also investigated vanadium/crystalline silicon reactions. They determined that the growth of VSi_2 was interface controlled with an activation energy of 1.7 ± 0.1 eV. Recent work by Psaras et al.¹² has shown that in vanadium/amorphous-silicon bilayer thin film reactions, the growth of VSi_2 is interface controlled with an activation energy of 2.3 ± 0.4 eV. This is in good agreement with the value of 2.5 ± 0.1 eV for VSi_2 growth from vanadium/amorphous-silicon reactions derived by Clevenger et al.⁹ using calorimetric techniques.

For titanium/silicon reactions, no one has been able to determine the activation energy for TiSi_2 growth between titanium and single crystal silicon. This is presumed to be due to the fact that TiSi_2 does not grow in a planar fashion at this interface.²² This has prevented the use of Rutherford Backscattering and equations 3 and 4 to determine kinetic activation energies for growth. However, for titanium/amorphous-silicon reactions, both amorphous-titanium-silicide and crystalline TiSi_2 grow in a one dimensional planar mode,¹⁶⁻¹⁸ which has allowed for the determination of activation energies using equations 3 and 4. Holloway et al.¹⁷ suggested that the activation energy for amorphous-titanium-silicide growth was 1.0 ± 0.1 eV. Hung et al.¹⁶ discovered that the activation energy for TiSi_2 growth from a titanium/amorphous-silicon reaction was 1.8 ± 0.1 eV. In Holloway's work, this activation energy was determined from thickness measurements of the amorphous-titanium-silicide phase using cross-sectional transmission electron microscopy. For Hung's work, this activation energy was derived from thickness measurements done with Rutherford Backscattering.

2.3 Thermodynamics of Intermetallic Phase Formation

Research in the field of thermodynamics of amorphous and crystalline intermetallic formation has become more popular in recent years due to the discovery by various researchers that thermodynamically unstable amorphous intermetallic phases could be formed by solid state reactions.^{8,17,18,27-30} Saunders and Miodownik³¹ were the first to suggest the use of Gibbs free energy versus composition diagrams to explain the thermodynamics behind amorphous phase formation. They proposed that an amorphous intermetallic phase would form under two conditions:^{28,31} first, the free energy of the amorphous intermetallic phase must be less than a mixture of the pure components and second, kinetic barriers must prevent stable crystalline intermetallics from forming. In this thesis, chapter 6 builds upon Saunders and Miodownik's work to discuss the various thermodynamic aspects of nucleation and growth of amorphous and crystalline intermetallic phases by a solid-state reaction.

2.4 Structural Transitions in Amorphous-Silicon Thin Films

Amorphous-silicon thin films have been extensively investigated due to their electronic device applications.³² However, the structure of amorphous-silicon thin films and its effect on the film's physical and electronic properties are not yet fully understood. The research on structural transitions in amorphous-silicon consists of only a few publications.³³⁻³⁹ Fan and Anderson³⁵ were the first to study the

crystallization temperature and heat of crystallization of amorphous-silicon thin films prepared by sputtering. Later Donovan et al.³⁶ determined that the heat of crystallization of amorphous-silicon films amorphized by ion bombardment was approximately -11.95 kJ/g-atom. Recently both Roorda et al.³⁷ and DeAvillez et al.³⁹ have seen calorimetric evidence for a low temperature structural relaxation in ion amorphized amorphous-silicon thin films (Roorda et al.) and electron beam evaporated amorphous-silicon thin films (DeAvillez et al.). Finally DeAvillez et al.³⁹ have also recently reported that an electron beam evaporated film underwent an endothermic reaction at high temperatures which was related to a change in the intermediate ordering in the thin film. In chapter 6, we report on the work of DeAvillez et al.

2.5 Explosive Silicidation

Explosive silicidation is a reaction where the transformation from a metal/amorphous-silicon multilayer thin film to a homogeneous crystalline silicide can be initiated at room temperature. Floro⁴⁰ was the first to report this reaction occurring in rhodium/amorphous-silicon multilayer films which had been electron-beam evaporated onto thermally oxidized silicon wafers with atomic concentration ratios of 1 Rh atom to 1 Si atom or 1 Rh atom to 2 Si atoms and with modulation periods varying from 57 to 70 nm. Later, Clevenger et al.⁶⁻⁹ reported explosive silicidation occurring in nickel/amorphous-silicon and vanadium/amorphous-silicon thin films with various atomic concentration ratios and modulation periods. Wickersham et al.⁴¹ have also recently reported explosive silicidation

occurring in zirconium/amorphous-silicon multilayer thin films with modulation periods varying from 7.4 to 29.2 nm and an atomic concentration ratio of 1 Zr atom to 2 Si atoms.

Besides the work of Clevenger et al.,⁶⁻⁹ there has been no published attempt at determining reaction front velocities, temperatures, and resulting crystalline silicide microstructures. However, phenomena of explosive crystallization of amorphous thin films has been reported for a variety of systems, including Sb,⁴² Ge,⁴³ and CdTe.⁴⁴ A model of how the reaction front velocity varies with the film thickness of these films has been proposed by van Saarloos and Weeks.⁴⁵

2.6 References

1. J.M. Poate, K.N. Tu and J.W. Mayer, Thin Films -- Interdiffusion and Reactions, Wiley, New York (1978)
2. K.N. Tu, W.K. Chu and J.W. Mayer, *Thin Solid Films*, 25, 403 (1975)
3. J.O. Olowolafe, M.-A. Nicolet and J.W. Mayer, *Thin Solid Films*, 38, 143 (1976)
4. M. Nathan, *Appl. Phys. Lett.* 49, 257 (1986)
5. E. Ma, W.J. Meng, W.L. Johnson, M.-A. Nicolet and M. Nathan, *Appl. Phys. Lett.* 53, 2033 (1988)
6. L.A. Clevenger, C.V. Thompson, R.C. Cammarata and K.N. Tu, *Appl. Phys. Lett.*, 52, 795 (1988)
7. L.A. Clevenger, C.V. Thompson, R.C. Cammarata and K.N. Tu, *Mater. Res. Symp. Proc.* 103, 191 (1988)

8. L.A. Clevenger, C.V. Thompson, A. Judas and K.N. Tu, First MRS International Meeting on Advanced Materials, 10, 431 (1989)
9. L.A. Clevenger, C.V. Thompson, R.R. De Avillez and K.N. Tu, to appear in the Proceedings of the Symposium on Chemistry and Defects in Semiconductor Heterostructures the Spring 1989 Meeting of the Materials Research Society, edited by M. Kawabe, T. Sands, E. Weber and R.S. Williams
10. K.N. Tu, J.F. Ziegler and C.J. Kercher, *Appl. Phys. Lett.*, 23, 498 (1973)
11. H. Krautle, M.-A. Nicolet and J.W. Mayer, *J. Appl. Phys.*, 45, 3304 (1974)
12. P. A. Psaras, M. Eizenberg and K.N. Tu, *J. Appl. Phys.*, 56, 3439 (1984)
13. M. Nathan, *J. Appl. Phys.*, 63, 5539 (1988)
14. G. Oya, H. Inabe, Y. Onodera, Y. Sawanda, *J. Appl. Phys.*, 53, 1115 (1982)
15. Y Moto, N. Toyota, K. Noto, K. Akutsu, M. Isino and T. Fukase, *J. Low Temp. Phys.*, 34, 617 (1979)
16. L.S. Hung, J. Gyulai, J.W. Mayer, S.S. Lau and M.A. Nicolet, *J. Appl. Phys.* 54, 5076 1983
17. K. Holloway and R. Sinclair, *J. Appl. Phys.* 61, 1359 (1987)
18. I.J.M.M. Raaijmakers, P.H. Oosting, and A.H. Reader, *Mater. Res. Symp. Proc.*, 103, 229 (1988)
19. R. Butz, G.W. Rubloff, T.Y. Tan and P.S. Ho, *Phys. Rev. B* 30, 5421 (1984)
20. G.W. Rubloff, R.M. Tramp and E.J. van Loenen, *Appl. Phys. Lett.* 48, 1600 (1986)

21. M.O. Aboelfotoh, H.M. Tawancy and F.M. d'Heurle, Appl. Phys. Lett. 50, 1453 (1987)
22. S.P. Muraka, Silicides for VLSI Applications, Academic, Orlando (1983)
23. R. Beyers and R. Sinclair, J. Appl. Phys. 57, 5240 (1985)
24. W.K. Chu, S.S. Lau, J.W. Mayer, H. Muller and K.N. Tu, Thin Solid Films, 25, 393 (1974)
25. U. Gosele and K.N. Tu, J. Appl. Phys., 53, 3252 (1982)
26. V. Koos and H.G. Neumann, Phys. Stat. Solid., 29, K115 (1975)
27. S. Herd, K.N. Tu and K.Y. Ahn, Appl. Phys. Lett., 42, 597 (1983)
28. R.B. Schwarz and W.L. Johnson, Phys. Rev. Lett., 51, 415 (1983)
29. E.J. Cotts, W.J. Meng and W.L. Johnson, Phys. Rev. Lett., 57, 2295 (1986)
30. H.U. Krebs and K. Samwer, Europhys. Lett., 2, 141 (1986)
31. N. Saunders and A.P. Miodownik, J. Mater. Res., 1, 38 (1986)
32. Properties of Silicon, INSPEC, The Institution of Electrical Engineers, London, 1988.
33. J. S. Lannin, J. of Non-Crystalline Solids 97, 39 (1987).
34. W. Sinke, T. Warabisako, M. Miyao, T. Tokuyama, S. Roorda and F. W. Saris, J. of Non-Crystalline Solids 99, 308 (1988).
35. J. C. C. Fan and C. Anderson, Jr., J. Appl. Phys. 52, 4003 (1981).
36. E. P. Donovan, F. Spaepen, D. Turnbull, J. M. Poate and D. C. Jacobsen, J. Appl. Phys. 57, 1795 (1985).
37. S. Roorda and W. C. Sinke, poster session, Symposium on Selected Topics in Electronic Materials, Materials Research Society 1988 Fall Meeting, Boston, Nov. 28 - Dec 3 (1988).
38. J. S. Lannin, J. of Non-Crystalline Solids 97 203 (1987).

39. R.R. DeAvillez, L.A. Clevenger and C.V. Thompson, to be published in *J. Mat. Research*
40. J.A. Floro, *J. Vac. Sci. Technol. A*, 4, 631 (1986)
41. L.A. Clevenger, C.V. Thompson, A. Judas and K.N. Tu, First MRS International Meeting on Advanced Materials, 10, 431 (1989)
42. T. Takamari, R. Messier and R. Roy, *Appl. Phys. Lett.* 20, 201 (1972)
43. A. Mineo, A. Matsuda, T. Kurasu and M. Kikuchi, *Solid State Comm.* 123, 329 (1973)
44. E.G. Colgan, B.S. Tsaur and J.W. Mayer, *Appl. Phys. Lett.* 37, 938 (1980)
45. W. von Saarloos and J. Weeks, *Phys. Rev. Lett.*, 51, 1046 (1983)

3 Experimental Procedures and Analysis

3.1 Experimental Methods Used

3.1.1 Deposition of Thin films

In this thesis, we have examined both controlled and explosive silicidation of metal/amorphous-silicon multilayer thin films (with nickel, vanadium or titanium as the chosen metal) with a combination of differential scanning calorimetry, transmission electron microscopy, high-speed optical pyrometry and high-speed photography. Free standing metal/amorphous-silicon multilayer films and pure amorphous-silicon thin films were used for calorimetric, plan view microscopy and X-ray analysis. Metal/amorphous-silicon multilayer films and pure amorphous-silicon films on substrates were used for cross-sectional transmission electron microscopy, and explosive reaction front temperature and velocity measurements.

Free standing metal/amorphous-silicon multilayer thin films were prepared by first coating microscope slides with Shipley 1400-25 photoresist to a thickness of 1 μm . The slides were then post-baked at 90°C for 25 minutes and loaded into an Airco Temescal CV-8 evaporator. Metal (either nickel, vanadium or titanium) and silicon were then alternately evaporated at room temperature with various modulation periods and atomic concentration ratios. These conditions are summarized in table 1. The vacuum before the deposition was never higher than 1×10^{-7} Torr and the total number of layers deposited was always 10 (5 metal and 5 silicon).

After the deposition, the slides were removed from the evaporator and soaked in acetone for 5 to 60 minutes to dissolve away the photoresist and remove the multilayer films. The films were then collected and used for a variety of experiments.

Table 1: Summary of the different samples used for controlled silicidation of metal/amorphous-silicon multilayer films with either nickel, vanadium or titanium as the chosen metal. The modulation period is defined as the sum of the thicknesses of the individual metal and silicon layers. All samples had a total of 5 periods.

type of thin film	atomic concentration ratio	modulation period (nm)
Ni/amorphous-Si	2 Ni to 1 Si	100.0
		50.0
		25.0
		14.0
	1 Ni to 2 Si	116.2
		95.0
		58.1
		33.0
V/amorphous-Si	1 V to 2 Si	50.0
		14.0
Ti/amorphous-Si	1 Ti to 2 Si	30.0

Free-standing pure amorphous-silicon thin films were prepared by first evaporating silicon onto photoresist coated glass slides as described above for metal/amorphous-silicon multilayer thin films. The deposition rate was either 0.2 or 0.3 nm/sec and the total film thickness was 21.2 nm. After deposition, the slides were taken out of the evaporator and the amorphous-silicon films were removed from the substrates as described above.

For the cross-sectional transmission electron microscopy of multilayer films, the films were evaporated onto thermally oxidized silicon wafers using the same deposition conditions as for the free-standing thin films. The atomic concentration ratio of nickel to silicon was 2 Ni atoms to 1 Si atom. This corresponded to a nickel to silicon layer thickness ratio of 1 to 1 and a modulation period equal to twice the nickel or silicon layer thickness.

For explosive silicidation reaction front velocity and temperature measurements, nickel/amorphous-silicon multilayer films were deposited onto photoresist coated glass slides as described above, with the modification that the films were not removed from the substrate, and that they were deposited by alternate ion-beam-sputtering of nickel and silicon. For explosive silicidation experiments, two different total film thicknesses of 0.73 μm and 1.62 μm were deposited. For the 0.73 μm thick multilayer films, modulation periods of 14 nm, 20.8 nm, and 28 nm were prepared, and for the 1.63 μm multilayer thin films modulation periods of 14 nm, 28 nm and 56 nm were deposited. This resulted in six different films for reaction front temperature and velocity measurements.

3.1.2 Calorimetry

Power compensated differential scanning calorimetry was used to measure the heat evolved from amorphous and crystalline silicide formation and growth or structural transitions in amorphous-silicon and amorphous titanium silicide. These measurements are made as either a function of temperature (constant-heating-rate calorimetry) or time (isothermal calorimetry). With calorimetry, a reference, which does not go through any transitions, and a sample are heated at a constant-heating-rate or annealed at a constant temperature and the calorimeter adjusts the power input difference between the reference and the sample to keep them at the same temperature T . When a reaction occurs in the sample, this power input difference is equivalent to the heat released pure unit time, dH/dt , of the sample. The data obtained from calorimetry is dH/dt versus temperature (constant-heating-rate) or time (isothermal).

The starting temperature for all the calorimetry used in this work was 310 K and the sensitivity of the calorimeter was either 0.5 or 1.0 mcal/sec. For constant-heating-rate experiments, the heating rate was varied from 1.25 to 40 K/min, depending on the sample, and the maximum temperature used was 900 K. After the initial run, the samples were quenched from 900 K to 310 K at 320 K/min, and a second run was made without disturbing the sample and with the same heating rate used in the first run. The second DSC trace was then used as the baseline and subtracted from the first trace.

For isothermal calorimetry experiments, a sample was heated at 320 K/min to a temperature approximately 20 K below the desired reaction

temperature and allowed to stabilize. After stabilization, the sample was heated at 320 K/min to the desired reaction temperature and held at this temperature while the heat released during either silicide formation or structural transitions as a function of time was measured. After the reaction was completed, the sample was quenched at 320 K/min to 310 K. The heating treatment of the first run was then repeated and the isothermal trace at the desired temperature was used as a baseline and subtracted from the first run. For calorimetric analysis of metal/amorphous-silicon multilayer thin film reactions, approximately 2 mg of free-standing thin film was used. While for the calorimetric analysis of amorphous-silicon structural relaxations, the sample size varied between 0.5 and 1.0 mg.

3.1.3 Transmission Electron Microscopy

Cross-sectional transmission electron microscopy was used for the analysis of structural changes that occurred in metal/amorphous-silicon multilayer thin films upon heating. Plan view transmission electron microscopy was used to examine the microstructures of free-standing amorphous-silicon thin films before and after annealing and to examine explosively formed crystalline metal silicides. Cross-sectional transmission electron microscopy sample preparation began by loading thermally oxidized (100) silicon wafers into an electron-beam evaporator. A 7.5 nm layer of NiCr followed by the multilayer film was then evaporated onto the wafers. The layer of NiCr improved the adhesion of the multilayer thin films during sample preparation, and it was shown to not react with the multilayer films. Ten alternating layers of metal (either nickel,

vanadium or silicon) were deposited as described in section 3.1.1. The thickness of the metal and the silicon were always the same as that of the free-standing multilayer films used for corresponding calorimetry experiments. If any heat treatment was required, the samples were heated with the multilayer film surface in contact with the sample pan in the differential scanning calorimeter at 20 K/min to the temperature of interest and then quenched at 320 K/min to room temperature. The highest annealing temperature was always chosen to correspond to exothermic or endothermic reactions observed in the calorimetric data of the corresponding free-standing film. The samples were then epoxied together, with the multilayer films facing each other. Next, the samples were mounted in the middle of a 3 mm molybdenum rod which had a 0.6 mm wide by 0.5 in long slit down the center. This rod was then sliced in cross-section into 500 μm thick disks. Each disk was mechanically polished to a thickness of 100 μm and then dimpled to a thickness of 5 μm at the metal/amorphous-silicon multilayer thin film/ SiO_2 interface. The samples were then ion milled on a liquid nitrogen cooled cold stage until the multilayer film was electron transparent. During sample preparation, the films were never heated over 323 K. Microstructural analysis was done using a JEOL 200 electron microscope operating at 200 KeV. Composition analysis of the multilayer thin films was done using energy dispersive X-ray analysis in a Vacuum Generator HB5 scanning transmission electron microscope (STEM) operating at 100 KeV. The estimated size of the STEM probe including beam broadening effects was 5 nm.

Plan view transmission electron microscopy was done to examine the structure of explosively formed nickel silicide and thermally annealed amorphous-silicon. The films were free standing thin films supported by

copper grids. Structural analysis was done using a JEOL 200 electron microscope operating at 200 KeV.

3.1.4 X-ray Diffraction

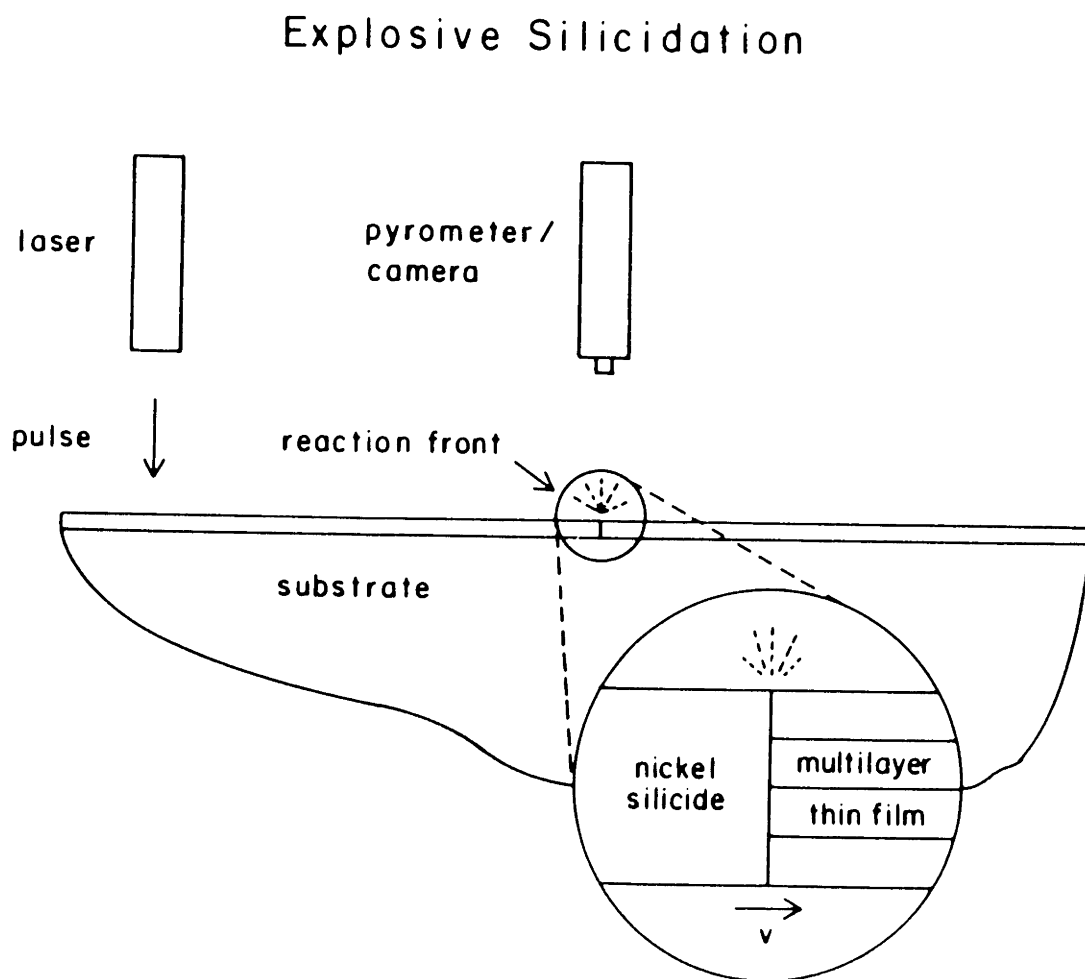
For phase identification, we used thin film X-ray diffraction of free-standing films that had been annealed in the calorimeter. The system used was a Rigkai 300 thin film X-ray diffraction apparatus with a rotating copper anode, operating at 10 kW. The incident angle of the X-ray beam was 8 degrees and the scan rate was 10°/min. The data obtained was compared to Joint Committee on Powder Diffraction Standards to identify the crystalline phases present in the thin film.

3.1.5 High Speed Pyrometry/Photography

The experimental configuration for high speed photography and temperature measurements is schematically illustrated in figure 1. The reaction front velocities were measured using a Kodak Ekta Pro high-speed camera shooting at 6000 frames/sec. The temperature measurements were done with a modified Capintec Ratioscope II two-color pyrometer operating at narrow near infrared wavelength bands centered at 0.81 μm and 0.95 μm . A digital oscilloscope and specially designed amplification system were used to obtain a temperature data sampling rate of 1 measurement every 500 nsec.¹

Both the optical pyrometer and the high speed camera were mounted directly above the multilayer thin film. The distance between the pyrometer and multilayer thin film was 15 cm and the distance between the high

Figure 1 Schematic illustration of the experimental configuration for high-speed photography and temperature measurements.



speed camera and the multilayer thin film was 30 cm. The field of view of the optical pyrometer was approximately 0.7 cm, and for the high speed camera the field of view was approximately 5 cm. The explosive reaction was initiated outside the field of view of the optical pyrometer and high speed camera. After initiation, the reaction front propagated across the field of view of the pyrometer and camera.

The optical pyrometer was calibrated by first preparing a 4 gram mixture of high purity nickel and silicon with an atomic concentration ratio the same as the multilayer thin films (2 Ni atoms to 1 Si atom). This mixture was then melted at approximately 1800 K and allowed to congruently solidify into Ni_2Si . The intensity of infrared wavelengths at the melting point of Ni_2Si was then recorded and these values were assigned to correspond to the melting temperature of Ni_2Si (1565 K).² These values were used as a calibration standard for measurements of the temperature of the explosive reaction front.

3.2 Analysis of Calorimetric Data

3.2.1 Activation Energies

In chapter 2, we demonstrated how activation energies for silicide growth could be determined by measuring the thickness of the growing silicide phase as a function of time and annealing with Rutherford Backscattering. Interface reaction coefficients or diffusion coefficients could then be calculated from equations 1 or 2 of chapter 2, and activation energies for growth could be calculated from equations 3 or 4 of chapter 2. Similar information about activation energies for silicide growth and formation can be obtained with constant-heating-rate calorimetric analysis.

With constant-heating-rate calorimetry, one measures the heat released per unit time, dH/dt , from the sample versus temperature T at a heating rate R . dH/dt is directly proportional to the volume transformed per unit time (i.e. the reaction rate) of the forming silicide by,

$$\frac{dH}{dt} = (\Delta H_f) (V_f) \frac{dX_v}{dt} \quad (1)$$

where ΔH_f is the heat of formation of the silicide, V_f the final volume transformed and dX_v/dt the change in the fraction transformed with time.

The activation energy for a thermally activated process can be determined from calorimetric data when the reaction rate dX_v/dt is a separable function of the fraction transformed and the temperature, i.e.^{3,4}

$$\frac{dX_v}{dt} = f(X_v) g(T) \quad (2)$$

$g(T)$ can be expressed as

$$g(T) = C_o \exp\left(-\frac{Q_o}{KT}\right) \quad (3)$$

Combining equations 2 and 3, with the fact that the scan rate R is equal to dT/dt where T is temperature and t is time, we obtain

$$\frac{dX_v}{f(X_v)} = \frac{C_o}{R} \exp\left(-\frac{Q_o}{KT}\right) dT \quad (4)$$

The left hand side of equation 4 can be integrated from $X_v=0$ to $X_v=X_p$, where X_p is the fraction transformed at the peak in dH/dt versus

temperature for the thermally activated process. The right side of equation 4 can be integrated from $T=T_0$ to $T=T_p$ where T_0 is the temperature at which the reaction starts and T_p is the temperature at a scan rate R at which there is a peak in dH/dt versus temperature data. Equation 4 then becomes

$$\int_0^{X_p} \frac{dX_v}{f(X_v)} = \int_{T_0}^{T_p} \frac{C_0}{R} \exp\left(-\frac{Q_0}{KT}\right) dT \quad (5)$$

Boswell⁴ has shown that $\int_0^{X_p} \frac{dX_v}{f(X_v)}$ is a constant whose value does not depend on the scan rate, but does depend on the fraction transformed X_p and the form of $f(X_v)$.

The form of $f(X_v)$ depends on whether the process is nucleation, or growth controlled. Assuming that the fraction transformed at the peak temperature X_p does not depend on scan rate, we obtain

$$R C_1 = \int_{T_0}^{T_p} \exp\left(-\frac{Q_0}{KT}\right) dT \quad (6)$$

where C_1 is a constant which can be expressed as

$$C_1 = \frac{\int_0^{X_p} \frac{dX_v}{f(X_v)}}{C_0} \quad (7)$$

The right hand side of equation 6 can be integrated, assuming $T_p \gg T_0$ and $Q_0/kT \gg 1$ to give

$$\int_{T_0}^{T_p} \exp\left(-\frac{Q_0}{KT}\right) dT \approx \frac{KT_p^2}{Q} \exp\left(-\frac{Q_0}{KT_p}\right). \quad (8)$$

Combining equations 6 and 8 and rearranging, we obtain^{3,4}

$$\ln \frac{R}{T_p^2} = C_2 - \frac{Q_0}{KT_p} \quad (9)$$

where C_2 is

$$C_2 = \frac{K}{QC_1} \quad (10)$$

Equation 9 can then be used to determine the activation energy for a reaction by plotting $\ln (R/T_p^2)$ for different scan rates versus $1/kT_p$ for the peak temperature at a scan rate R , and taking the slope of a straight line through the data points to be Q . Clevenger et al.⁵ has shown this technique to be effective in measuring activation energies for crystalline silicide formation in nickel/amorphous-silicon and vanadium/amorphous-silicon thin film reactions.

3.2.2 The Analysis of Nucleation Controlled Versus Growth Controlled Phase Selection in Thin Film Reactions Using Calorimetric Techniques

As shown in chapter 2, Rutherford Backscattering can be used to determine activation energies and pre-exponential coefficients for amorphous and crystalline silicide growth at a metal/silicon interface.

There are two major problems with using Rutherford Backscattering to investigate silicide formation: this technique is sensitive only to compositional, not structural, changes, and the probe size of the beam is limited to sizes greater than approximately 1 μm .⁶⁻¹⁰ These facts limit the depth resolution of Rutherford Backscattering to approximately 10 nm and the lateral resolution to an area the size of the beam diameter. This allows Rutherford Backscattering to be used only to study growth of silicides phases after they are already 10 nm thick. One cannot use Rutherford Backscattering to study the earlier stages of silicide formation in order to determine whether nucleation or growth mechanism controls phase selection in thin film reactions. In order to study the early stage of nucleation and growth of amorphous and crystalline silicides, we have developed a methodology that uses calorimetric analysis combined with cross-sectional transmission and scanning transmission electron microscopy and thin film X-ray diffraction.

With calorimetric analysis, the change in the heat released with time due to an atomic interaction, whether this interaction is due to phase formation, structural relaxations or atomic interdiffusion, is measured as a function of temperature (constant-heating-rate calorimetry) or time (isothermal calorimetry). This change in this heat released with time is related to the volume fraction transformed (assuming intermetallic phase formation) by:

$$\frac{dH}{dt} = -(\Delta H_f)(V_f) \frac{dX_v}{dt} \quad (11)$$

where ΔH_f is the heat of formation of the silicide, V_f the final volume transformed and $\frac{dX_v}{dt}$ the change in the fraction transformed of the forming phase with time. If silicide phase formation is nucleation controlled, $\frac{dH}{dt}$ will be of the form:¹¹

$$\frac{dH}{dt} = (-\Delta H_f) (V_f) n C t^{n-1} e^{-\alpha t^n} \quad (12)$$

where t is time, n the Avrami exponent and C has the form $C=C_0e^{(-Q/kT)}$ where Q is an energy which is a function of the activation energies for nucleation and growth. If no nucleation is occurring, $\frac{dH}{dt}$ will have the following form for interface controlled growth ¹²

$$\frac{dH}{dt} = (-\Delta H_f) (V_f) \frac{K_{l,o}}{w_{max}} e^{\left(\frac{-Q_l}{kT}\right)} \quad (13)$$

and the following form for diffusion controlled growth,¹²

$$\frac{dH}{dt} = (-\Delta H_f) (V_f) \frac{D_{p,o}}{w_{max} w} e^{\left(\frac{-Q_p}{kT}\right)} \quad (14)$$

where w is the thickness of the silicide layer, w_{max} the maximum thickness that the silicide layer grows to, $K_{l,o}$ and $D_{p,o}$ are temperature independent constants for interface limited and diffusion limited growth, respectively, and Q_l and Q_p are activation energies for interface limited and diffusion limited growth respectively.

A major advantage of calorimetric analysis is that for a nucleation controlled reaction (equation 12), interface controlled reaction (equation 13), or diffusion controlled reaction (equation 14) the change in the heat released

with time will be different. This allows us to use calorimetry, in conjunction with electron microscopy and X-ray diffraction, to determine whether nucleation or growth controls phase selection in thin film reactions. In this thesis we use equations 11 - 14 to determine whether nucleation or growth mechanisms control amorphous and crystalline silicide formation in nickel/amorphous-silicon multilayer thin film reactions (section 4.5) and vanadium/amorphous-silicon multilayer thin film reactions (section 5.2).

3.3 References

1. T. Picone, M.S. thesis, Massachusetts Institute of Technology (1984)
2. Sebina an Mey, Z. Metallkle 77, 805 1986
3. H.E. Kissinger, Anal. Chem., 29, 1702 (1957)
4. P.G. Boswell, J. Thermal. Anal. 18, 353 (1980)
5. L.A. Clevenger, C.V. Thompson, R.C. Cammarata and K.N. Tu, Appl. Phys. Lett., 52, 795 (1988)
6. S.P. Muraka, Silicides for VLSI Applications, Academic, Orlando (1983)
7. J.M. Poate, K.N. Tu and J.W. Mayer, Thin Films - Interdiffusion and Reactions, Wiley, New York (1978)
8. M.-A. Nicolet, J.W. Mayer and I.V. Mitchell, Science, 177, 841 (1972)
9. W.K. Chu, S.S. Lau, J.W. Mayer, H. Muller and K.N. Tu, Thin Solid Films, 25, 393 (1974)
10. V. Koos and H.G. Neumann, Phys. Stat. Solid., 29, K115 (1975)

11. J.W. Christian, The Theory of Transformations in Metals and Alloys, Pergamon, Oxford (1965), first edition
12. U. Gosele and K.N. Tu, J. Appl. Phys., 53, 3252 (1982)

4 Controlled Silicidation of Nickel/Amorphous-Silicon Multilayer Thin Films with Atomic Concentration Ratios of 2 Ni Atoms to 1 Si Atom

4.1 Introduction

In the literature review (chapter 2) we discussed contributions to the understanding of nickel/crystalline silicon and nickel/amorphous-silicon reactions by various authors. In this section, we build upon this previous work to investigate nickel/amorphous-silicon multilayer thin film reactions. The main goal of this section is to obtain a quantitative understanding of the silicide reactions that occur when a nickel/amorphous-silicon multilayer film is heated, with an emphasis on determining kinetic activation energies for silicide formation, and on determining the atomic mechanism that controls silicide phase selection.

This chapter is divided into 5 sections. In section 4.2, we investigate the formation sequence of silicide phases that form upon heating a nickel/amorphous-silicon multilayer thin film as a function of modulation period using calorimetric, thin film X-ray diffraction, and cross-sectional microscopy analysis. In section 4.3, we move on to discuss the reaction kinetics of these silicide phases, while in section 4.4, we discuss the kinetic modeling of increasing peak temperatures in constant-scan-rate calorimetric data with increasing modulation periods for silicide growth reactions. Section 4.5 discusses the use of thermodynamic, constant-scan-rate calorimetric and isothermal calorimetric analysis to determine the

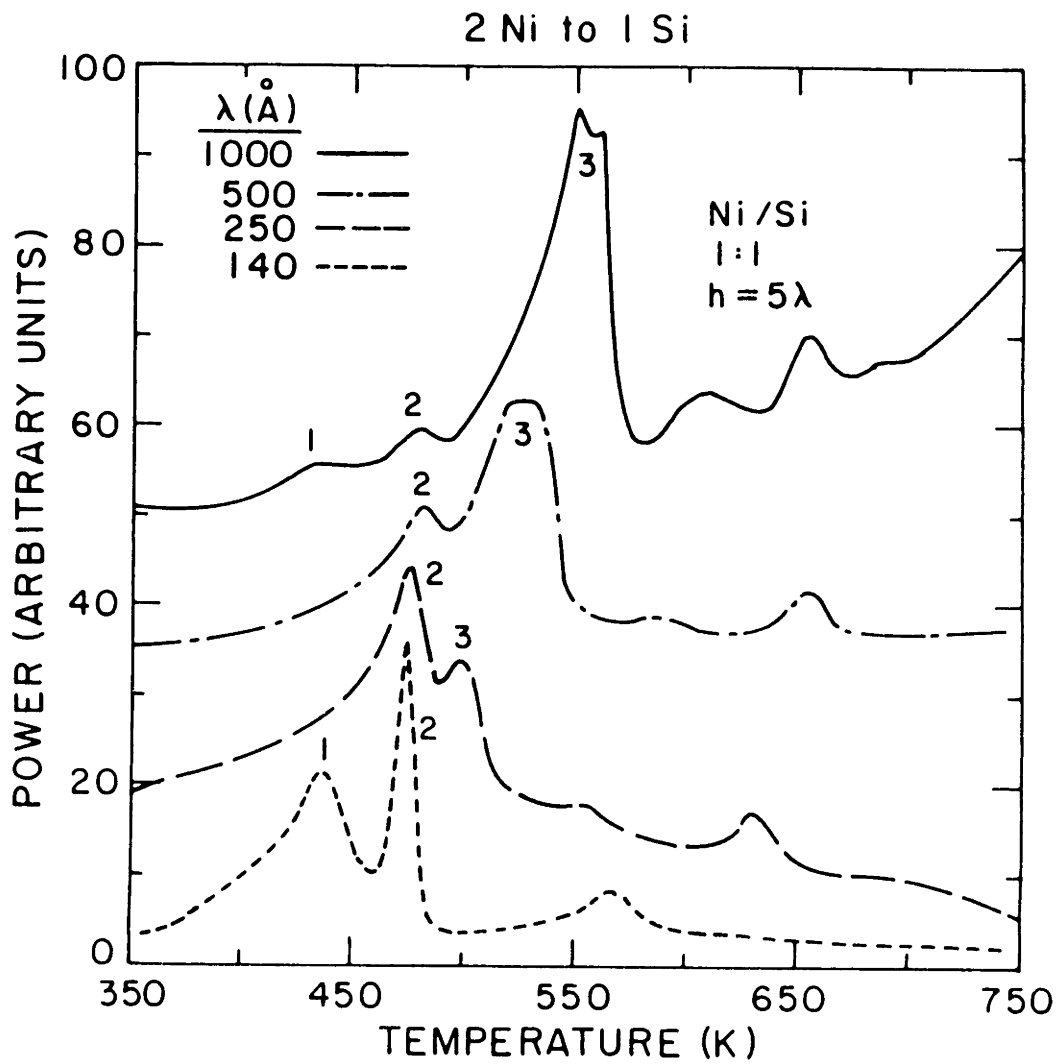
atomic mechanism responsible for silicide phase selection in nickel/amorphous-silicon multilayer thin films. Finally, in section 4.6 we present an analysis which predicts the relative magnitudes of the nucleation surface energies of both amorphous and crystalline nickel silicide phases.

4.2 Phase Formation Sequence Upon Heating Nickel/Amorphous-Silicon Thin Films with Atomic Concentration Ratios of 2 Ni Atoms to 1 Si Atoms

To determine the phase formation sequence in nickel/amorphous-silicon multilayer thin film reactions, constant-scan-rate calorimetry, thin film X-ray diffraction and cross-sectional transmission electron microscopy were performed on nickel/amorphous-silicon multilayer films with an atomic concentration ratio of 2 Ni atoms to 1 Si atom. In figure 1, we present constant-heating-rate calorimetric traces for nickel/amorphous-silicon multilayer thin films with an atomic concentration ratio of 2 Ni atoms to 1 Si atom. The modulation period of the films was either 14, 25, 50 or 100 nm. The scan rate for all the traces is 20 K/min and each trace has multiple peaks which correspond to exothermic reactions. As the modulation period of the multilayer film is changed from 14 to 100 nm, peak 1 disappears, peak 2 decreases in intensity but does not disappear or shift in temperature and peak 3 appears for the 25 nm multilayer thin film and increases in peak temperature with increasing modulation period.

To determine which of the exothermic peaks in figure 1 were due to crystalline silicide formation, the 14 nm and the 100 nm multilayer thin

Figure 1 Constant-heating-rate differential scanning calorimeter traces for nickel/amorphous-silicon multilayer films with atomic concentration ratios of 2 Ni to 1 Si and modulation periods of 14, 25, 50 and 100 nm.



films were heated in the calorimeter at 20 K/min to 450 K, 475 K, 550 K and 850 K and cooled at 320 K/min to room temperature for thin film X-ray analysis. X-ray data for both multilayer thin films in the as-deposited condition and for samples annealed to 450 K, indicated the presence of only nickel and amorphous-silicon. This indicated that peak 1 of figure 1 was not due to crystalline silicide formation. X-ray data for the multilayer films heated to 475 K compared with the data from reference 1 indicated the formation of Ni_2Si . This allowed us to tentatively identify peak 2 with the formation of Ni_2Si . For the 14 nm multilayer thin film this reaction completely transforms the film into Ni_2Si , while for thicker multilayer films it did not. X-ray data for the 100 nm multilayer film heated to 550 K, indicated the further conversion of the multilayer thin film into Ni_2Si , suggesting that peak 3 of figure 1 was due to the one-dimensional growth of Ni_2Si to transform the multilayer thin films with modulation periods greater than 25 nm into Ni_2Si .

To obtain a clearer interpretation of the reactions occurring as a result of heating these films, the 100 nm multilayer thin film was prepared for cross-sectional transmission electron microscopy in the as-deposited condition and after heating to 460 K, 490 K and 535 K. Bright field micrographs are shown in figures 2-5. Figure 2 shows an area of an as-deposited sample. This figure shows that the nickel layers have a polycrystalline structure. The lighter colored layers are amorphous-silicon and have a typical amorphous appearance. Between the nickel and amorphous-silicon layers there is a region of darker contrast which has no crystalline structure. Microdiffraction patterns taken from this layer suggests that it is amorphous and we identify it as an amorphous-nickel-silicide. In the as-deposited film, this amorphous-nickel-silicide between

Figure 2 Bright field transmission electron microscope image of an as deposited nickel/amorphous silicon multilayer thin film; (a) polycrystalline nickel; (b) gray featureless layer with no crystalline contrast; (c) amorphous silicon. The microdiffraction pattern (d) is taken from layer (b) and indicates that this layer is an amorphous nickel silicide

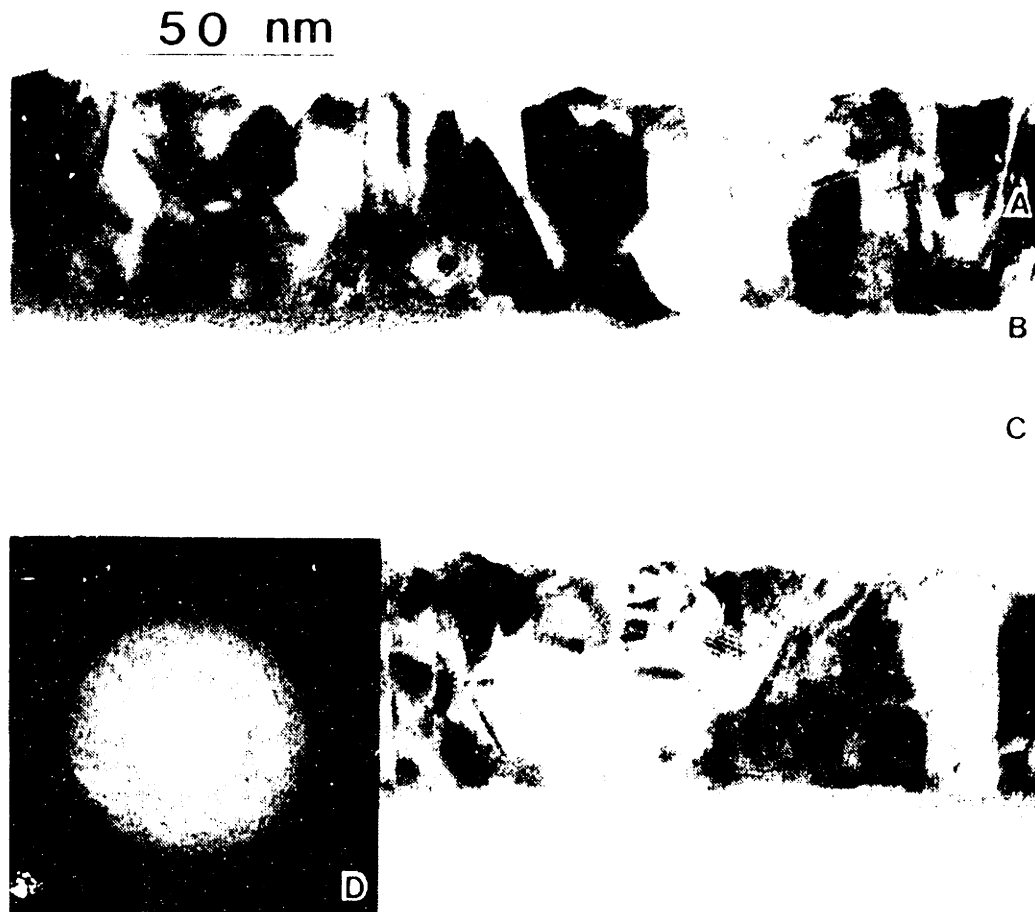


Figure 3 Bright field transmission electron microscope image of the multilayer film of figure 2 which has been heated at 20 K/min to 460 K and quenched to room temperature; (a) polycrystalline nickel; (b) amorphous-nickel-silicide; (c) amorphous-silicon.

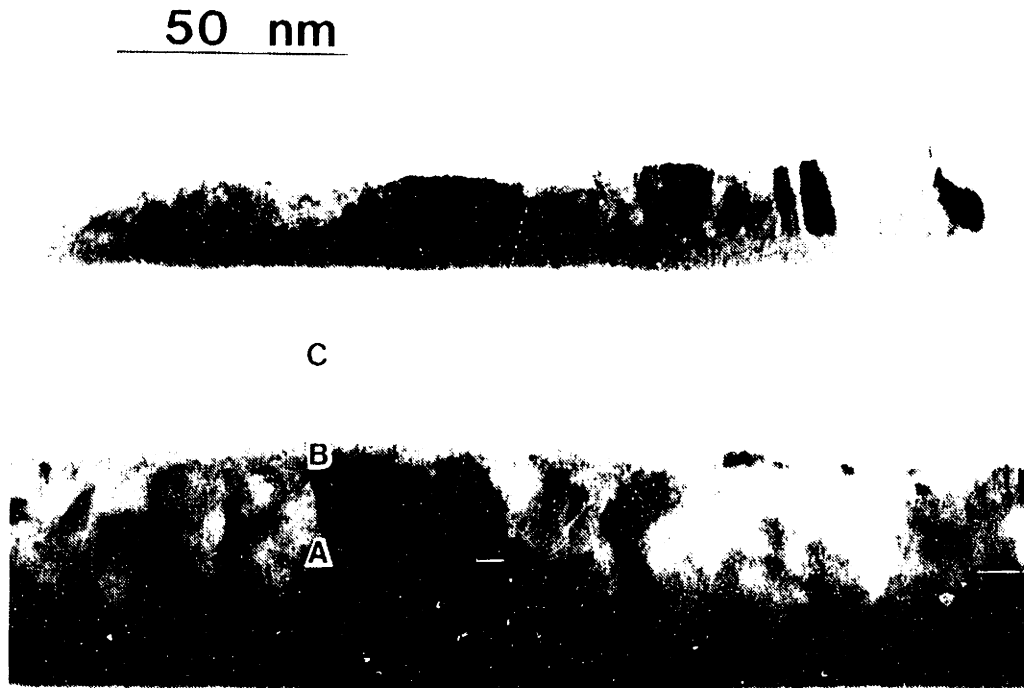


Figure 4 Bright field transmission electron microscope image of the multilayer film of figure 2 which has been heated at 20 K/min to 490 K and quenched to room temperature; (a) polycrystalline nickel; (b) Ni₂Si; (c) amorphous-nickel-silicide; (d) amorphous-silicon. Arrows point to the layer of polycrystalline Ni₂Si which has formed at the nickel/amorphous nickel-silicide interface.

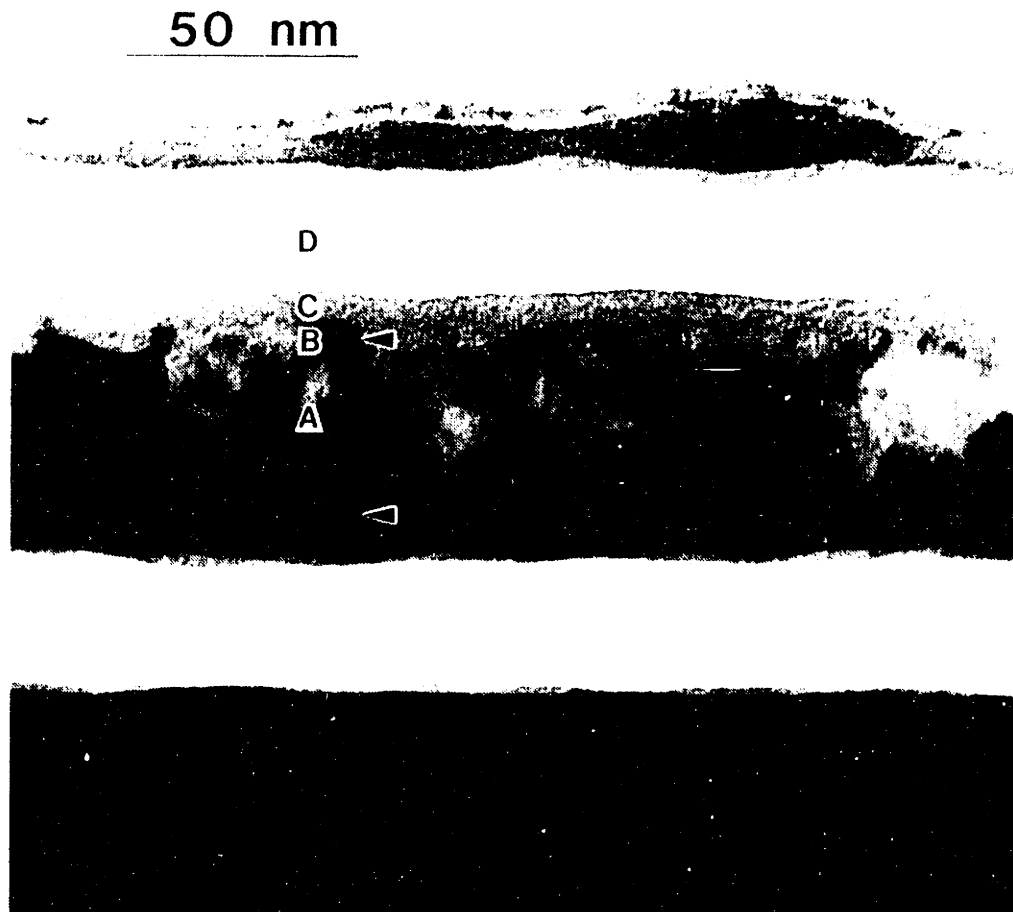
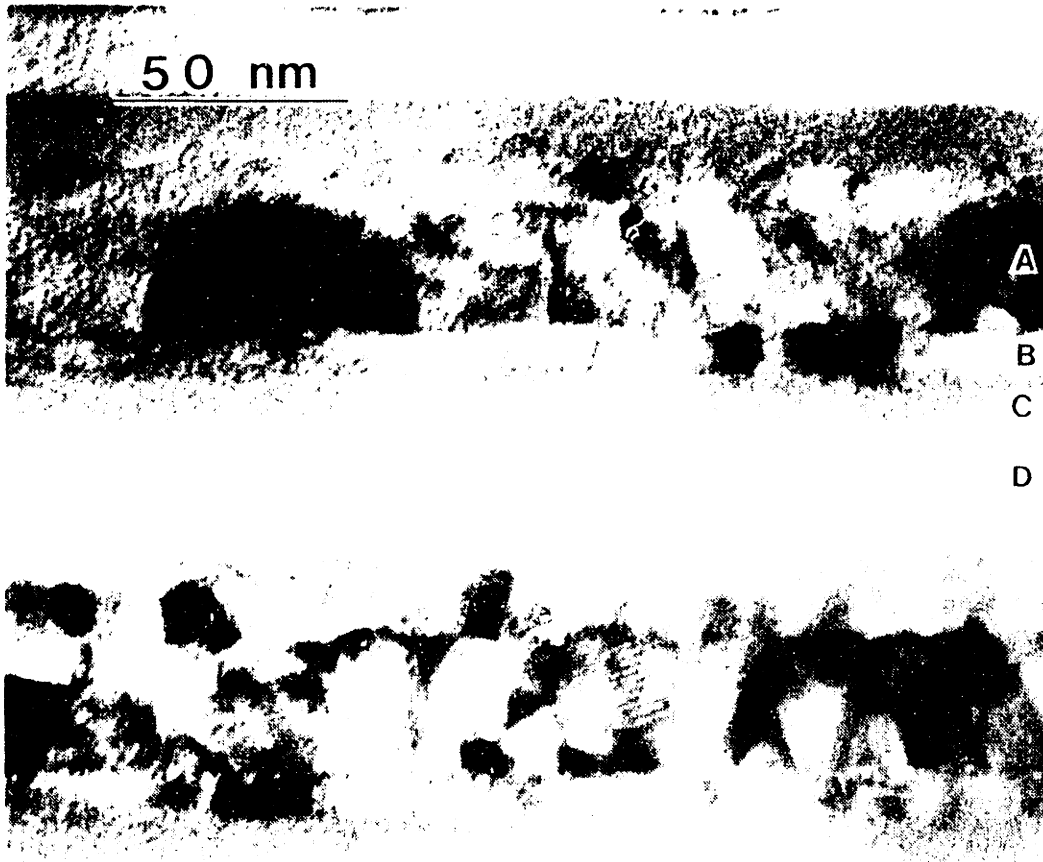


Figure 5 Bright field transmission electron microscope image of the multilayer film of figure 2 which has been heated at 20 K/min to 535 K and quenched to room temperature; (a) polycrystalline nickel; (b) Ni_2Si ; (c) amorphous-nickel-silicide; (d) amorphous silicon



the nickel and silicon layers has a thickness of approximately 4 nm. This amorphous-nickel-silicide layer was found by cross-sectional electron microscopy to exist in all the as-deposited nickel/amorphous-silicon multilayer thin films.²⁻⁵

Figure 3 shows a bright field micrograph of a portion of a 100 nm multilayer film heated to 460 K. This corresponds to a temperature slightly below the temperature of peak 2 in figure 1. The structure of the film heated to 460 K is similar to that of the as-deposited multilayer film in figure 2. The amorphous-nickel-silicide is still present in this sample and has grown to a thickness of about 5.5 nm. At this annealing temperature, there is no microscopic indication of crystalline silicide formation. For the 14 nm multilayer film, it has been previously shown that this amorphous-nickel-silicide growth completely consumes the amorphous-silicon layer and then stops,²⁻⁵ leading to peak 1 of figure 1. In the 100 nm multilayer film peak 1 is not seen because the amorphous-silicide phase continues to grow until the temperature of peak 2 due to the larger amounts of amorphous-silicon and nickel present in the as-deposited film.

The structure of a multilayer film with a 100 nm modulation period after heating to 490 K is shown in figure 4. The structure of this film is similar to that of the sample heated to 460 K in figure 3. Figure 4 also shows that a 5.0 nm thick layer of crystalline Ni₂Si has formed between the nickel and amorphous-nickel-silicide layers. This allows identification of peak 2 in figure 1 with the formation of a continuous layer of crystalline Ni₂Si between the amorphous-nickel-silicide and polycrystalline nickel. As shown in figure 5, heating a film to 535 K causes the amorphous-silicon and polycrystalline nickel to decrease in thickness while the amorphous-nickel-silicide and the crystalline Ni₂Si increase in thickness. This allows

identification of peak 3 in figure 1 as corresponding to the simultaneous growth of both amorphous-nickel-silicide and crystalline Ni_2Si . This simultaneous growth of amorphous-nickel-silicide and crystalline Ni_2Si has also recently been reported by Ma et al.⁶ and Clevenger et al.⁵ The double hump structure of peak 3 is due to the amorphous-nickel-silicide undergoing one-dimensional growth to consume the amorphous-silicon layer and stopping (the first hump) and Ni_2Si undergoing one-dimensional growth to consume the amorphous-nickel-silicide and remaining nickel to transform the film completely to Ni_2Si (second hump).

Thus, constant-scan-rate calorimetry, thin film X-ray diffraction, and cross-sectional transmission electron microscopy indicate the following reaction sequence for nickel/amorphous-silicon multilayer films with atomic concentration ratios of 2 Ni atoms to 1 Si atom. During deposition, an 4.0 nm thick layer of amorphous-nickel-silicide is formed between the nickel and amorphous-silicon layers. Heating at 20 K/min causes the amorphous-nickel-silicide layer to grow. If the modulation period of the thin film is less than 14 nm, this growth will consume the amorphous-silicon and stop at approximately 460 K leading to peak 1 of figure 1. For longer modulation period multilayer films, this growth continues above 460 K due to the larger amounts of amorphous-silicon and nickel present in the as-deposited thin film. Heating to temperatures above 475 K causes a continuous layer of Ni_2Si to form at the nickel/amorphous-nickel-silicide interface. For the 14 nm multilayer thin film, this formation completely transforms the film into Ni_2Si . For longer multilayer thin films, further heating causes amorphous-nickel-silicide and Ni_2Si to grow simultaneously, leading to peak 3 of figure 1.

4.3 Activation Energy of Silicide Formation in Nickel/Amorphous-Silicon Multilayer Thin Films with Atomic Concentration Ratios of 2 Ni Atoms to 1 Si Atom

Activation energies for the formation of a continuous layer of Ni₂Si between the nickel and the amorphous-nickel-silicide layer and for the one-dimensional growth of both amorphous-nickel-silicide and Ni₂Si can be determined using calorimetry. In figure 6, we present constant-heating-rate DSC traces for the 100 nm multilayer thin film of figure 1 for five scan rates varying from 1.25 to 20 K/min. Figure 6 shows that as the heating rate is decreased, the peaks shift to lower temperatures. This peak shift with decreasing scan rate is related to the activation energy of the reaction using equation 6 developed in section 3.2. In this section, we determined that the activation energy Q , of a reaction can be determined from the slope of a plot of $\ln(H/T_p^2)$ versus $1/T_p$, where H is the heating rate, T_p is the peak temperature observed at heating rate H . Figure 7 shows plots of $\ln(H/T_p^2)$ versus $1/T_p$ for the data of figure 6. From this analysis, Q for peaks 2,3, and 4 was determined to be 1.4, 1.5 and 1.5 eV respectively. These activation energies correspond to the formation of a continuous layer of Ni₂Si between the nickel and amorphous-nickel-silicide layers (1.4 eV), the one-dimensional growth of amorphous-nickel-silicide (1.5 eV) and the one-dimensional growth of Ni₂Si (1.5 eV).

Figure 6 Constant-heating-rate DSC traces for multilayer films with atomic concentration ratios of 2 Ni atoms to 1 Si atom and with a modulation period of a 100 nm. Each curve corresponds to a different scan rate.

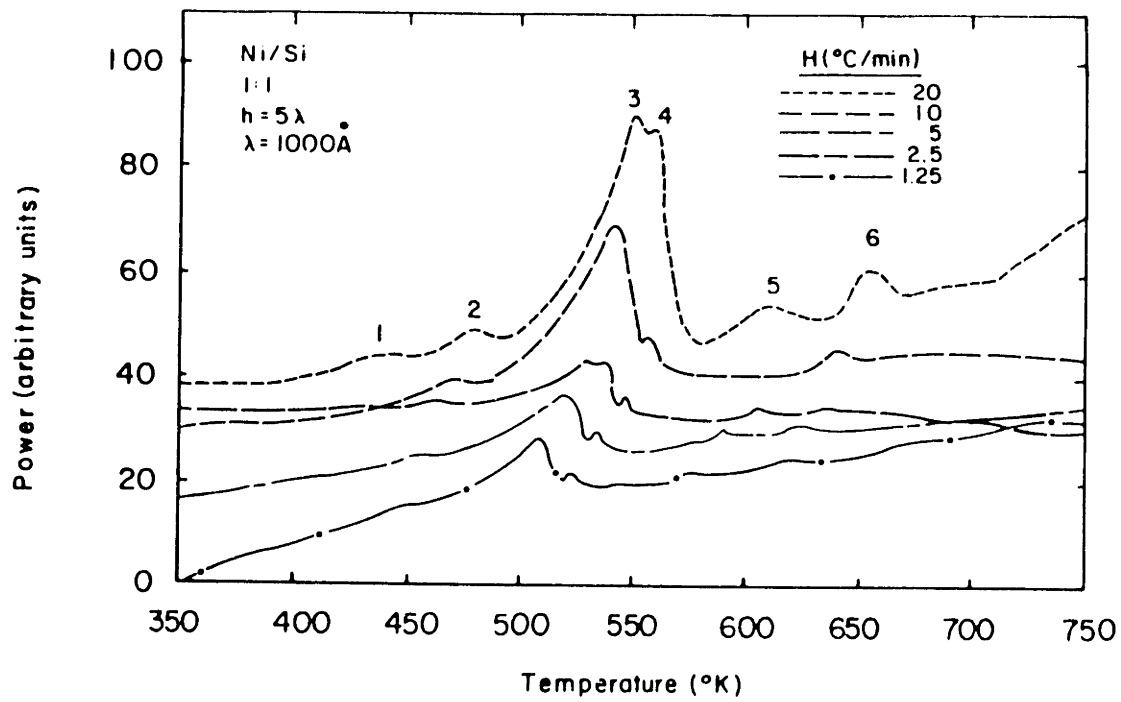
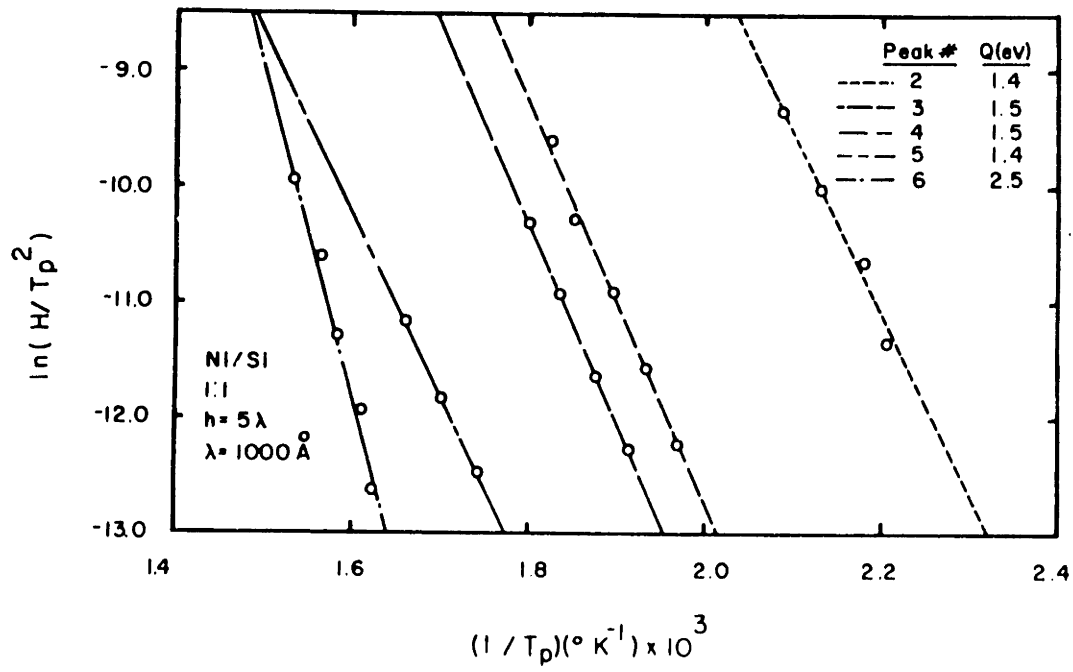


Figure 7 Plot of $\ln(H/T_p^2)$ versus $1/T_p$ for the data of figure 6.



4.4 Effect of Layer Thickness on the Reaction Kinetics of Nickel/Amorphous-Silicon Multilayer Films

In figure 1, we demonstrated that the peak temperature for amorphous-nickel-silicide and Ni_2Si growth increased with increasing modulation period at a constant scan rate H . The modulation period dependence of the Ni_2Si peak temperature can be explained using arguments analogous to those used in explaining similar observations during amorphous phase formation in metallic multilayer thin films. The rate of increase in width w of the silicide layer is given by,⁷

$$w \frac{dw}{dt} = D_{\text{eff}} = D_{\text{eff},0} \exp(-Q/kT) \quad (1)$$

where D_{eff} is the effective interdiffusivity for Ni_2Si formation and is related to the actual interdiffusivity, the silicide concentration range and the mole fraction of nickel and silicon in Ni_2Si .^{4,7} $D_{\text{eff},0}$ is a temperature independent coefficient and Q is the activation energy for interdiffusion. The area under a Ni_2Si peak, A_p , is given by,^{3,4}

$$A_p = \gamma \alpha \Delta H_t A_f w \quad (2)$$

where γ is a proportionality constant, ΔH_t is the heat of transition, A_f is the area of the film and α is the number of interfaces at which the reaction is occurring ($\alpha=9$ for the films studied here).

By differentiating equation 2 with respect to time and combining the result with equation 1, we get

$$A_p \frac{dA_p}{dt} = \gamma^2 D_{\text{eff},o} \alpha^2 (\Delta H_t)^2 A_f^2 \exp(-Q/kT) \quad (3)$$

This equation can be integrated from $A_p=A_o$ at $t=0$ to $A_p=A_t$ at $t=t_f$, where A_o corresponds to the heat released due to formation of a continuous layer of Ni_2Si between the nickel and amorphous-nickel-silicide layers and A_p is the heat released by the complete conversion of the film to Ni_2Si . By assuming that the heat of transition is not a function of temperature or time, equation 3 becomes,

$$A_p^2 - A_o^2 = \frac{2\gamma^2}{H} D_{\text{eff},o} (\Delta H_t)^2 A_f^2 \alpha^2 \int_{T_o}^{T_p} \exp(-Q/kT) dT \quad (4)$$

given

$$A_p = \gamma \left(h - \frac{\lambda}{2} \right) A_f \Delta H_t \quad (5)$$

and

$$A_o = \gamma \alpha A_f w_o \Delta H_t \quad (6)$$

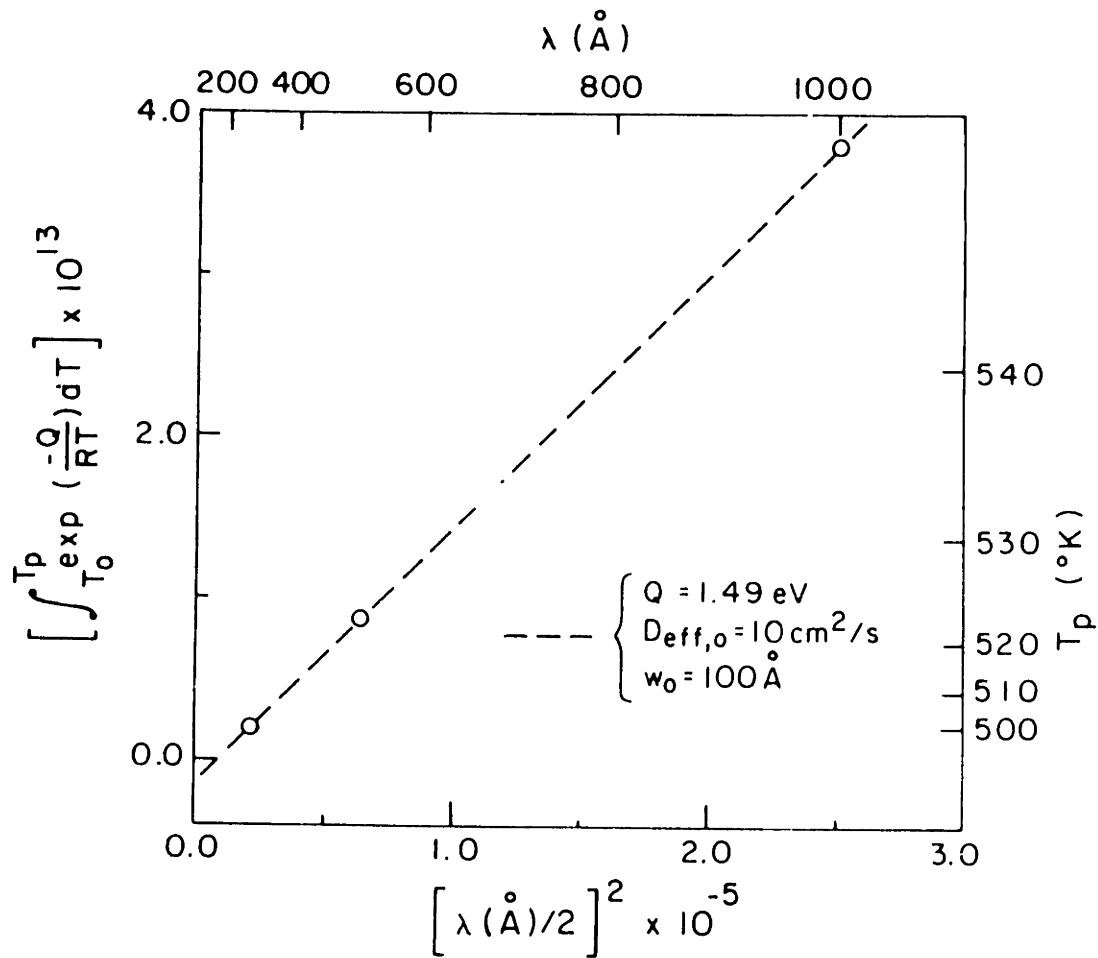
where w_o is the initial silicide thickness. We can combine equations (4), (5), and (6) to give²⁻⁴

$$\int_{T_0}^{T_p} \exp(-Q/kT) dT = \left(\frac{H}{2D_{\text{eff},o}} \right) [(\lambda/2)^2 - w_o^2] \quad (7)$$

where λ is the modulation period of the multilayer films and T_0 is the temperature at which Ni_2Si one-dimensional growth starts in the DSC and T_p is the temperature at which it ends.

Figure 8 shows calculations using equation 7 and the results for Ni_2Si growth in figure 1 for multilayer films with modulation periods of 100 nm, 50 nm, and 25 nm. It can be seen that given $Q=1.49$ eV, the values of equation 7 for the different modulation periods greater than 25 nm all fall on a straight line. From the slope of this line $D_{\text{eff},o}$ was determined to be $10 \text{ cm}^2/\text{sec}$ and from the y-intercept of the line w_o was found to be 10 nm. Our $D_{\text{eff},o}$ is in very good agreement with a value of $4 \text{ cm}^2/\text{sec}$ derived from the results of Tu et al.¹ The value of Q which provides the best fit to the data using this analysis, 1.49 eV, is also in excellent agreement with the Q value obtained in section 4.3 and with the value reported by Tu et al.⁹ The w_o value of 10 nm is consistent with the thickness of Ni_2Si when it forms into a continuous layer between the nickel and amorphous-nickel-silicide layers as shown by the cross-sectional transmission electron micrograph of figure 4. The agreement between theory and experiment indicates that the observed decrease in the silicide thickening temperature (peak 3 in fig.1) with decreasing layer thickness is due to decreased reaction time required for complete silicidation of the multilayer film.

Figure 8 The relationship between the peak temperature T_p for Ni_2Si one-dimensional growth in figure 1 and the modulation period λ as indicated by equation 7.



4.5 Determination of Whether Nucleation and Growth or Growth Alone Controls Phase Selection in Nickel/Amorphous-Silicon Thin Film Reactions

In this section, we discuss the mechanism which controls phase selection in nickel/amorphous-silicon reactions. The mechanism responsible for product phase selection in nickel/silicon and other thin film reactions has been discussed for many years. Two basic models have been proposed which we will call the growth control model and the nucleation control model. In the growth control model,¹⁰ nucleation is implicitly assumed to be possible for all phases, so that the silicide phase that forms during deposition and/or heat treatment is assumed to be the phase that grows the fastest. In the "nucleation model",¹¹ the silicide phase that forms is the phase which has the highest nucleation rate or the smallest nucleation barrier. For the growth control model, the quantities that control phase selection are the silicide interface reaction rates and interdiffusion rates, while for the nucleation control model, the important parameters for phase selection are silicide interface energies and thermodynamic driving forces.

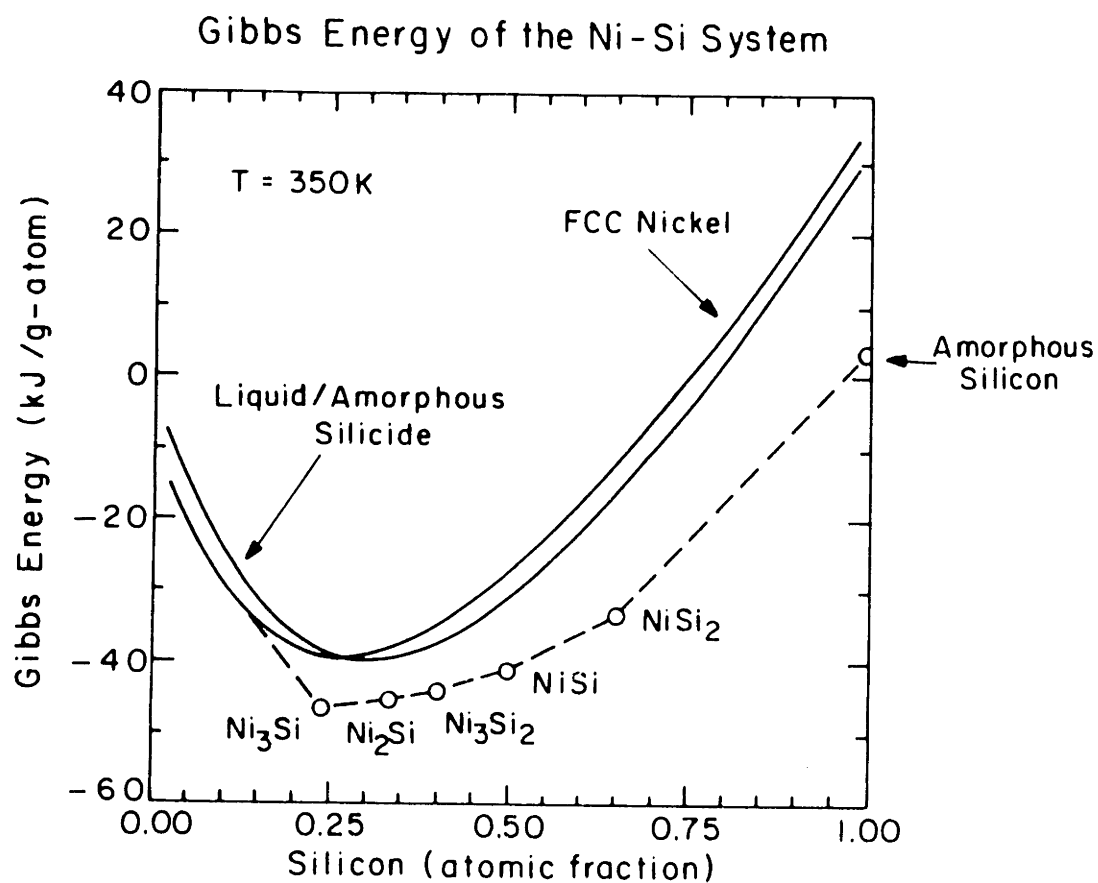
The determination of which model, nucleation or growth, controls silicide formation in nickel/amorphous-silicon multilayer thin films can be done by thermodynamic analysis of amorphous-nickel-silicide formation and by constant-scan-rate and isothermal calorimetric analysis of Ni_2Si formation and growth. To begin with consider figure 2 which demonstrated that the first silicide phase to form from a reaction between

layers of nickel and amorphous-silicon is an amorphous-nickel-silicide. This can be explained by considering the Gibbs free-energy versus composition diagram for the nickel/silicon system shown in figure 9. In this figure, the free energies at 350 K of fcc nickel, covalently bonded amorphous-silicon, crystalline nickel silicides and the undercooled nickel-silicon liquid solution are plotted as a function of silicon concentration, based on data reported by Mey¹², Donovan et al.¹³ and calculations presented in appendix C. Mey's data has been modified so that the enthalpy and the entropy of the pure fcc nickel and diamond cubic silicon was 0 at 0 K. We have assumed in figure 9 that the free energy of amorphous-nickel-silicide is approximately the same as that of the undercooled metallic liquid.

In figure 9, the common tangents between fcc nickel, the crystalline silicides and pure amorphous-silicon have been drawn in. The amorphous-nickel-silicide free energy curve lies above these common tangents, indicating that the amorphous-nickel-silicide is unstable with respect to the crystalline silicides (if they are all present, or if any one but Ni_3Si , NiSi or NiSi_2 is present). This implies that an amorphous-nickel-silicide would not form at the nickel/amorphous-silicon interface if there were no kinetic barriers to the formation of the crystalline silicides.

Because amorphous-nickel-silicide forms at the nickel/amorphous-silicon interface, there must be kinetic barriers that prevent the formation of the crystalline silicides. As discussed previously, two models for the nature of these kinetic barriers have been proposed, one based on the presence of a nucleation barrier and the other based on growth competition. In section 1.3, we presented a model for these kinetic barriers based on growth competition which was originally developed by Gosele and Tu.¹⁰ In

Figure 9 Gibbs free energy versus composition diagram for the nickel/silicon system at a temperature of 350 K. The crystalline silicides are distinguished by "O". Ni_5Si_2 is not plotted due to a lack of reliable information for its free energy. Dashed lines are the common tangents for fcc nickel, the crystalline silicides and amorphous-silicon.



the following analysis, we examine their model to see if it will predict, as observed experimentally, that amorphous-nickel-silicide will be the first silicide phase to form at the nickel/amorphous-silicon interface. In this analysis we consider only thermodynamically stable Ni_2Si and unstable amorphous-nickel-silicide. For amorphous-nickel-silicide to be the first silicide phase to form by Gosele and Tu's model, it must have a larger growth rate than Ni_2Si . As was shown in section 1.3, these growth rates can be expressed as:

$$\frac{dX_{\text{Ni}_2\text{Si}}}{dt} = (A2)(j^{\text{Ni}_2\text{Si}}) - (A3)(j^{\alpha\text{-NiSi}}) \quad (8)$$

$$\frac{dX_{\alpha\text{-NiSi}}}{dt} = (A4)(j^{\alpha\text{-NiSi}}) - (A5)(j^{\text{Ni}_2\text{Si}}) \quad (9)$$

where A_i 's are positive constants, and $\alpha\text{-NiSi}$ stands for amorphous-nickel-silicide. The diffusion fluxes through each layer are defined by:

$$j_{\text{Ni}_2\text{Si}} = \frac{(\Delta C_{\text{Ni}_2\text{Si}}^{\text{eq}})(K_{\text{Ni}_2\text{Si}})}{1 + (X_{\text{Ni}_2\text{Si}})(K_{\text{Ni}_2\text{Si}}) / (\tilde{D}_{\text{Ni}_2\text{Si}})} \quad (10)$$

$$j_{\alpha\text{-NiSi}} = \frac{(\Delta C_{\alpha\text{-NiSi}}^{\text{eq}})(K_{\alpha\text{-NiSi}})}{1 + (X_{\alpha\text{-NiSi}})(K_{\alpha\text{-NiSi}}) / (\tilde{D}_{\alpha\text{-NiSi}})} \quad (11)$$

where the K 's and D 's are the interface reaction rate constants and interdiffusion coefficients for the amorphous-nickel-silicide and the Ni_2Si layers, and $\Delta C_{\alpha\text{-NiSi}}^{\text{eq}}$ and $\Delta C_{\text{Ni}_2\text{Si}}^{\text{eq}}$ can be expressed as:

$$\Delta C_{\text{Ni}_2\text{Si}}^{\text{eq}} = C_{\text{Ni}_2\text{Si} / \alpha\text{-NiSi}} - C_{\text{Ni}_2\text{Si} / \text{Ni}} \quad (12)$$

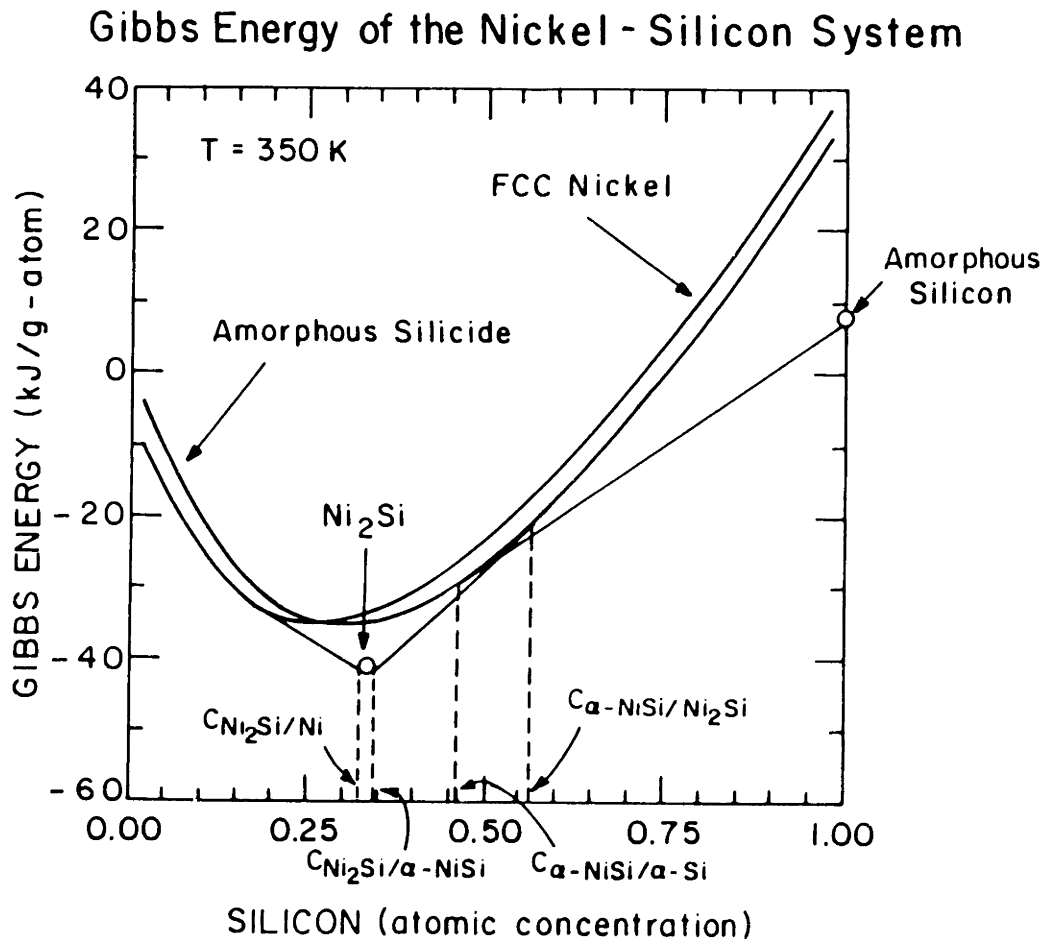
$$\Delta C_{\alpha\text{-NiSi}}^{\text{eq}} = C_{\alpha\text{-NiSi} / \alpha\text{-Si}} - C_{\alpha\text{-NiSi} / \text{Ni}_2\text{Si}} \quad (13)$$

where $C_{\text{Ni}_2\text{Si} / \text{a-NiSi}}$, $C_{\alpha\text{-NiSi} / \alpha\text{-Si}}$, $C_{\text{Ni}_2\text{Si} / \text{Ni}}$ and $C_{\alpha\text{-NiSi} / \text{Ni}_2\text{Si}}$ are defined as shown in figure 10. With this model, amorphous-nickel-silicide will form first at the nickel/amorphous-nickel-silicide interface if $\frac{dX_{\alpha\text{-NiSi}}}{dt}$ is positive and larger than $\frac{dX_{\text{Ni}_2\text{Si}}}{dt}$. However from figure 10 and equation 13, at 350 K $\Delta C_{\alpha\text{-NiSi}}^{\text{eq}}$ is always negative for unstable amorphous-nickel-silicide in the presence of stable Ni_2Si . This implies by equations 8-11 that amorphous-nickel-silicide would have a negative growth rate and Ni_2Si would have a positive growth rate. Thus, from a growth control model for silicide formation, considering only Ni_2Si and amorphous-nickel-silicide, Ni_2Si should form at the nickel/amorphous-silicon interface and amorphous-nickel-silicide should never be seen.

These conclusions are contrary to the results shown in figure 2 in which it is illustrated that amorphous-nickel-silicide is the first phase to form at the nickel/amorphous-silicon interface. Similar arguments can be made for the formation of Ni_3Si_2 in comparison to amorphous-nickel-silicide at the nickel-silicide interface. This indicates that simple growth barriers for Ni_2Si and Ni_3Si_2 cannot control phase selection at the nickel/amorphous-silicon interface. Rather there must be nucleation barriers that prevent the formation of these stable crystalline silicides so that the thermodynamically unstable amorphous-nickel-silicide can form.

For the sake of completeness we note here that amorphous-nickel-silicide is thermodynamically stable with respect to Ni_3Si , NiSi and NiSi_2 at 350 K and that the model of Gosele and Tu¹⁰ could apply in these cases to

Figure 10 Gibbs free energy versus composition curve for the nickel/silicon system at a temperature of 350 K considering only fcc nickel, amorphous-nickel-silicide, amorphous-silicon and crystalline Ni_2Si . The common tangents are drawn between fcc nickel and Ni_2Si , Ni_2Si and amorphous-nickel-silicide, and amorphous-nickel-silicide and amorphous-silicon. The common tangents define $C_{\text{Ni}_2\text{Si}/\text{a-NiSi}}$, $C_{\text{a-NiSi}/\text{a-Si}}$, $C_{\text{Ni}_2\text{Si}/\text{Ni}}$ and $C_{\text{a-NiSi}/\text{Ni}_2\text{Si}}$.



explain why the amorphous-nickel-silicide forms before these three silicide phases. However, due to the calorimetric evidence presented later in this section, we believe that nucleation barriers also prevent the formation of these silicide phases at the nickel/amorphous-silicon interface.

With nucleation barriers preventing the formation of the crystalline silicides, we can remove the crystalline silicides from the Gibbs free energy versus composition diagram of figure 9. The resulting diagram is shown in figure 11, with the common tangents now drawn between the fcc nickel, amorphous-silicon and amorphous-nickel-silicide. This construction indicates that with nucleation barriers to the formation of the crystalline silicides, amorphous-nickel-silicide can form from, and be in equilibrium with nickel and amorphous-silicon. This diagram also allows the prediction that the amorphous-nickel-silicide has an approximate composition range of 35 to 55 atomic percent silicon. To check this, the composition of the amorphous-nickel-silicide was investigated using energy dispersive X-ray microanalysis in a scanning transmission electron microscope. This data is shown in figure 12 for the same sample as in figure 5. In this figure, the nickel concentration versus distance measured in a plane perpendicular to the plane of the layers is plotted for one modulation period of the multilayer film. These results suggest that the composition of the amorphous-nickel-silicide is approximately 1 Ni to 1 Si atom, which is in agreement with the predicted range of values from figure 11.

The instability of the amorphous-nickel-silicide with respect to the crystalline silicides also indicates that the simultaneous growth of amorphous-nickel-silicide and Ni_2Si will not occur at 350 K. At higher temperatures, this simultaneous growth is observed.^{5,6} This can be

Figure 11 Same as figure 9, except that we have assumed that nucleation barriers prevent the formation of the crystalline silicides; α represents fcc nickel and β represents the amorphous-nickel-silicide. Common tangents are drawn in for fcc nickel, amorphous-nickel-silicide and amorphous-silicon.

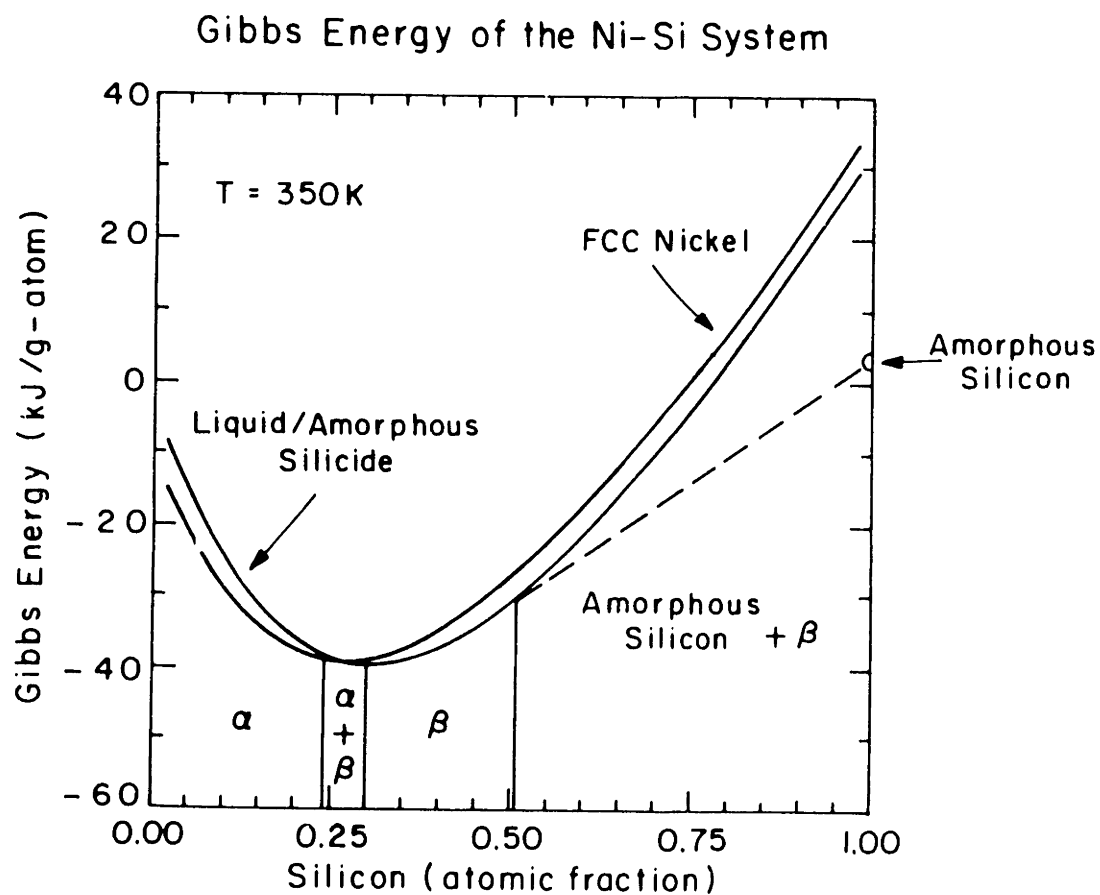
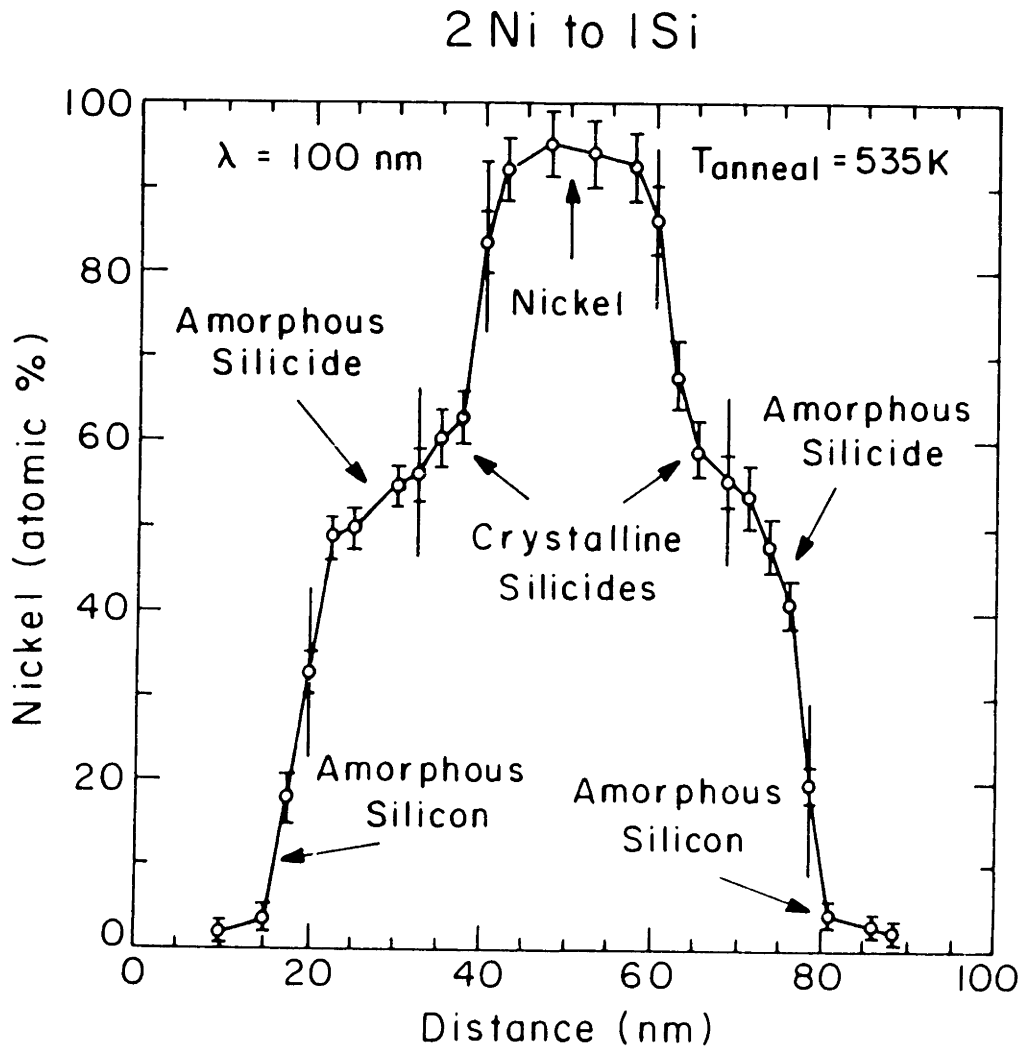


Figure 12 Nickel composition versus distance across one modulation period of a nickel/amorphous-silicon multilayer film heated to 535 K. The position of the interfaces between different layers is marked by solid vertical lines. This figure suggests that the composition of the amorphous-nickel-silicide under these annealing conditions is approximately 1 Ni atom to 1 Si atom.



explained by examining the Gibbs free energy versus composition diagram for the nickel/system at temperatures higher than 350 K. In figure 13, we plot the Gibbs free energy of the nickel/silicon system at 650 K, considering only the fcc nickel, amorphous-silicon, Ni₂Si and amorphous-nickel-silicide. In figure 13, the common tangents are drawn between fcc nickel, Ni₂Si and amorphous-silicon. The free energy curve of amorphous-nickel-silicide intersects the common tangent drawn between Ni₂Si and amorphous-silicon. This indicates that, by raising the annealing temperature from 350 K, the amorphous-nickel-silicide has become thermodynamically stable with respect to crystalline Ni₂Si, and that the simultaneous growth of the two phases can occur.

Further evidence for nucleation barriers controlling silicide phase selection is provided in the constant-scan-rate calorimetric data for the formation of a continuous layer of Ni₂Si at the nickel/amorphous-nickel-silicide interface and the subsequent growth of this layer to consume the entire thin film. In figure 14, we present constant-scan-rate calorimetric data for a nickel/amorphous-silicon multilayer film with a modulation period of 100 nm. In this figure, the heat released per unit time, dH/dt, for Ni₂Si formation and/or amorphous-nickel-silicide growth is plotted as a function of temperature. As discussed in section 3.2.1, dH/dt is related to the volume of the new phase by,

$$\frac{dH}{dt} = (-\Delta H_f) \frac{dV}{dt} \quad (14)$$

where $-\Delta H_f$ is the heat of formation for the forming phase (per unit volume) and dV/dt is the change in volume of this phase with time. dV/dt can be expressed as:

Figure 13 Gibbs free energy versus composition diagram for the nickel/silicon system at a temperature of 650 K considering only fcc nickel, amorphous-nickel-silicide, amorphous-silicon and Ni_2Si . The common tangents are drawn between fcc nickel and Ni_2Si , and Ni_2Si and amorphous-silicon.

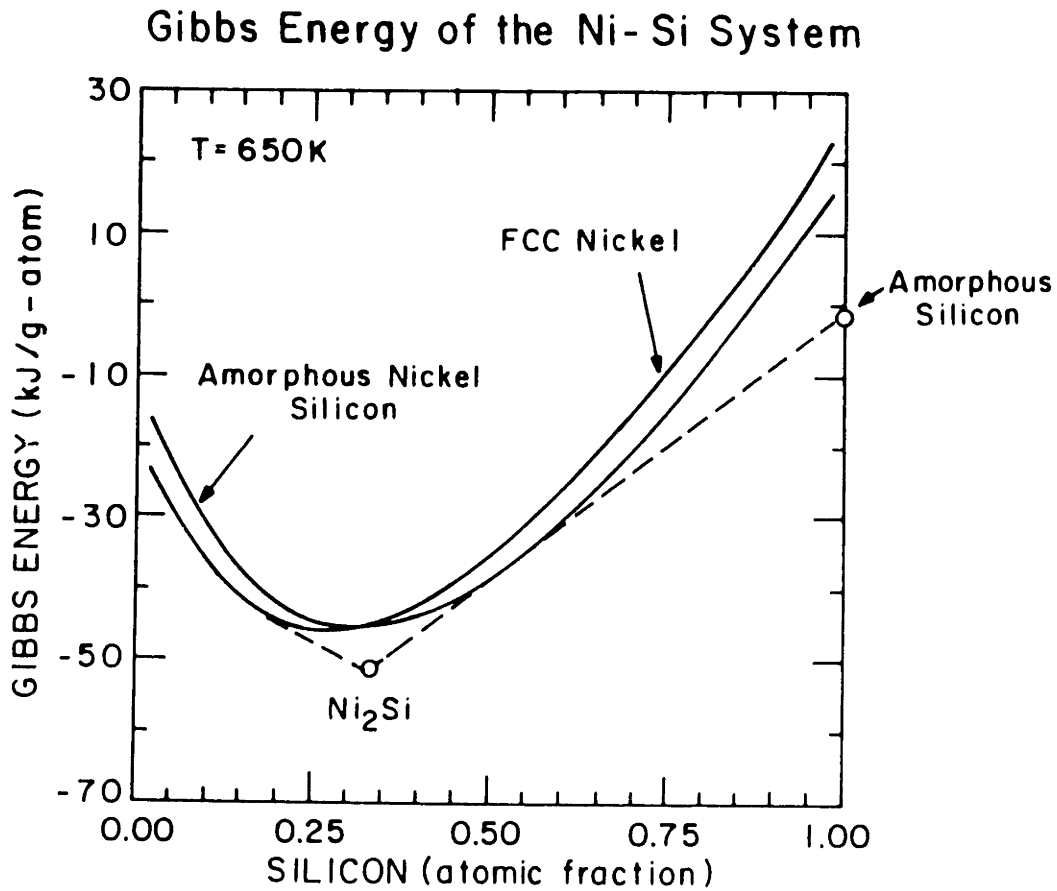
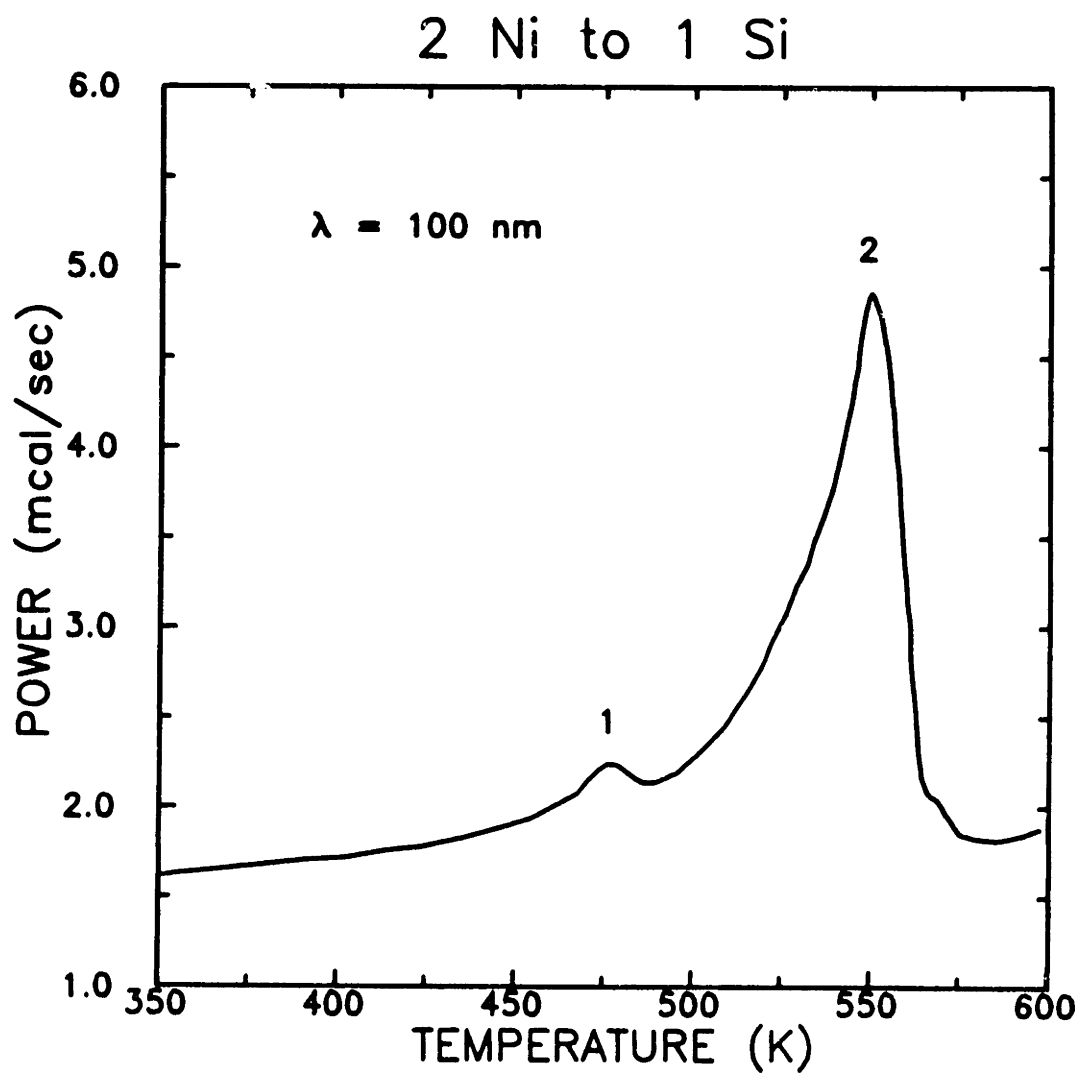


Figure 14 Calorimetric data at a scan rate of 20 K/min for a 100 nm modulation period multilayer film.



$$\frac{dV}{dt} = (V_f) \frac{dX_v}{dt} \quad (15)$$

where V_f is the final transformed volume and dX_v/dt is the change in the fraction transformed with time.

With the constant-scan-rate calorimetric trace of figure 14 for the 100 nm multilayer film, X-ray and cross-sectional transmission electron microscope analysis presented earlier in this chapter indicated that peak 1 is related to the formation of a continuous layer of Ni_2Si between the nickel and amorphous-nickel-silicide layers and peak 2 to the one-dimensional growth of this continuous layer to completely transform the film into Ni_2Si . Recently, Coffey et al¹⁴ have developed a model for the change in the fraction transformed of Ni_2Si for the 100 nm multilayer film as a function of time, assuming nucleation controlled phase selection. A detailed discussion of this model is presented in Appendix B. Their expression is:

$$\frac{dX_v}{dt} = \left(\frac{dX_a}{dt} \right) \frac{w}{w_{max}} + \left(\frac{dw}{dt} \right) \frac{X_a}{w_{max}} \quad (16)$$

where w is the thickness of Ni_2Si , w_{max} is the maximum thickness that the Ni_2Si grows to, dw/dt is the one-dimensional growth rate, X_a is the areal fraction of Ni_2Si in a plane parallel to the plane of the original layers, and dX_a/dt is the change in the areal fraction as a function of time ($w, dw/dt, X_a$ and dX_a/dt are defined further in Appendix B).

With constant-scan-rate calorimetry, the scan rate is defined as,

$$R = \frac{dT}{dt} \quad (17)$$

where dT/dt is the change in annealing temperature with time. Combining equations 14 through 17, we obtain

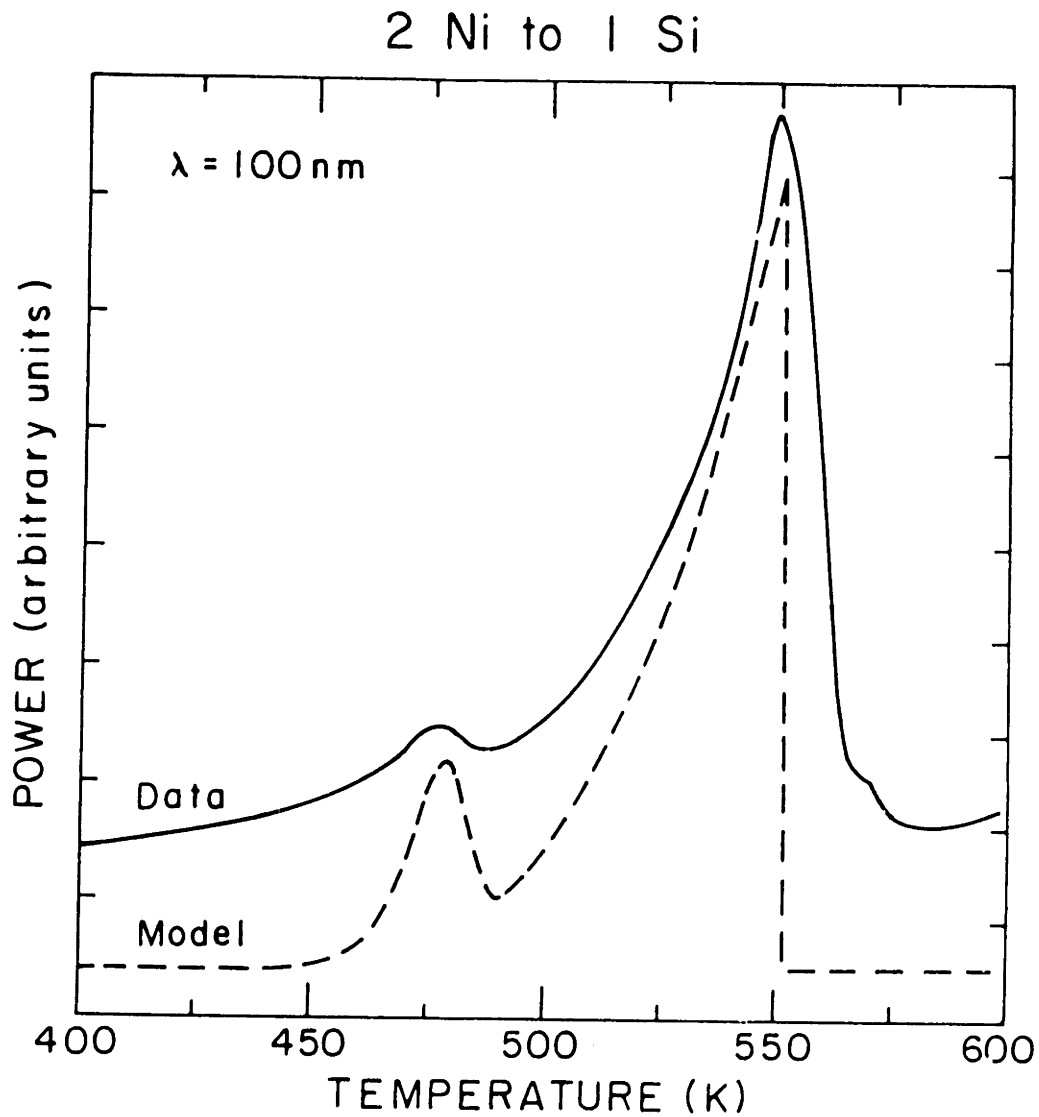
$$\frac{dH}{dt} = (-\Delta H_f V_f) R \left(\left(\frac{dX_a}{dT} \right) \frac{w}{w_{\max}} + \left(\frac{dw}{dT} \right) \frac{X_a}{w_{\max}} \right) \quad (18)$$

In figure 15, we compare the actual calorimetric data to predictions made using equation 18. As demonstrated in this figure, there is good agreement between the shape and magnitude of the real data and the model.

There are three important points to be made about figure 15. First, in the model, a diffusion pre-exponential coefficient of $55 \text{ cm}^2/\text{sec}$ and an activation energy of 1.5 eV were used to characterize Ni_2Si growth. These are in good agreement with the values of $10 \text{ cm}^2/\text{sec}$ and 1.49 eV determined by Clevenger et al.²⁻⁴ Second, equation 18 results from a modified Johnson-Mehl-Avrami analysis of Ni_2Si formation and growth. This type of analysis requires that nucleation, instead of growth, controls silicide phase selection. Finally, this model predicts the double peak structure observed in the data (peaks 1 and 2 of figure 15) for the formation of Ni_2Si . These characteristics of the calorimetric data cannot be accounted for by a model which is based on simple thickening of the silicide, as is treated in growth-controlled models for phase selection.

Further evidence for nucleation controlled phase selection in nickel silicide reactions can also be provided by isothermal calorimetric measurements. In this work, isothermal calorimetry was done to independently study the growth of amorphous-nickel-silicide (peak 1 of figure 1) and the formation of crystalline Ni_2Si (peak 2 of figure 1). We

Figure 15 Constant-scan-rate calorimetric data for a 100 nm modulation period multilayer film plotted along with predicted calorimetric data (dashed line) derived from equation 5. The parameters used for the model were $K_{l,0}^2 = 10^{28} \text{ sec}^{-2}$, $w_0 = 10 \text{ nm}$, $Q_l = 1.5 \text{ eV}$, $D_{p,0} = 55 \text{ cm}^2/\text{sec}$ and $Q_p = 1.5 \text{ eV}$ (see appendix B).



chose the 14 nm multilayer thin film for isothermal studies because it was the only sample for which the growth of the amorphous-nickel-silicide terminates before the formation of crystalline Ni₂Si between the amorphous-nickel-silicide and polycrystalline nickel. Figure 16 presents isothermal calorimetry data for this multilayer thin film. This sample was heated to 420 K and held at this temperature (figure 16a) for 6 minutes before being heated to 455 K (figure 16b). Figure 16a shows calorimetric data for the growth of amorphous-nickel-silicide and illustrates that this growth is characterized by a decreasing amount of heat released with increasing time. In figure 16b, there is also a gradual decrease in the heat output with time, corresponding to further thickening of the planar amorphous-silicide. Superimposed on this decrease there is also a peak indicating first an increase in heat released, followed by a decrease. This peak is associated with formation of crystalline Ni₂Si.

In these measurements, the fraction transformed X_v , for nucleation controlled silicide phase selection can be expressed as:^{15,16}

$$X_v = 1 - e^{-X_{ex}} \quad (19)$$

where X_{ex} is the extended volume fraction of the silicide if impingement of the nuclei has not occurred. X_{ex} can be expressed as:

$$X_{ex} = Ct^n \quad (20)$$

where t is time, n the Avrami exponent and C has the form $C=C_0e^{(-Q/kT)}$ where Q is an energy which is a function of the activation energies for nucleation and growth. Using equations 19 and 20, the change in the

Figure 16a Isothermal differential scanning calorimetry trace for a nickel/amorphous-silicon multilayer film annealed at 420 K. The modulation period of the multilayer film was 14 nm.

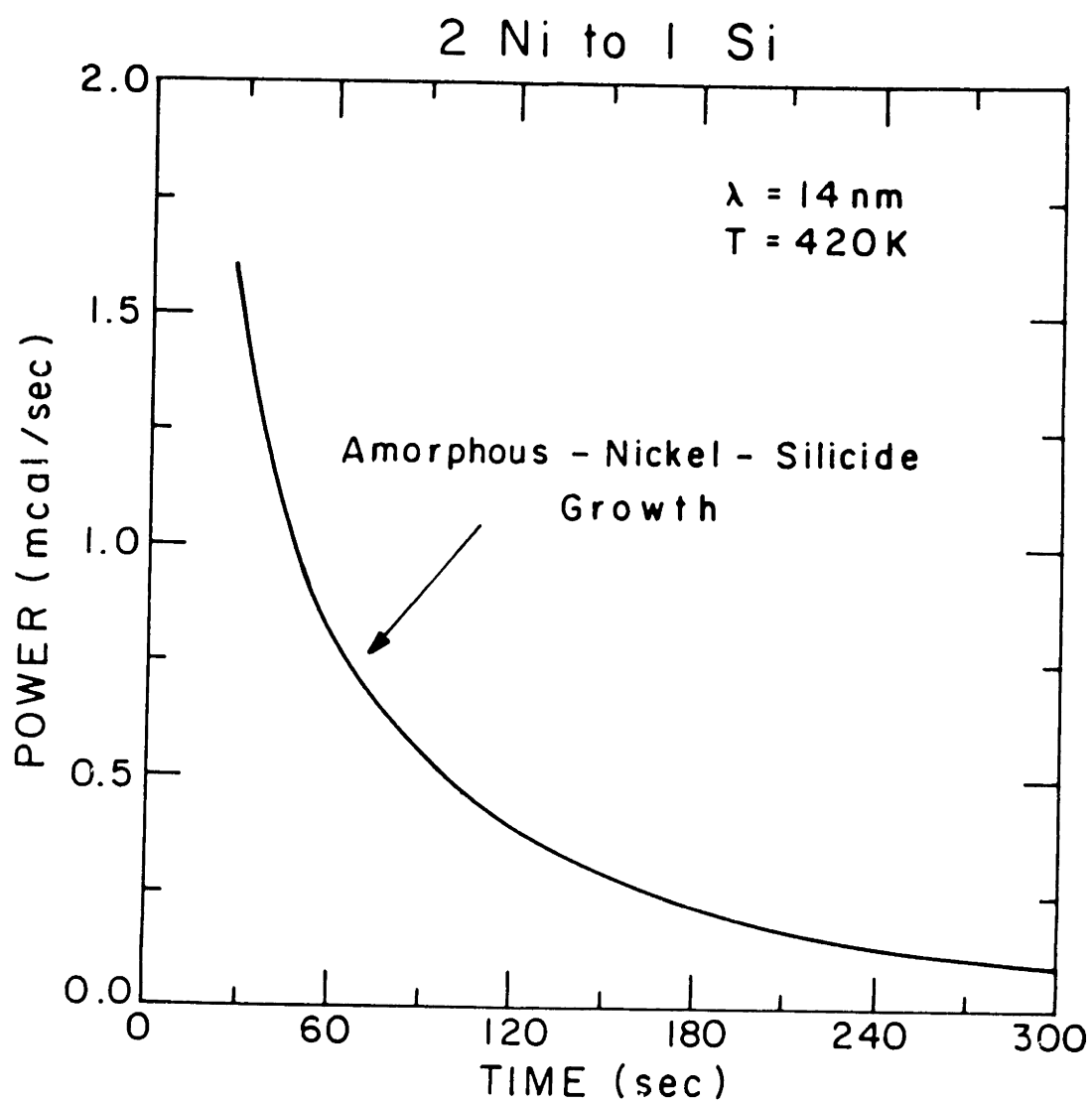
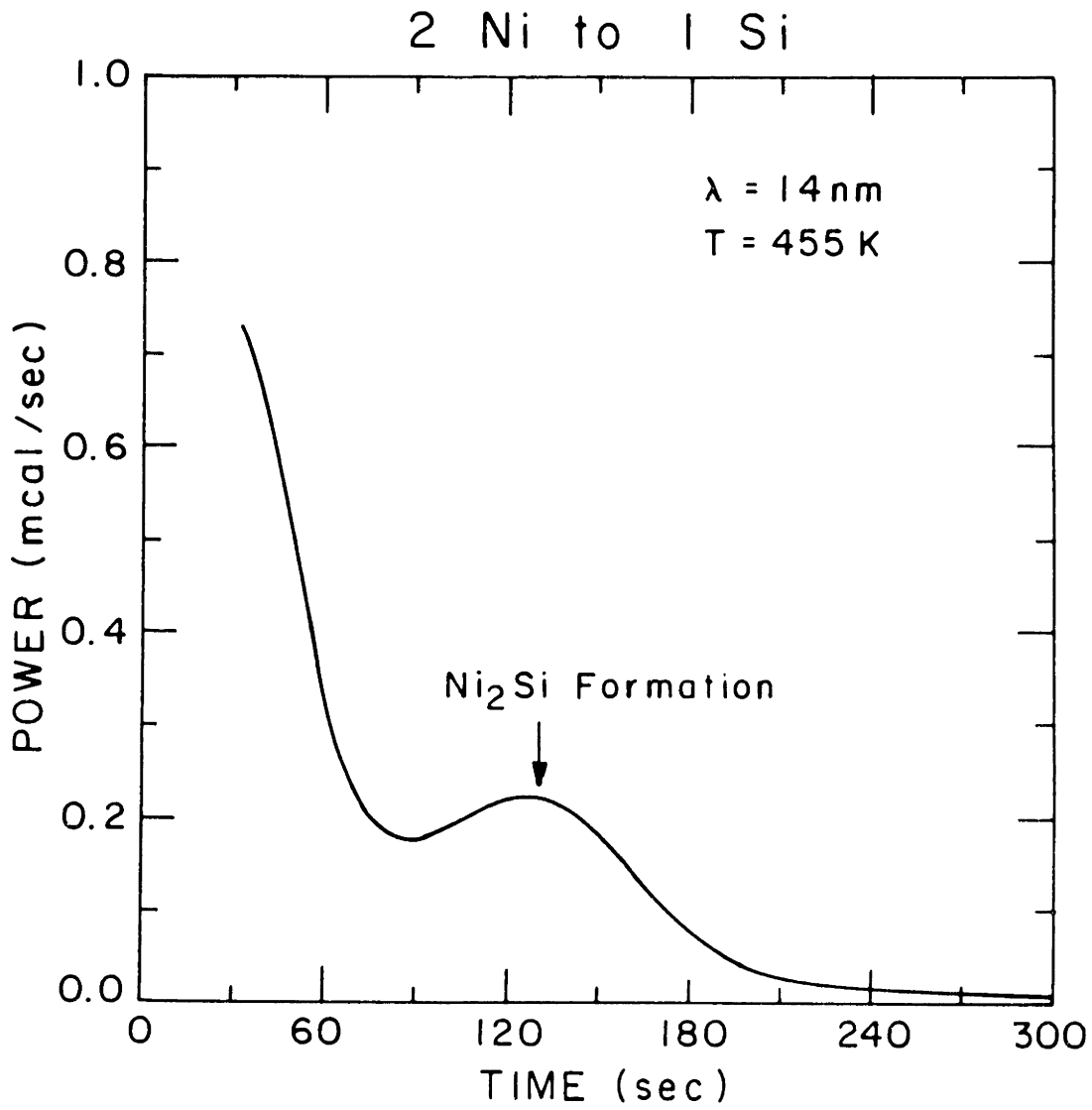


Figure 16b Isothermal differential scanning calorimetry trace for the nickel/amorphous-silicon film of figure 16a annealed at 455 K.



fraction transformed as a function of time dX_v/dt for nucleation controlled phase selection can be expressed as,

$$\frac{dX_v}{dt} = n C t^{n-1} e^{-Ct^n} \quad (21)$$

Combining equations 14,15, and 21, we can write that an isothermal calorimetric signal as a function of time for nucleation controlled silicide phase selection is:

$$\left(\frac{dH}{dt}\right)_{nuc} = (-\Delta H_f) V_f n C t^{n-1} e^{-Ct^n}. \quad (22)$$

If silicide phase selection were growth controlled, or if a one-dimensional growth process were occurring, dX_v/dt in equation 21 and $(dH/dt)_{nuc}$ in equation 22 would have a different form.

For 1-dimensional interface limited growth, dX_v/dt would have the form,¹⁰

$$\frac{dX_v}{dt} = \frac{K_{l,o} C_2}{W_{max}} e^{\left(\frac{-Q_l}{kT}\right)} \quad (23)$$

where C_2 is a dimensionless constant whose value depends on the equilibrium concentrations at the reacting interfaces, $K_{l,o}$ is taken to be a temperature independent constant, k the Boltzman's constant and Q_l is the activation energy for interface limited growth. If the one-dimensional thickening is diffusion limited, dX_v/dt would have the form,¹⁰

$$\frac{dX_v}{dt} = \frac{D_{p,o} C_2}{W_{max} W} e^{\left(\frac{-Q_p}{kT}\right)} \quad (24)$$

where $D_{p,o}$ is a temperature independent constant, w the thickness of the growing silicide layer, Q_p is the activation energy for the diffusion limited process and w_{max} and k are defined above. Most growth controlled processes start out interface limited, and then with increasing layer thicknesses become diffusion limited. In this case dX_v/dt is a combination of equations 23 and 24 to give,¹⁰

$$\frac{dX_v}{dt} = \frac{C_2}{w_{max}} \left(\frac{1}{K_{l,o} e^{\left(\frac{-Q_l}{kT}\right)}} + \frac{1}{\frac{D_{p,o}}{w} e^{\left(\frac{-Q_p}{kT}\right)}} \right)^{-1} \quad (25)$$

Combining equations 14, 15 and 25, the rate of heat release during thickening of a silicide layer can be written as:

$$\left(\frac{dH}{dt}\right)_{growth} = \frac{-\Delta H_f V_f C_2}{w_{max}} \left(\frac{1}{K_{l,o} e^{\left(\frac{-Q_l}{kT}\right)}} + \frac{1}{\frac{D_{p,o}}{w} e^{\left(\frac{-Q_p}{kT}\right)}} \right)^{-1} \quad (26)$$

Theoretical isothermal calorimetry curves for simple 1-dimensional growth (thickening) without nucleation (equation 24) and the formation and growth of nuclei (equation 20) are shown in figures 17a and 17b.

The most striking feature of figure 17 is that for growth without nucleation (figure 17 a), the heat released due to silicide formation dH/dt is either constant or decreasing with increasing time. However, when nucleation is required for silicide formation (figure 17b), the rate of heat release, dH/dt , initially increases before subsequently decreasing with increasing time.

Figure 17a Theoretical isothermal calorimetry curve for simple one-dimensional growth (or thickening) of a silicide, without nucleation.

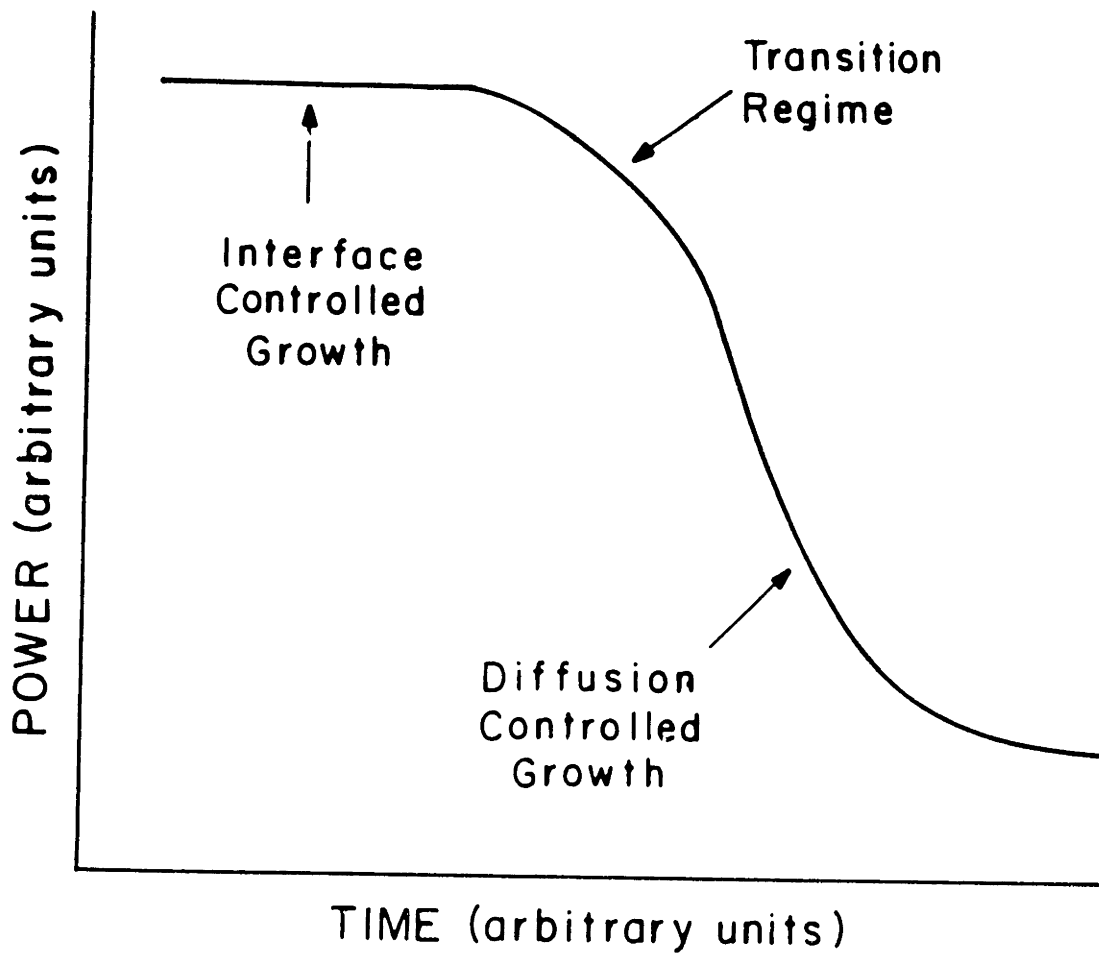
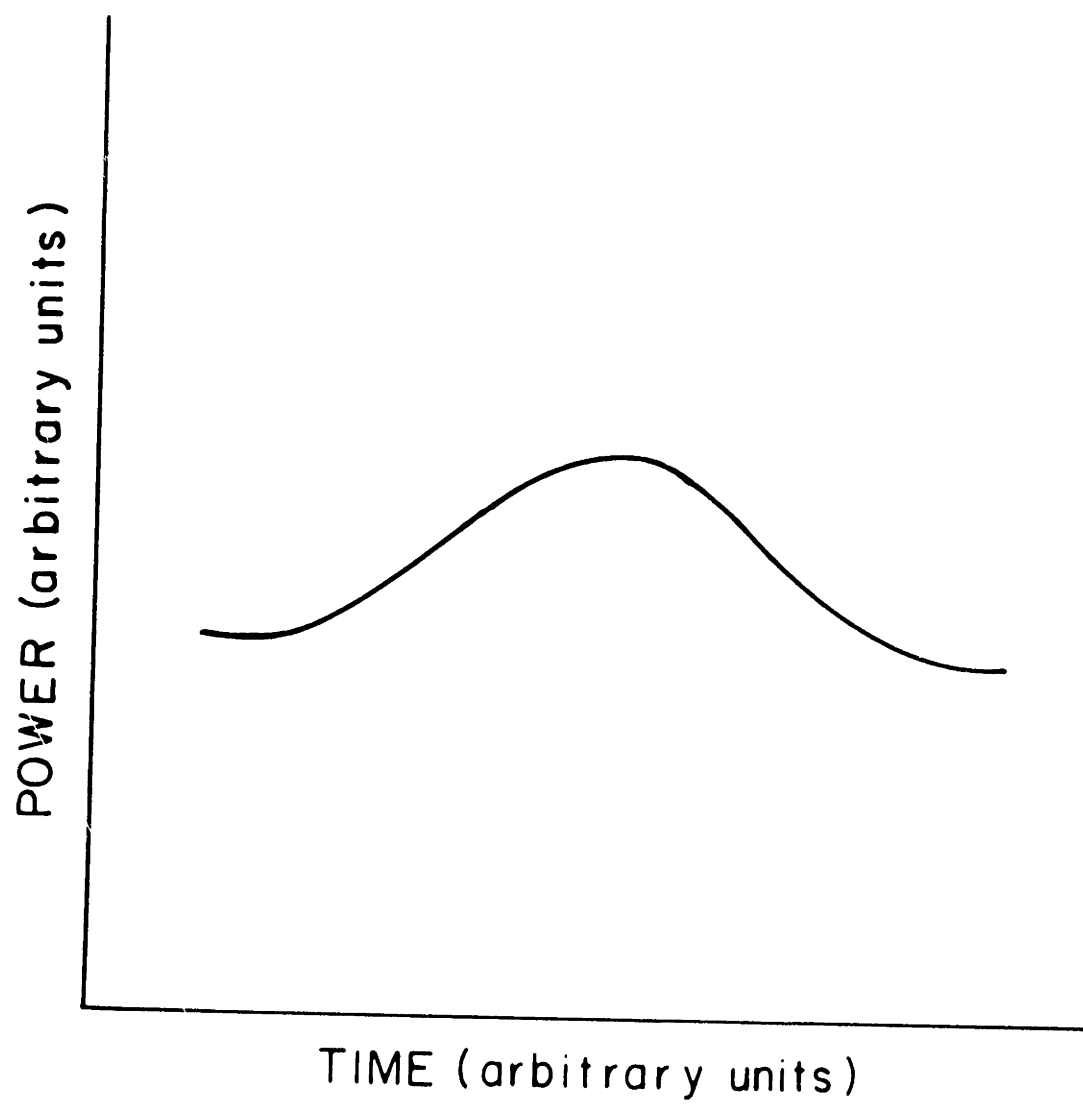


Figure 17b Theoretical isothermal calorimetry curve for nucleation and growth of a silicide.



In examining the actual isothermal calorimetric data of figure 16, we see that for figure 16a, the calorimetric data for the growth of amorphous-nickel-silicide is characterized by a continuously decreasing amount of heat released with increasing time. This curve has the same shape as the one in figure 17a, and indicates that the growth of amorphous-nickel-silicide is diffusion controlled. Calorimetric evidence for nucleation controlled formation of the amorphous-silicide is not seen due to the fact that amorphous-nickel-silicide growth initiates during deposition of the multilayer thin film, a fact demonstrated in figure 2.

In examining figure 16b, we see that there is a peak in the curve for dH/dt versus time for Ni_2Si formation at the nickel/amorphous-nickel-silicide interface. This data has a similar form to figure 17b, where nucleation is the rate controlling mechanism for silicide formation. The peak of figure 16b for Ni_2Si formation can not be explained by a pure planar growth mechanism for Ni_2Si formation. Thus, isothermal calorimetry further supports the conclusion drawn from the constant-scan-rate calorimetric analysis and thermodynamic analysis in demonstrating that nucleation as opposed to growth controls silicide phase selection in nickel/amorphous-silicon multilayer thin film reactions.

4.6 Comments on Nucleation Energies of Silicide Phases

As shown in section 4.6, nucleation barriers control silicide formation at the nickel/amorphous-silicon interface. With this observation, we can make some comparisons between the nucleation surface energies of the phase that does form first at this interface, amorphous-nickel-silicide,

and the nucleation surface energies of the crystalline silicide phases. To begin with, we assume that the first phase to form at this interface has the lowest nucleation barrier to formation. These nucleation barriers are characterized by,¹⁷

$$\Delta G^* = \frac{16\pi}{3} \times \frac{(\Delta\sigma)^3}{(\Delta G_v)^2} \quad (25)$$

where ΔG_v is the thermodynamic driving force and $\Delta\sigma$ is the "nucleation surface energy" for amorphous or crystalline nickel silicide formation at the nickel/amorphous-silicon interface. The "nucleation surface energy" for heterogeneous nucleation of lense shaped nuclei at the nickel/amorphous-silicon interface is given by,¹⁷

$$\Delta\sigma = \left(\sigma_{n-sl}^3 \left(\frac{2-3\cos\theta + (\cos\theta)^3}{4} \right) + \sigma_{as-sl}^3 \left(\frac{2-3\cos\theta' + (\cos\theta')^3}{4} \right) \right)^{\frac{1}{3}} \quad (26)$$

where σ_{n-sl} , σ_{s-sl} , θ and θ' are defined in figure 18.

If we assume local thermodynamic equilibrium at the interface, the maximum driving force ΔG_v , can be expressed as:

$$\Delta G_v = G_{Ni_xSi_y} - (\bar{G}_{Ni} + X_{Si}(\bar{G}_{Si} - \bar{G}_{Ni})) \quad (27)$$

where $G_{Ni_xSi_y}$ is the free energy of the amorphous or crystalline silicide phase, \bar{G}_{Ni} and \bar{G}_{Si} are the chemical potential of nickel and silicon respectively and X_{Si} is the atomic fraction of silicon in Ni_xSi_y . The ΔG_v calculated in this way corresponds to the maximum driving force, based on

the assumption that interdiffusion has lead to equilibrium compositions. However the $\Delta\sigma$ ratio calculated below represents a lower bound regardless of the amount of interdiffusion.¹⁸

For amorphous-nickel-silicide to form first at the nickel/amorphous-silicon interface, we must have,

$$\Delta G^{\circ}_{\text{Ni}_v\text{Si}_w} > \Delta G^{\circ}_{\text{am-NiSi}} \quad (28)$$

Combining this equation with equation 1 and rearranging, we obtain,

$$\Delta\sigma_{\text{Ni}_v\text{Si}_w} > \left(\frac{\Delta G_{v,\text{Ni}_v\text{Si}_w}}{\Delta G_{v,\text{am-NiSi}}} \right)^{\frac{2}{3}} \Delta\sigma_{\text{am-NiSi}} \quad (29)$$

where Ni_vSi_w stands for the crystalline silicides and am-NiSi stands for amorphous-nickel-silicide. Combining equations 29 and 27 we can calculate a lower bound for nucleation surface energies of crystalline silicides compared to amorphous-nickel-silicide. The lower bound for nucleation surface energies along with thermodynamic driving forces for amorphous and crystalline silicide formation for a reaction temperature of 350 K are shown in table 1.

Table 1 demonstrates that, except for Ni_3Si , all the crystalline nickel silicides have higher driving forces for formation at an equilibrium nickel/amorphous-silicon interface than amorphous-nickel-silicide. Table 1 also indicates that the nucleation surface energy of a crystalline silicide needs to be from 1.6 to 3.0 times larger than the nucleation surface energy of amorphous-nickel-silicide in order for amorphous-nickel-silicide to form first at the nickel/amorphous-silicon interface.

Figure 18 Ideal lense shaped silicide nucleus forming at the nickel/amorphous-silicon interface. σ_{n-sl} , σ_{s-sl} and σ_{ns} are the nickel/silicide, amorphous-silicon/ silicide and nickel/amorphous-silicon interface energies respectively. θ and θ' are the contact angles for the nickel/silicide and the amorphous-silicon/silicide interfaces respectively.

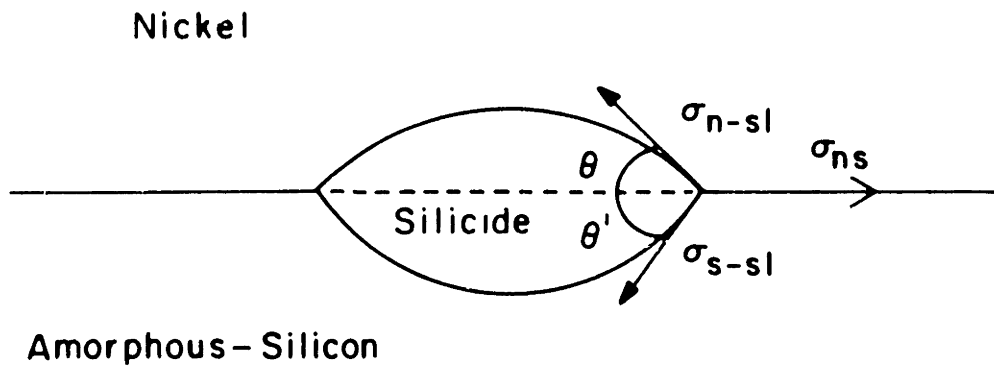


Table 1: Calculated lower bound for the nucleation surface energies of crystalline nickel silicides compared to amorphous-nickel-silicide for silicide formation at a nickel/amorphous-silicon interface. Also shown are thermodynamic driving forces for silicide formation at a equilibrium nickel/amorphous-silicon interface. ΔG_V for amorphous-nickel-silicide corresponds to the maximum $|\Delta G_V|$ for amorphous-nickel-silicide formation.

Phase	ΔG_V (kJ/g-atom)	$\left(\frac{\Delta G_{V, Ni_v Si_w}}{\Delta G_{V, am-NiSi}} \right)^{\frac{2}{3}}$
Ni ₃ Si	-1.8	0.7 <
amorphous-NiSi	-2.8	----
Ni ₂ Si	-6.0	1.6 <
Ni ₃ Si ₂	-9.2	2.2 <
NiSi	-12.5	2.7 <
NiSi ₂	-14.3	3.0 <

The lower nucleation surface energy of amorphous-nickel-silicide compared to that of crystalline nickel silicides can not be quantitatively explained. However, qualitatively, a low surface energy between amorphous-nickel-silicide and amorphous-silicon might be expected due to the amorphous nature of both structures. The nickel/silicide interface energies for both the crystalline silicides and amorphous-nickel-silicide on the other hand, might be expected to be similar due to the dissimilarity between the nickel (fcc) and either silicide structure. Thus combining surface energy contributions at both the nickel/silicide and silicide/amorphous-silicon interfaces, it seems reasonable that amorphous-

nickel-silicide would have the lowest nucleation surface energy of all the silicide phases.

4.7 Conclusion for Controlled Silicidation of Nickel/Amorphous-Silicon Thin Film Reactions With Atomic Concentration Ratios of 2 Ni Atoms to 1 Si Atom

For nickel/amorphous-silicon films with atomic concentration ratios of 2 Ni atoms to 1 Si atom we have shown that the first silicide phase to form from a nickel/amorphous-silicon reaction is amorphous-nickel-silicide, and that the composition of this phase is approximately 1 Ni to 1 Si. In these films the amorphous-nickel-silicide will grow until Ni_2Si forms at the crystalline nickel/amorphous-nickel-silicide interface. If the modulation period of the films is over 25.0 nm, both the amorphous-nickel-silicide and polycrystalline Ni_2Si will grow simultaneously until the amorphous-silicon is consumed. At this point, the amorphous-nickel-silicide growth stops, and the crystalline Ni_2Si continues to grow to convert the entire thin film to Ni_2Si .

We have demonstrated that calorimetry can be used to determine an activation energy of 1.4 eV for the formation of Ni_2Si , an activation energy of 1.5 eV for amorphous-nickel-silicide growth and an activation energy of 1.5 eV for the growth of Ni_2Si to consume the entire thin film. We also determined that the peak temperature for Ni_2Si growth shifted to higher temperatures with increasing modulation period. This peak shift with increasing modulation period was modeled to give an activation energy for

Ni₂Si growth of 1.5 eV and a diffusion pre-exponential coefficient of 10 cm²/sec, in agreement with earlier work.

Constant-scan-rate calorimetric data indicated a double exothermic peak structure for the formation and growth of Ni₂Si while isothermal calorimetric data indicated an exothermic peak for Ni₂Si formation. These calorimetric results were characteristic of nucleation controlled, not growth controlled, silicide phase selection. This combined with thermodynamic analysis of amorphous-nickel-silicide formation at the nickel/amorphous-silicon interface indicated that in nickel/amorphous-silicon thin film reactions, nucleation controls phase selection. With nucleation controlling phase selection, we determined that the nucleation surface energies of the crystalline nickel silicides, besides Ni₃Si, had to be 1.6 to 3.0 times larger than the nucleation surface energy of amorphous-nickel-silicide in order for this phase to be the first phase to form at the nickel/amorphous-silicon interface.

4.8 References

1. F.M d'Heurle, C.S. Petersson, J.E.F. Baglin, S.J. Placa, and C.Y. Wong, J. Appl. Phys., 55, 4208 (1984)
2. L.A. Clevenger, C.V. Thompson, R.C. Cammarata and K.N. Tu, Appl. Phys. Lett., 52, 795 (1988)
3. L.A. Clevenger, C.V. Thompson, R.C. Cammarata and K.N. Tu, Mater. Res. Symp. Proc. 103, 191 (1988)
4. L.A. Clevenger, C.V. Thompson, A. Judas and K.N. Tu, First MRS International Meeting on Advanced Materials, 10, 431 (1989)

5. L.A. Clevenger, C.V. Thompson, R.R. De Avillez and K.N. Tu, to appear in the Proceedings of the Symposium on Chemistry and Defects in Semiconductor Heterostructures the Spring 1989 Meeting of the Materials Research Society, edited by M. Kawabe, T. Sands, E. Weber and R.S. Williams
6. E. Ma, W.J. Meng, W.L. Johnson, M.-A. Nicolet and M. Nathan, Appl. Phys. Lett. 53, 2033 (1988)
7. E.J. Cotts, W.J. Meng and W.L. Johnson, Phys. Rev. Lett. 57, 2295 (1986)
8. R.J. Highmore, J.E. Evetts, A.L. Greer, and R.E. Somekh, Appl. Phys. Lett., 50, 566 (1987)
9. K.N. Tu, W.K. Chu and J.W. Mayer, Thin Solid Films, 25, 403 (1975)
10. U. Gosele and K.N. Tu, J. Appl. Phys. 53, 3252 (1982)
11. F.M. d'Heurle, J. Mater. Res. 3, 167 (1988)
12. Sabine an Mey, Z. Metallkde, 77, 805 (1986)
13. E.P. Donovan, F. Spaepen, D. Trunbull, J.M. Poate and D.C. Jacobson, J. Appl. Phys. 57, 4208 (1984)
14. K.R. Coffey, L.A. Clevenger, K. Barmack, D.A. Rudman and C.V. Thompson, to be published
15. M. Avrami, J. Chem. Phys. 9, 177 (1941)
16. J.W. Christen, Theory of Transformations of Metals and Alloys
17. W.C. Johnson, C.L. White, P.E. Marth, P.K. Ruf, S.M. Tuominen, K.D. Wade, K.C. Russell and H.I. Aaronson, Met. Trans. A, 6A, 911 (1975)
18. R.R. de Avillez, L.A. Clevenger and C.V. Thompson, unpublished work

5 Controlled Silicidation of Vanadium/Amorphous-Silicon Multilayer Thin Films

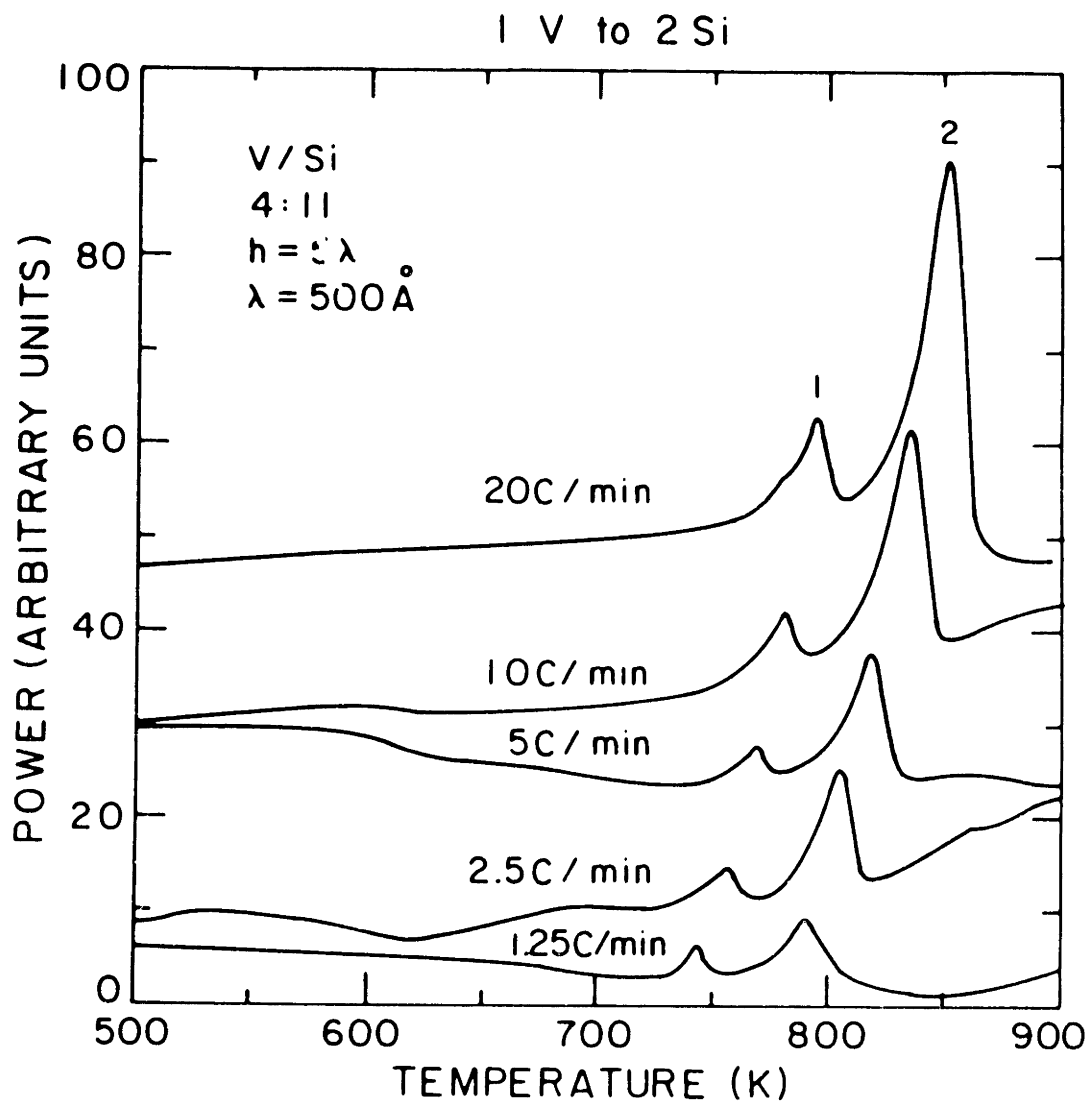
5.1 Introduction

This chapter is a quantitative discussion of vanadium/amorphous-silicon reactions. The emphasis is similar to that of the work for nickel/amorphous-silicon reactions presented in chapter 4. This chapter is divided into two sections. In section 5.2, we discuss the kinetics of crystalline VSi_2 formation and growth, while in section 5.3, we determine whether nucleation mechanisms or growth mechanisms are responsible for amorphous and crystalline vanadium silicide formation from vanadium/amorphous-silicon reactions.

5.2 Reaction Kinetics

In order to investigate the kinetics of vanadium/amorphous-silicon reactions calorimetric analysis of vanadium/amorphous-silicon multilayer thin films with a modulation period of 50 nm was performed. Constant-heating-rate traces for this multilayer thin film for five scan rates ranging from 1.25 to 20 K/min are shown in figure 1. Each of the traces has two peaks labeled 1 and 2 which correspond to exothermic reactions. Samples for X-ray diffraction were prepared in the as-deposited condition and after heating at 20 K/min to either 793 K or 870 K and cooled at 320 K/min to room temperature. X-ray analysis of the as-deposited sample indicated the

Figure 1 DSC traces for multilayer films with atomic concentration ratios 1 V to 2 Si, with a modulation period of 50 nm and with a total film thickness of 250 nm. Each curve corresponds to a different scan rate.



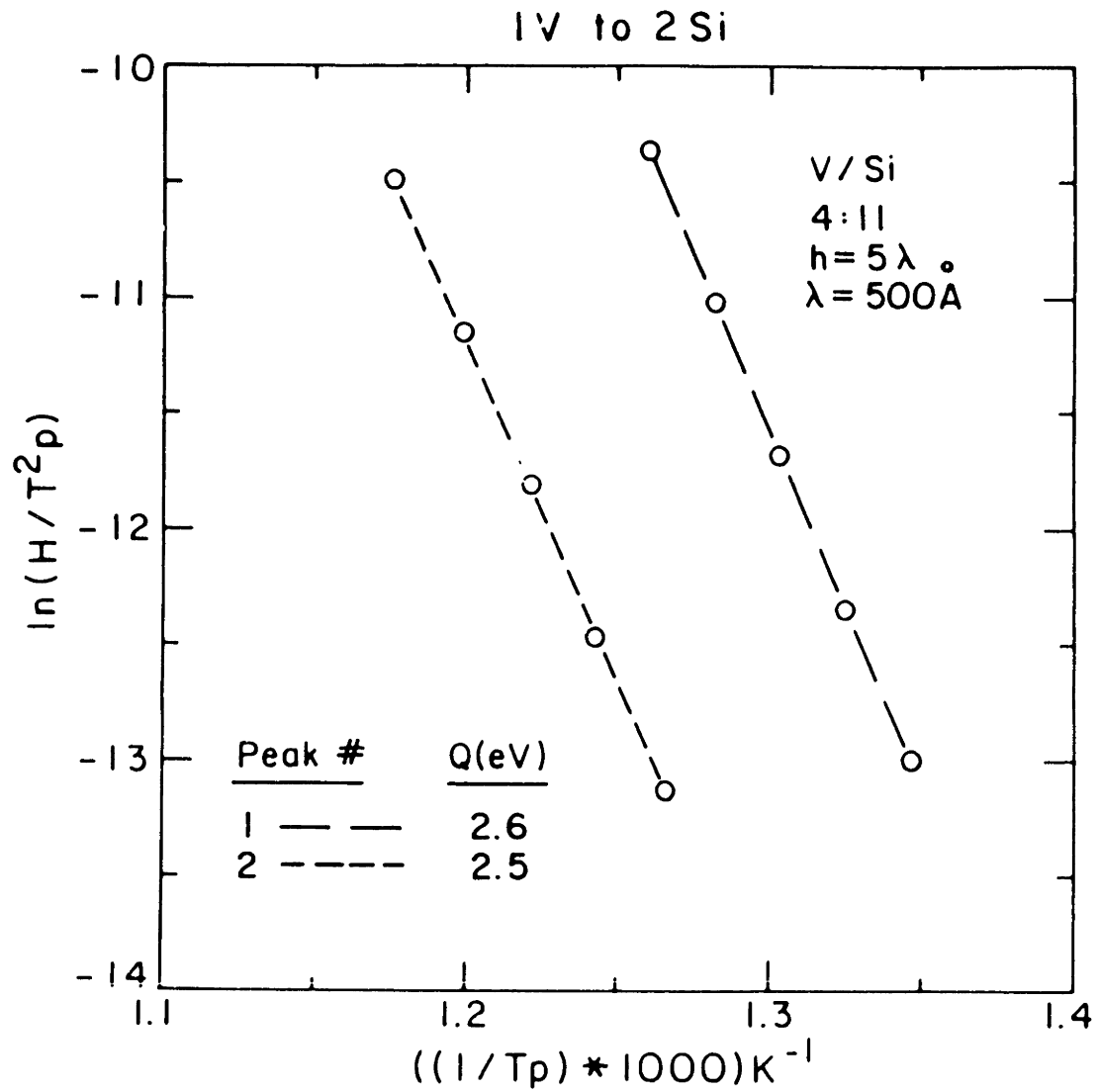
presence of only vanadium and amorphous-silicon. The X-ray data for the sample heated to 793 K indicated the presence of vanadium, amorphous-silicon and crystalline VSi_2 . This suggests that peak 1 of figure 1 is due to the formation of VSi_2 . X-ray data from a sample heated to 870 K indicated the presence of only VSi_2 , allowing peak 2 of figure 1 to be associated with the growth of VSi_2 to transform the entire thin film into VSi_2 .¹

As demonstrated in figure 1, as the heating rate is decreased, both peaks 1 and 2 shift to lower temperatures. This is similar to results reported in section 4.3 for amorphous-nickel-silicide and Ni_2Si formation and growth in nickel/amorphous-silicon thin film reactions. Following the method outlined in section 3.2.1, the activation energies for peaks 1 and 2 can be determined from the slope of a plot of $\ln(H/T_p^2)$ versus $1/T_p$ where H is the heating rate and T_p is the peak temperature at that heating rate. Figure 2 shows plots of $\ln(H/T_p^2)$ versus $1/T_p$ for the data of figure 1. From this analysis the activation energy for the formation of VSi_2 is 2.6 eV (peak 1) and the activation energy for the growth of VSi_2 is 2.5 eV (peak 2). These values are in agreement with the value of 2.3 eV reported by Psaras et al.² for VSi_2 formation from a vanadium/amorphous-silicon bilayer reaction.

5.3 Determination of the Mechanism that Controls Silicide Phase Selection in Vanadium/Amorphous-Silicon Reactions

To understand whether nucleation mechanisms or growth mechanisms control silicide phase selection in vanadium/amorphous-silicon reactions, we have used a combination of cross-sectional transmission electron microscopy, thermodynamic analysis, constant-

Figure 2 Plot of $\ln(H/T_p^2)$ vs $(1/T_p)$ for the data in figure 1 where H is the heating rate and T_p is the peak temperature.



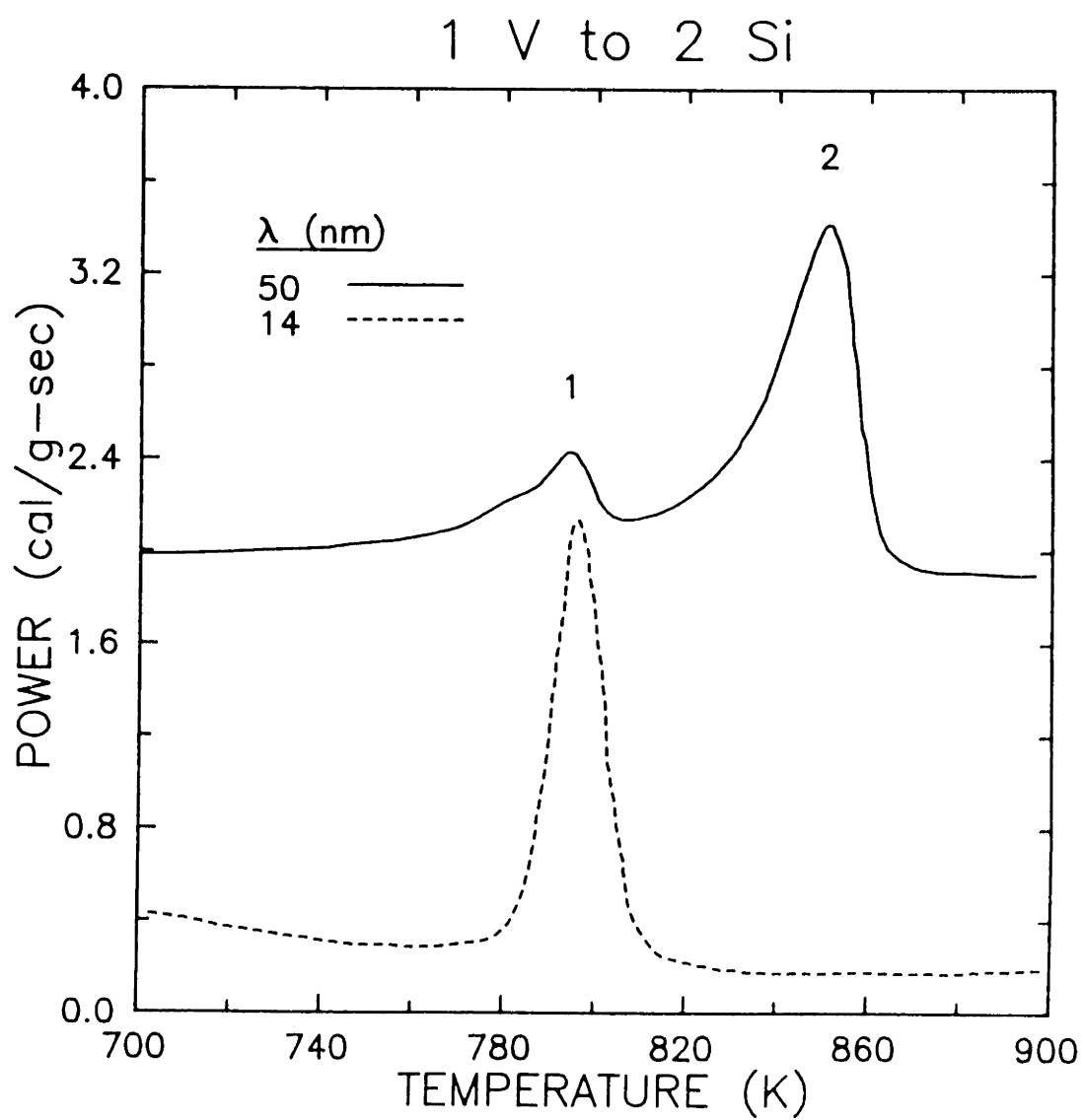
heating-rate calorimetry and isothermal calorimetry. The methodology presented in this section is similar to that presented in section 4.5, where we used the techniques listed above to demonstrate that nucleation mechanisms control phase selection in nickel/amorphous-silicon thin film reactions.

5.3.1 Results

In figure 3, we present a constant-scan-rate calorimetric trace for a vanadium/amorphous-silicon multilayer thin film with a modulation period of 14 nm and another film with a period of 50 nm. The scan rate for both traces was 20 K/min and as discussed in section 5.2, all the peaks in figure 3 correspond to exothermic reactions. As the modulation period of the multilayer thin film is increased from 14 to 50 nm, peak 1 decreases in intensity but does not disappear or shift while peak 2 appears for the 50 nm multilayer thin film. As discussed in section 5.2 and reference 1, thin film X-ray diffraction established two important points: first, that peaks 1 and 2 were due to the formation and growth of crystalline VSi_2 and secondly, for annealing temperatures over 820 K for the 14 nm multilayer thin film or 860 K for the 50 nm thin film, that the thin film had been completely transformed to crystalline VSi_2 .

In order to study the early stages of VSi_2 formation, samples with 50 nm modulation periods were prepared for cross-sectional transmission electron microscopy after being heated at 20 K/min to 758 K, 783 K and 808 K and then quenched to room temperature at 320 K/min. These temperatures correspond to a temperature slightly lower than peak 1 (758 K), at the middle of peak 1 (783 K) and slightly higher than peak 1 (808 K). The

Figure 3 Constant-heating-rate differential scanning calorimeter traces for vanadium/amorphous-silicon multilayer films with atomic concentration ratios of 1 V atom to 2 Si atoms and modulation periods of 14 and 50 nm.



corresponding micrographs are shown in figures 4 through 6. These micrographs are dark field imaging made using the V (100) polycrystalline diffraction ring (figure 4) and the V (100) and VSi₂ (1121) polycrystalline diffractions rings (figures 5 and 6). The V (100) and VSi₂ (1121) atomic planes have the same interatomic spacing and their polycrystalline diffraction rings in transmission electron diffraction overlap.

Figure 4 shows that the structure of a vanadium/amorphous-silicon multilayer film heated to 758 K is made up of polycrystalline vanadium layers and amorphous-silicon (dark) layers. Between the vanadium and the amorphous-silicon layers there is a layer which is approximately 5 nm thick, is brighter than the amorphous-silicon layer and has no crystalline contrast as shown for the vanadium layer. We identify this reacted layer as an amorphous-vanadium-silicide phase and its existence as the first phase to form from a reaction between vanadium and amorphous-silicon has been previously reported by Nathan.³

In figure 5, we show a portion of a 50 nm multilayer film heated to 783 K. The structure of this film is similar to that of the sample heated to 758 K in figure 4. Annealing at this temperature has caused the amorphous-vanadium-silicide (lighter colored layer) to thicken by about 1 nm compared to figure 4. Figure 5 also shows that nuclei of VSi₂ have started to form at the amorphous-silicon/amorphous-vanadium-silicide interface. Several of these nuclei are marked by arrows. At this temperature, most of these nuclei have not yet formed a continuous layer between the amorphous-vanadium-silicide and amorphous-silicon layers.

The structure of a 50 nm multilayer thin film heated to 808 K is shown in figure 6. The structure of this film is similar to that of the sample heated to 783 K shown in figure 5, except that VSi₂ has grown into a continuous

Figure 4 Dark field transmission electron micrograph (using the (110) vanadium polycrystalline diffraction ring) of a vanadium/amorphous-silicon multilayer film which has been heated at 20 K/min to 758 K and quenched to room temperature; (a) polycrystalline vanadium; (b) amorphous-vanadium-silicide (highlighted by arrows); (c) amorphous-silicon.

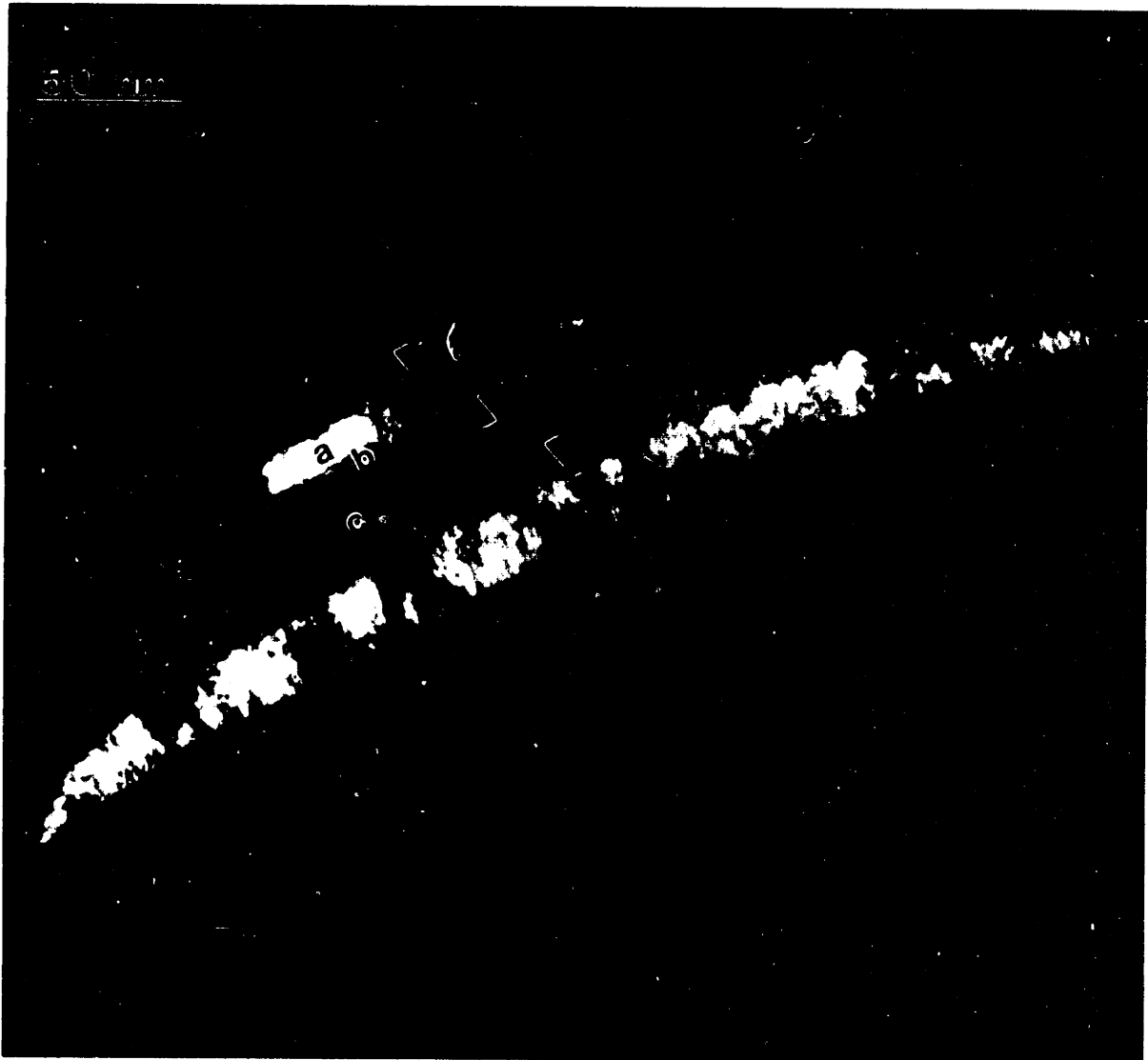


Figure 5 Dark field transmission electron micrograph (using the (110) vanadium and (1121) VSi_2 diffraction rings) of a vanadium/amorphous-silicon multilayer film which has been heated at 20 K/min to 783 K and quenched to room temperature; (a) polycrystalline vanadium; (b) amorphous-vanadium-silicide; (c) amorphous-silicon. Nuclei of VSi_2 have formed at the amorphous-vanadium-silicide/amorphous-silicon interface and several of them are marked by arrows.

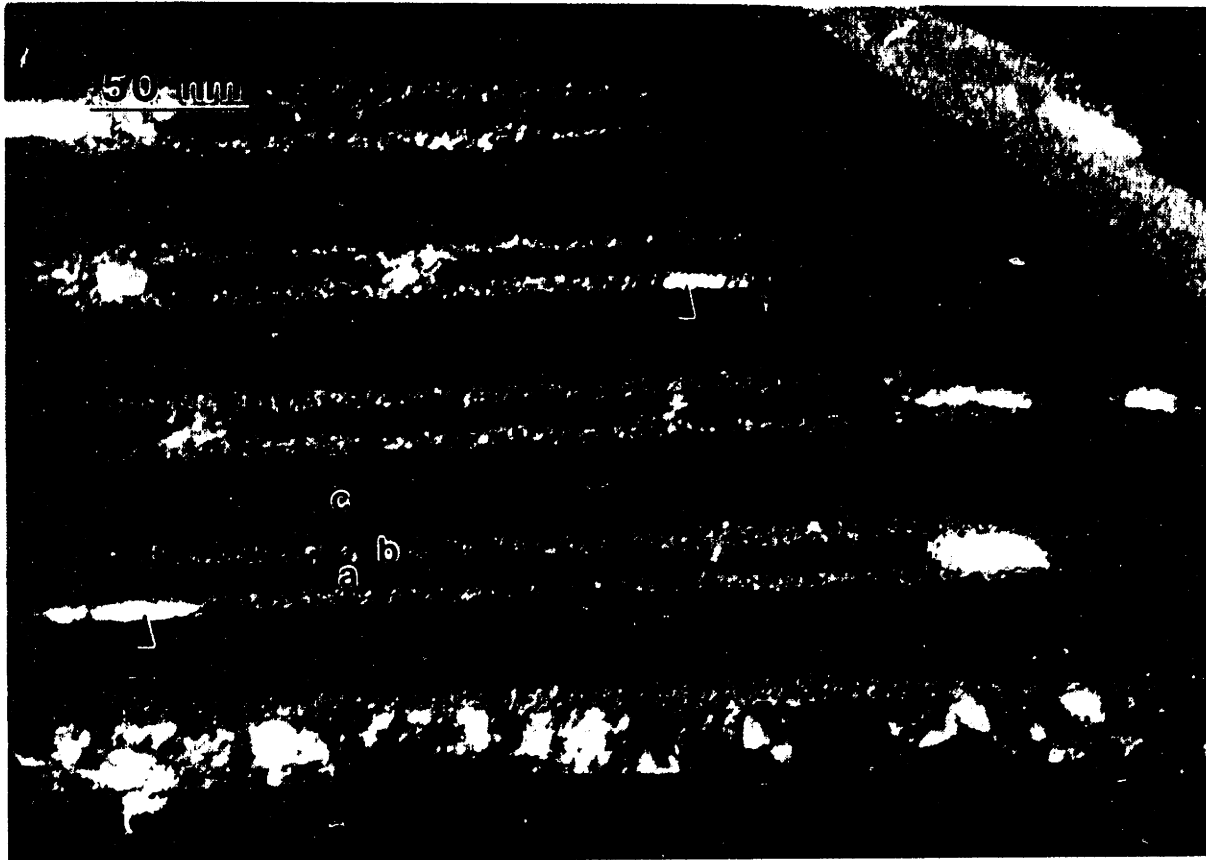
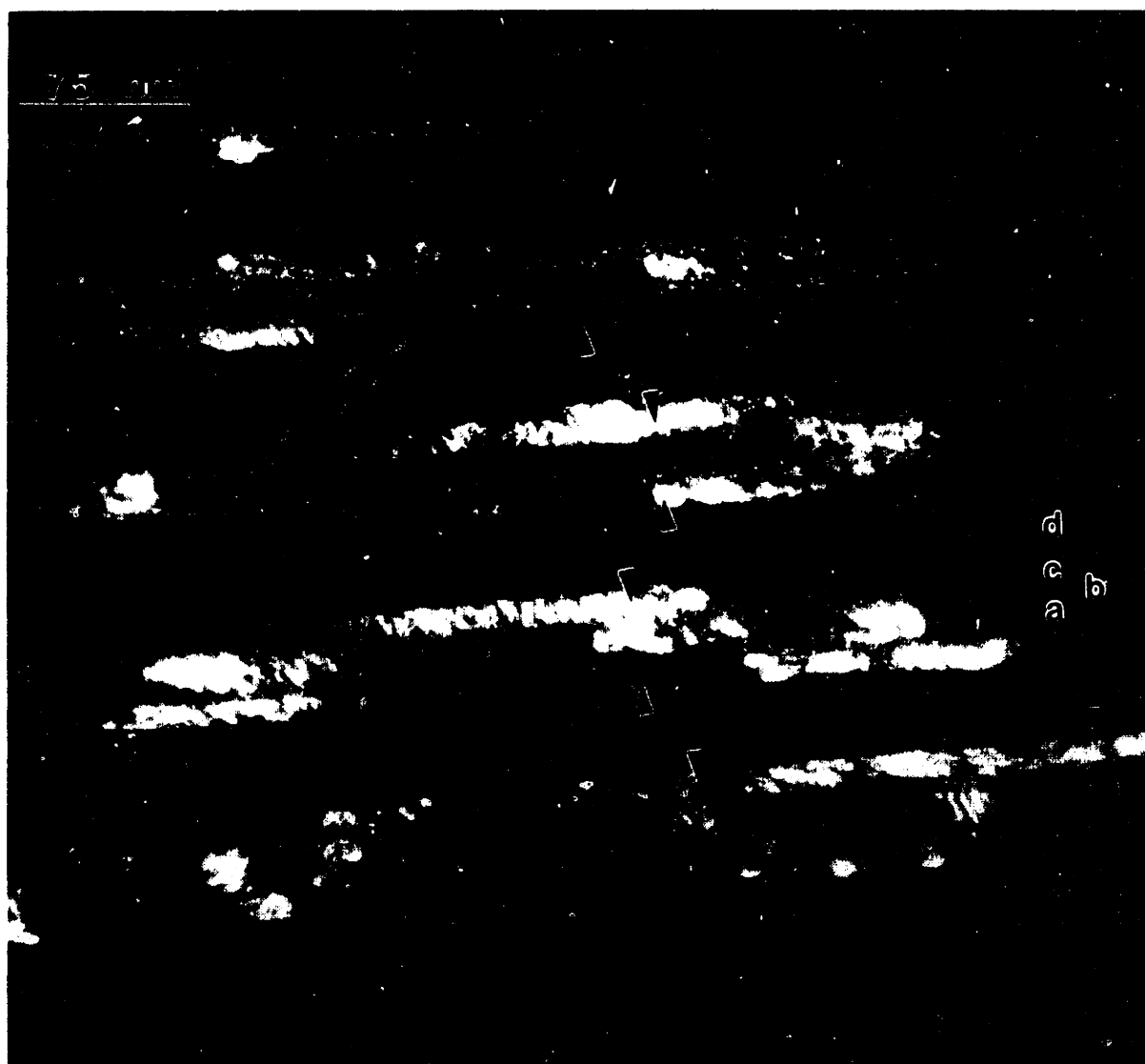


Figure 6 Dark field transmission electron micrograph (using the (110) vanadium and (1121) VSi_2 diffraction rings) of a vanadium/amorphous-silicon multilayer film which has been heated at 20 K/min to 808 K and quenched to room temperature; (a) polycrystalline vanadium; (b) amorphous-vanadium-silicide; (c) VSi_2 which has formed into a continuous layer (marked by arrows) between the amorphous-silicon and amorphous-vanadium-silicide; (d) amorphous-silicon.



layer between the amorphous-silicon and amorphous-vanadium-silicide layers. This allows us to identify peak 1 of figure 3 with the nucleation and two-dimensional growth of VSi_2 into a continuous layer between the amorphous-silicon and amorphous-vanadium-silicide layers. Heating the 50 nm thin film past 808 K causes the VSi_2 layer to undergo one-dimensional thickening to transform the entire film into VSi_2 , leading to peak 2.

Isothermal calorimetry was done to independently study the formation of VSi_2 (peak 1 of figure 3) and the one-dimensional growth of VSi_2 (peak 2 of figure 3). We chose the 14 nm multilayer thin film for isothermal studies because it was the only sample for which there was no one-dimensional VSi_2 growth after the VSi_2 formation. Figure 7 presents isothermal calorimetry data for this film. This sample was heated at 320 K/min from 310 to 730 K and allowed to stabilize, then heated at 320 K/min to 750 K and held at this temperature for 10 minutes. Figure 7 is characterized by an initial increase in the amount of heat released with increasing time followed by a decrease to give a peak in the calorimetric data. Thin film X-ray diffraction was used to associate this peak with the formation of VSi_2 .

5.3.2 Discussion

As demonstrated in figure 4, the first phase that forms from a reaction between vanadium and amorphous-silicon is an amorphous-vanadium-silicide. This can be explained by considering the Gibbs free energy versus composition diagram shown in figure 8. In this figure, the free energies at 750 K of bcc vanadium, covalently bonded amorphous-

Figure 7 Isothermal differential calorimetry trace for a vanadium/amorphous-silicon multilayer film annealed at 750 K. The modulation period of the film was 14 nm.

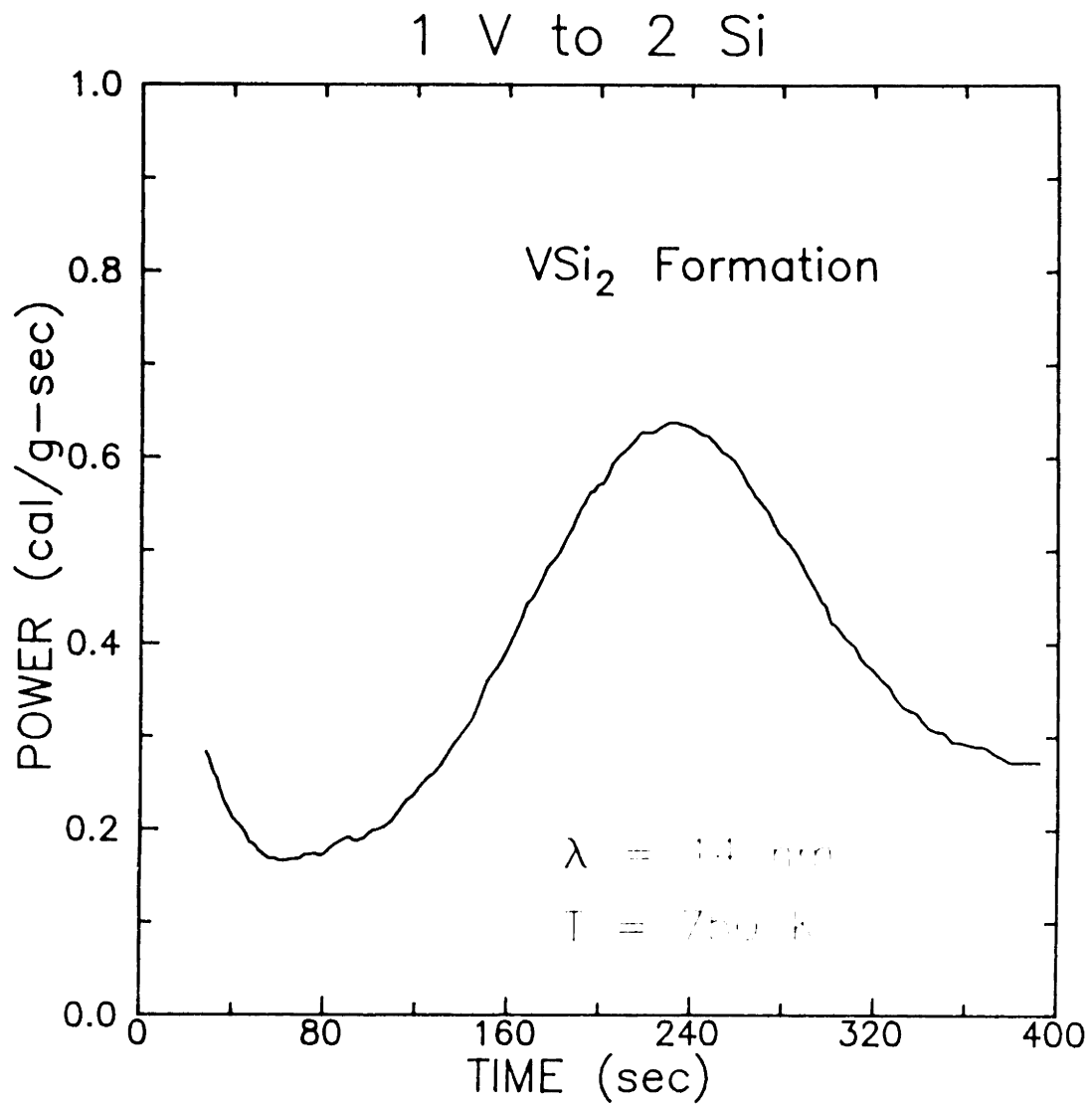
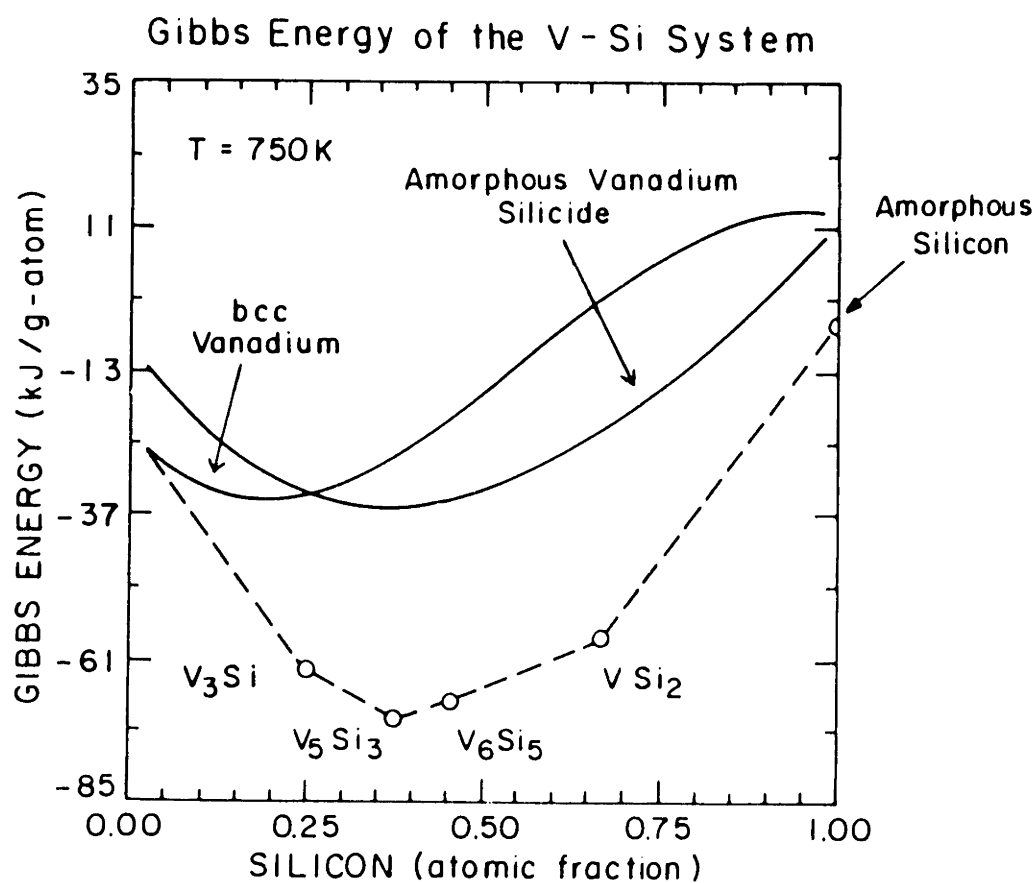


Figure 8 Gibbs free energy versus composition diagram for the vanadium/silicon system at a temperature of 750 K. The crystalline silicides are distinguished by the symbol "O". Dashed lines are common tangents for bcc vanadium, the crystalline silicides and amorphous-silicon.



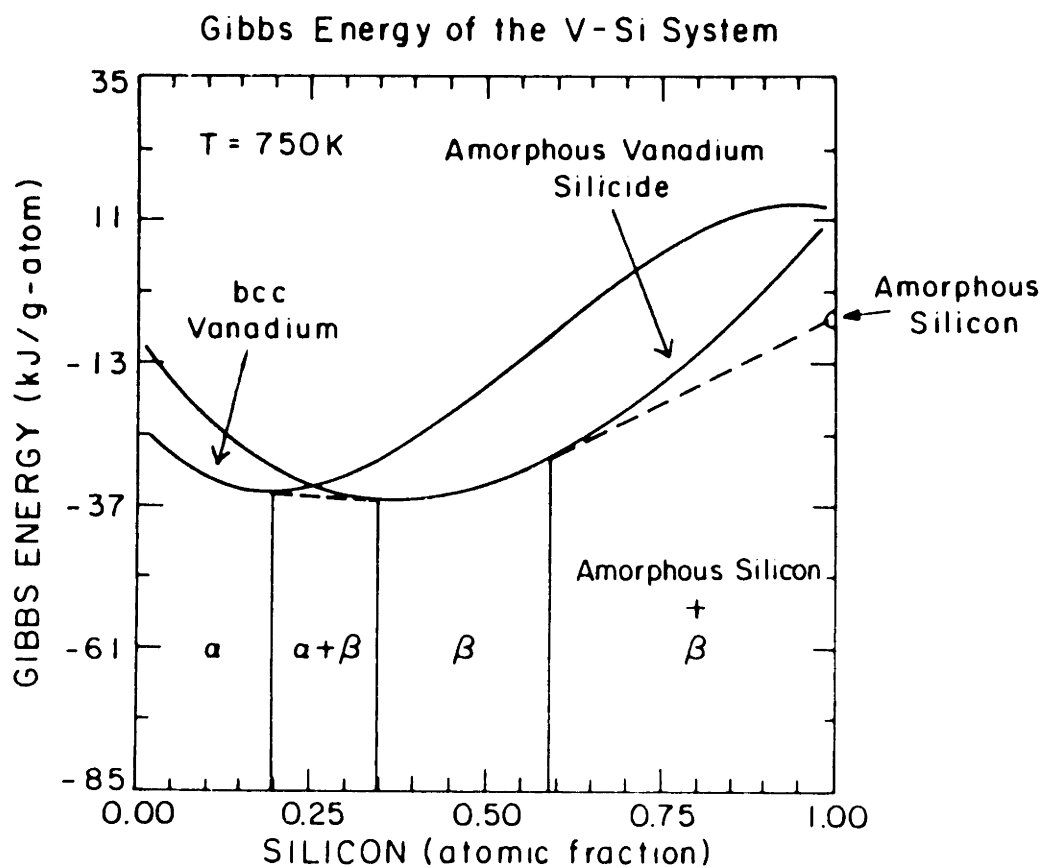
silicon, crystalline vanadium silicides and amorphous-vanadium-silicide are plotted as a function of composition based on calculations discussed in appendix C.

The common tangents for bcc vanadium, the crystalline vanadium silicides and pure amorphous-silicon have been included in figure 8. The amorphous-vanadium-silicide free energy curve lies above the common tangents, indicating that the amorphous-vanadium-silicide is unstable with respect to the crystalline silicides if all or anyone of the crystalline silicides are present. This implies that an amorphous-vanadium-silicide would not form at the vanadium/amorphous-silicon interface if there were no kinetic barriers preventing the formation of the crystalline silicides.

Because amorphous-vanadium-silicide forms at the vanadium/amorphous-silicon interface, there must be kinetic barriers that prevent the formation of the crystalline vanadium silicides. As discussed previously in section 4.5, two models for the nature of these kinetic barriers have been proposed, one based on the presence of nucleation barriers⁴ and the other based on growth barriers.⁵ As discussed in detail in section 4.5 for amorphous-nickel silicide formation in nickel/amorphous-silicon reactions, it is only possible to form a thermodynamically unstable amorphous-silicide phase *before* the formation of thermodynamically stable crystalline silicides if there are nucleation barriers to the formation of the crystalline silicides at the metal/amorphous-silicon interfaces.

With nucleation barriers preventing the formation of the crystalline silicides, we can remove the crystalline silicides from the Gibbs free energy versus composition diagram of figure 3. The resulting diagram is shown in figure 9, with the common tangents now drawn between bcc vanadium, amorphous-vanadium-silicide and amorphous-silicon. This construction

Figure 9 Same diagram as figure 6, except that we have assumed that nucleation barriers prevent the formation of the crystalline silicides. Common tangents are drawn in for bcc vanadium (α), amorphous-vanadium-silicide (β) and amorphous-silicon.

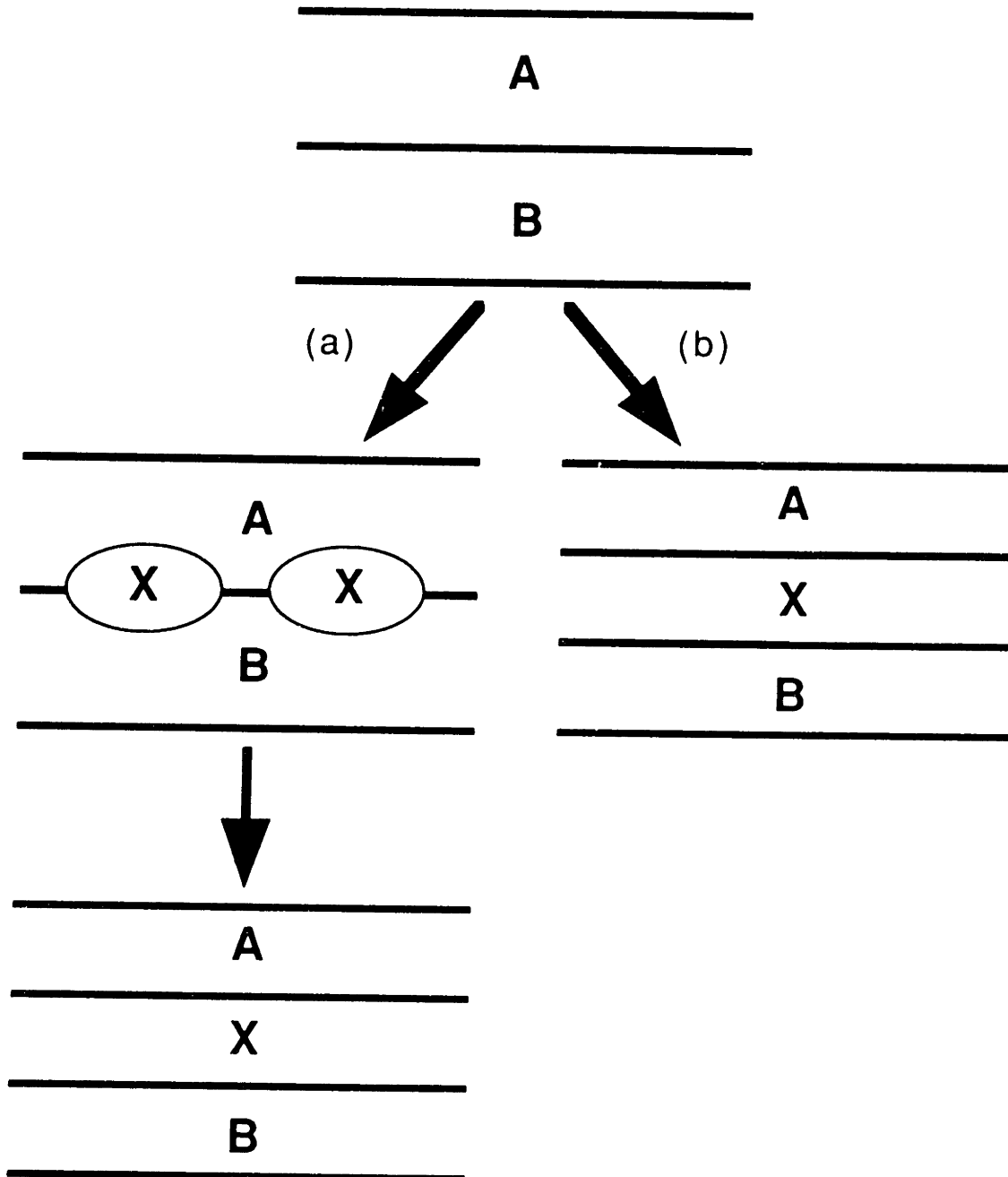


indicates that with nucleation barriers preventing the formation of the crystalline silicides, amorphous-vanadium-silicide can form from and be in equilibrium with vanadium and amorphous-silicon. This diagram also predicts that the amorphous-vanadium-silicide should have a composition range of approximately 35 to 60 atomic percent silicon at 750 K.

Further evidence for nucleation controlling phase selection is provided in the cross-sectional micrographs of VSi_2 formation in figures 4-6. To begin with, consider an idealized case where a crystalline intermetallic phase X forms between an A and a B layer. At the early stages of formation, the morphology of the X layer will be very different if nucleation as opposed to growth controls X formation. If nucleation controls X formation, X will nucleate as isolated islands at the A/B interface and then undergo growth both perpendicular and parallel to the plane of the layers until a continuous X layer is formed between the A and the B layers. At this stage further growth of the X layer will be in a direction perpendicular to the original layers. The locations along the A/B interface where the X phase has not yet formed into a continuous layer can only be explained by nucleation barriers preventing the formation of X at most of the A/B interface. In contrast, if growth mechanisms control X formation, X will form as a continuous layer between the A and B layers. The morphology for nucleation controlled and growth controlled X formation is shown in figures 10.

In comparing the predicted morphology for X formation from figure 10 to the actual morphology of VSi_2 forming at the amorphous-vanadium-silicide/amorphous-silicon interface shown in figures 4 through 6, we see that these figures suggest that nucleation barriers are controlling crystalline silicide phase selection in vanadium/amorphous-silicon

Figure 10 Morphology for the idealized case of phase X forming at an A/B interface for (a) nucleation controlled formation and (b) growth controlled formation.



reactions. This is demonstrated by figures 5 and 6 in which crystalline VSi_2 forms at the amorphous-vanadium-silicide/amorphous-silicon interface as isolated islands which then grow into a continuous layer. This morphology is consistent with nucleation controlled phase selection (figure 10a) and is not consistent with growth controlled phase selection (figure 10b).

Further evidence for nucleation barriers controlling silicide phase selection is provided in the calorimetric data of figures 3 and 7. In these figures, the heat released per unit time dH/dt is related to the volume fraction of VSi_2 transformed by:

$$\frac{dH}{dt} = (-\Delta H_f) (V_f) \frac{dX_v}{dt} \quad (1)$$

where ΔH_f is the heat of formation for the forming phase (per unit volume), V_f is the final transformed volume and dX_v/dt is the change in the fraction transformed of VSi_2 with time.

With the constant-scan-rate trace of figure 3 for the 50 nm film, peaks 1 and 2 are related to the formation and growth of VSi_2 . Recently Coffey et al.⁶ have developed a model for the rate of formation of a product phase which nucleates at a planar interface between two layers (see appendix B). Their expression for VSi_2 formation at the amorphous-vanadium-silicide/amorphous-silicon interface is,

$$\frac{dX_v}{dt} = R \left(\left(\frac{dX_a}{dT} \right) \frac{w}{w_{\max}} + \left(\frac{dw}{dT} \right) \frac{X_a}{w_{\max}} \right) \quad (2)$$

where w is the thickness of VSi_2 , w_{max} is the maximum thickness that VSi_2 can grow to in a plane perpendicular to the plane of the layers and is a function of the modulation period, R is the scan rate, T is the temperature, X_a is the areal fraction of VSi_2 in a plane parallel to the plane of the original layers, and dX_a/dT and dw/dT are the change in the areal fraction and thickness of the VSi_2 layer, respectively, with temperature. Combining equations 1 and 2, we obtain:

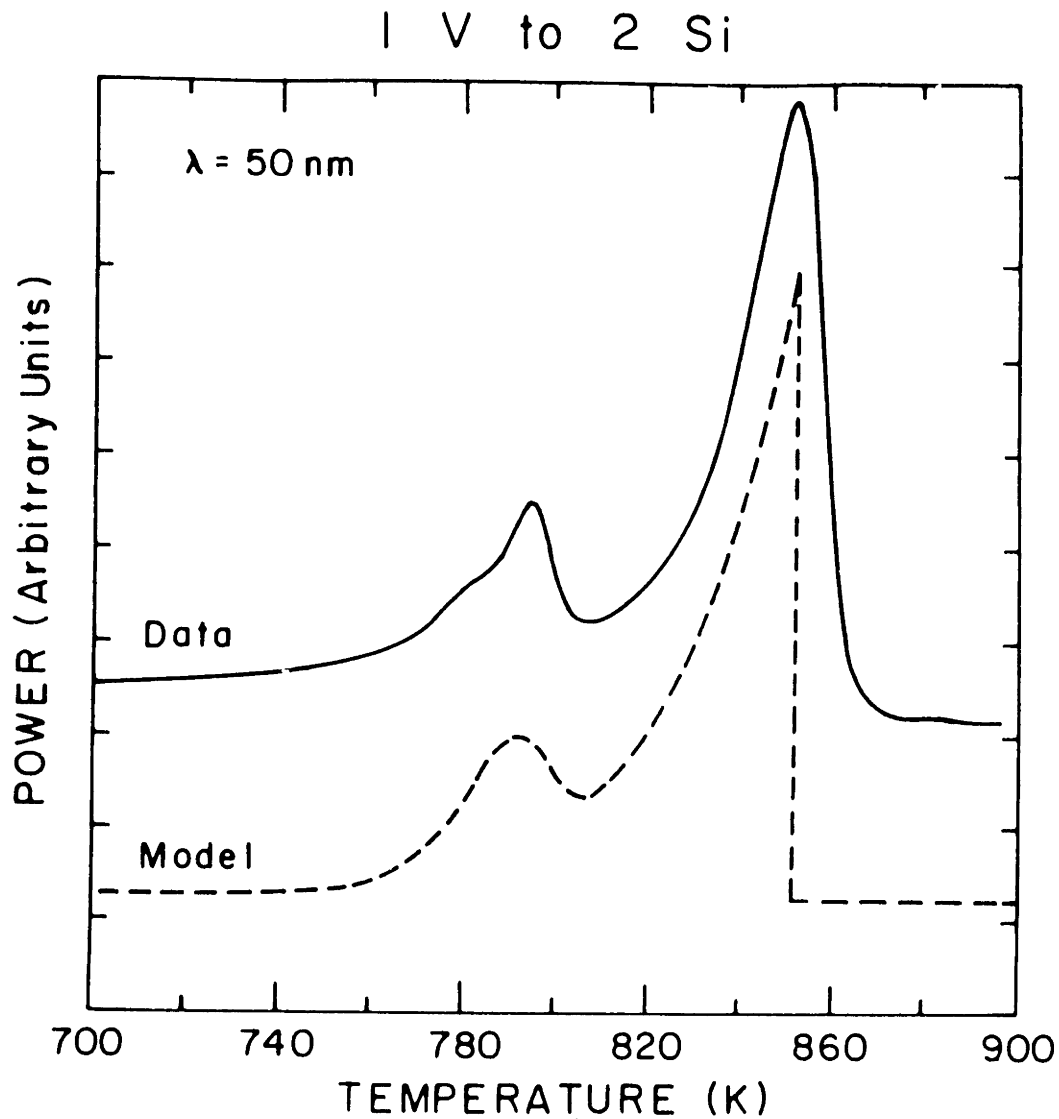
$$\frac{dH}{dt} = (-\Delta H_f)(V_f)R \left(\left(\frac{dX_a}{dT} \right) \frac{w}{w_{\text{max}}} + \left(\frac{dw}{dT} \right) \frac{X_a}{w_{\text{max}}} \right) \quad (3)$$

In figure 11, we compare the actual calorimetric data for VSi_2 formation in the 50 nm thin film to predictions made using equation 3. As shown by this figure, there is good agreement between the shape and magnitude of the real data and the model.

There are two important points about figure 11. First, equation 3 results from a modified Johnson-Mehl-Avrami analysis of VSi_2 formation and growth. This type of analysis requires that nucleation, not growth, control vanadium silicide phase selection. Secondly, this model predicts the double peak structure (peaks 1 and 2 of figure 1) for the formation and growth of VSi_2 . These characteristics of the constant-scan-rate calorimetric data cannot be accounted for by a model which is based on growth controlled silicide phase selection.

Finally, further evidence of nucleation controlled phase selection in vanadium/amorphous-silicon reactions is present in the isothermal calorimetric measurements of the heat released during VSi_2 formation in the 14 nm film shown in figure 7. In isothermal calorimetric

Figure 11 Constant-scan-rate calorimetric data for a 50 nm modulation period multilayer film plotted with predicted calorimetric data (dashed line) derived from equation 3. The parameters used for the model were $\lambda = 50$ nm, $w_0 = 7.5$ nm, $Q_i = 2.6$ eV, $k_0 = 3.0 \times 10^7$ cm/sec, $Q_0 = 2.5$ eV and $Nk_{i,0}^2 = 2.59 \times 10^{29}$ #/sec² (see appendix B).



measurements, the heat released per unit time is related to the fraction of silicide phase transformed as shown in equation 1. If silicide phase selection is nucleation controlled, the fraction of silicide phase transformed with respect to time, dX_v/dt can be expressed as (see section 4.5):

$$\frac{dX_v}{dt} = n C t^{n-1} e^{-Ct^n} \quad (4)$$

where n is the Avrami exponent, t is time and C has the form $C=C_0e^{(-Q/kT)}$ where Q is an energy which is a function of the activation energies for nucleation and growth and C_0 is a temperature independent constant. Combining equations 1 and 4, we can write that the isothermal calorimetry signal as a function of time for nucleation controlled silicide phase selection is:

$$\left(\frac{dH}{dt}\right)_{nuc} = (-\Delta H_f) V_f n C t^{n-1} e^{-Ct^n} \quad (5)$$

If silicide phase selection were controlled by one-dimensional growth, the fraction transformed dX_v/dt of equation 4 would have a different form. Assuming for growth controlled silicide phase selection that the growth process starts out being interface limited and then with increasing layer thickness becomes diffusion limited, dX_v/dt can be expressed as (from section 4.5):

$$\frac{dX_v}{dt} = \frac{C_2}{w_{max}} \left(\frac{1}{K_{i,o} e^{\left(\frac{-Q_I}{kT}\right)}} + \frac{1}{\frac{D_{p,o}}{w} e^{\left(\frac{-Q_P}{kT}\right)}} \right)^{-1} \quad (6)$$

where C_2 is a dimensionless constant whose value depends on the equilibrium concentrations at the reacting interfaces,⁴ $K_{l,o}$ and $D_{p,o}$ are temperature independent constants for interface limited and diffusion limited growth, respectively and Q_l and Q_p are activation energies for interface limited and diffusion limited growth respectively. Combining equations 1 and 6, the rate of heat release during growth controlled silicide formation is:

$$\left(\frac{dH}{dt}\right)_{\text{growth}} = \frac{-\Delta H_f V_f C_2}{w_{\text{max}}} \left(\frac{1}{K_{l,o} e^{\left(\frac{-Q_l}{kT}\right)}} + \frac{1}{\frac{D_{p,o}}{w} e^{\left(\frac{-Q_p}{kT}\right)}} \right)^{-1} \quad (7)$$

Theoretical calorimetry curves for nucleation controlled and growth controlled silicide phase selection are shown in figures 12a and 12b respectively.

In figure 12, with nucleation controlled phase selection (figure 10a) the rate of heat released due to silicide formation dH/dt initially increases before subsequently decreasing with time. With pure growth controlled phase selection without nucleation (figure 12b), the rate of heat released due to silicide formation is either constant or decreasing with time. In examining the actual calorimetric data for figure 7, we see that there is a peak in the curve for dH/dt versus time for VSi_2 formation at the amorphous-vanadium-silicide/amorphous-silicon interface. This curve has the same shape as the curve in figure 12a, where nucleation of the silicide is the rate controlling mechanism for silicide formation. The peak of figure 7 for VSi_2 formation cannot be explained by a pure planar growth mechanism. Thus, isothermal calorimetry further supports the conclusion drawn from thermodynamic analysis, cross-sectional

Figure 12a Theoretical isothermal calorimetry curve for nucleation and growth of a silicide.

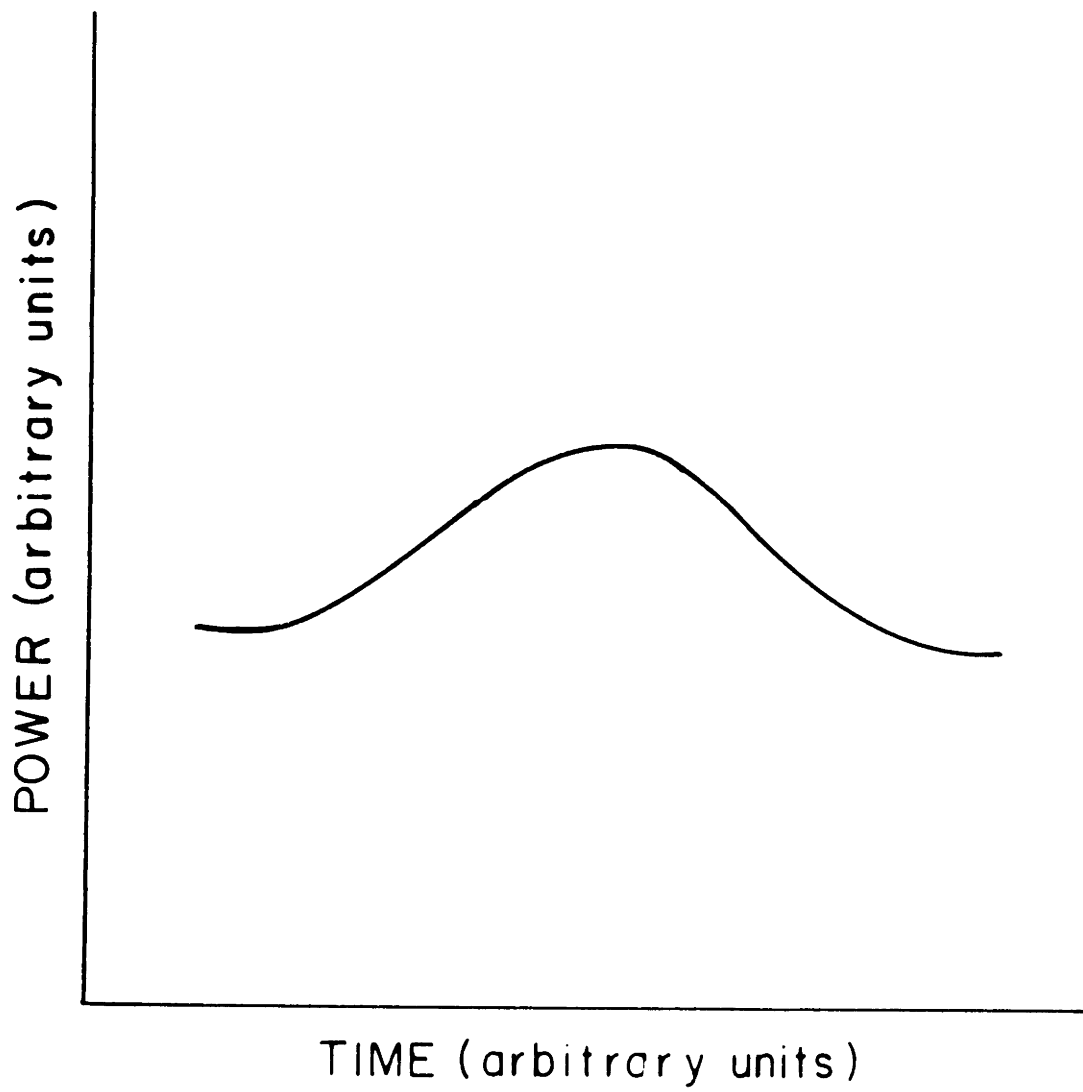
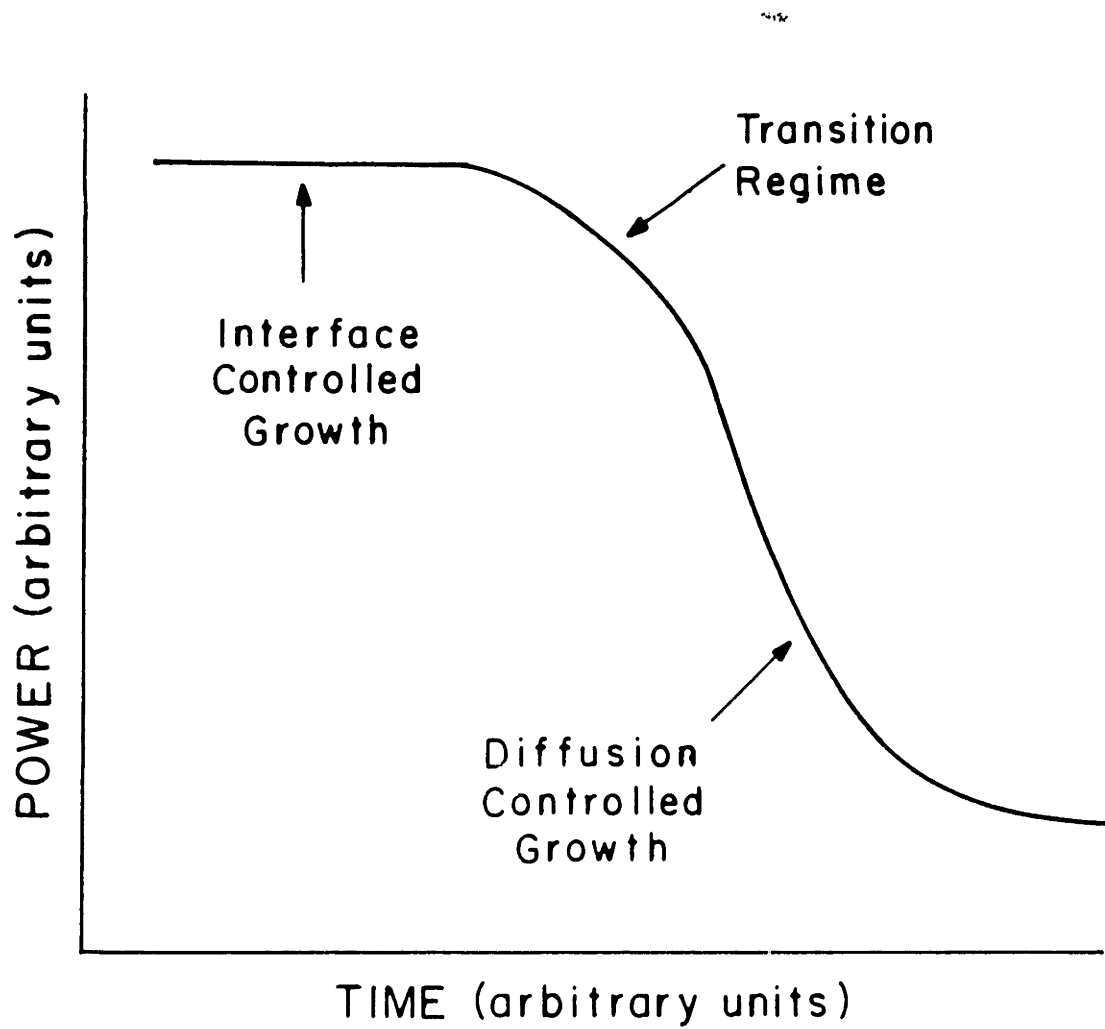


Figure 12b Theoretical isothermal calorimetry curve for simple one-dimensional growth of a silicide without nucleation.



transmission electron microscopy and constant-scan-rate calorimetry that nucleation as opposed to growth controls amorphous and crystalline silicide phase selection in vanadium/amorphous-silicon thin film reactions.

5.4 Conclusions

We have presented thermodynamic, microscopic and calorimetric evidence indicating that nucleation barriers are responsible for amorphous and crystalline phase selection in vanadium/amorphous-silicon thin film reactions. For these reactions, an amorphous vanadium silicide is the first phase to form at the vanadium/amorphous-silicon interface. Analysis of Gibbs free energy diagrams indicates that the amorphous vanadium silicide can form and be in equilibrium with vanadium and amorphous-silicon if there are nucleation barriers to the formation of the crystalline silicides. Heating these thin films over 750 K caused VSi_2 to form at the amorphous vanadium silicide/amorphous-silicon interface. The shape of the VSi_2 nuclei and the shape of both isothermal and constant-scan-rate calorimetric exothermic peaks for VSi_2 formation are characteristic of nucleation controlled, not growth controlled, silicide phase selection. We have also used calorimetric analysis to determine that the activation energy for the formation of a continuous layer of VSi_2 at the amorphous-vanadium-silicide/amorphous-silicon interface was 2.6 eV, and that the activation energy for the growth of VSi_2 to consume the entire thin film was 2.5 eV.

5.5 References

1. L.A. Clevenger, C.V. Thompson, A. Judas and K.N. Tu, First MRS International Meeting on Advanced Materials, 10, 431 (1989)
2. P.A. Psaras, M. Eizenberg and K.N. Tu, *J. Appl. Phys.*, 56, 3439 (1984)
3. M. Nathan, *J. Appl. Phys.*, 63, 5539 (1988)
4. U. Gosele and K.N. Tu, *J. Appl. Phys.*, 53, 3252 (1982)
5. F.M. d'Heurle, *J. Mater. Res.*, 3, 167 (1988)
6. K.R. Coffey, L.A. Clevenger, K. Barmack, D.A. Rudman and C.V. Thompson (to be published)

6 Controlled Silicidation of Titanium/Amorphous-Silicon Multilayer Thin Films with Atomic Concentration Ratios of 1 Ti Atom to 2 Si Atoms.

6.1 Introduction

In this chapter, we discuss controlled silicidation of titanium/amorphous-silicon multilayer thin films with a modulation period of 30 nm and an atomic concentration ratio 1 Ti atom to 2 Si atoms. The purpose of this chapter is to obtain a quantitative understanding of amorphous and crystalline silicide formation in titanium/amorphous-silicon reactions using the same techniques as was used to study nickel/amorphous-silicon reactions (chapter 4) and vanadium/amorphous-silicon reactions (chapter 5). The emphasis of this chapter is on discussions of the silicide phase formation sequence from a reaction between polycrystalline titanium and amorphous-silicon, growth of amorphous-titanium-silicide, structural transitions in amorphous-titanium-silicide and/or amorphous-silicon and the kinetics of crystalline C-49 TiSi_2 formation. The main difference between titanium/amorphous-silicon reactions and nickel/amorphous-silicon (chapter 4) and vanadium/amorphous-silicon (chapter 5) is that atomic structural transitions are observed to occur in amorphous-titanium-silicide upon heating with calorimetric analysis. These transitions are not observed to occur in amorphous-nickel-silicide or amorphous-vanadium-silicide phases when they are heated.

6.2 Phase Formation Sequence and Kinetics of Titanium/Amorphous-Silicon Reactions

6.2.1 Results

To investigate titanium/amorphous-silicon multilayer thin film reaction, we have used constant-heating-rate calorimetry for kinetic analysis, cross-sectional transmission electron microscopy for structural analysis, thin film X-ray diffraction for crystalline silicide phase identification and Auger spectroscopy for composition analysis of amorphous and crystalline titanium silicides. In figure 1, we present constant-heating-rate traces for five scan rates of 2.5 to 40 K/min for amorphous-silicon multilayer film with a modulation period of 30 nm and an atomic concentration ratio of 1 Ti atom to 2 Si atoms. Concentrating on the 20 K/min trace, three distinct characteristics can be observed: an increasing exothermic baseline below 700 K, an endothermic step labeled 1 at approximately 700 K and an exothermic peak labeled 2 at 860 K. Samples for cross-sectional transmission electron microscopy were prepared in the as-deposited state as well as after heating in the calorimeter at 20 K/min to 670 K, 790 K, 860 K, and 900 K and cooled at 320 K/min to room temperature. This was done to correlate the thermal changes seen in the calorimetric data to structural changes observed with transmission electron microscopy. The bright field micrographs for these samples are shown in figures 2, 3, 5, 6 and 7.

Figure 1 DSC traces for heating rates of 2.5, 5, 10, 20, 40 K/min for titanium/amorphous-silicon multilayer thin films with a modulation period of 30 nm and an atomic concentration ratio of 1 Ti atom to 2 Si atoms.

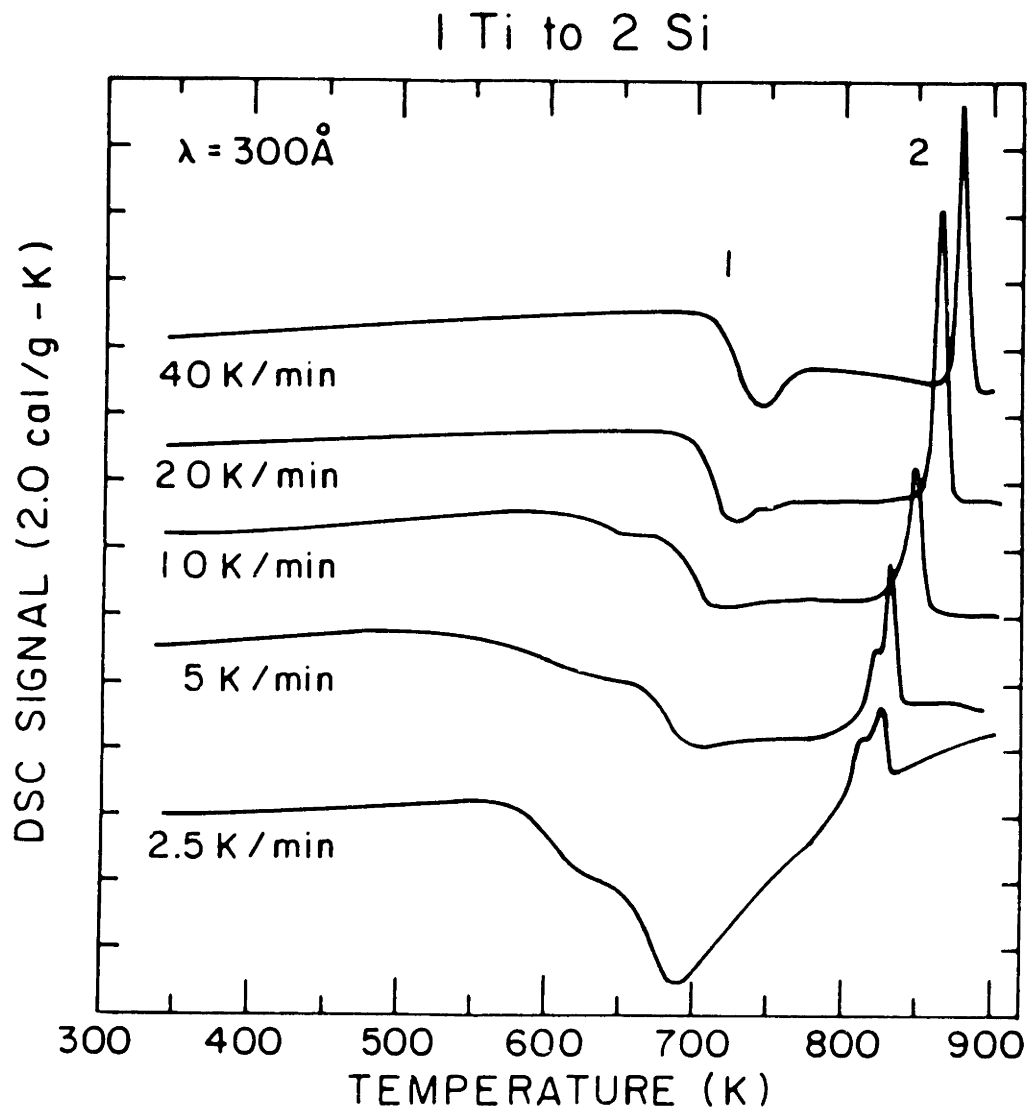


Figure 2 Bright field transmission electron microscope image of an as-deposited titanium amorphous silicon multilayer thin film. The bright layers are amorphous silicon, the layers with crystalline contrast are titanium. Between the titanium and the amorphous silicon there are gray featureless layers which are amorphous titanium silicide. Several of these amorphous titanium silicide layers are marked by arrows.

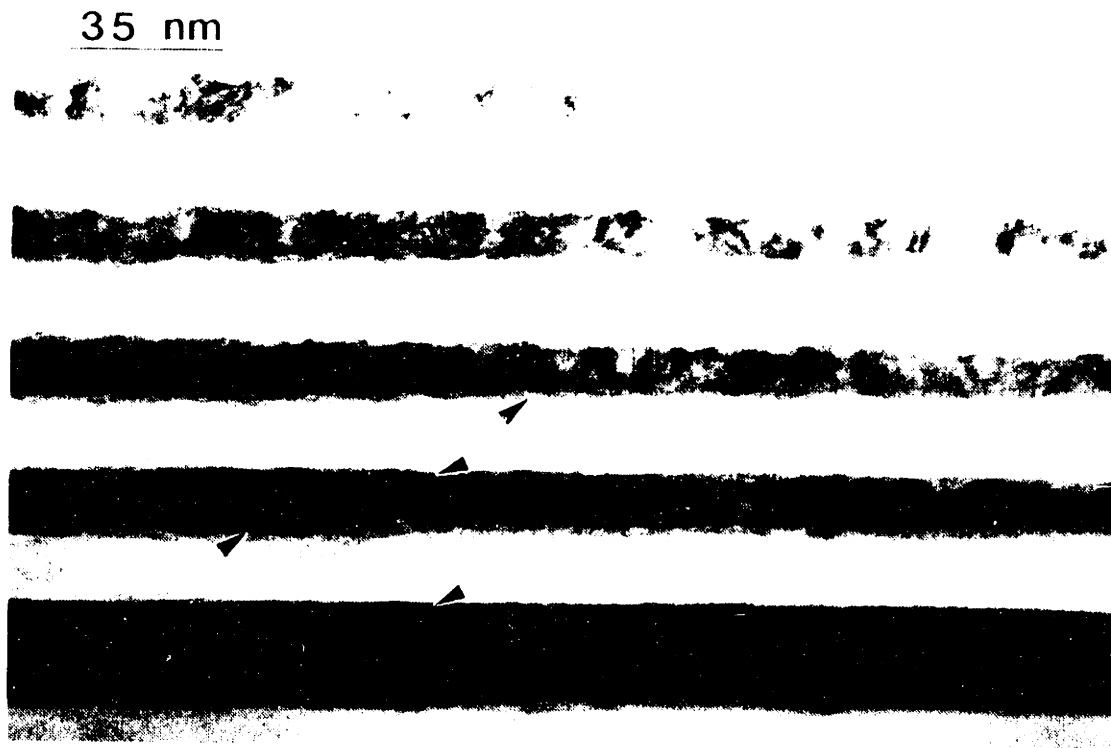


Figure 3 Bright field transmission electron microscope image of a titanium amorphous silicon multilayer thin film heated to 670 K. The bright layers are amorphous silicon. The grayer layers are amorphous titanium silicide. At this anneal temperature the remaining unreacted titanium (distinguished by arrows) is present as dark spots in the middle of the amorphous titanium silicide layers.

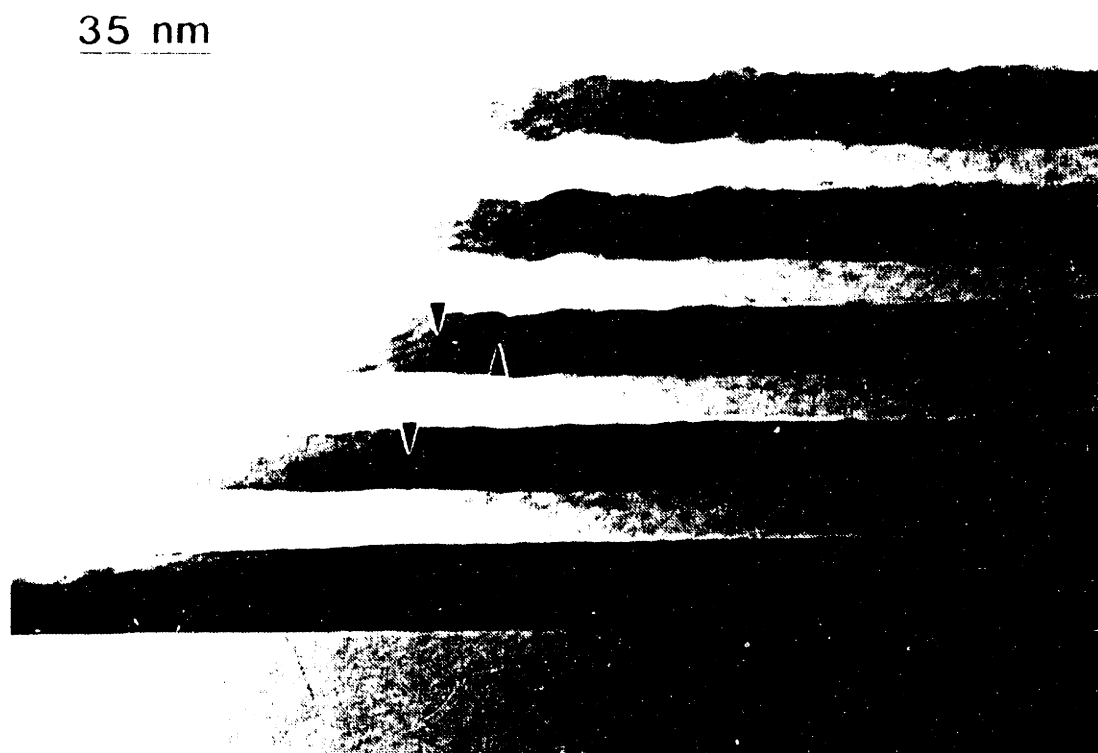


Figure 2 shows that the as-deposited multilayer films are made up of amorphous-silicon (light colored) layers and polycrystalline titanium (darker) layers. Between the amorphous-silicon and the polycrystalline titanium there is a very thin layer of reacted material which has a thickness of approximately 2.5 nm and no crystalline contrast. This reacted layer which has also been observed by other groups,^{2,9} is a metastable amorphous-titanium-silicide phase.

Heating the titanium/amorphous-silicon multilayer thin film to 670 K (right before the endothermic step of figure 1), causes a change in the microstructure as shown in figure 3. The amorphous-titanium-silicide has grown by consuming part of both the amorphous-silicon and the titanium layers. The small amount of unreacted titanium that is left is present as dark spots in the middle of the amorphous-titanium-silicide layers. These spots are easily seen with dark field imaging using the (0110) hcp titanium diffraction ring. The light regions are still amorphous-silicon. The clear visual contrast between these two amorphous regions indicates that they have distinct properties and therefore may be considered different amorphous phases.

In figure 4, we plot the calorimetric data for the 20 K/min trace of figure 1 up to a temperature of 700 K. A dashed line is drawn in figure 4 which is a baseline for zero heat evolved from the sample. The calorimetric data shows a broad exothermic peak above this baseline for temperatures below 700 K. This data and the results of figure 3 suggests that the broad exothermic peak of figures 4 and 1 below 700 K correspond to the growth of amorphous-titanium-silicide.

Figure 5 shows that heating these thin films from 670 K to 790 K causes further thickening of the the amorphous-titanium-silicide by only 1

Figure 4 DSC trace for a titanium/amorphous-silicon multilayer film with a modulation period of 30 nm and an atomic concentration ratio of 1 Ti atom to 2 Si atoms heated at 20 K/min to 700 K.

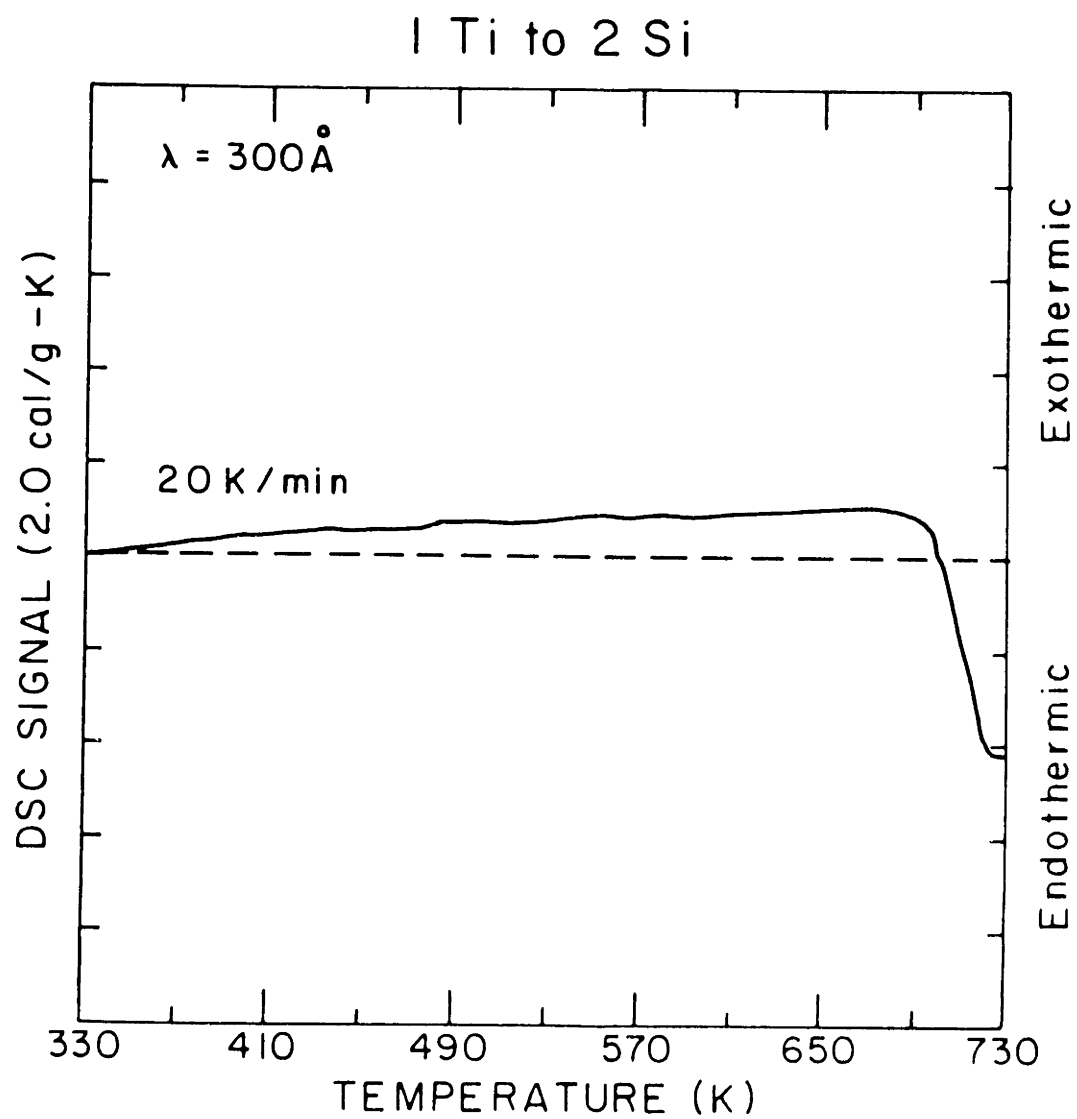


Figure 5 Bright field transmission electron microscope image of a titanium/amorphous silicon multilayer thin film heated to 790 K. The bright layers are amorphous silicon and the grayer layers are amorphous titanium-silicide (the amorphous-titanium-silicide layers are marked by arrows). There is no unreacted titanium remaining.

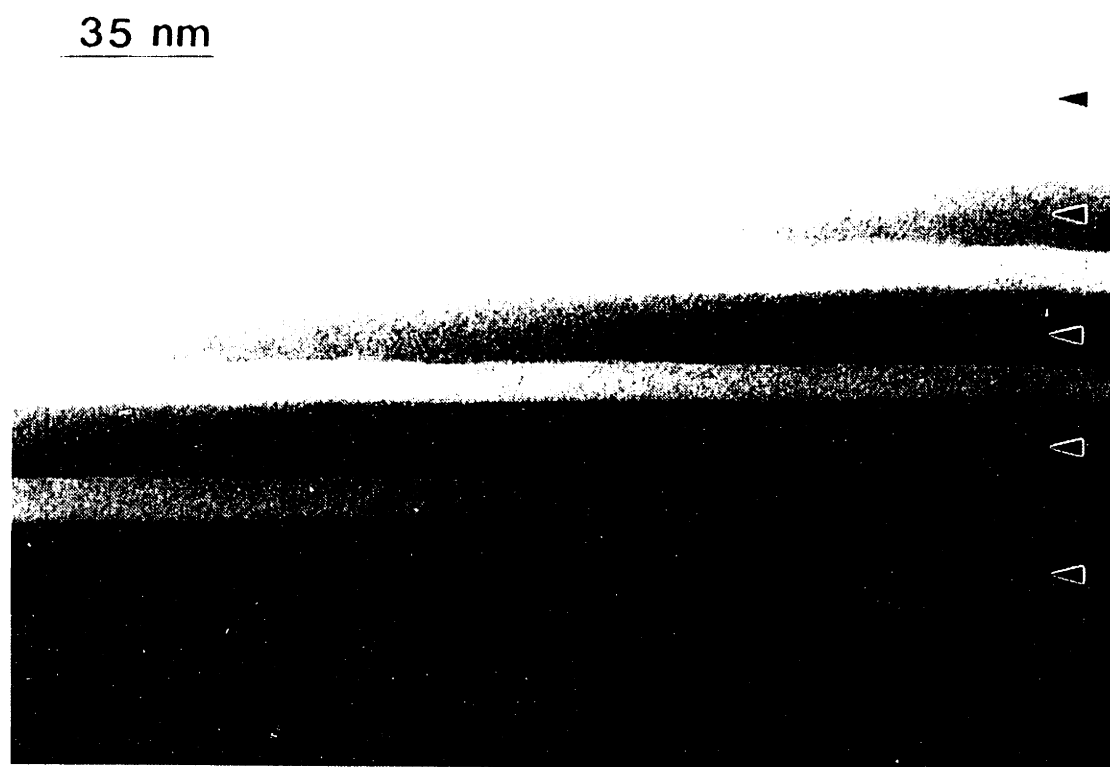


Figure 6. Bright field transmission electron microscope image of a titanium/amorphous silicon multilayer thin film heated to 860 K. The bright layers are amorphous silicon (a) and the grayer layers are amorphous titanium silicide (b). C19 TiSi₂ formation (nitrate) at the top surface of the film.

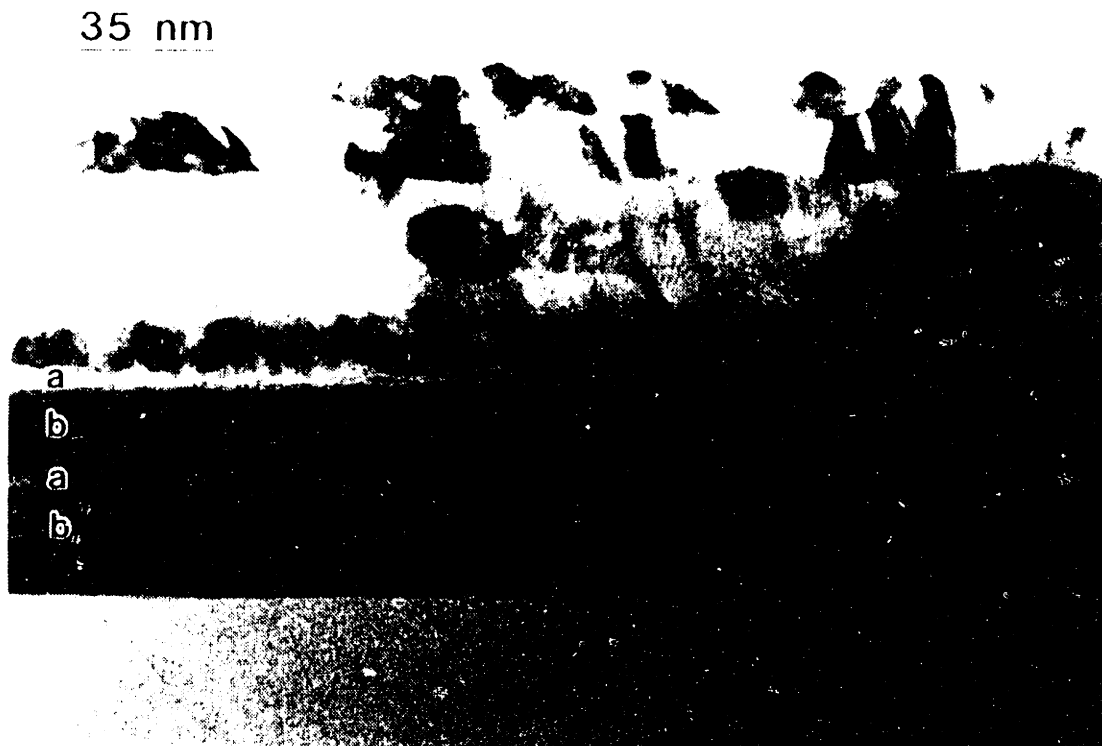
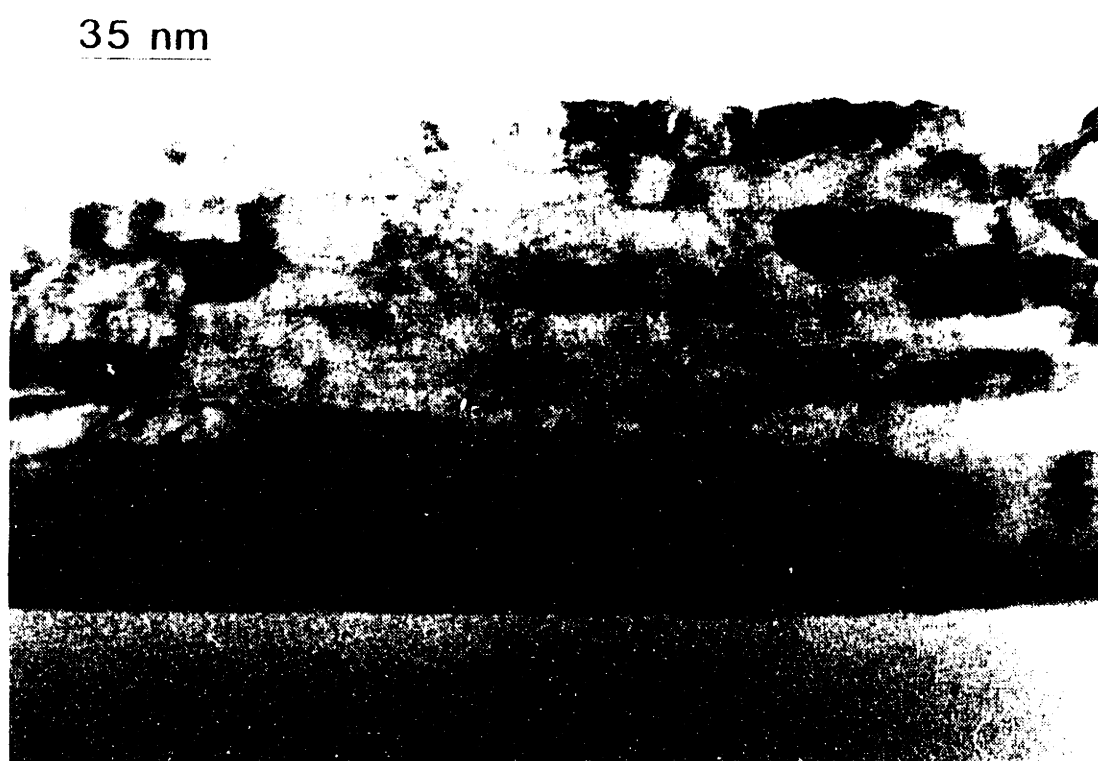


Figure 7. Bright field transmission electron microscope image of a titanium/amorphous silicon multilayer thin film heated to 900 K. The structure of the film is homogeneous C19 TiSi₂. There are nine distinct polycrystalline TiSi₂ layers.



nm. There is no evidence of any new crystalline or amorphous phase. We use this evidence to rule out a phase transition as a possible explanation for the endothermic step labeled 1 in figure 1. Rather, we believe that this step is related to densification and/or homogenization occurring in the amorphous-titanium-silicide and/or the amorphous-silicon layers. A similar step has been observed in pure amorphous-silicon samples.¹⁰

Heating a titanium/amorphous-silicon multilayer thin film to 860 K, which corresponds to the exothermic peak labeled 2 in figure 1, results in the microstructure shown in figure 6. Figure 6 shows that crystalline silicide formation started from the top layers and moved towards the substrate. This was due to a temperature gradient in the film since the heat conduction occurred through the top surface of the film. Thin film X-ray diffraction indicated that the crystalline silicide formed was C49 TiSi₂.¹¹

Heating the thin film to 900 K produced the structure shown in figure 7. This figure clearly shows that TiSi₂ formation is complete by 900 K and allows us to identify the exothermic peak labeled 2 in figure 1 as being due to the formation of C49 TiSi₂. The TiSi₂ formation resulted in well defined polycrystalline silicide layers. It was not possible to obtain TEM micrographs showing discrete TiSi₂ nuclei. However, the number of distinct polycrystalline TiSi₂ layers in figure 7 (9) is the same as the number of amorphous-titanium-silicide/amorphous-silicon interfaces, supporting the hypothesis that crystalline TiSi₂ nucleated at the amorphous-titanium-silicide/amorphous-silicon interface rather than in the interior of either the amorphous-titanium-silicide or amorphous-silicon layers.

Auger composition depth profiling was used to confirm the interpretations of the DSC and cross-sectional microscopy analyses. Samples were prepared by depositing multilayer thin films onto thermally

oxidized silicon wafers. The samples were then examined in the as-deposited state and also heated in the calorimeter at 20 K/min to 670 K, 790 K and 860 K and then quenched at 320 K/min to room temperature. The resulting depth profiles are shown in figure 8. The top silicon layer of the films remained always partially unreacted for all treatments. The thickness of the unreacted amorphous-silicon is about half the thickness of the deposited silicon layer. The composition profiles clearly show that the intermixing of titanium and silicon is well advanced at 790 K, a temperature slightly above the endothermic step of figure 1. This correlates with the intermixing of titanium and silicon illustrated by the cross-sectional transmission electron micrograph in figure 5. At 865 K, which is just past the exothermic peak of figure 1, the composition of the thin film is homogeneous, with an atomic composition ratio of roughly 1 Ti atom to 2 Si atoms. This confirms the X-ray diffraction identification of the crystalline silicide phase as TiSi_2 .

Figure 1 demonstrates that as the heating rate is decreased both the endothermic step and the exothermic peak for TiSi_2 formation shift down to lower temperatures. The peak shift to lower temperatures with decreasing scan rate for TiSi_2 formation can be related to the activation energy of TiSi_2 formation using the analysis developed in section 3.2.1, showing that:

$$\ln\left(\frac{H}{T_p^2}\right) = C_2 - \frac{Q}{kT_p} \quad (1)$$

where H is the heating rate, T_p is the peak temperature, C_2 is a constant, k is Boltzmann's constant and Q is the activation energy. Figure 9 shows a plot of equation 1 for the data of peak 2, figure 1. From this analysis, the

Figure 8a Auger composition profiles of an as deposited titanium/amorphous-silicon multilayer thin film with a modulation period of 30 nm and an atomic concentration ratio of 1 Ti atom to 2 Si atoms.

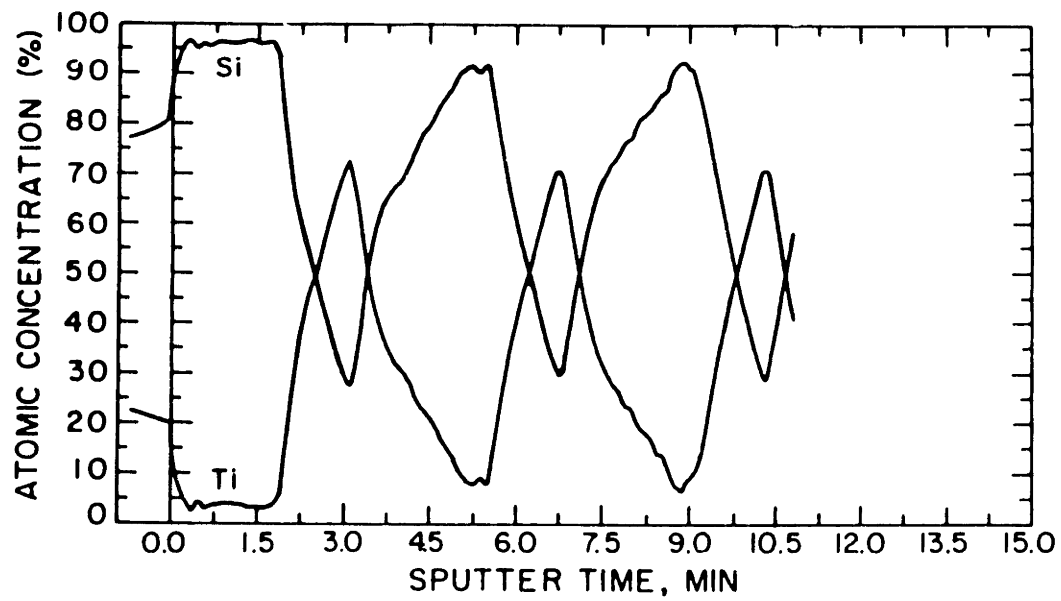


Figure 8b Auger composition profiles of a titanium/amorphous-silicon multilayer thin film with a modulation period of 30 nm and an atomic concentration ratio of 1 Ti atom to 2 Si atoms heated at 20 K/min to 790 K and quenched at 320 K/min to room temperature. The top silicon layer remains unreacted.

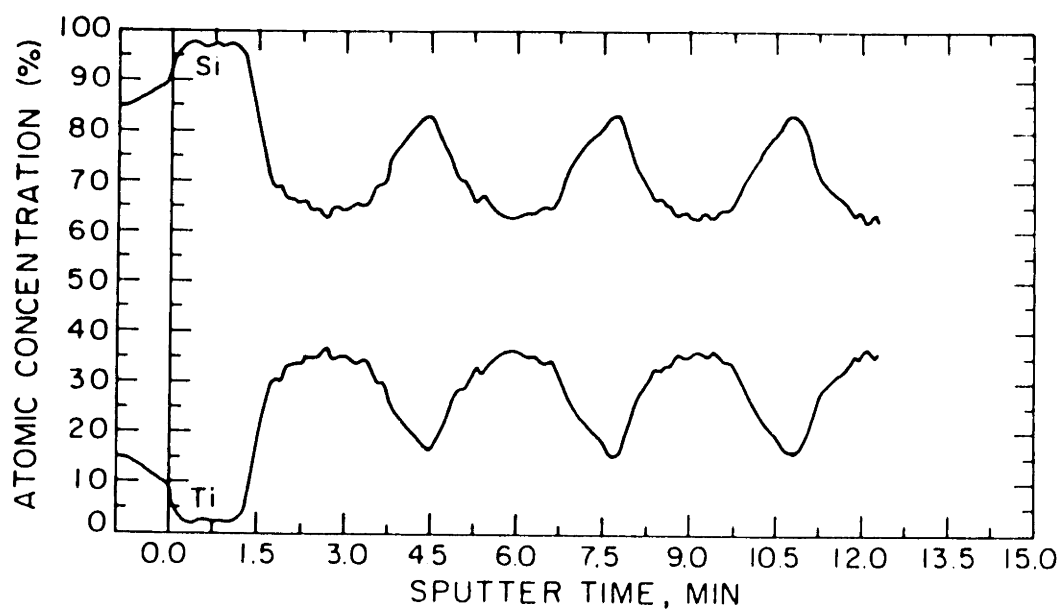


Figure 8c Auger composition profiles of a titanium/amorphous-silicon multilayer thin film with a modulation period of 30 nm and an atomic concentration ratio of 1 Ti atom to 2 Si atoms heated at 20 K/min to 860 K and quenched at 320 K/min to room temperature. The top silicon layer remains unreacted.

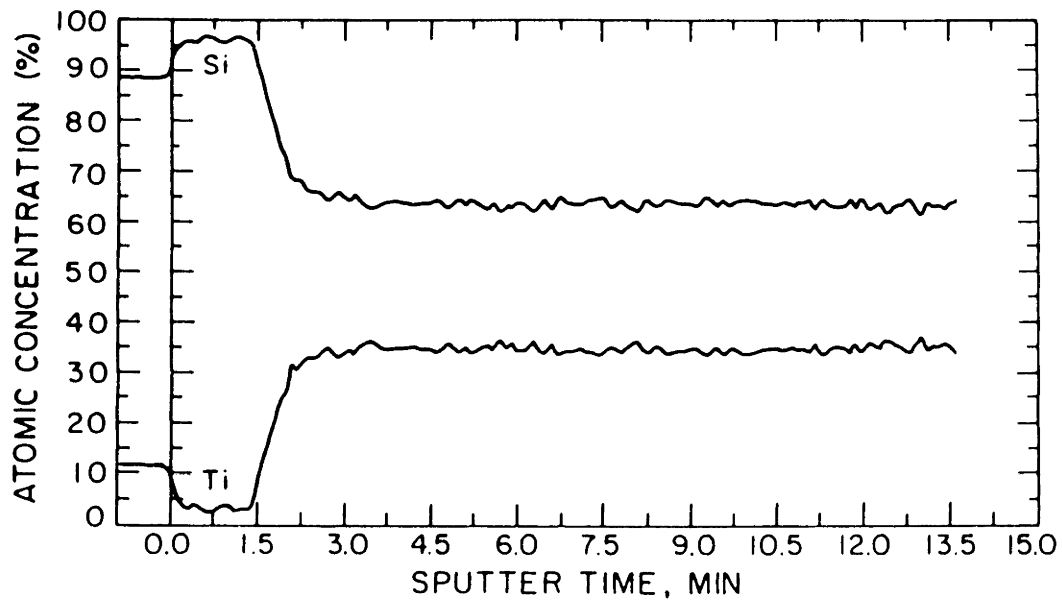
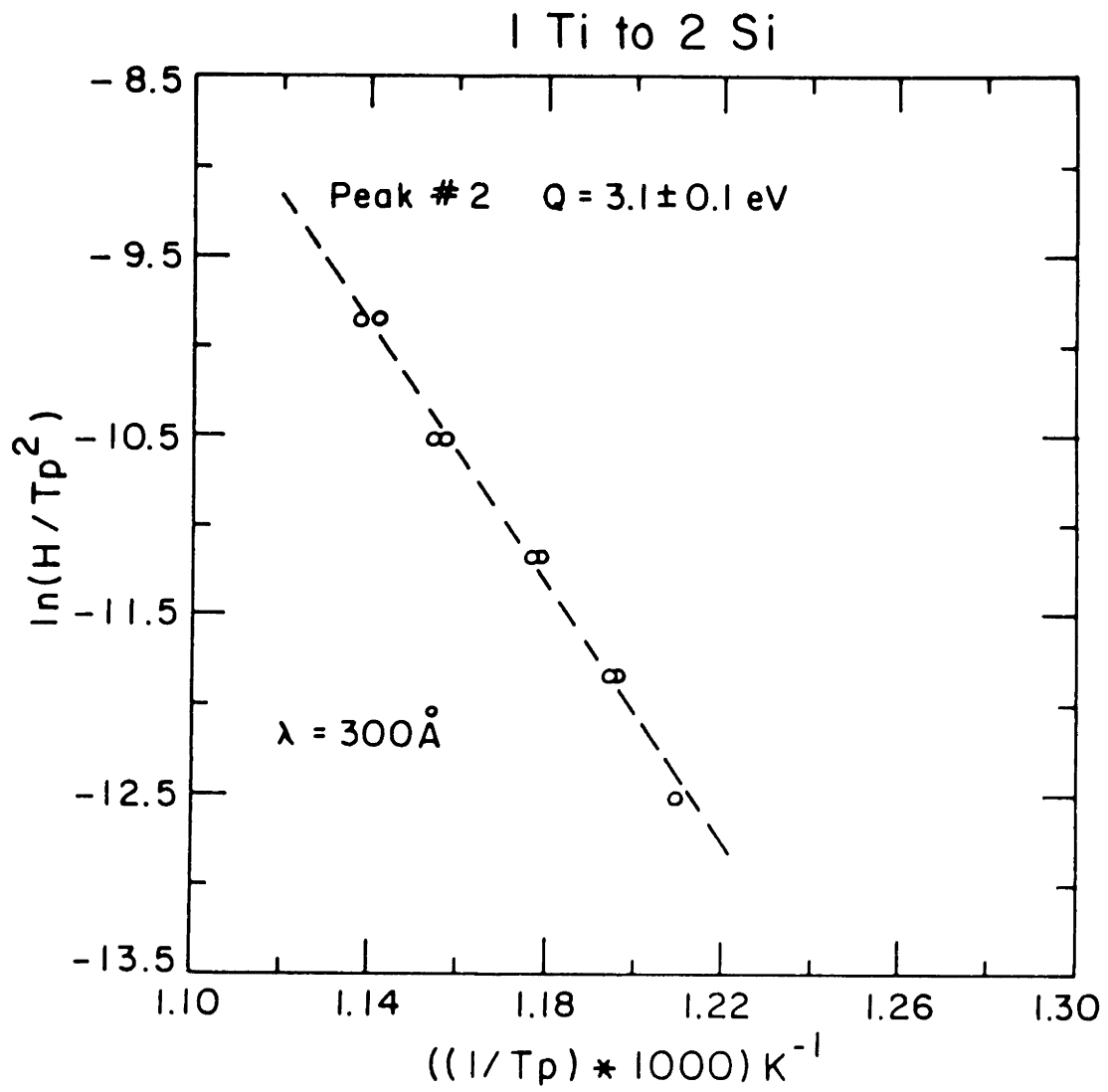


Figure 9 Plot of $\ln(H/T_p^2)$ versus $1/T_p$ for the data for peak 2 of figure 1.



activation energy for formation of TiSi_2 from the reaction between amorphous-titanium-silicide and amorphous-silicon was determined to be 3.1 ± 0.1 eV. Also by integrating the area under peak 2, the heat of formation of TiSi_2 from the reaction between amorphous-titanium-silicide and amorphous-silicon was determined to be -25.8 ± 8.8 kJ/mol- TiSi_2 .

Figure 1 also shows that at the two lowest scan rates, peak 2 for TiSi_2 formation splits into two peaks. We believe that this is due to either the formation of another crystalline silicide⁹ in addition to C49 TiSi_2 or the separate nucleation and growth of a continuous TiSi_2 layer, followed by its thickening.¹⁴

6.2.2 Discussion

The calorimetric data of figures 1 and 4 and the cross-sectional transmission electron micrographs of figures 2,3 and 5, indicate that an amorphous-titanium-silicide layer is formed between the titanium and amorphous-silicon during the deposition of the multilayer thin film and that this layer will grow upon heating. We cannot determine an activation energy for amorphous-titanium-silicide growth using equation 1 because there is no clear exothermic peak for amorphous-titanium-silicide growth in our calorimetric data. We believe this is due to the fact that the termination of amorphous-titanium-silicide growth overlaps with the endothermic step of figure 1. However, Holloway et al.¹⁵ recently reported an activation energy of 2.0 eV and a diffusion pre-exponential of $2.35 \text{ cm}^2/\text{sec}$ for amorphous-titanium-silicide growth. Using cross-sectional transmission electron microscopy, Holloway calculated these values by first measuring the change in thickness of amorphous-titanium-silicide as a

function of temperature for anneals of constant time. A diffusion coefficient for each temperature was calculated using the following formula:⁷

$$\frac{(\Delta X)^2}{t} = D \quad (2)$$

where ΔX is the change in thickness of the amorphous-titanium-silicide from an initial thickness, t is the annealing time and D is the diffusion coefficient.

A more accurate method of calculating the diffusion coefficient, D , is to start with the following equation:^{8,16}

$$X \frac{dX}{dt} = D \quad (3)$$

where X is the thickness of the amorphous-silicide. Integrating equation 2, from X_0 , the initial thickness of the amorphous-titanium-silicide to X_t , the thickness of the amorphous-titanium-silicide after annealing at a temperature T for time t , we get:

$$\frac{X_t^2 - X_0^2}{2t} = D. \quad (4)$$

Using Holloway's data¹⁵ for X_t and X_0 , we can calculate the values in Table 1 for D shown, using equation (3) for a 30 second anneal time.

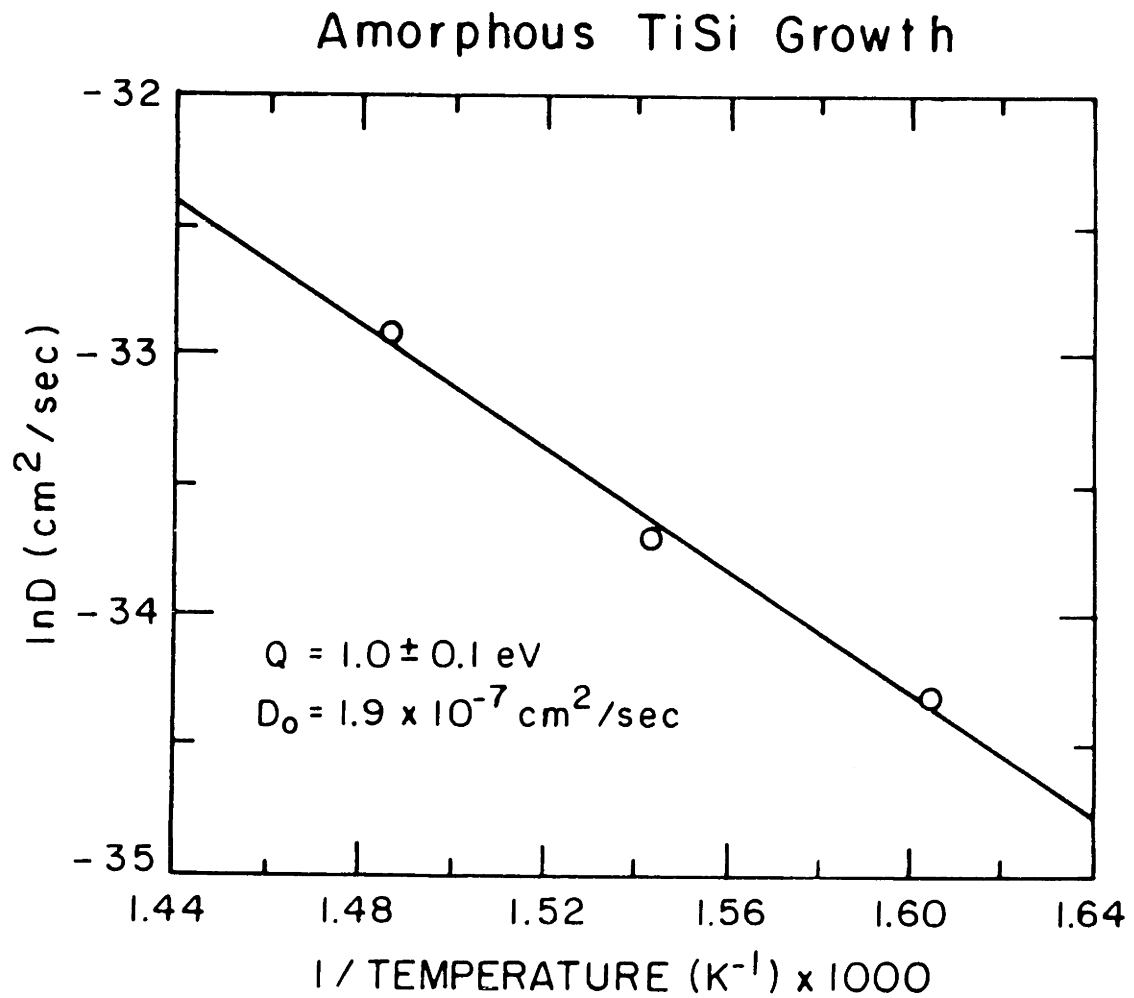
Table 1: Diffusion coefficients for planar growth of amorphous-titanium-silicide. X_0 is the thickness of the amorphous-titanium-silicide after a 30 second anneal at 300°C.

Temperature(°C)	x_t (nm)	x_0 (nm)	D(cm ² /sec)
350	3.7	2.5	1.24x10 ⁻¹⁵
375	4.47	2.5	2.29x10 ⁻¹⁵
400	6.05	2.5	5.60x10 ⁻¹⁵

In figure 10, we present a plot of the natural log of the diffusivity versus 1/Temperature from the data of table 1. From the slope of this plot we obtain an activation energy for growth of amorphous-titanium-silicide of 1.0 ± 0.1 eV, and from the y-intercept we obtain a diffusion pre-exponential coefficient for amorphous-titanium-silicide growth of 1.9×10^{-7} cm²/sec. These values are different from those originally calculated by Holloway.¹⁵ However, they are in excellent agreement with the work of Chambers et al.¹⁷ who derived values of $1.0 \pm .4$ eV and $1.1-1.2 \times 10^{-7}$ cm²/sec for an activation energy and diffusion pre-exponential respectively for the interdiffusion of silicon into a thin film (10 nm) of titanium. Chambers' results were based on measurements made using photoelectron spectroscopy.

The endothermic step occurring between 600 to 760 K in figure 1 has a shape that is characteristic of a glass transition in an amorphous material.¹⁸ However, in titanium/amorphous-silicon multilayer thin film reactions this step does not appear to be due to a glass transition in either the amorphous-titanium-silicide or the unreacted silicon, since the endothermic step is not a reversible relaxation as would be expected if it had

Figure 10 Chemical diffusivity determined from the amorphous-titanium-silicide growth data reported by Holloway, as a function of temperature.



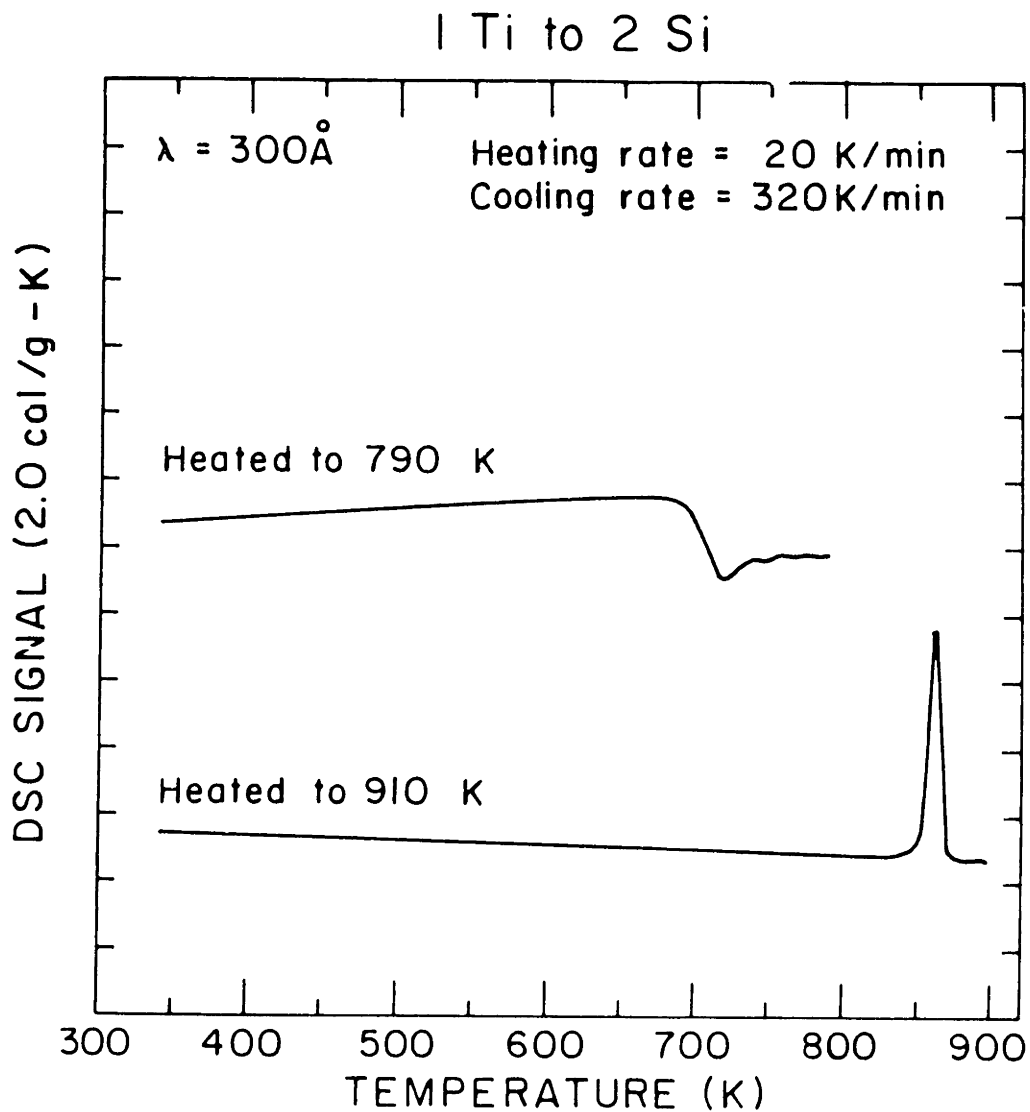
been caused by a glass transition.^{19,20} This irreversible relaxation is demonstrated in figure 11, where we present calorimetric data for a 8.8 nm titanium/21.2 nm amorphous-silicon multilayer thin film heated at 20/K.min to 790 K (curve 1), then cooled at 320 K/min to room temperature and reheated at 20 K/min to 910 K to cause formation of crystalline C49 TiSi₂ (curve 2). The endothermic step is present in the first curve, but not the second curve. This indicates that the endothermic step is an irreversible relaxation.

Insight into the source of the irreversible endothermic step is gained by realizing that the DSC signal is proportional to the heat capacity of the sample, which can be described by:

$$C_p = T \left(\frac{dS}{dT} \right)_p \quad (5)$$

where C_p is the heat capacity of the multilayer film at constant pressure, S is the entropy, and T is the temperature. The endothermic step corresponds to an increase in the heat capacity of the sample, which by equation 5 will lead to an increase in entropy S , since dT and T are positive in these experiments. We believe that this increase in entropy can be related to a compositional homogenization and/or densification in the multilayer thin film.¹⁰ Auger depth profiling indicates that a compositional homogenization is occurring in the amorphous-titanium-silicide layers during the endothermic step. However a simultaneous densification of either the amorphous-titanium-silicide or amorphous-silicon layers could also contribute to the endothermic step.¹⁰

Figure 11 DSC trace for a titanium/amorphous-silicon multilayer thin film with a modulation period of 30 nm and an atomic concentration ratio of 1 Ti atom to 2 Si atoms, heated at 20 K/min to 790 K, cooled at 320 K/min to room temperature and then heated at 20 K/min to 910 K.



The activation energy for C49 TiSi₂ formation, 3.1 ± 0.1 eV, is higher than the value 1.8 ± 0.1 eV reported by Hung²¹ for TiSi₂ formation from a titanium/amorphous-silicon bilayer thin film. There are at least two possible explanations for this difference: First, Hung did not report on whether they were investigating C49 or C54 TiSi₂ formation (in the work reported here C49 TiSi₂ formation was studied) and second, the minimum TiSi₂ thickness detected in Hung's study was equal to the maximum thickness of TiSi₂ measured in this work. The activation energy reported by Hung is for the 1-dimensional growth of TiSi₂ from a thickness of 30 nm to 70 nm, while due to the multilayer structure of the as-deposited thin film, the activation energy determined in this work is due to the nucleation as well as the growth of C49 TiSi₂ to form a layer 30 nm thick.

Finally, the heat of formation for TiSi₂ of -25.8 ± 8.8 kJ/mole measured here is lower than the reported value for the heat of formation of TiSi₂ of -132.5 kJ/mol-TiSi₂.²² This is to be expected since in this work, the measured value is for the formation of TiSi₂ from a reaction between amorphous-silicon and amorphous-titanium-silicide at approximately 850 K, while the reported value for the heat of formation is for a reaction between titanium and crystalline silicon at 298 K. By combining the above heats of formation for TiSi₂ with the heat of crystallization of amorphous-silicon of -11.95 kJ/mole,²³ an estimate for the energy of formation of stoichiometric amorphous-titanium-silicide of -130.6 kJ/mole was calculated.

6.3 Conclusion

In this chapter, we have discussed the formation of amorphous-titanium-silicide and crystalline C49 TiSi_2 in titanium/amorphous-silicon multilayer thin films with as-deposited multilayer atomic concentration ratios of 1 Ti to 2 Si and with a modulation period of 30 nm. The experimental techniques used were differential scanning calorimetry, Auger depth profiling, thin film X-ray diffraction and cross-sectional transmission electron microscopy. We have observed that, in the as-deposited condition, a thin amorphous-titanium-silicide layer is present between the amorphous-silicon and the titanium layers, and that heating causes this amorphous-titanium-silicide layer to grow by the diffusion of silicon across the amorphous-titanium-silicide layer to the titanium/amorphous-titanium-silicide interface where it reacts with titanium to form more amorphous-titanium-silicide. Reevaluation of previously reported data, suggests that for thickening of amorphous-titanium-silicide layers, the activation energy is 1.0 ± 0.1 eV with a pre-exponential coefficient to be $1.9 \times 10^{-7} \text{cm}^2/\text{sec}$. This is in excellent agreement with data reported in the literature for thin film experiments.¹⁷ An irreversible endothermic step in the calorimetric data near the end of amorphous-titanium-silicide growth was observed and was attributed to densification and/or compositional homogenization occurring in the amorphous-titanium-silicide and/or the unreacted amorphous-silicon layers.

Further heating caused the formation of crystalline C49 TiSi_2 at the amorphous-titanium-silicide/amorphous-silicon interface. A heat of

formation for TiSi_2 of -25.8 ± 8.8 kJ/mol was measured as well as an activation energy for formation of 3.1 eV. This activation energy was interpreted to be due to both the nucleation and growth of TiSi_2 . The heat of formation of amorphous titanium silicide was estimated to be -130.6 kJ/mole.

6.4 References

1. K. Holloway and R. Sinclair, *J. Appl. Phys.* **61**, 1359 (1987)
2. M. Nathan, *J. Appl. Phys.* **63**, 5539 (1988)
3. I.J.M.M. Raaijmakers, P.H. Oosting, and A.H. Reader, *Mater. Res. Symp. Proc.*, **103**, 229 (1988)
4. R.R DeAvillez, L.A. Clevenger and C.V. Thompson, to be published in *J. Mat. Research*
5. R. Beyers and R. Sinclair, *J. Appl. Phys.* **57**, 5240 (1985)
6. K.R. Coffey, L.A. Clevenger, K. Barmak, D.A. Rudman and C.V. Thompson to be published
7. K. Holloway and R. Sinclair, *Thin Solid Films* **140**, 139 (1988)
8. K.N. Tu, W.K. Chu and J.W. Mayer, *Thin Solid Films* **25**, 403 (1975)
9. L.A. Clevenger, C.V. Thompson, R.C. Cammarata and K.N. Tu, *Mater. Res. Symp. Proc.* **103**, 191 (1988)
10. E.J. Cotts, W.J. Meng and W.L. Johnson, *Phys. Rev. Lett.* **57**, 2295 (1986)
11. S.A. Chambers, D.M. Hill, F. Xu and J.H. Weaver, *Phys. Rev. B* **35**, 634 (1987)
12. L.E. Tanner, *Acta Met.* **28**, 1805 (1980)

13. L.E. Tanner and R.Ray, *Scripta Met.* 11, 783 (1977)
14. D. Turnbull, *Trans Metall. Soc. A.I.M.E.* 221, 422 (1961)
15. L.S. Hung, J. Gyulai, J.W. Mayer, S.S. Lau and M.A. Nicolet, *J.Appl. Phys.* 54, 5076 1983
16. R. Hultgren, R.L. Orr, P.D. Anderson and K.K.Kelly, *Selected Values of Thermodynamic Properties of Metals and Alloys*, J. Wiley, New York (1963)
17. E.P. Donovan, F. Spaepen, D. Turnbull, J.M. Poate and D.C. Jacobson, *J. Appl. Phys.* 57, 4208 (1985)

7 Thermodynamics of Amorphous and Crystalline Intermetallic Phase Formation in Thin Films

7.1 Introduction

Thin film reactions have been extensively studied in the past few decades due to their applications in microelectronic circuits.¹ There are two important ways in which the possible intermetallic phases that can form during thin film reactions are different from bulk reactions of the same starting materials. First, many of the equilibrium crystalline intermetallics that form in a bulk study are not present in a thin film reaction;² and second, in thin film reactions, the formation of a thermodynamically unstable amorphous-intermetallic phase by a solid state reaction is more commonly observed.³⁻⁵

In the past, various kinetic models have been proposed to explain intermetallic phase formation in thin film reactions.⁶⁻⁸ In this chapter we will demonstrate the use of thermodynamics, through Gibbs free energy versus composition diagrams, to analyze both amorphous and crystalline intermetallic formation in thin film reactions. The discussion will focus on three main points. First, we will present the thermodynamic and kinetic requirements for the formation of an amorphous-intermetallic phase by a solid state reaction. Secondly, we will show under what thermodynamic conditions the simultaneous growth of a crystalline intermetallic phase and an amorphous-intermetallic phase is possible. Finally, we will show how the driving force for nucleation of an intermetallic phase at an

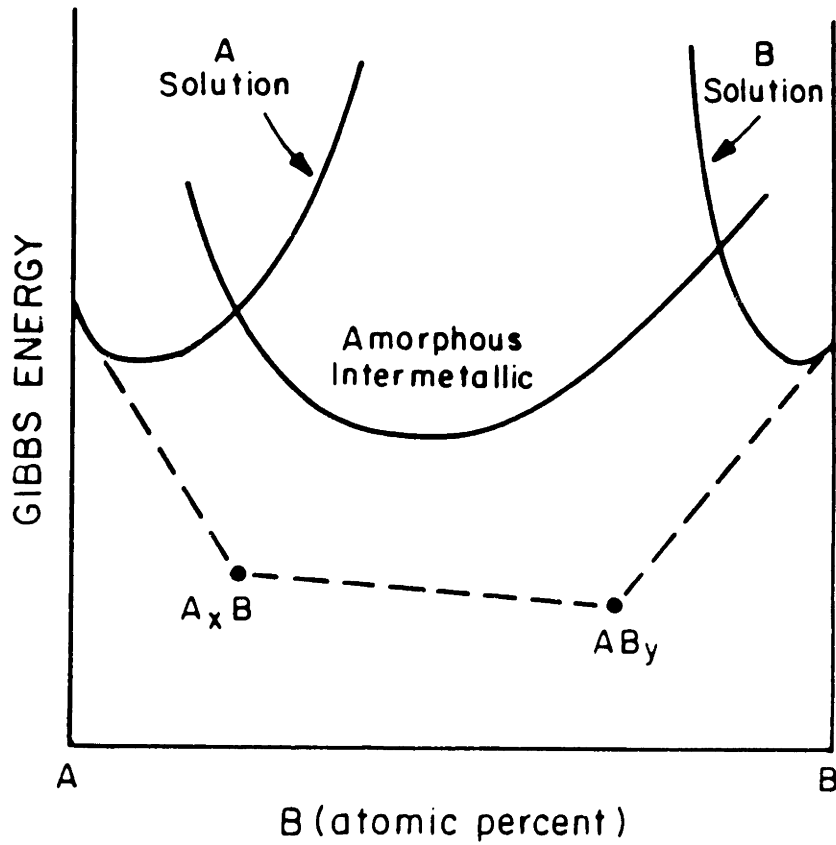
element/amorphous-intermetallic interface is a function of both the atomic composition at the interface and whether the crystalline intermetallic nucleates in the element or the amorphous-intermetallic layer. All the examples will be related to metal/amorphous-silicon multilayer thin films with either nickel or vanadium as the chosen metal. It should be noted that while all the examples used in this paper are for metal/amorphous-silicon thin films, the concepts that are presented are valid for any type of thin film reaction. The thermodynamic data used for the nickel/amorphous-silicon and vanadium/amorphous-silicon systems is summarized in Appendix C.

7.2 Formation of an Amorphous-Intermetallic Phase

Herd et al⁹ and Schwartz and Johnson¹⁰ were the first to show that an amorphous-intermetallic phase could be formed through a solid state reaction of elemental components. Since these early reports, numerous authors have demonstrated that a variety of thin film systems form amorphous-intermetallic phases.^{3,4,11,12} An understanding of why amorphous-intermetallic phases form can be obtained by examining the Gibbs free energy versus composition diagram for the system of interest.^{13,14} In figure 1, we present a Gibbs free energy versus composition diagram for an idealized A-B system. In this diagram, the free energies of the A, B and amorphous-AB intermetallic phases vary continuously from pure A to pure B, while the crystalline intermetallics A_xB and AB_y are assumed to be line compounds.

In figure 1, the common tangents between A, the crystalline intermetallics and B have been drawn in. The amorphous-intermetallic

Figure 1 Gibbs free energy versus composition diagram for an idealized A-B system. Dashed lines are common tangents for the A solution, crystalline intermetallics A_xB and AB_y and the B solution.



free energy curve lies above these common tangents, indicating that the amorphous-intermetallic is unstable with respect to the crystalline intermetallic. This implies that the amorphous-intermetallic would not form at the A/B interface if there were kinetic barriers to the formation of the crystalline intermetallics.

For the amorphous-intermetallic to form at the A/B interface, there must be kinetic barriers that prevent the formation of the crystalline intermetallics. With kinetic barriers preventing the formation of the crystalline intermetallics, we can remove the crystalline intermetallics from the Gibbs free energy versus composition diagram of figure 1. The resulting diagram is shown in figure 2, with the common tangents now being drawn between A, the amorphous-intermetallic and B. This construction indicates that with kinetic barriers to the formation of the crystalline intermetallics, the amorphous-intermetallic can form from and be in equilibrium with the A and B layers.

The generalized discussion illustrated in figures 1 and 2 can be compared with experimental results for nickel/amorphous-silicon and vanadium/amorphous-silicon thin film reactions.^{4,15-18} The Gibbs free energy versus composition diagram for the nickel/silicon system calculated for a temperature of 400 K is shown in figure 3a and the Gibbs free energy versus composition diagram for the vanadium/silicon system calculated for a temperature of 750 K is shown in figure 3b. For both of these diagrams it has been assumed that the amorphous silicide has the same free energy as the undercooled metallic liquid (see Appendix C for details). Figures 3a and 3b are similar to figure 1 in that an amorphous-silicide phase will form at the metal/amorphous-silicon interface only if there are kinetic barriers to the formation of the crystalline silicides. In figures 4a and 4b we replot

Figure 2 Same as figure 1 except that we have assumed that kinetic barriers prevent the formation of the crystalline intermetallics. Common tangents are drawn between the A solution, the amorphous-intermetallic phase and the B solution.

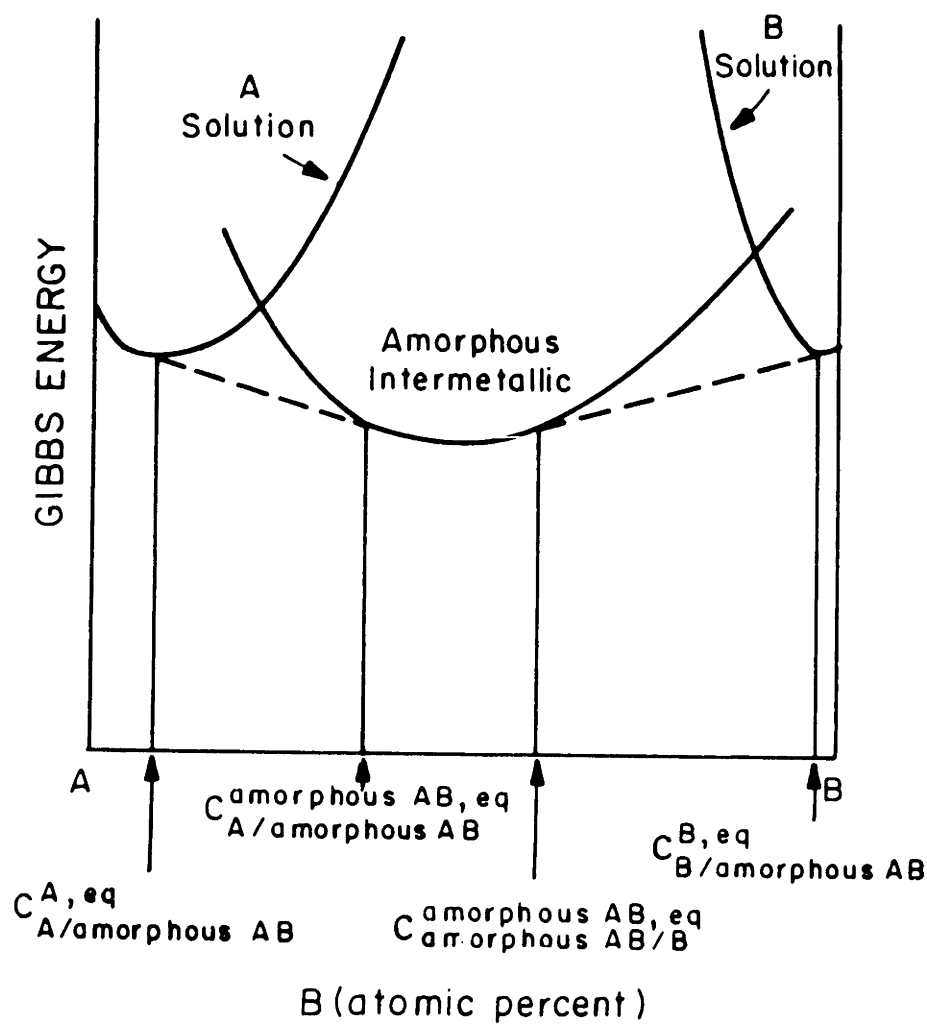


Figure 3a Gibbs free energy versus composition diagram for the nickel/silicon system at a temperature of 400 K. The crystalline nickel silicides are indicated by "O"s. Dashed lines are the common tangents for fcc nickel, the crystalline nickel silicides and amorphous-silicon.

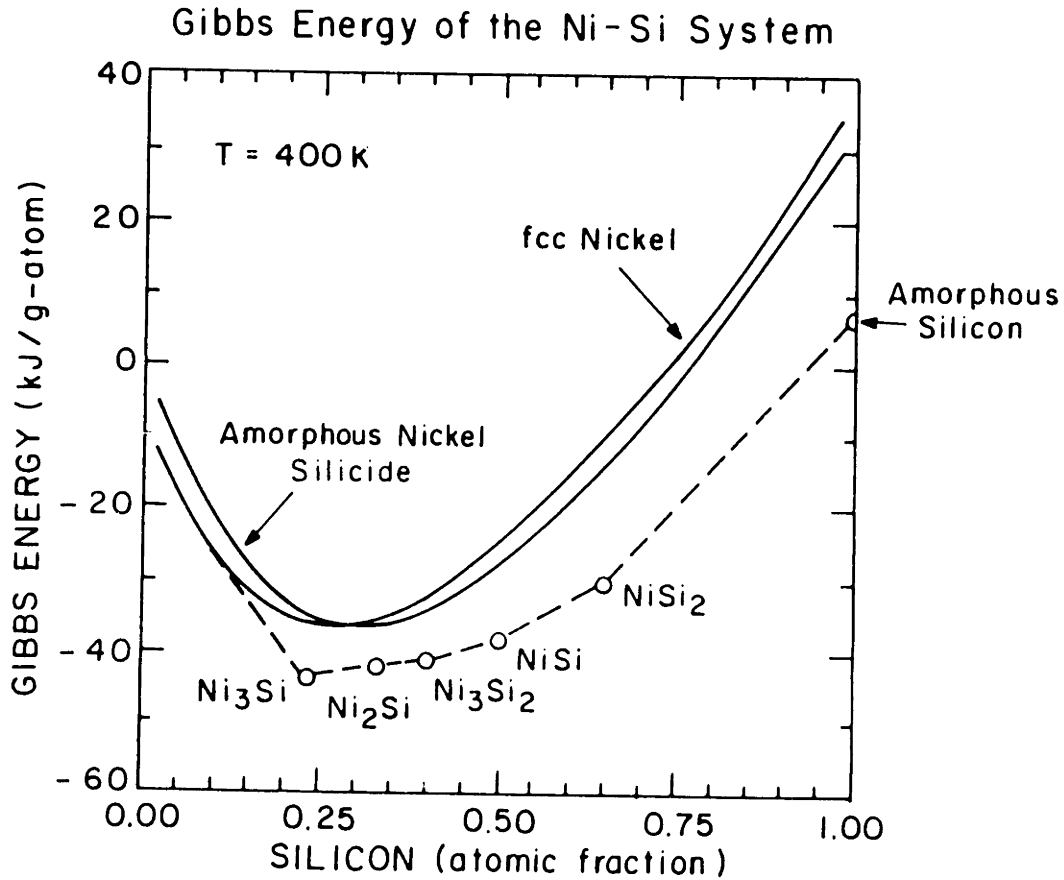


Figure 3b Gibbs free energy versus composition diagram for the vanadium/silicon system at a temperature of 750 K. The crystalline vanadium silicides are indicated by "O"s. Dashed lines are the common tangents for bcc vanadium, the crystalline vanadium silicides and amorphous-silicon.

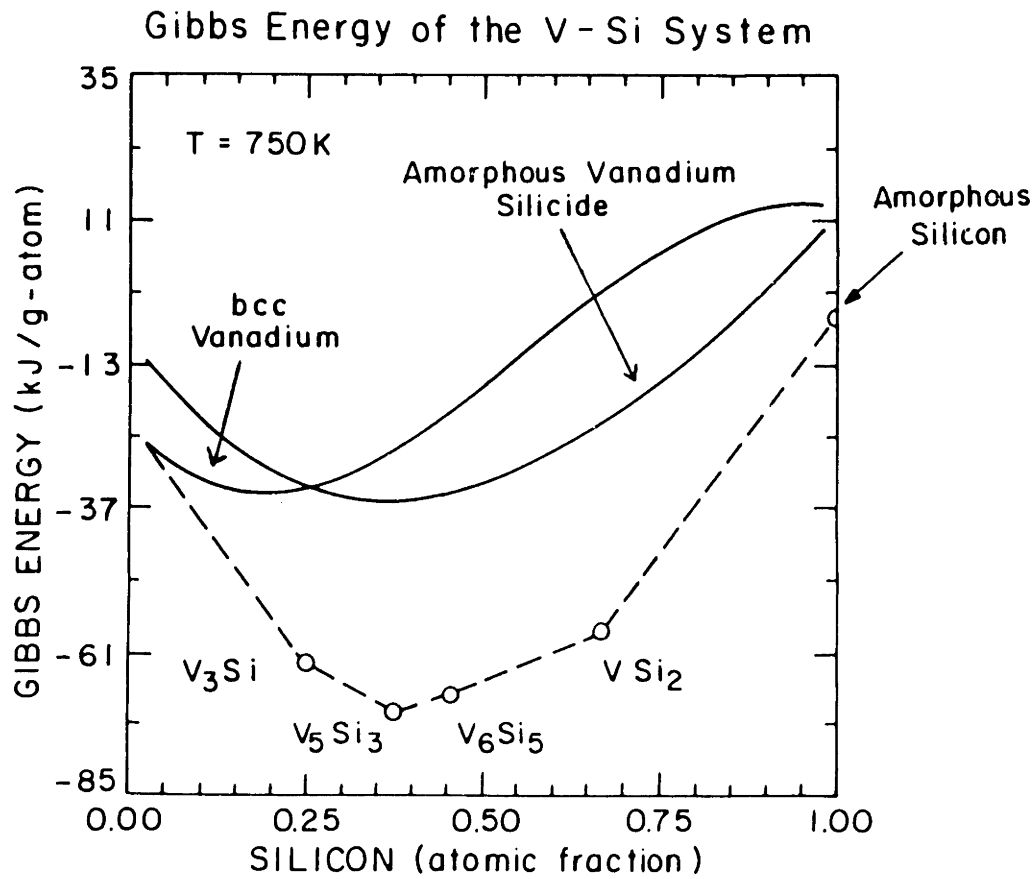


Figure 4a Same as figure 3a, with the assumption that nucleation barriers prevent the formation of the crystalline nickel silicides. Common tangents are drawn for fcc nickel (α), amorphous-nickel-silicide (β) and amorphous-silicon.

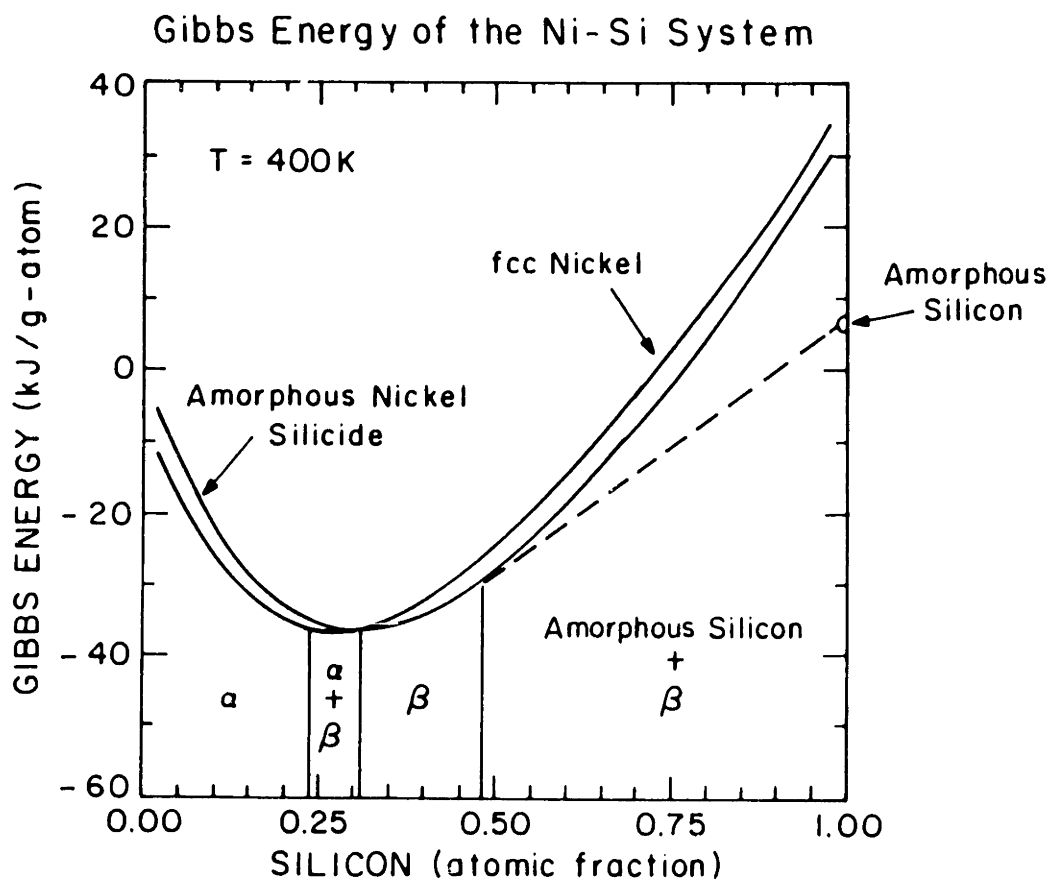
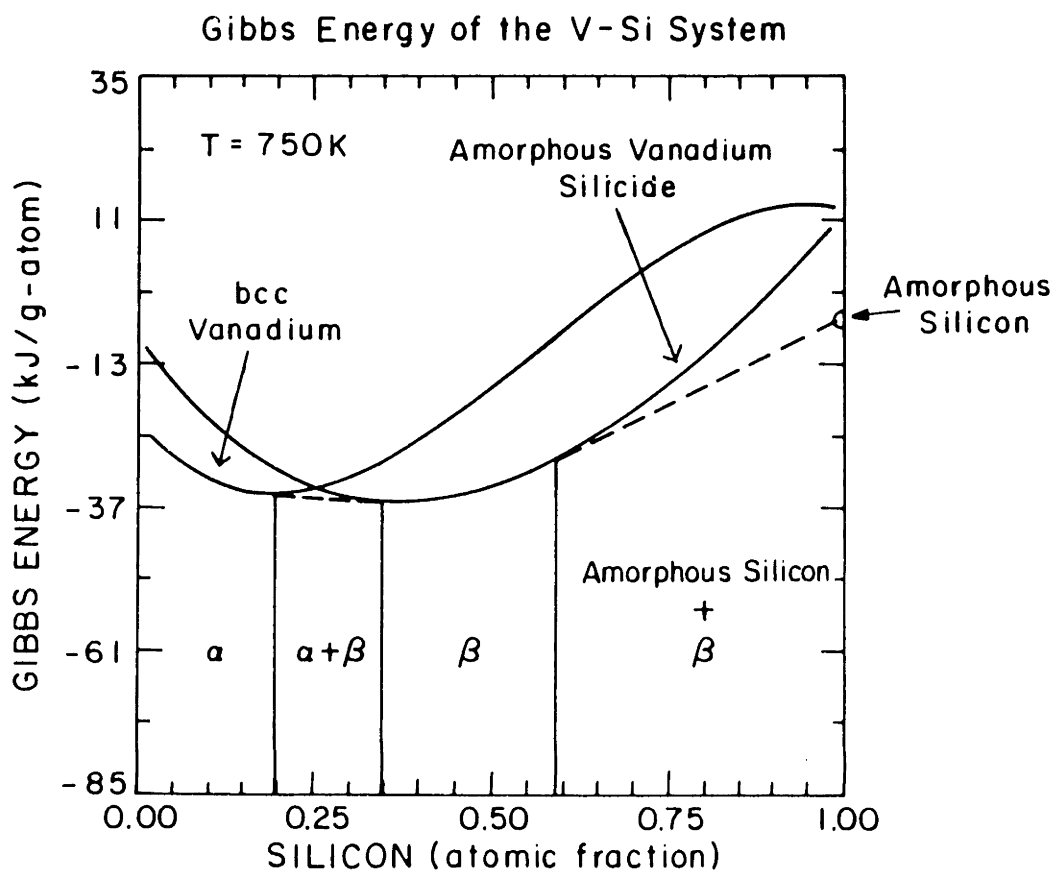


Figure 4b Same as figure 3b with the assumption that kinetic nucleation barriers prevent the formation of the crystalline vanadium silicides. Common tangents are drawn for bcc vanadium (α), amorphous-vanadium-silicide (β) and amorphous-silicon.



figures 3a and 3b, assuming that kinetic barriers do prevent the formation of the crystalline silicides. Under these conditions, figure 4a suggests that amorphous-nickel-silicide with a composition range of approximately 35 to 55 atomic percent silicon can form at a nickel/amorphous-silicon interface; and figure 4b predicts that amorphous-vanadium-silicide with a composition range of 35 to 60 atomic percent silicon can form at a vanadium/amorphous-silicon interface .

Experimentally, it has been shown that in nickel/amorphous-silicon and vanadium/amorphous-silicon systems, there are nucleation barriers that prevent the formation of crystalline silicides at the metal/amorphous-silicon interface and allow an amorphous-metal-silicide to be the first silicide phase to form.^{8,18} Clevenger et al^{15,18} have also recently determined that the composition of amorphous-nickel-silicide formed from a reaction between nickel and silicon is approximately 1 Ni atom to 1 Si atom. This value is within the range of 35 to 55 atomic percent silicon predicted in figure 4a.

7.3 Simultaneous Growth of an Amorphous and Crystalline Intermetallic Phase

Gibbs free energy versus composition diagrams may also be used to determine whether an amorphous-intermetallic phase will shrink or continue to grow when a crystalline intermetallic forms at the amorphous-intermetallic/elemental interface. The Gibbs free energy versus composition diagram for the A-B system when an amorphous-intermetallic phase has formed at the A/B interface was presented in figure 2. In figure

5 we replot figure 2, extending the common tangents between the amorphous-intermetallic phase and A, and the amorphous-intermetallic phase and B. This construction divides the free energy diagram into the 6 distinct regions labeled in figure 5. Any crystalline intermetallic with a free energy in region 4 or 6 can nucleate at the A/amorphous-intermetallic interface while any crystalline intermetallic with a free energy in region 5 or 6 can nucleate at the B/amorphous-intermetallic interface. Crystalline silicides with free energies in regions 1,2 or 3 may not nucleate at either the A/amorphous-intermetallic or the B/amorphous-intermetallic interface, although they could form inside the amorphous-intermetallic phase.

Consider a crystalline intermetallic with a free energy in region 4 that forms at the A/amorphous-intermetallic interface. The thin film system would then have the following sequence of layers: A/crystalline intermetallic/amorphous-intermetallic/B. The resulting Gibbs free energy versus composition diagram after crystalline intermetallic formation is shown in figure 6, with the common tangents drawn in between the respective phases. This figure demonstrates that an A atom diffusing from A through the intermetallic phases to B will decrease its chemical potential. This indicates that the diffusion of A and/or B through each of the layers is possible which could lead to simultaneous growth of both the crystalline and amorphous-intermetallic phases. A similar discussion can be applied to a crystalline intermetallic with a free energy in region 5, except that in this case the crystalline intermetallic will form at the amorphous-intermetallic/B interface.

Next consider a crystalline intermetallic with a free energy in region 6. This crystalline intermetallic could form at either the A/amorphous-intermetallic or amorphous-intermetallic/B interface. If the crystalline

Figure 5 Same as figure 2 with the common tangents between the amorphous-intermetallic phase and A and the amorphous-intermetallic phase and B extended to intersect the Gibbs free energy axes. These common tangents divide the diagram into six regions labeled 1 through 6.

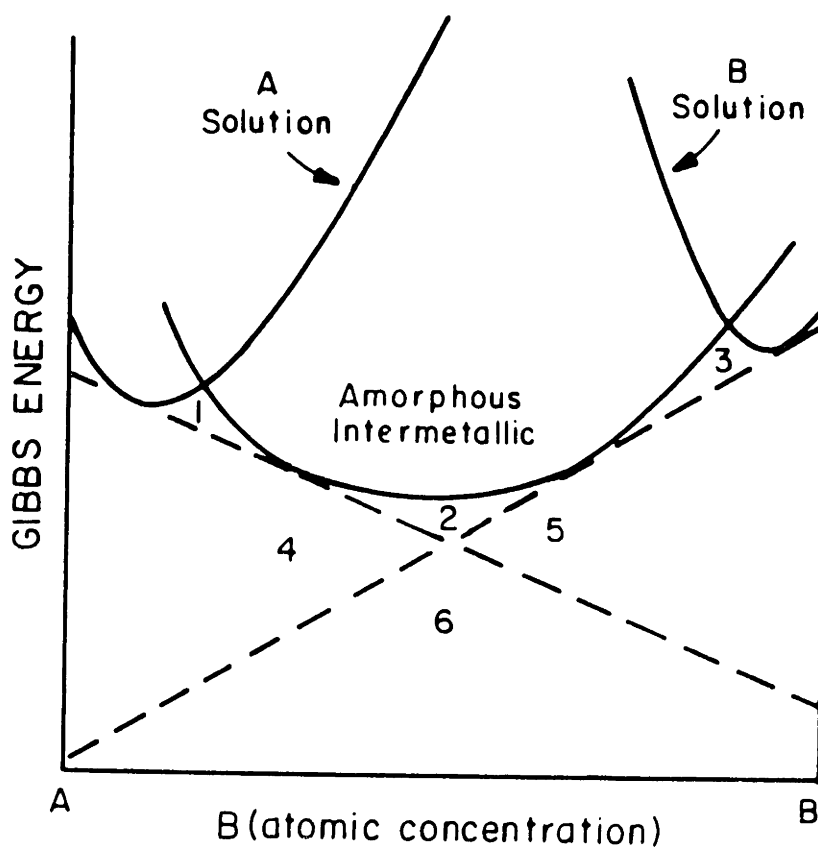
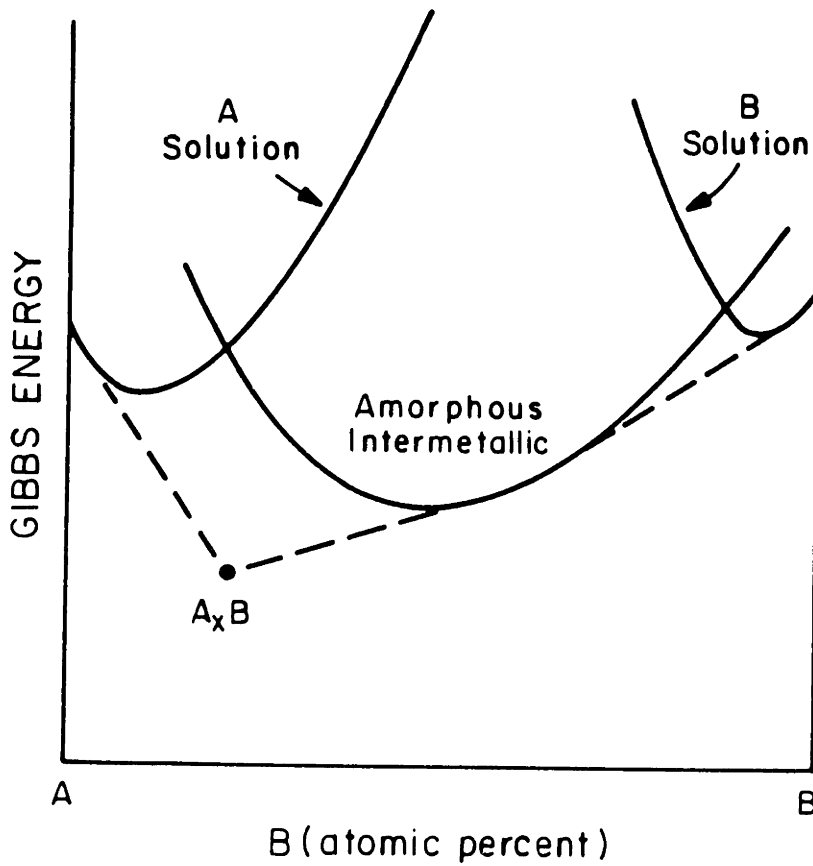


Figure 6 Same as figure 2 with a crystalline intermetallic A_xB , that has formed at the A/amorphous-intermetallic interface. The A_xB crystalline intermetallic has a free energy located in region 4 of figure 5. Common tangents are drawn in between A and A_xB , A_xB and the amorphous-intermetallic phase and the amorphous-intermetallic phase and B.



intermetallic formed at the amorphous-intermetallic/B interface, the thin film system would have the following sequence of layers: A/amorphous-intermetallic/crystalline intermetallic/B. The resulting Gibbs free energy versus composition diagram is shown in figure 7 with common tangents drawn in between A and the amorphous-intermetallic, the amorphous-intermetallic and the crystalline intermetallic, and the crystalline intermetallic and B. Figure 7 indicates that in this case, the chemical potential of A atoms would increase if the A atom diffused from A through the amorphous-intermetallic phase to the crystalline intermetallic. This implies that there would be no driving force for the diffusion of A or B atoms inside the amorphous-intermetallic. Thus, the amorphous-intermetallic will not continue to grow once the crystalline intermetallic is formed and the crystalline intermetallic will grow at the expense of the amorphous-intermetallic and B layers. A similar reasoning may be applied to crystalline intermetallic formation at the A/amorphous-intermetallic interface and it indicates that any crystalline intermetallic with a free energy in region 6 will stop the further growth of the amorphous-intermetallic phase.

The above predictions can be compared with experimental results in nickel/amorphous-silicon and vanadium/amorphous-silicon thin film reactions. In nickel/amorphous-silicon thin films, several authors have reported^{15,17} the simultaneous growth at temperatures ranging from 500 to 650 K of both an amorphous-nickel-silicide and crystalline Ni₂Si which had formed at a fcc nickel/amorphous-nickel-silicide interface. In figure 8, we present the Gibbs free energy versus composition curve at 650 K for the nickel/amorphous-silicon system considering only the fcc nickel, amorphous-nickel-silicide, amorphous-silicon and crystalline Ni₂Si. In

Figure 7 Same as figure 2 , with a crystalline intermetallic A_xB that has formed at the amorphous-intermetallic/B interface. The A_xB crystalline intermetallic has a free energy located in region 6 of figure 5. Common tangents are drawn between A and the amorphous-intermetallic phase, the amorphous-intermetallic phase and A_xB and A_xB and B.

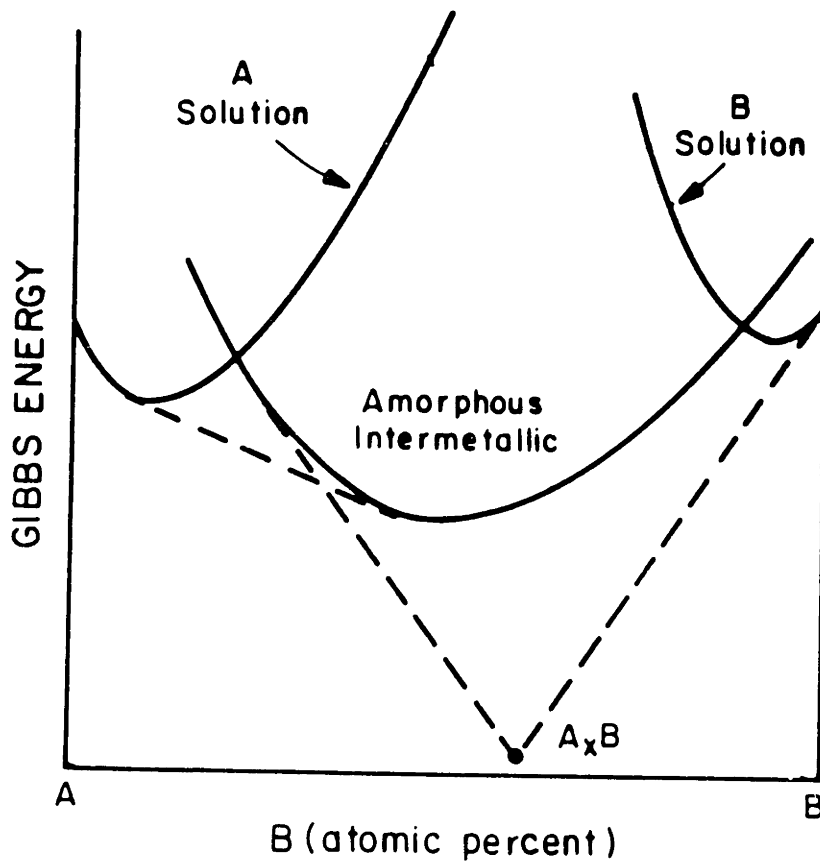
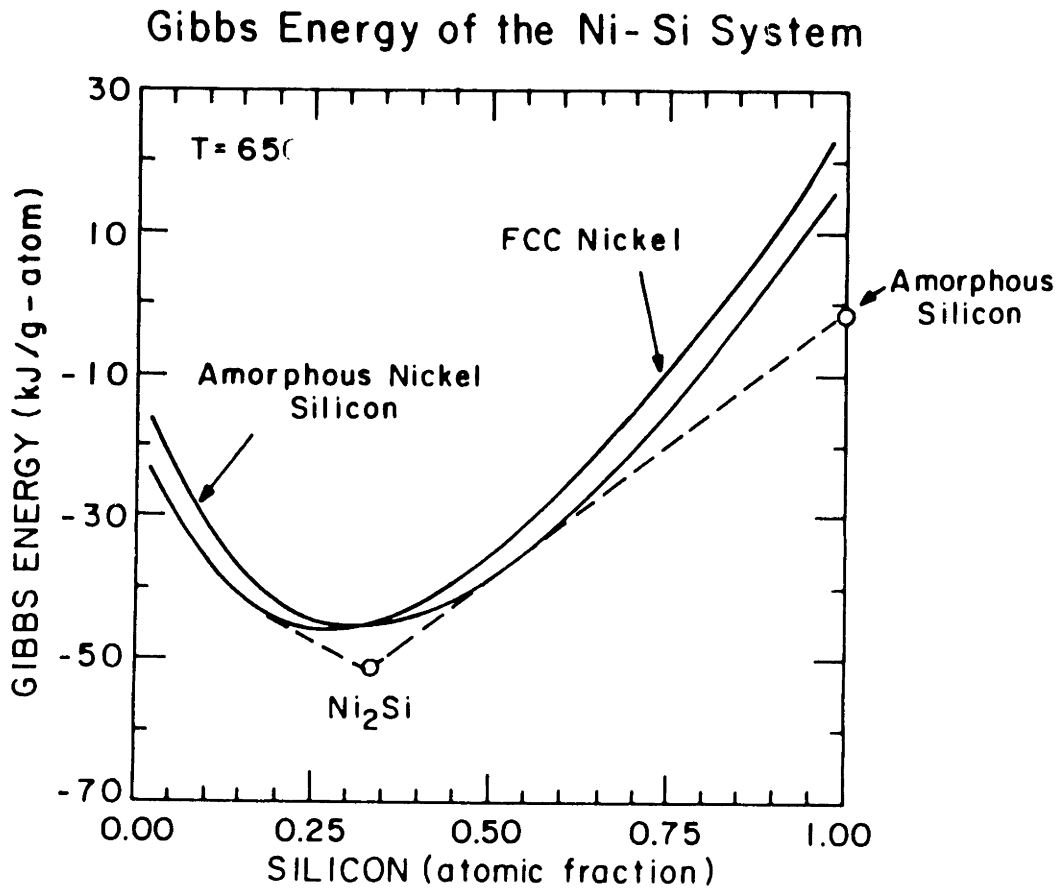


Figure 8 Gibbs free energy versus composition diagram at 650 K for the nickel/silicon system considering only fcc nickel, amorphous-nickel-silicide, Ni_2Si and amorphous-silicon. Common tangents are drawn between fcc nickel and Ni_2Si , Ni_2Si and amorphous-nickel-silicide and amorphous-nickel-silicide and amorphous-silicon.

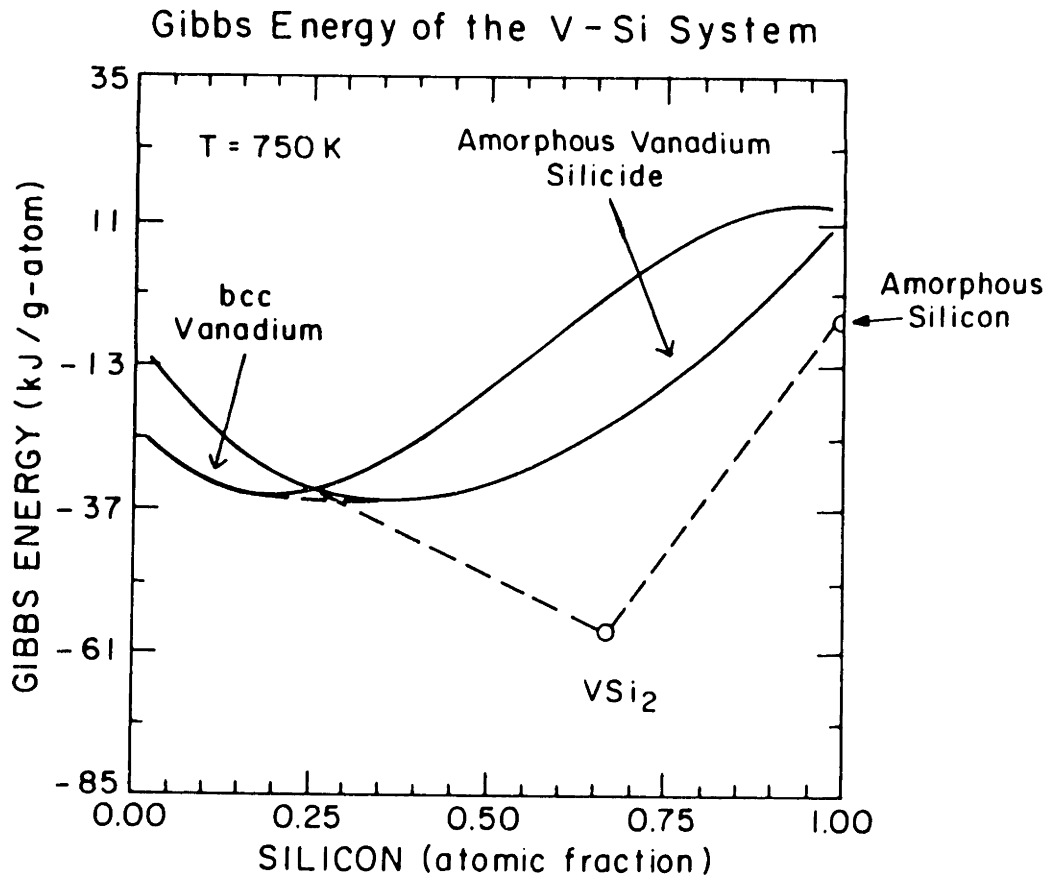


comparing this figure with figures 6 and 7, we see that this diagram has a similar structure to figure 6. This indicates that the simultaneous growth of both amorphous-nickel-silicide and crystalline Ni_2Si is thermodynamically possible at this temperature. In contrast, Clevenger et al^{4,18} have recently shown that in vanadium/amorphous-silicon thin film reactions, the first crystalline silicide phase to form is VSi_2 at approximately 750 K at the amorphous-vanadium-silicide/amorphous-silicon interface. In figure 9, we present the Gibbs free energy versus composition diagram at 750 K for the vanadium/amorphous-silicon system considering only bcc vanadium, amorphous-vanadium-silicide, amorphous-silicon and VSi_2 . In comparing this figure with figures 6 and 7, we see that this diagram has a similar structure to figure 7, indicating that the simultaneous growth of both amorphous-vanadium-silicide and VSi_2 is not expected at 750 K. It has not yet been experimentally determined if amorphous-vanadium-silicide and VSi_2 undergo simultaneous growth. However in molybdenum/amorphous-silicon reactions (which one would expect to be similar to vanadium/amorphous-silicon reactions) the simultaneous growth of crystalline MoSi_2 and amorphous-molybdenum-silicide has been shown not to occur.¹⁹

7.4 Thermodynamic Driving Forces for Crystalline Intermetallic Formation

The Gibbs free energy versus composition diagram of figure 1 can also be used to calculate how the driving force for crystalline intermetallic formation varies with atomic concentration and with the reaction interface

Figure 9 Gibbs free energy versus composition diagram at 750 K for the vanadium/silicon system considering only bcc vanadium, amorphous-vanadium-silicide, VSi_2 and amorphous-silicon. Common tangents are drawn between bcc vanadium and amorphous-vanadium-silicide, amorphous-vanadium-silicide and VSi_2 and VSi_2 and amorphous-silicon.



in an A-B thin film in which an amorphous-intermetallic phase has formed at the A/B interface. Consider a crystalline intermetallic A_xB that nucleates in either the A,B or amorphous-intermetallic solutions. The driving force for the formation of A_xB as a function of the composition of one of these solutions can be expressed as:

$$\Delta G_v = (G_{A_xB} - (G_{\text{solution}})_{X_s}) - \left(\frac{dG_{\text{solution}}}{dX_B} \right)_{X_s} (X_{A_xB} - X_s) \quad (1)$$

where X_s is the composition of the solution from which A_xB forms, X_{A_xB} is the composition of A_xB , G_{A_xB} the free energy of A_xB , $(G_{\text{solution}})_{X_s}$ the free energy of the solution with a composition X_s , and $\left(\frac{dG_{\text{solution}}}{dX_B} \right)_{X_s}$ is the slope of the free energy curve of the solution at a composition X_s . A graphical interpretation of equation 1 is presented in figure 10. An important point illustrated in equation 1 is that for the driving force for A_xB formation at an A/B interface to be negative, there must be some interdiffusion of element B into the A layer and/or element A into the B layer.

In an A-B thin film reaction, the composition of either the A,B or amorphous-intermetallic solution from which A_xB nucleates is restricted to 0 to $C_{A/\text{amorphous AB}}^{A,\text{eq}}$ for the A solution, $C_{A/\text{amorphous AB}}^{\text{amorphous AB, eq}}$ to $C_{\text{amorphous AB/B}}^{\text{amorphous AB, eq}}$ for the amorphous-intermetallic solution and $C_{B/\text{amorphous AB}}^{B,\text{eq}}$ to pure element B for the B solution, where these compositions are defined by the common tangent construction of figure 2. From equation 1, these compositional restrictions in turn restrict the range of driving forces for A_xB formation in each of the solutions.

The interface at which A_xB forms determines the possible solutions from which A_xB can nucleate. If the free energy of A_xB is in region 4 of

Figure 10 Gibbs free energy versus composition diagram for an idealized A-B system demonstrating how the driving force ΔG_v , for crystalline A_xB formation from an arbitrary solution is calculated.

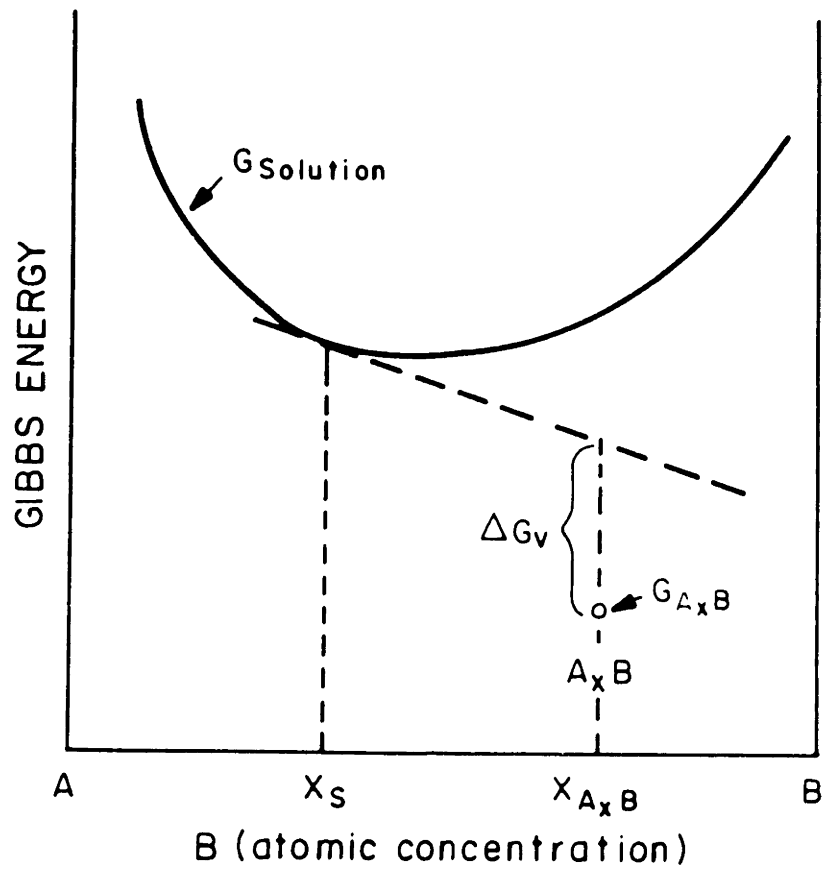


figure 5, the A_xB will form at the A/amorphous-intermetallic interface. At this interface, A_xB could nucleate within either the A layer, amorphous-intermetallic layer or between the A and the amorphous-intermetallic layer. Similarly, if the free energy of A_xB is in region 5 of figure 5, then A_xB will form at the amorphous-intermetallic/B interface and it will nucleate in either the amorphous-intermetallic layer, B layer or between the amorphous-intermetallic and B layers. If the free energy of A_xB is in region 6 of figure 5, A_xB could form at either interface; which interface it forms at will depend on which interface it nucleates at. For simplicity, we assume that when a crystalline intermetallic forms at an interface, it will nucleate only within a layer, not across layers. Thus if a crystalline intermetallic forms at the A/amorphous-intermetallic interface it can form in the A layer or the amorphous-intermetallic which has a high composition of element A, while if the crystalline intermetallic forms at the B/amorphous-intermetallic interface, it can form in the B layer or the amorphous-intermetallic which has a high concentration of element B. These are four different environments for crystalline intermetallic formation and from equation 1, each one will have a different driving force for crystalline intermetallic formation.

Thus, the thermodynamic driving force for crystalline intermetallic formation depends on the interface at which the intermetallic forms, the layer in which the intermetallic forms and the composition of the layer where the intermetallic nucleates. The calculation of driving forces for crystalline intermetallic formation using equation 1, combined with experimental observations, provides insight into what mechanisms control phase selection in thin film reactions. For example, in nickel/amorphous-silicon thin films, crystalline silicide formation occurs at the

nickel/amorphous-nickel-silicide interface and in vanadium/amorphous-silicon reactions crystalline silicide formation occurs at the amorphous-vanadium-silicide/amorphous-silicon interface.^{8,18} In figures 11a and 11b we plot the driving forces for crystalline nickel silicide formation at the nickel/amorphous-nickel-silicide interface as a function of silicon composition in the fcc nickel layer (figure 11a) and in the amorphous-nickel-silicide layer (figure 11b). In figure 11c, we plot the driving force for crystalline vanadium silicide formation at the amorphous-vanadium-silicide/amorphous-silicon interface as a function of silicon composition in the amorphous-vanadium-silicide layer at 750 K. In vanadium/silicon reactions, the driving force for crystalline silicide formation at the amorphous-vanadium-silicide/amorphous-silicon interface as a function of silicon composition in the amorphous-silicon layer is not plotted because we have assumed that the amorphous-silicon is pure silicon, and thus the crystalline silicide cannot form within this layer. In figure 11, the composition ranges of the fcc nickel (figure 11a), amorphous-nickel-silicide (figure 11b) and amorphous-vanadium-silicide (figure 11c) are restricted by the common tangent construction of figure 4 to be from 0 to 25 atomic percent silicon for the fcc nickel solution, 35 to 55 atomic percent silicon for the amorphous-nickel-silicide solution and 35 to 60 atomic percent silicon for the amorphous-vanadium-silicide solution.

Consider crystalline silicide formation at the nickel/amorphous-nickel-silicide interface. In figure 11a, we have plotted the driving force for formation at 400 K for each of the crystalline silicide phases at this interface if they form in the fcc nickel layer. This diagram demonstrates two important points. First, for any of the crystalline silicides to have a negative driving force for formation in the nickel layer, there must be a

Figure 11a Driving force for crystalline nickel silicide formation at 400 K from fcc nickel as a function of composition of the nickel. The composition of the fcc nickel is restricted from 0 to 25 atomic percent silicon.

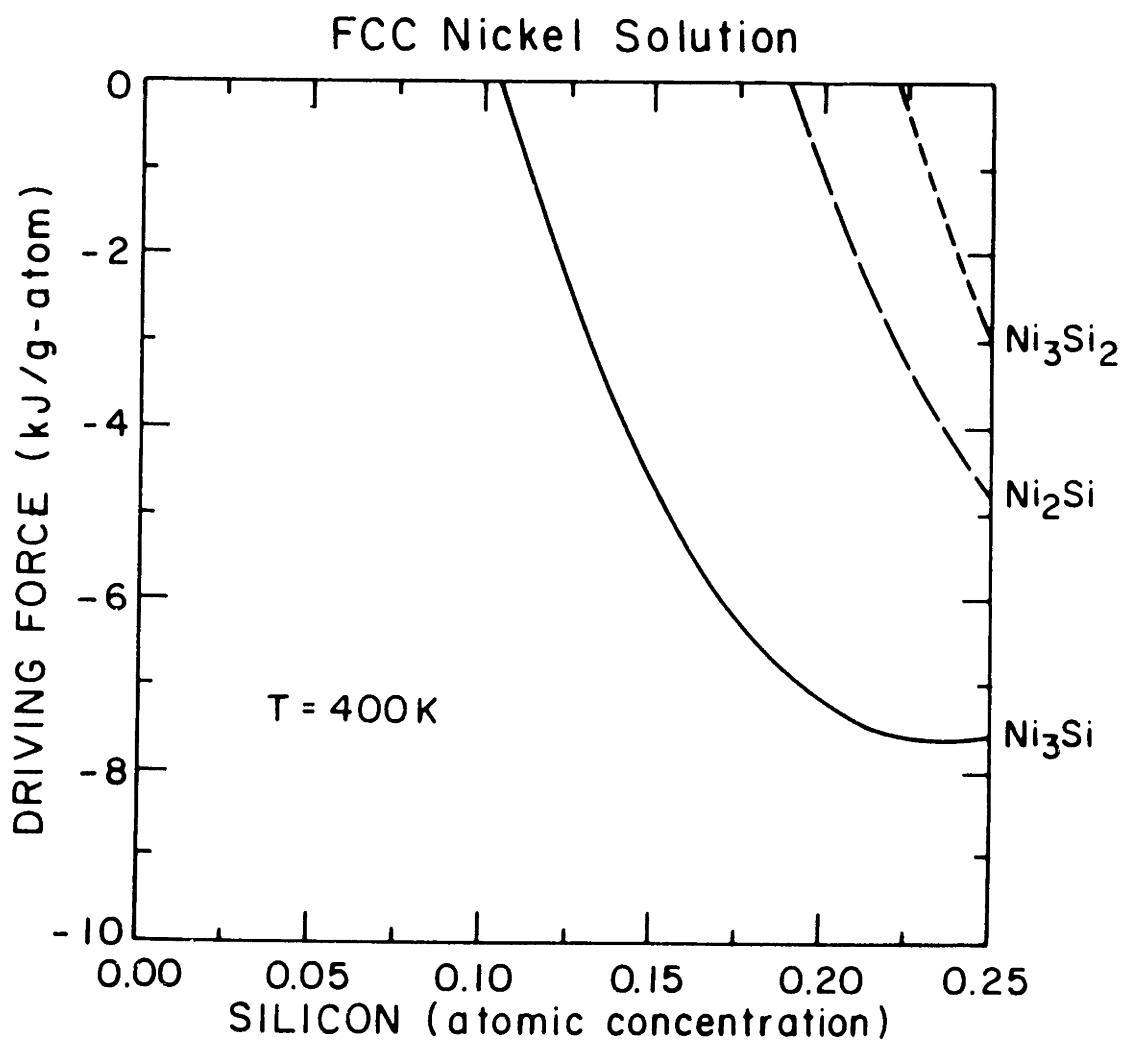


Figure 11b Driving force for crystalline nickel silicide formation at 400 K from amorphous-nickel-silicide as a function of composition of the amorphous-nickel-silicide. The composition of the amorphous-nickel-silicide is restricted to from 30 to 50 atomic percent silicon.

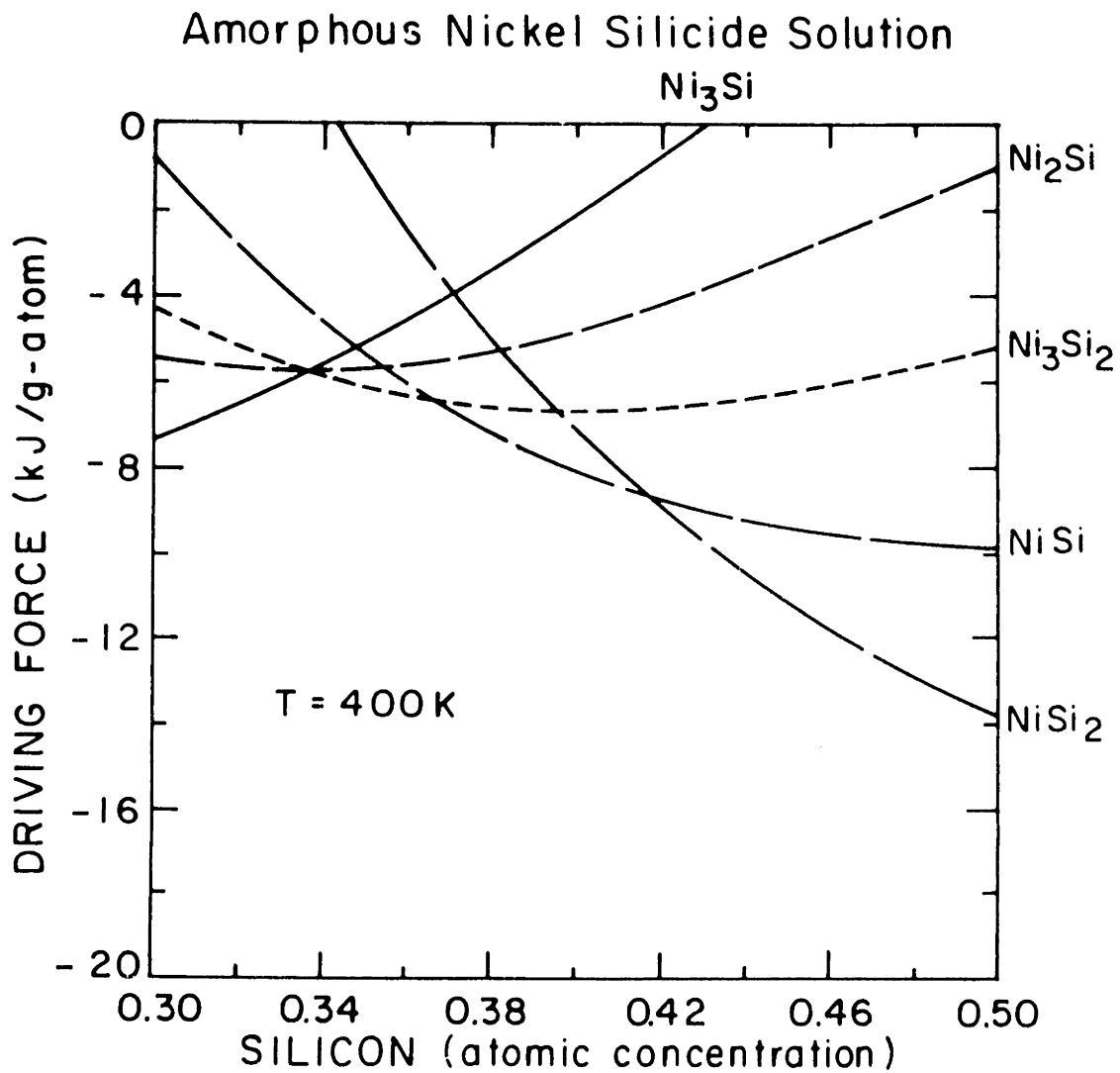
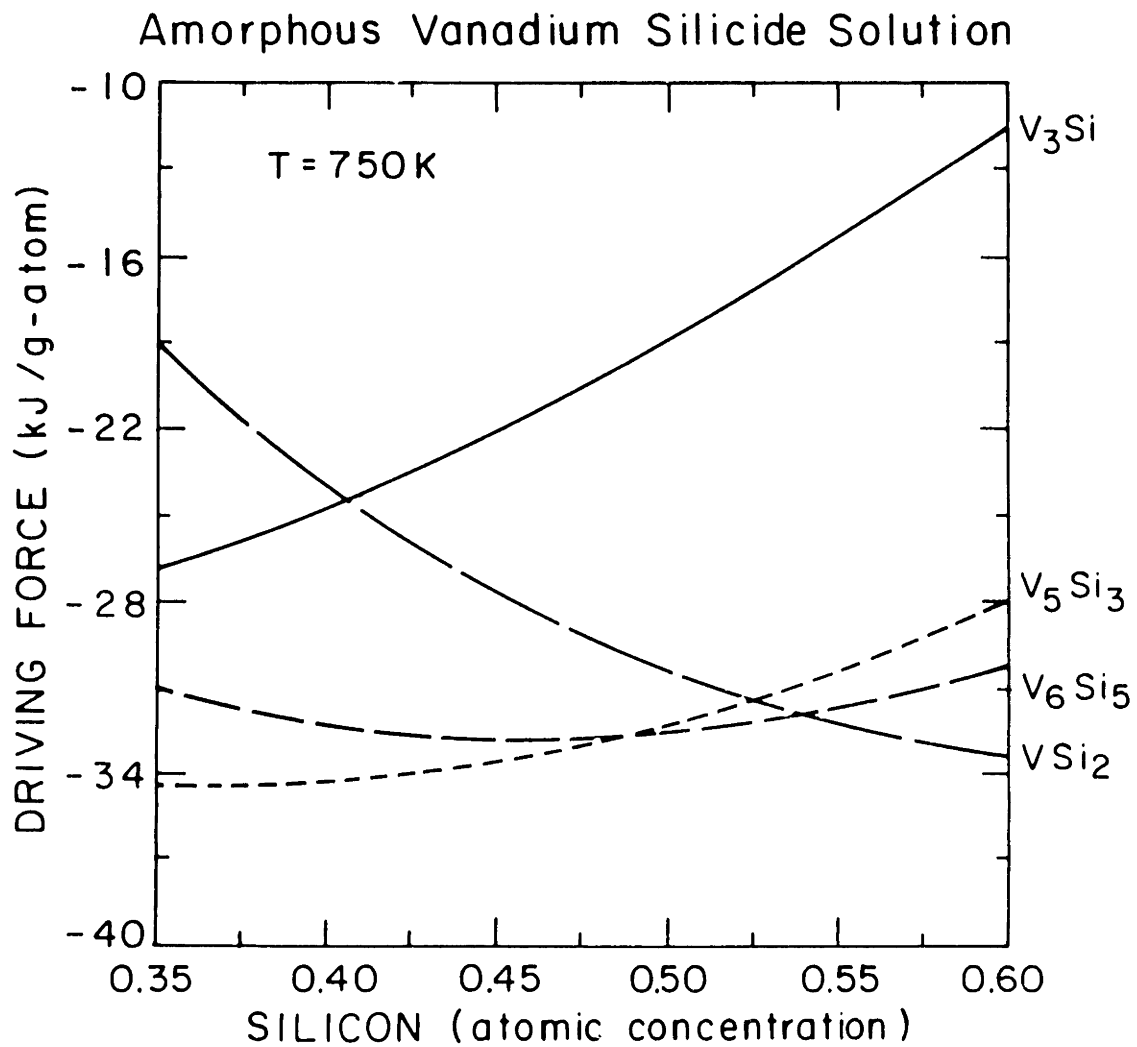


Figure 11c Driving force for crystalline vanadium silicide formation at 750 K from amorphous-vanadium-silicide as a function of the composition of the amorphous-vanadium-silicide. The composition of the amorphous-vanadium-silicide is restricted to from 35 to 60 atomic percent silicon.



significant amount of interdiffusion into this layer. The composition of the nickel layer at this interface has to be at least 10 atomic percent silicon for Ni_3Si to form and more for the other crystalline silicides. The second point is that at the maximum silicon composition in the nickel layer only three out of the five possible crystalline silicide phases have a negative driving force for formation. These phases are Ni_3Si , Ni_2Si and Ni_3Si_2 . Both NiSi and NiSi_2 do not have a negative driving force for formation and will not form in the nickel layer.

If the crystalline nickel silicide formation at the nickel/amorphous-nickel-silicide interface occurs in the amorphous-nickel-silicide layer, the driving force for crystalline silicide formation is that plotted in figure 11b. This figure demonstrates that in this case, the possible crystalline silicides that can form depend on the concentration of silicon in the amorphous-nickel-silicide at the nickel/amorphous-nickel-silicide interface. If this composition is close to the equilibrium value of 30 atomic percent silicon, the phases that can form are Ni_3Si , Ni_2Si , Ni_3Si_2 and NiSi . If this composition is close to 50 atomic percent silicon, then the silicide phases that can form are NiSi_2 , NiSi , Ni_3Si and Ni_2Si . In either case not all the crystalline silicides can form within the amorphous-nickel-silicide layer at the nickel/amorphous-nickel-silicide interface.

Various authors have shown that the first crystalline silicide phase to form at the nickel/amorphous-nickel-silicide interface is Ni_2Si .^{15,17,20} They have not been able to determine whether Ni_2Si forms in the nickel or the amorphous-nickel-silicide layer. However, in either case, figures 11a and 11b indicate that Ni_2Si does not have the highest driving force for formation in either of the layers. This suggests that thermodynamic

driving forces and nucleation surface energies combine to determine the first crystalline silicide phase in nickel/amorphous-silicon reactions.^{8,15,18}

As a final example, consider crystalline silicide formation at the amorphous-vanadium-silicide/amorphous-silicon interface. In figure 11c, we have plotted the driving force for formation at 750 K of each of the crystalline silicide phases at this interface assuming that they form in the amorphous-vanadium-silicide layer. This diagram demonstrates that no matter what the composition of the amorphous-vanadium-silicide, all the crystalline silicide phases have a negative driving force for formation. This is very different from crystalline silicide formation at the nickel/amorphous-nickel-silicide interface where a limited number of crystalline silicides had a negative driving force for formation. This diagram also demonstrates that if the composition of the amorphous-vanadium-silicide at the amorphous-vanadium-silicide/amorphous-silicon interface is near its equilibrium value of 60 atomic percent silicon, then crystalline VSi_2 has the highest driving force for formation followed by V_6Si_5 , V_5Si_3 and V_3Si . Experimentally, it has been determined that VSi_2 is the first crystalline silicide phase to form at this interface. This suggests that in vanadium/amorphous-silicon reactions the first crystalline silicide phase to form is the phase with the highest driving force for formation.

7.5 Conclusion

We have discussed how Gibbs free energy versus composition diagrams can be used to understand the thermodynamics of amorphous and crystalline intermetallic formation by a solid state reaction at the

interface in a thin film diffusion couple. We have shown that for an amorphous-intermetallic phase to form at nickel/amorphous-silicon and vanadium amorphous-silicon interfaces there have to be kinetic barriers that prevent the formation of the crystalline intermetallics. This is likely the case for many other materials systems. We have also shown that the simultaneous growth of both an amorphous and crystalline intermetallic is possible if the free energies of the crystalline intermetallic are within a predefined area of the Gibbs free energy versus composition diagram. Finally, we demonstrated how the thermodynamic driving force for crystalline intermetallic formation is a function of the phase from which it nucleates, the composition of this phase and the interface at which the intermetallic forms. The methodologies presented here are applicable to any type of interface reaction.

7.6 References

1. S.P. Murarka, Silicides for VLSI Applications, Academic Press, New York (1983)
2. J.E. Baglin and J.M. Poate, Thin Film Interfaces and Interactions, Electrochemical Society, New York (1980)
3. I.J.M.M. Raaijmakers, A.H. Reader and P.H. Oosting, *J. Appl. Phys.*, **63**, 2790 (1988)
4. L.A. Clevenger, C.V. Thompson, A. Judas and K.N Tu, First MRS International Meeting on Advanced Materials, **10**, 431 (1989)
5. E.J. Cotts, W.J. Meng and W.L. Johnson, *Phys. Res. Lett.*, **57**, 2295 (1986)

6. F.M. d'Heurle, *J. Mater. Res.*, **3**, 167 (1988)
7. U. Gosele and K.N. Tu, *J. Appl. Phys.*, **53**, 3252 (1982)
8. L.A. Clevenger and C.V. Thompson, to be published
9. S. Herd, K.N. Tu and K.Y. Ahn, *Appl. Phys. Lett.*, **42**, 597 (1987)
10. R. Schwartz and W.L. Johnson, *Phys. Rev. Lett.*, **51**, 415 (1983)
11. K. Holloway and R. Sinclair, *J. Appl. Phys.*, **61**, 1359 (1987)
12. H. Schroder, K. Samwer and U. Koster, *Phys. Rev. Lett.*, **54**, 197 (1985)
13. N. Saunders and A.P. Miodownik, *J. Mater. Res.*, **1**, 38 1986
14. K. Zoeltzer and R. Bormann, *J. Less-Common Metals*, **140**, 335 (1988)
15. L.A. Clevenger, C.V. Thompson, R.R. De Avillez and K.N. Tu to appear in the Proceedings of the Symposium on Chemistry and Defect in Semiconductor Heterostructures, the Spring 1989 Meeting of the Materials Research Society, edited by M. Kawabe, T.Sands, E. Weber and R.S. Williams
16. K. Holloway, R. Sinclair and M. Nathan, to be published
17. E. Ma, W.J. Meng, W.L. Johnson, M.-A. Nicolet and M. Nathan, *Appl. Phys. Lett.*, **53**, 2033 (1988)
18. L.A. Clevenger, R.R. De Avillez and C.V. Thompson, to be published
19. L.A. Clevenger, C.V. Thompson, R.C. Cammarata and K.N. Tu *Appl. Phys. Lett.*, **52**, 796 (1988)
20. K. Holloway and R. Sinclair to be published in *J. Appl. Phys.*

8 Structural Transitions in Electron-Beam Evaporated Amorphous-Silicon Thin Films

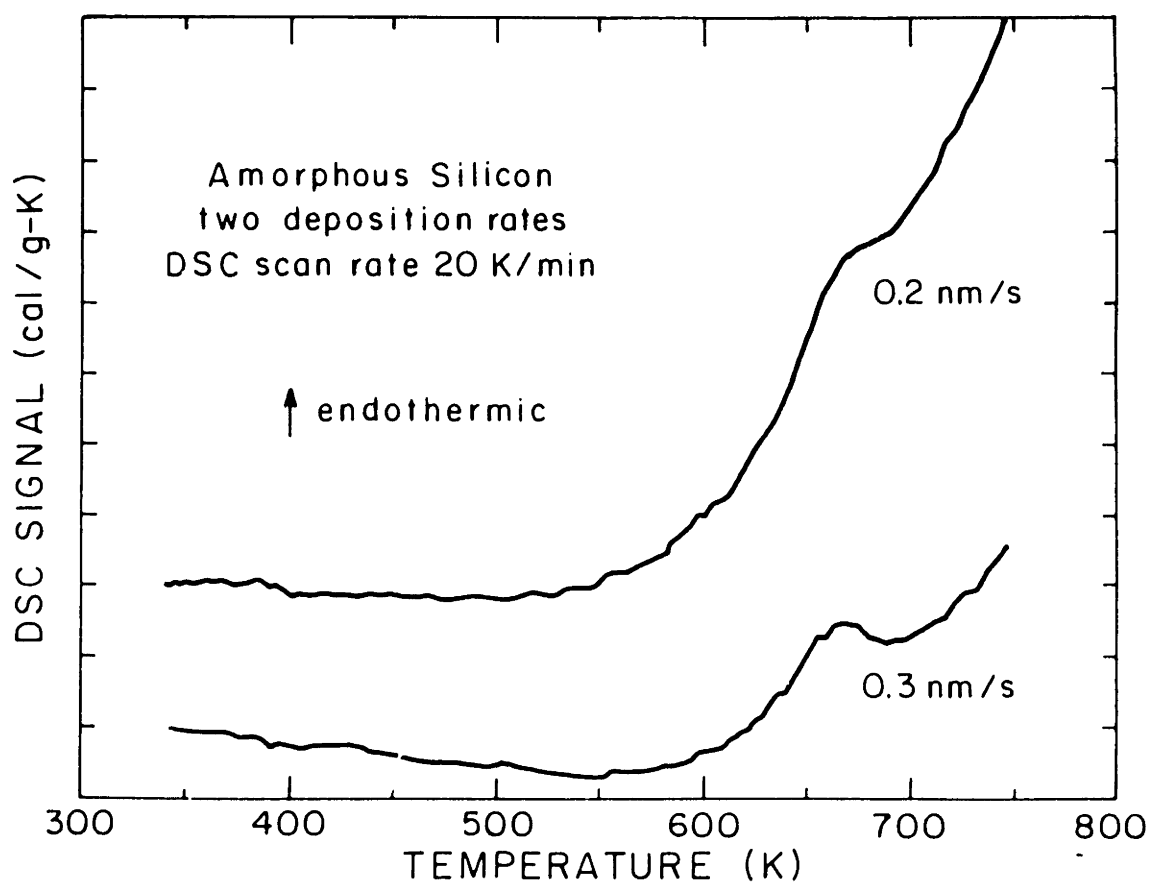
8.1 Introduction

Structural transitions in amorphous-silicon thin films have been studied by a number of researchers. Fan and Anderson¹ were the first to study the crystallization temperatures and heat of crystallization of amorphous-silicon thin films. Later, Donovan et al.² determined that the heat of crystallization of amorphous-silicon films amorphized by ion-bombardment was approximately -11.95 kJ/g-atom. Recently Roorda et al.³ have seen calorimetric evidence for a low temperature structural relaxation in ion-amorphized amorphous-silicon thin films. The purpose of this chapter is to investigate exothermic and endothermic structural transitions that occur in amorphous-silicon thin films prepared by electron-beam evaporation upon heating, using differential scanning calorimetry, plan view transmission electron microscopy and density measurements.

8.2 Results and Discussion

Figure 1 shows typical differential scanning calorimetry (DSC) traces for amorphous-silicon films deposited at two different rates. It shows a broad exothermic process below 600 K and an endothermic step beginning at about 600 K. In order to provide a good baseline for each DSC scan, the samples were held isothermally at the highest temperature and allowed to

Figure 1 Differential scanning calorimetry traces for amorphous silicon films prepared by electron beam evaporation with two different deposition rates.



relax. Then, a last scan was done and used as a baseline for all previous runs.

Figure 2 shows three DSC traces obtained from consecutive scans of the same sample. Trace 1 is for an as-deposited sample heated to 750 K and immediately quenched at 320 K/min to room temperature. Trace 2 corresponds to a second upward scan of this same sample to 750 K, which was followed by an isothermal treatment at 750 K for 23 min. Finally, trace 3 was taken after the isothermal treatment. A fourth scan was used as baseline. The first trace shows both the broad exothermic process and the endothermic step, but the second trace does not. This implies that both transitions are irreversible. The isothermal treatment was accompanied by a relaxation to a more stable amorphous state. This is confirmed by the almost horizontal trace 3, which clearly shows that no further changes occurred in the temperature range up to 750 K after the isothermal treatment.

The broad low-temperature exothermic process is probably due to the relief of bond distortions as suggested by Lannin⁴ and has already been observed by other researchers.^{1,3,5} The endothermic step is not associated with the crystallization of amorphous-silicon. This is supported by the inset of figure 3b which shows the transmission electron diffraction pattern characteristic of a sample heated at 20 K/min to 750 K and quenched (320 K/min) to room temperature. This diffraction pattern is characteristic of the amorphous-silicon and indicates that the film does not undergo any crystallization up to 750 K. Insight into the source of the endothermic step is gained by realizing that the DSC signal is proportional to the heat capacity of the sample, which can be described by the expression:

Figure 2 Differential scanning calorimeter traces for consecutive temperature scans from 330 to 750 K of an amorphous silicon film deposited at 0.2 nm/min.

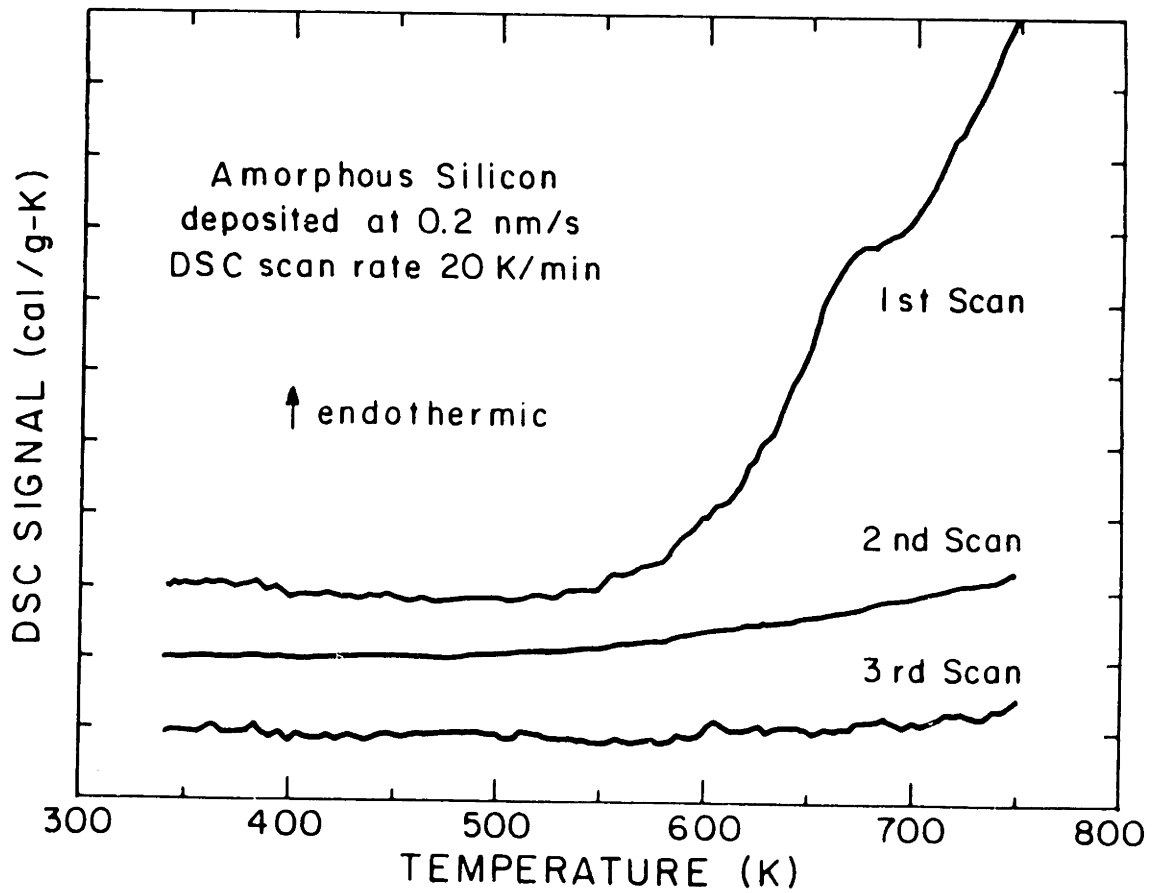


Figure 3a Transmission electron micrograph and diffraction pattern (insert) of an amorphous silicon film deposited at 0.2 nm/min, at room temperature.

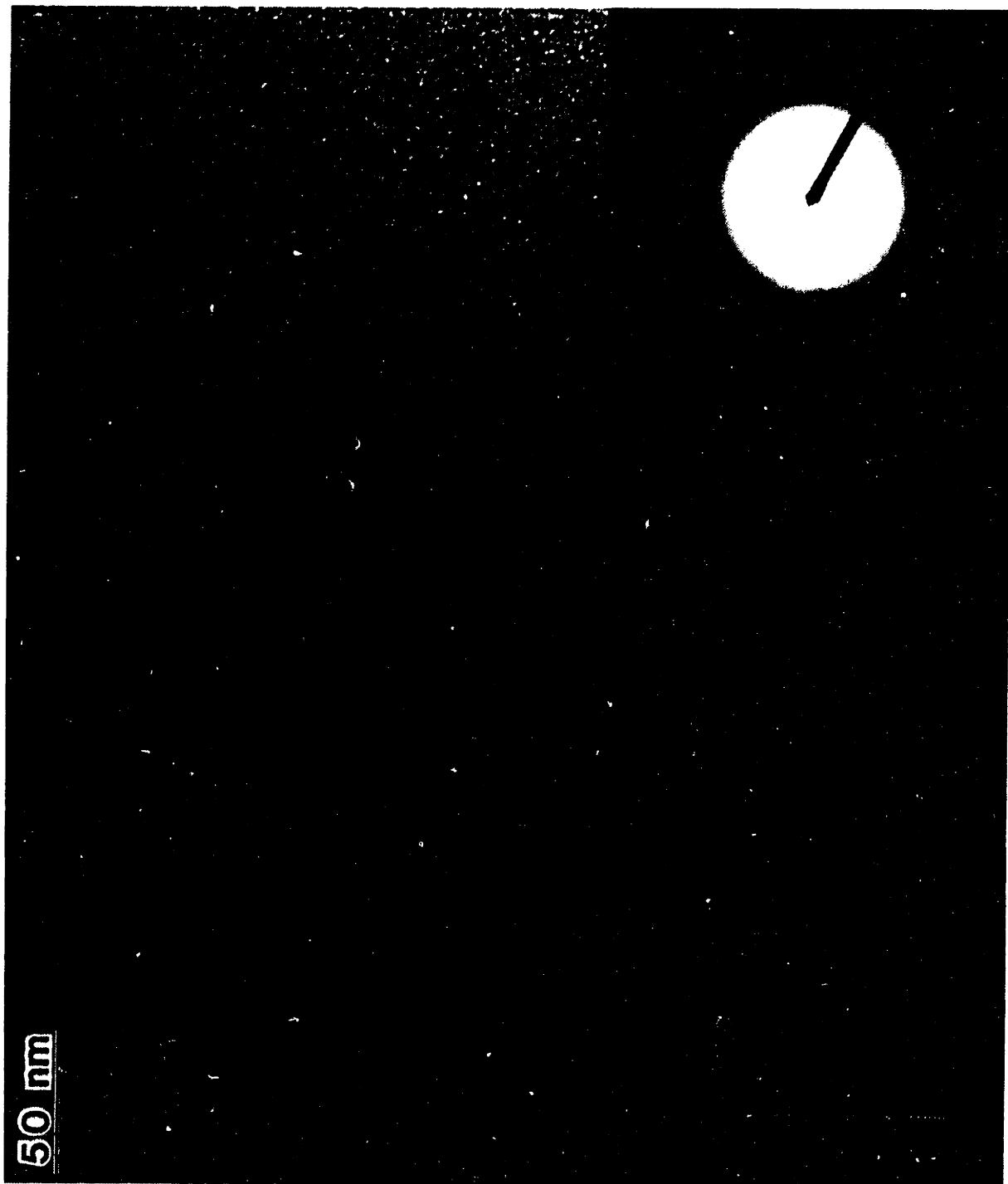
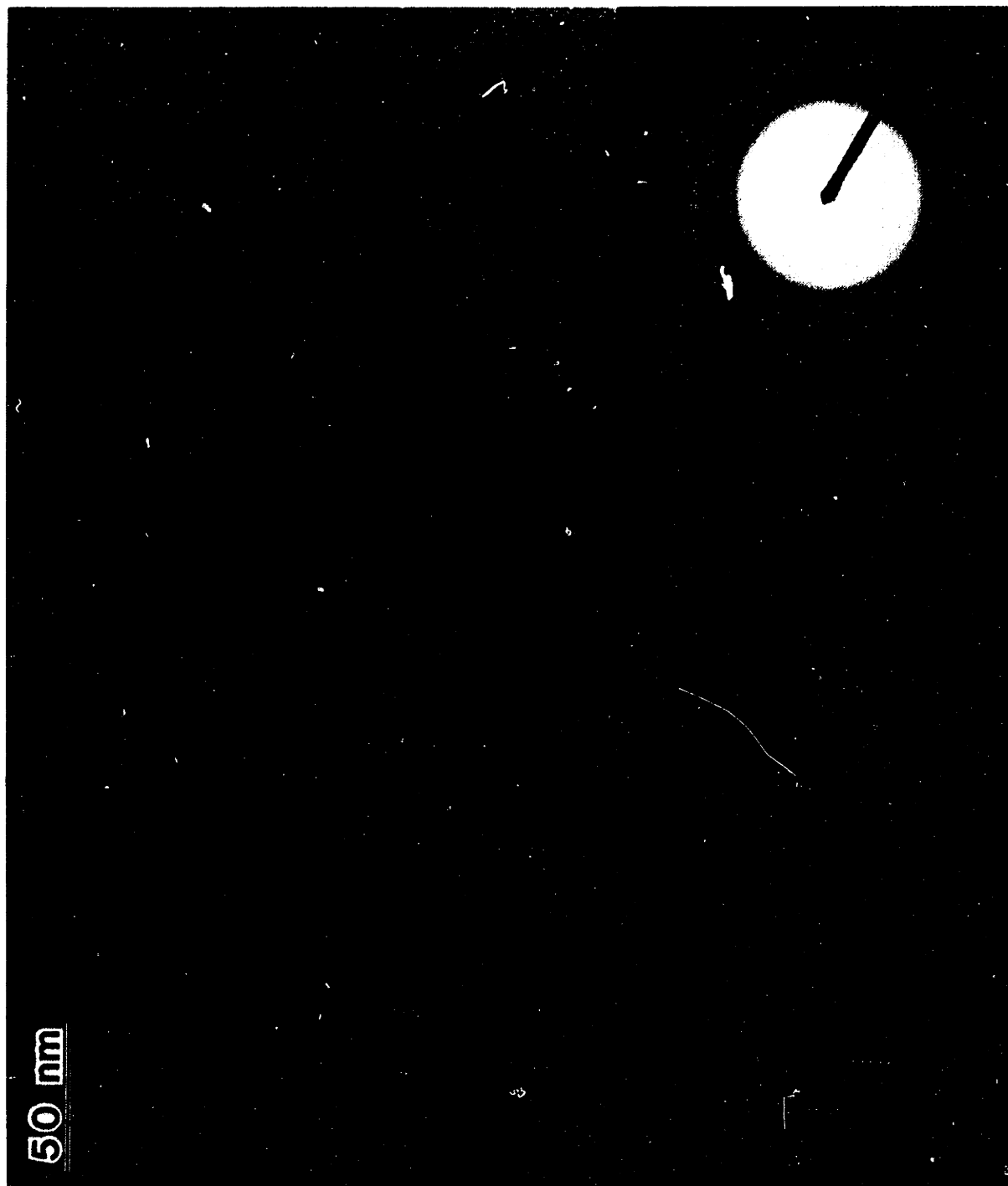


Figure 3b Transmission electron micrograph and diffraction pattern (insert) of an amorphous silicon film deposited at 0.2 nm/min, at room temperature, after being heated at 20 K/min from 330 to 750 K and quenched at 320 K/min.



$$C_p = T \left(\frac{dS}{dT} \right)_p \quad (1)$$

The endothermic step corresponds to an increase in the heat capacity of the sample which, according to equation 1, also corresponds to an increase in the entropy of the amorphous-silicon. Equation 1 may be rewritten as:

$$C_p = T \left(\frac{dV}{dT} \right)_p \left(\frac{dS}{dV} \right)_p \quad (2)$$

which shows that, at constant pressure, the partial derivative of entropy as a function of volume has the same sign as the partial derivative of volume as a function of temperature. Since C_p is always positive, any volume decrease during the heating of the amorphous-silicon film will be accompanied by an entropy increase. Indeed, the thickness of as-deposited amorphous-silicon films, measured using a profilometer, reduces about 17% after the DSC scan up to 750 K. This value is a little bit above the errors associated with the profilometer and must be considered with reserve. Nonetheless, it implies a volume decrease with increasing temperature and, according to equation 2, an entropy increase.

The endothermic step seems to be related to a structural homogenization and densification of the amorphous-silicon through the movement of single atoms or clusters. Such homogenization will increase the configurational entropy, and therefore, the heat capacity of the amorphous-silicon (cf. previous paragraph and equation 1). This hypothesis was supported by examining the structure of amorphous-silicon samples in the as-deposited condition (Figure 3a) and after heating to 750 K and quenching to room temperature (Figure 3b). Figure 3a shows that the

as-deposited film had a heterogeneous "cell-like" structure, with dense regions (darker structure) surrounded by less dense material (lighter structure). The diffraction pattern was characteristic of an amorphous material. A similar structure has been reported by Kruzelecky et al.⁶ for UHV evaporated amorphous-silicon films and by Viscor⁷ for UHV evaporated a-Ge films. In clear contrast, the structure of the amorphous-silicon films heated to 750 K is homogeneous, almost featureless (Figure 3b). The diffraction pattern does not seem to have changed. A similar homogenization and densification process was also observed by Viscor in amorphous-Ge films.^{7,8} Thus, the endothermic step presented in figure 1 can be associated with the homogenization and densification of the amorphous-silicon films. It is also possible that if gas is trapped inside the film during the deposition, a degassing process may occur during heating. Such degassing would also give rise to an endothermic process, which might not be distinguished from the present interpretation.

The relaxation at about 600 K causes a large structural change, as seen by TEM, and probably leaves the amorphous-silicon in a low energy state. Raman spectroscopy has also pointed to the existence of a stable state for annealed amorphous-silicon films.^{4,9} Tsu also suggests that this state is characterized by a unique topology, associated with a medium range order and the rearrangement of at least two ring topologies.^{10,11} However, Sinke et al.⁹ observed that the final state after annealing was dependent on the previous preparation procedures. The results showed in figure 2 support the presence of a low energy amorphous state for the silicon sample held isothermally at 750 K.

8.3 Conclusion

In this chapter, differential scanning calorimetry was used to characterize the structural transitions in electron beam evaporated amorphous-silicon. Upon heating, a broad exothermic reaction, probably due to the relief of bond distortions, occurs up at temperatures up to approximately 600 K. Above this temperature and below the beginning of crystallization, an endothermic process occurs and results in homogenization and densification of the amorphous-silicon. It is believed that this process provides a more stable amorphous structure.

8.4 References

1. J.C.C. Fan and C.H. Anderson, *J. Appl. Phys.*, 52, 4003 (1981)
2. E.P. Donovan, F. Spaepen, D. Turnbull, J.M. Poate and D.C. Jacobson, *Appl. Phys. Lett.*, 42, 698 (1983)
3. S. Roorda, S. Doorn, W.C. Sinke, P.M.L.O Scholte and E. Van Loenen, to be published
4. J. S. Lannin, *J. of Non-Crystalline Solids* 97, 39 (1987).
5. E. P. Donovan, F. Spaepen, D. Turnbull, J. M. Poate and D. C. Jacobsen, *J. Appl. Phys.* 57, 1795 (1985).
6. R. V. Kruzelecky, D. Racansky, S. Zukotynski, Y. C. Koo and J. M. Perz, *J. Non-Cryst. Sol.* 104, 237 (1988).
7. P. Viscor, *J. Non-Cryst. Solids* 101, 156 (1988).
8. P. Viscor, *J. Non-Cryst. Solids* 101, 170 (1988).

9. W. Sinke, T. Warabisako, M. Miyao, T. Tokuyama, S. Rourda and F. W. Saris, *J. of Non-Crystalline Solids* 99, 308 (1988).
10. R. Tsu, J. G. Hernandez and F. H. Pollak, *Solid State Comm.* 54, 447 (1985).
11. R. Tsu, *J. Non-Cryst. Solids* 97, 163 (1987).

9 Explosive Silicidation

9.1 Introduction

Explosive silicidation has been reported to occur in rhodium/amorphous-silicon,¹ nickel/amorphous-silicon,^{2,3} vanadium/amorphous-silicon³ and zirconium/amorphous-silicon multilayer thin films.⁴ It is a reaction that can occur in metal/amorphous-silicon multilayer thin films under certain experimental conditions. With this reaction, the transformation from an inhomogeneous multilayer thin film to a homogeneous crystalline silicide phase can be initiated at room temperature by a laser pulse, an electrical shock or the mechanical impact of a stylus. Once initiated, the reaction front propagates through the rest of the film, which is typically in a room temperature environment. The reaction occurs very quickly and is characterized by a flash of light due to heating. This bright flash of light allows us to measure the reaction front velocity and temperature using a high speed optical pyrometer and camera as described in section 3.1.5.

In this chapter, we discuss explosive silicidation of nickel/amorphous-silicon multilayer thin films. The chapter is divided into two sections. In the first section, we determine the explosive reaction front velocity and temperature, and the microstructure of crystalline Ni₂Si formed by this reaction. In the second section, we compare the measured reaction front temperature to predicted values and discuss whether explosive silicidation occurs by a solid state reaction or a liquid state reaction.

9.2 Experimental Determination of Reaction Front Velocities and Temperatures Along with the Microstructures of the Crystalline Silicide Formed

The phase that was formed by explosive silicidation of as-deposited 2 Ni to 1 Si atomic concentration ratio multilayer thin films, as identified by thin film X-ray diffraction, was Ni_2Si .⁵ This is the same phase that was obtained by conventional thermal annealing of the multilayer thin films to a temperature of 850 K.^{2,3} Figure 1 presents high speed temperature measurements of explosive silicidation occurring in a 2 Ni to 1 Si multilayer thin film on a substrate with a modulation period of 20.8 nm and a total film thickness of 0.73 μm . At zero time, the reaction front has just come into the field of view of the pyrometer and the temperature reading is approximately 1580 K, which is slightly above the melting point of Ni_2Si (1565 K). The front passes from the field of view of the pyrometer in about 0.4 milliseconds and the film then starts to cool back to room temperature. Similar temperatures were measured for explosive silicidation of all the nickel/amorphous-silicon multilayer films on substrates. The maximum measured temperature of this explosive reaction of 1580 K indicates that intense heating occurs during explosive silicidation.

Explosive silicidation in nickel/amorphous-silicon multilayer thin films is characterized by a bright flash of orange light due to heating at the reaction front. This light allows one to measure the reaction front velocity using a high-speed camera. Figure 2 shows a high speed photograph of explosive silicidation occurring in a nickel/amorphous-silicon multilayer

Figure 1 High speed temperature measurements for explosive silicidation occurring in a nickel/amorphous-silicon multilayer film with an atomic concentration ratio of 2 Ni atoms to 1 Si atom, a modulation period of 20.8 nm and a total film thickness of 0.73 μm .

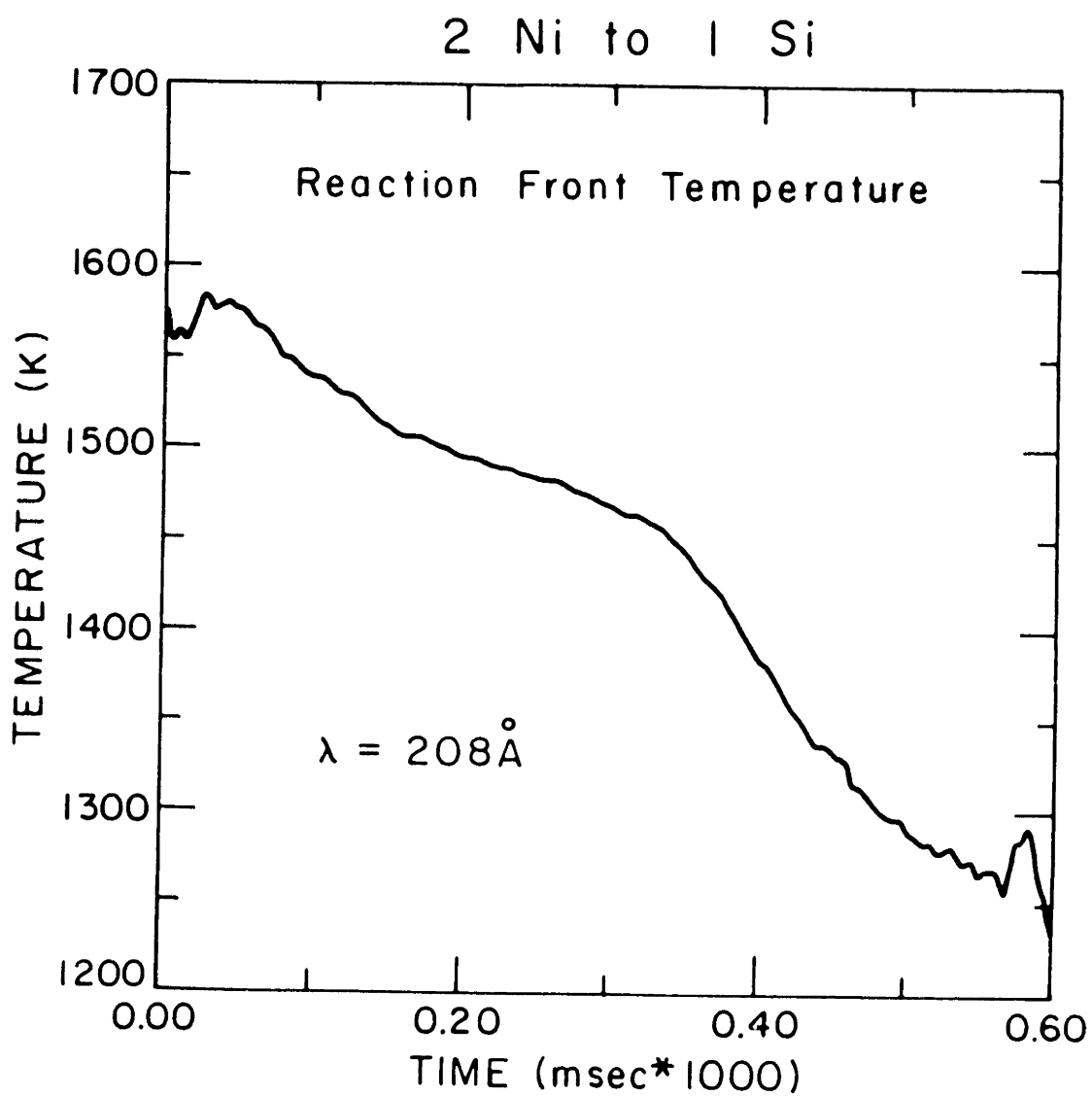
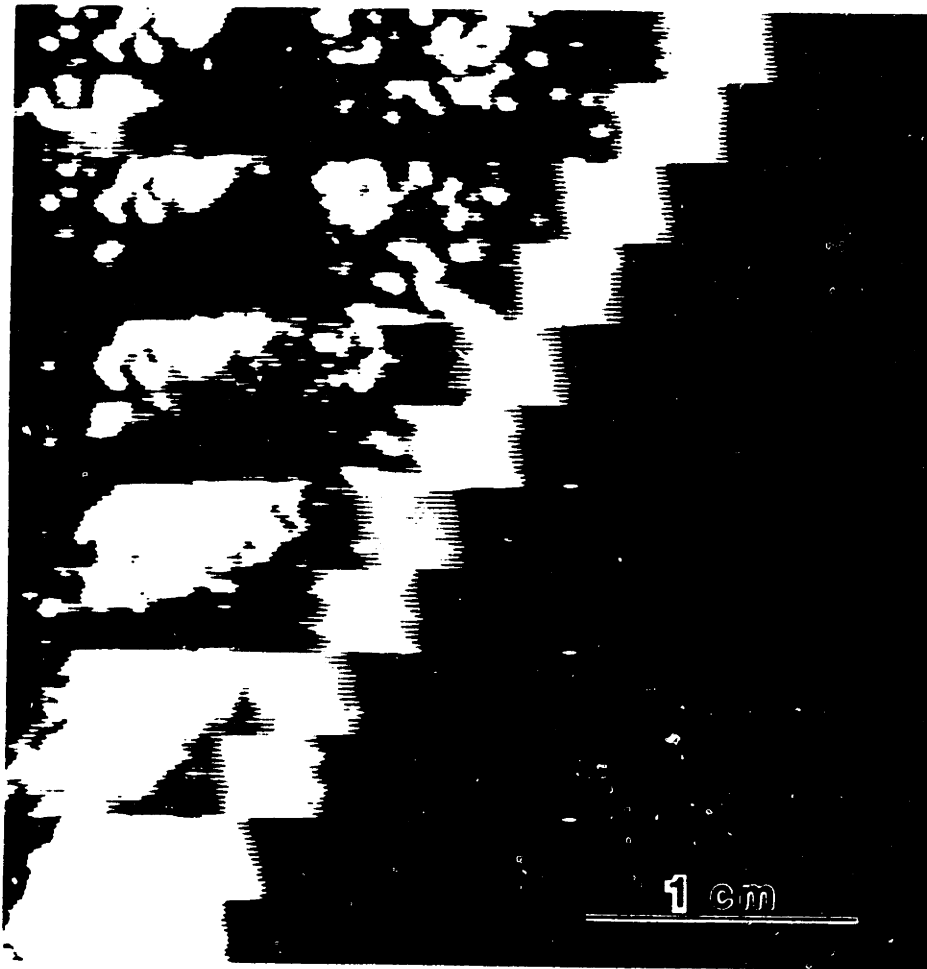


Figure 2 High-speed video output showing the explosive silicidation front (bright band) at 12 different times, 1/12 of a millisecond apart. This film was made in the same way as described in figure 1. The indicated front velocity was 23 m/sec.



thin film like that of figure 1. Figure 2 was shot at 6000 frames a second. The entire time scale for the figure is 1 millisecond and it is divided into 12 sections each showing the propagating front after a 1/12 of a millisecond time interval. The bright band in each section corresponds to an area of the multilayer film that is undergoing explosive silicidation and is glowing due to substantial heating caused by the explosive reaction. The reaction front velocity can be calculated from figure 2 by measuring the distance the front travels as a function of time. For the example shown in figure 2, the velocity was calculated to be 23 m/sec. A similar set of measurements was done for all the nickel/amorphous-silicon multilayer films deposited on substrates. The calculated velocities are shown in figure 3. They range from 21 to 27 m/sec for multilayer thin films with total thicknesses of 1.6 μm and from 22 to 23 m/sec for multilayer films with total thicknesses of 0.73 μm . Figure 3 indicates that within the range of deposition parameters used in this work, the explosive reaction front velocity does not strongly depend on the modulation period or the total film thickness of the as-deposited multilayer thin films.

The type of microstructural change that occurs during explosive silicidation is illustrated in figure 4. In this figure, we present three plan view transmission electron micrographs of an as-deposited free standing nickel/amorphous-silicon multilayer thin film (figure 4a), a portion of the same film that has been explosively reacted to form Ni_2Si (figure 4b), and another portion of the same free-standing, as-deposited nickel/amorphous-silicon multilayer thin film that has been heated at 20 K/min to 850 K to form Ni_2Si , and then quenched to room temperature (figure 4c). The thicknesses of the nickel and silicon layers in the as-deposited film were 7

Figure 3 Explosive reaction front velocities versus modulation period and total film thickness for 2 Ni to 1 Si multilayer thin films.

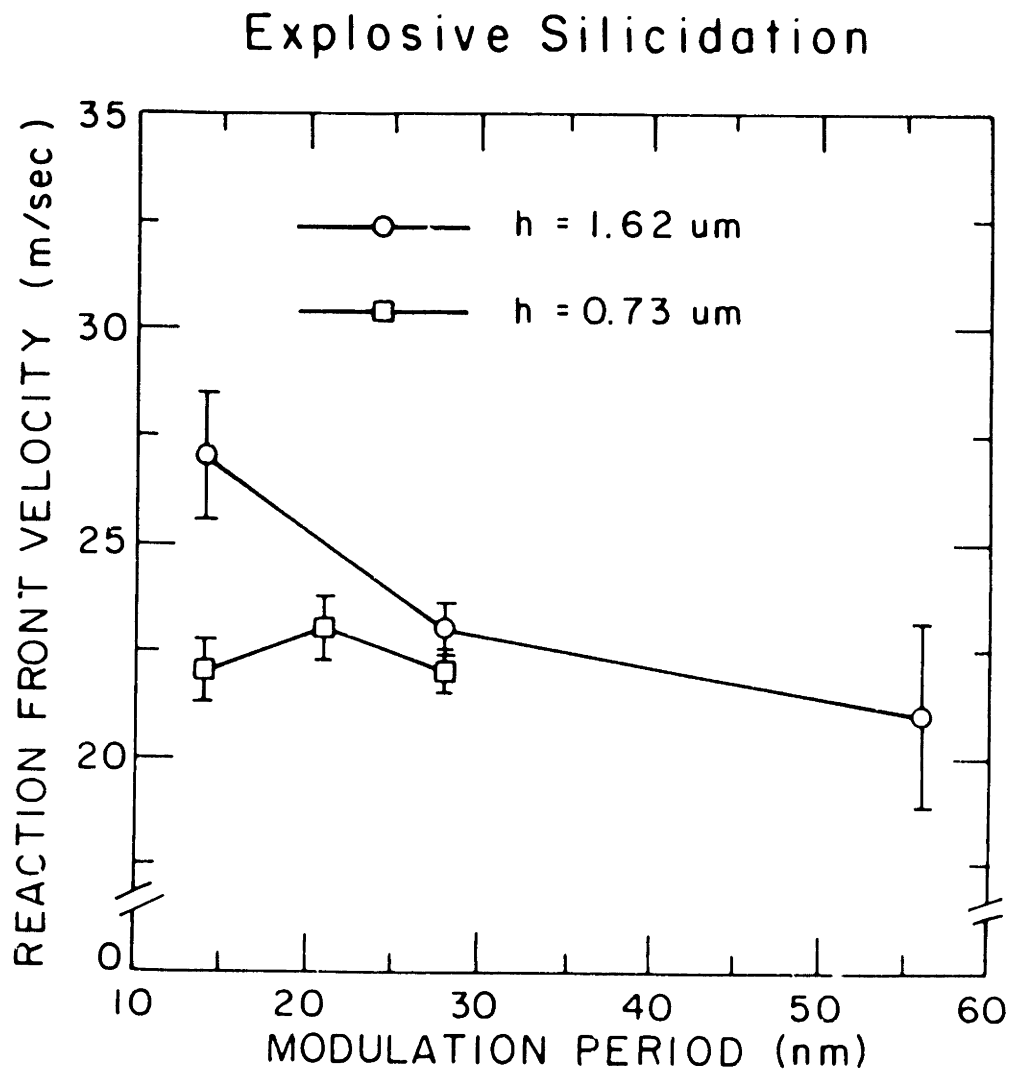


Figure 4a Plan view transmission electron micrograph of an as-deposited of 2 Ni to 1 Si multilayer thin film with modulation period of 14 nm and a total film thicknesses of 70 nm.

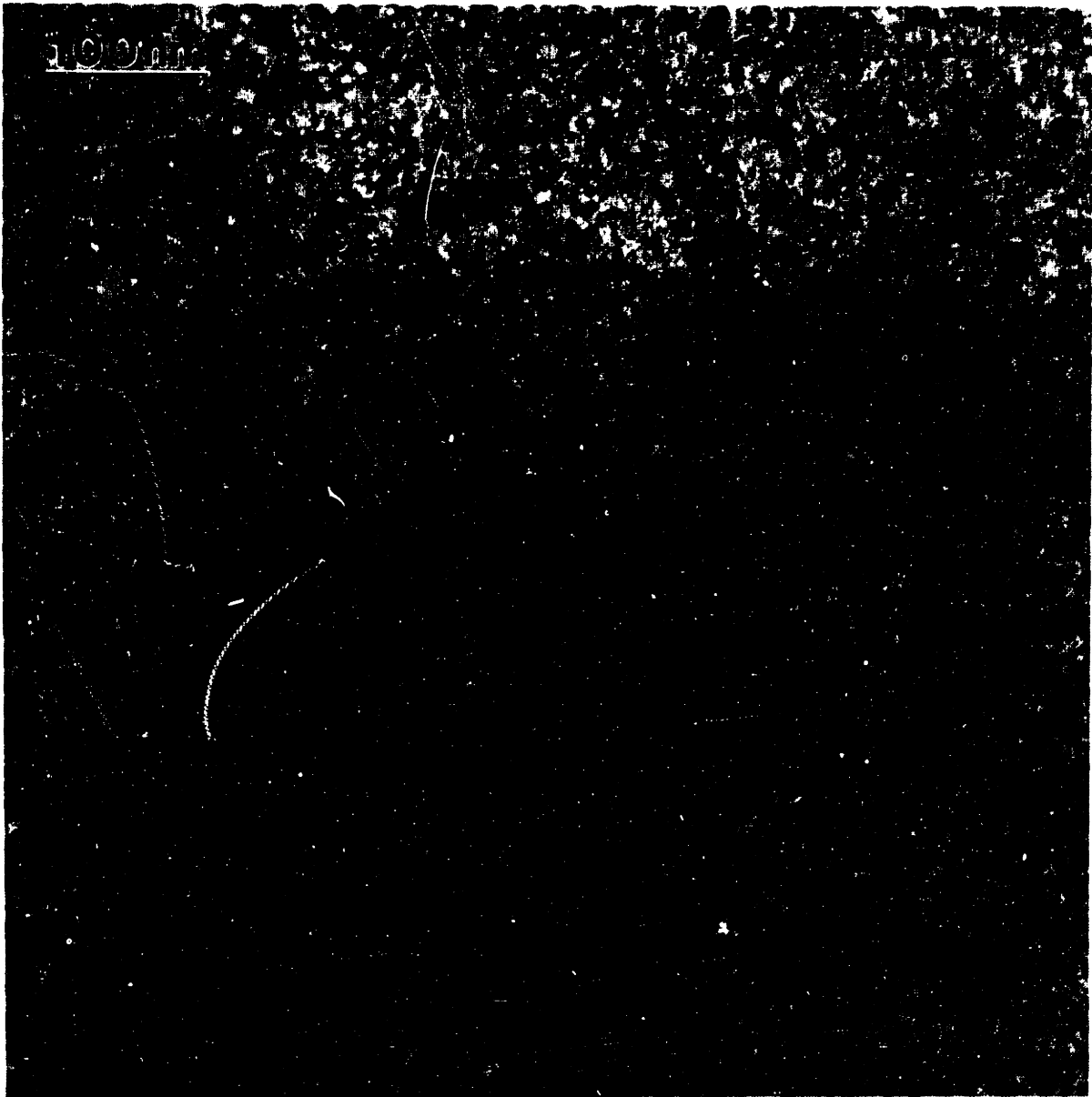


Figure 4b Plan view transmission electron micrograph of an 2 Ni to 1 Si multilayer thin film with modulation period of 14 nm and a total film thicknesses of 70 nm which has been explosively reacted to form Ni₂Si.



Figure 4c Plan view transmission electron micrograph of an 2 Ni to 1 Si multilayer thin film with modulation period of 14 nm and a total film thicknesses of 70 nm which has been thermally annealed to form Ni_2Si .



nm and the total number of layers was ten. This multilayer film was chosen due to its convenient use with electron microscopy.

Figure 4a is a view through 5 layers of nickel and 5 layers of amorphous-silicon in the as-deposited multilayer film. The dark spots are nickel grains in diffracting contrast and the average grain size is approximately 4 nm. When this film was explosively reacted, it formed homogeneous Ni_2Si with a columnar structure and an in-plane grain size of about 150 nm (figure 4b). The grain structure in the explosively formed Ni_2Si is relatively uniform and there are no defects within the grains.

In contrast, the grain size and of Ni_2Si formed through controlled heating (figure 4c) is larger than for explosively formed Ni_2Si . Another distinct characteristic of Ni_2Si formed by controlled annealing are the bands of light and dark contrast within most of the Ni_2Si grains. These bands are intragranular defects which we believe are due to annealing twins in Ni_2Si .⁶

9.3 Comparison of Measured Explosive Silicidation Temperatures to Predicted Values

The measured temperature of the explosive reaction of 2 Ni to 1 Si multilayer films is over 1500 K. This value is consistent with calculations of the temperature that might be reached due to the heat released during silicidation. A simple method of performing this calculation for explosive reactions in nickel/amorphous-silicon multilayer thin films is to assume that Ni_2Si forms at 298 K and that all the heat released goes into adiabatic heating of the Ni_2Si . The assumption of adiabatic heating provides an upper bound to the final temperature. However, due to the very high rate of

the reaction, near-adiabatic heating would be expected. For the explosive reactions discussed in this chapter, the sources of heat are the heat of formation of Ni_2Si and the heat of crystallization of amorphous-silicon at 298 K. These values have been determined experimentally to be:^{7,8}

$$\Delta H_{\text{formation, Ni}_2\text{Si, 298 K}} = -37.6 \text{ Kj/g-atom} \quad (1)$$

$$\Delta H_{\text{crystallization, } \alpha\text{-Si, 298 K}} = -14.2 \text{ Kj/g-atom} \quad (2)$$

Combining the heat of formation of Ni_2Si and the heat of crystallization of amorphous-silicon gives -51.8 kJ/g-atom for the heat generated by explosive silicidation of the nickel/amorphous-silicon multilayer film.

The heat required to raise the temperature of the explosively formed Ni_2Si consists of the heat required to heat Ni_2Si from 298 K to its melting point of 1565 K and, if necessary, the heat of fusion required to melt Ni_2Si . Both values can be calculated from thermodynamic data available in the literature. They are:

$$\Delta H_{\text{heating, Ni}_2\text{Si, from 298 K to 1565 K}} = 37.9 \text{ Kj/g-atom} \quad (3)$$

$$\Delta H_{\text{fusion, Ni}_2\text{Si, 1565 K}} = 14.0 \text{ Kj/g-atom} \quad (4)$$

Therefore 51.9 kJ/g-atom is required to raise the temperature of and melt Ni_2Si . These calculations suggest that the heat released by the explosive silicidation of nickel/amorphous-silicon multilayer film (51.8 kJ/g-atom) is enough to heat the film to the melting point of Ni_2Si (1565 K), and possibly

melt the Ni_2Si . A detailed description of how the values of equations 1 through 4 were calculated is presented in appendix D.

The high predicted and measured explosive reaction temperatures indicate that a liquid region may laterally propagate through the film, converting the inhomogeneous multilayer film to homogeneous Ni_2Si .⁹ To further test this hypothesis, an estimate for the required atomic diffusivity at the explosive reaction front can be determined from:

$$\frac{X^2}{t} \equiv D_{\min} \quad (5)$$

where X is the maximum distance that nickel and silicon have to interdiffuse in a direction perpendicular to the direction of motion of the front, t is the maximum time allowed for Ni_2Si formation and D_{\min} is the minimum required diffusivity.

The maximum diffusion distance for the multilayer films of figures 1 and 2 is 20.8 nm, the modulation period of the multilayer film. For a conservative estimate of the maximum time allowed for Ni_2Si formation by explosive silicidation, we take the width of the bright region shown in figure 2 (0.44 cm) and divide this by the front velocity (23 m/sec) to give 0.19 msec. Combining this time with equation 5, we get the minimum required diffusivity to be:

$$D_{\min} \equiv \frac{(20.8 \text{ nm})^2}{.19 \text{ millisecond}} \equiv 2.3 \times 10^{-8} \text{ cm}^2/\text{sec}. \quad (6)$$

For a completely solid state reaction, the atomic diffusion coefficient at the reaction front can be estimated using the temperature dependent

diffusion coefficient for growth of Ni₂Si as determined for low temperature reactions between nickel and silicon. Taking the measured explosive silicidation temperature to be 1565 K, and combining this with a previously determined activation energy and diffusion pre-exponential coefficient of 1.5 eV and 10 cm²/sec for Ni₂Si growth,³ the diffusion coefficient at a solid reaction front would be,

$$D_{\text{solid}} = 10 \text{ cm}^2/\text{sec} \exp\left(\frac{-1.5 \text{ eV}}{(1565 \text{ K})(8.62 \times 10^{-5} \text{ eV/K})}\right) \quad (7)$$

$$= 1.5 \times 10^{-4} \text{ cm}^2/\text{sec}$$

The atomic diffusion coefficient at a liquid reaction front would be expected to be on the order of 10⁻⁵ cm²/sec or higher, a typical value for liquid phase atomic diffusion.¹⁰

Extrapolation of the solid state formation rates of Ni₂Si to 1565 K using temperature-independent kinetic parameters is highly questionable. However in the absence of a better estimate for D_{solid} , the atomic diffusion coefficients for both an explosive *solid state* reaction and for a *liquid* reaction front are higher than the required minimum diffusivity derived in equation 5. This implies that the possibility of an explosive solid state reaction can not be ruled out. One observation that can be made is that the estimated diffusion coefficients for both a liquid phase and solid phase process are very high, suggesting that atomic diffusion does not limit the propagation of the explosive reaction front. Figure 3 confirms this in that increasing the modulation period of the multilayer thin film did not significantly affect the reaction front velocity.

The microstructures of an as-deposited nickel/amorphous-silicon multilayer thin film, explosively formed Ni_2Si and conventionally formed Ni_2Si are shown in figures 4a, 4b and 4c respectively. Explosively formed Ni_2Si has a uniform columnar grain size of approximately 150 nm with no intragranular defects. This indicates that explosively formed Ni_2Si does not retain the inhomogeneous multilayer thin film microstructure of the as-deposited sample. If the explosive reaction front is a solid front, this means that Ni_2Si grain growth occurs after the silicide reaction. If the explosive reaction front is a liquid front, the resulting columnar microstructure could be obtained by solidification of melted Ni_2Si and/or Ni_2Si grain growth after the front has passed through the film. We believe that the sharp contrast in microstructures of Ni_2Si formed by explosive silicidation and by controlled annealing is due to the very different reaction conditions. For explosive formation of Ni_2Si , the reaction occurs in less than a millisecond and the films are heated to a temperature near or over the melting point of Ni_2Si . For Ni_2Si formed using conventional heating, the annealing time was approximately twenty minutes and the thin film was never heated over 850 K.

9.4 Conclusion

The explosive silicidation of nickel/amorphous-silicon multilayer thin films has been investigated using a combination of high speed temperature and velocity measurements of reaction fronts, thin film X-ray diffraction and plan view transmission electron microscopy. The temperature of the explosive silicidation front was determined to be over

1500 K and the reaction front velocity was found to vary between 22 and 27 m/sec and not to be strongly dependent on the modulation period or total film thickness of the multilayer thin film. Calculations suggest that atomic diffusion does not limit the propagation of the reaction front. We were not able conclusively to determine whether there was a liquid region at the reaction front or whether the process occurs entirely in the solid state. However, there is evidence that a molten zone might form.

9.5 References

1. J.A. Floro, *J. Vac. Sci. Technol. A*, **4**, 631 (1986)
2. L.A. Clevenger, C.V. Thompson, R.C. Cammarata and K.N. Tu, *Appl. Phys. Lett.*, **52**, 795 (1988)
3. L.A. Clevenger, C.V. Thompson, A. Judas and K.N. Tu, First MRS International Meeting on Advanced Materials, **10**, 431 (1989)
4. C.E. Wickersham and J.E. Poole, *J. Vac. Sci. Technol. A*, **6**, 1699 (1988)
5. F. M. d'Heurle, C.S. Petersson, J.E.F. Baglin, S.J. Placca and C.Y. Wong, *J. Appl. Phys.* **55**, 4208 (1984)
6. B.D. Cullity, Elements of X-ray Diffraction, Addison Wesley, Reading Massachusetts, (1978)
7. Sebina an Mey, *Z. Metallkde* **77**, 805 1986
8. E.P. Donovan, F. Spaepen, D. Turnbull, J.M. Poate and D.C. Jacobson, *J. Appl. Phys.* **57**, 1795 (1985)
9. R.B. Gold, J.F. Gibbons, T.J. Magee, J. Peng, R. Ormond, V.R. Deline and C.A. Evans, in Laser and Electron Beam Processing of

Materials, edited by C.W. White and P.S. Peercy (Academic, New York 1980), p.221

10. J.W. Christian, Theory of Transformations in Metals and Alloys, Pergamon Press, New York 1965, p.576

10 Summary and Future Work

In order to produce integrated circuits with submicron dimensions, new materials need to be developed for metal interconnects and metal/silicon diffusion barriers. Metal silicides have been used for both applications and have therefore been heavily studied during the last 15 years. The purpose of this thesis was to perform a quantitative analysis of silicide formation from metal/amorphous-silicon reactions.

This thesis describes the controlled and explosive silicidation of metal/amorphous-silicon multilayer thin films with nickel, vanadium or titanium as the chosen metal. Chapter 2 presented a literature review of previous work in this field while chapter 3 discussed the experimental techniques used in this research. In chapters 4 through 6, the controlled silicidation of nickel/amorphous-silicon, vanadium/amorphous-silicon and titanium/amorphous-silicon multilayer films was discussed. In chapter 7, the thermodynamics of amorphous and crystalline intermetallic formation by a solid state reaction was discussed while in chapter 8 we investigated structural transitions in evaporated amorphous-silicon thin films. Finally, in chapter 9 explosive silicidation of nickel/amorphous-silicon multilayer thin films was discussed.

In chapter 4, we described the controlled silicidation of nickel/amorphous-silicon thin films with an atomic concentration ratio of 2 Ni atoms to 1 Si atom. It was with these reactions that we first demonstrated the concept of using calorimetry combined with thin film x-ray diffraction and cross-sectional transmission electron microscopy to investigate the kinetics and phase formation sequence in

nickel/amorphous-silicon reactions. It was determined that calorimetry was effective in measuring kinetic activation parameters. We were able to determine activation energy for crystalline Ni₂Si growth to be 1.5 ± 0.1 eV. In chapter 4 we also demonstrated that with constant-scan-rate calorimetric analysis, the crystalline silicide growth terminates at higher temperatures with increasing modulation period. For Ni₂Si growth, this peak shift was modeled to give an activation energy of 1.5 eV and a diffusion pre-exponential coefficient of 10 cm²/sec. We further demonstrated that the first phase to form at a nickel/amorphous-silicon interface was an amorphous-nickel-silicide and that crystalline-silicides would form at higher annealing temperatures. The important question of whether nucleation and growth or growth alone controls silicide phase selection was investigated. We demonstrated, for the first time, that thermodynamic analysis combined with isothermal and constant-scan-rate calorimetry indicate that nucleation mechanisms control amorphous and crystalline phase selection in nickel/amorphous-silicon thin film reactions. Finally, we considered the implications of nucleation controlled phase selection on the nucleation surface energies of the silicide phases. With the assumption that the first silicide phase to form from a nickel/amorphous-silicon reaction is the one with the smallest free energy barrier to formation, we demonstrated that for an amorphous-nickel-silicide phase to form first at the nickel/amorphous-silicon interface, it must have the lowest nucleation surface energy.

In chapter 5, we investigated vanadium/amorphous-silicon multilayer thin film reactions with an atomic concentration ratio of 1 V atom to 2 Si atoms. We demonstrated that the first silicide phase to form in these reactions was an amorphous-vanadium-silicide, similar to what was

seen in the nickel/silicon system. With further heating, it was shown that VSi_2 would form at the amorphous-vanadium-silicide/amorphous-silicon interface and grow to consume the entire thin film. With calorimetric analysis, we were able to determine the activation energy for the formation of a continuous layer of VSi_2 between the amorphous-vanadium-silicide and amorphous-silicon layers to be 2.6 eV and the activation energy for the one-dimensional growth of this layer to consume the entire multilayer thin film to be 2.5 eV. As with the nickel/silicon system, thermodynamic analysis, isothermal and constant-scan-rate calorimetry combined with cross-sectional transmission electron microscopy indicated that nucleation mechanisms controlled both amorphous-vanadium-silicide and crystalline vanadium silicide formation.

In chapter 6, we moved on to a discussion of titanium/amorphous-silicon multilayer thin film reactions, where the thin films had an atomic concentration ratio of 1 Ti to 2 Si. In this system an amorphous-titanium-silicide phase is the first phase to form at the titanium/amorphous-silicon interface. Heating the thin film causes the amorphous-titanium-silicide to grow until C-49 TiSi_2 forms at the amorphous-titanium-silicide/amorphous-silicon interface and transforms the entire thin film to C-49 TiSi_2 . Calorimetric analysis of these reactions was used to detect the exothermic growth and compositional homogenization of amorphous-titanium-silicide, and determined the activation energy of 3.1 ± 0.1 eV for formation and growth of C-49 TiSi_2 .

The thermodynamics of amorphous and crystalline intermetallic formation were discussed in chapter 7. The analysis presented was general in nature although the examples were related to amorphous and crystalline silicide formation in nickel/amorphous-silicon and

vanadium/amorphous-silicon thin films. In this section, we discussed three main points. First, we determined that for amorphous intermetallic phases to form in a thin film reaction, there must be nucleation barriers that prevent the formation of the crystalline intermetallics. Second, we discussed the thermodynamic conditions required for the simultaneous growth of amorphous and crystalline intermetallic phases. Finally, we demonstrated that the driving force for formation of an intermetallic phase depends on the interface at which the intermetallic forms, the layer in which the intermetallic forms and the composition of the layer where the intermetallic nucleates.

Structural transitions that occurred upon heating amorphous-silicon thin films prepared by electron beam evaporation were discussed in chapter 8. In this chapter we used calorimetry to investigate both exothermic and endothermic transitions and determined that these transitions were due to bond angle relaxations and densification of the amorphous-silicon thin films. Similar results were seen for amorphous-titanium-silicide films (chapter 6).

Finally, in chapter 9 we discussed the phenomena of explosive silicidation of nickel/amorphous-silicon multilayer thin films. Explosive silicidation is a reaction in which the transformation from an inhomogeneous nickel/amorphous-silicon multilayer to homogeneous crystalline nickel silicide could be initiated at room temperature by a laser pulse. For 2 Ni atoms to 1 Si atom atomic concentration ratio multilayer thin films, this reaction was shown to occur with velocities of approximately 25 m/sec and at temperatures near 1500 K.

This thesis is intended to provide a quantitative understanding of silicide formation in metal/amorphous-silicon thin film reactions. This

research demonstrated four important concepts for the first time. First, we demonstrated how calorimetry can be used in combination with other techniques to obtain kinetic information on amorphous and crystalline silicide formation and structural transitions in amorphous thin films. Secondly, we discussed how thermodynamic, electron microscopy, and calorimetric techniques indicate that nucleation controls silicide phase selection in nickel/amorphous-silicon and vanadium/amorphous-silicon thin film reactions. Third, we discussed the thermodynamics of amorphous and crystalline phase formation in thin film reactions. Finally, we discussed explosive silicidation in nickel/amorphous-silicon thin films.

For future work, there are a number of areas to be investigated. For controlled silicidation, a detailed study of the formation and growth of amorphous-silicide along with a study of the thermodynamic properties of amorphous intermetallic phases should be undertaken. Thermodynamic analysis indicates that the formation of amorphous-silicide phases are controlled by nucleation, but experimental evidence is lacking. The calorimetric techniques used in this work to detect nucleation events for crystalline silicides could be applied to the formation of amorphous silicide phases under certain experimental conditions. For growth of amorphous silicide phases there is some controversy as to whether the growth is interface or diffusion controlled. The use of isothermal calorimetric analysis should help to easily determine whether this growth is interface or diffusion controlled. For the thermodynamics of amorphous phases, work still needs to be done on the modeling of the free energy of these phases and the experimental determination of their composition ranges. For explosive silicidation, the key questions are whether the reaction front has a liquid or solid structure, and how to model the reaction front velocity as a function of

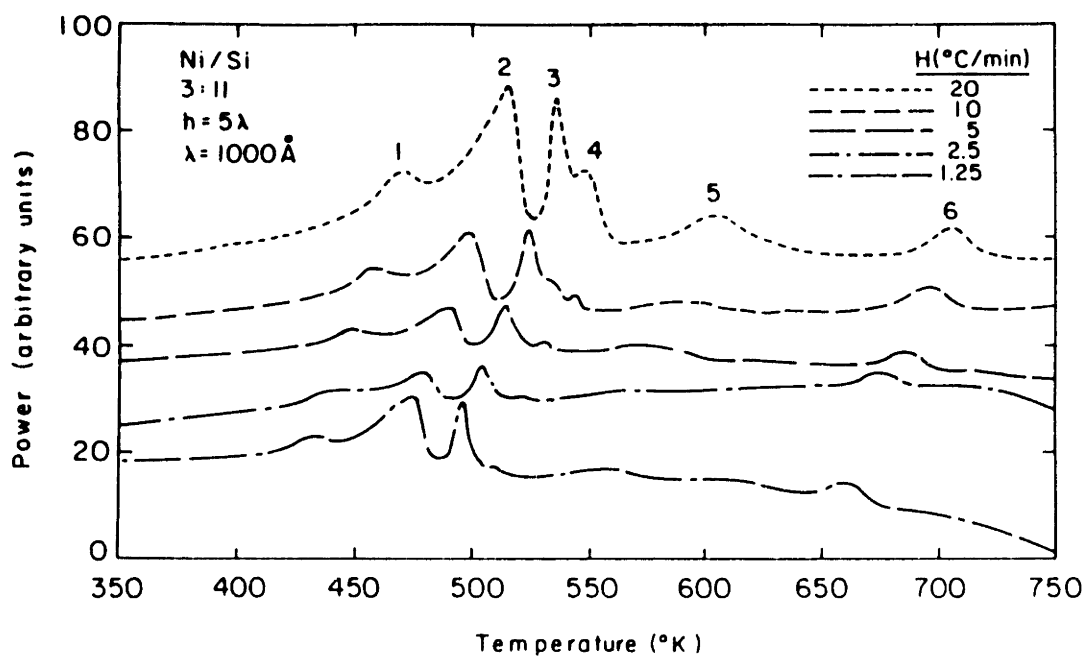
the modulation period and the total film thickness. Work in all these areas should contribute to a deeper understanding of thin film reactions.

Appendix A. Controlled Silicidation of Nickel/Amorphous-Silicon Multilayer Films With Atomic Concentration Ratios of 1 Ni Atoms to 2 Si Atoms

A.1 Phase Formation Sequence and Reaction Kinetics

In figure 1, we present constant-heating-rate DSC traces for scan rates of 1.25 to 20 K/min for nickel/amorphous-silicon multilayer films with atomic concentration ratios of 1 Ni atom to 2 Si atoms and a modulation period of 95 nm. The 20 K/min trace has six labeled peaks which correspond to exothermic reactions. Comparing figure 1 to previous work and the discussion of section 4.2, allows us to identify peak 1 of figure 1 with the formation of a continuous layer of Ni₂Si at the polycrystalline nickel/amorphous-nickel-silicide interface, peak 2 of figure 1 with the one-dimensional growth of Ni₂Si and peak 3 of figure 1 with the formation of crystalline NiSi. Figure 1 shows that as the heating rate is decreased the peaks shift down to lower temperatures. Using equation 9 of chapter 3, we can determine the activation energies for these peaks from the slope of a plot of $\ln(H/T_p^2)$ versus $1/T_p$ where H is the heating rate and T_p is the peak temperature observed at heating rate H . Using this method for analysis of figure 1 gives an activation energy of 1.5 eV for the formation of a continuous layer of Ni₂Si between the nickel and amorphous-nickel silicide layers (peak 1 of figure 1), 1.5 eV for the growth of Ni₂Si (peak 2 of figure 1) and 1.4 eV for the formation of crystalline NiSi (peak 3 of figure 1). These values are in agreement with the results of chapter 4.

Figure 1 Constant-heating-rate DSC traces for multilayer films with atomic concentration ratios of 1 Ni atom to 2 Si atoms and with a modulation period of 95 nm. Each curve corresponds to a different scan rate.

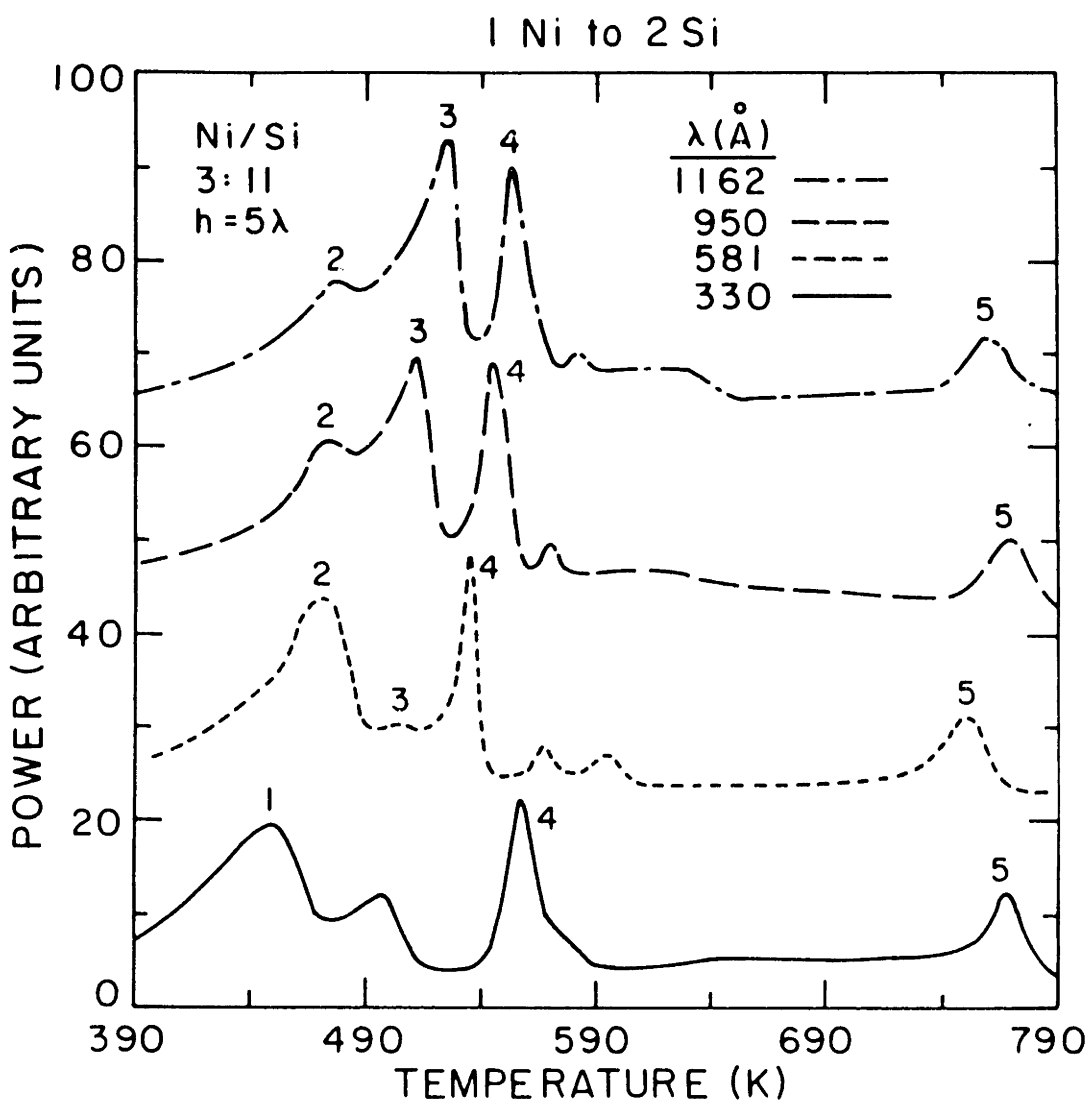


A.2 Effect of Modulation Period

In figure 2, we present constant-heating-rate calorimetric traces (at a scan rate of 20 K/min) for nickel/amorphous-silicon multilayer films with an atomic concentration ratio of 1 Ni atom to 2 Si atoms and modulation periods of 116.2, 95.0, 58.1 and 33.0 nm. DSC traces for the 116.2, 95.0 and 58.1 nm multilayer films have 4 labeled peaks numbered 2-5. In comparing the 95.0 nm trace of figure 2, with the 95.0 nm trace of figure 1, we can identify peak 2 of figure 2 with the formation of a continuous layer of Ni_2Si between the nickel and amorphous-nickel silicide layers, peak 3 of figure 2 with the growth of Ni_2Si and peak 4 of figure 2 with the formation of crystalline NiSi . For modulation periods greater than 58.1 nm the peak temperatures for both Ni_2Si growth and NiSi growth shift down to lower temperatures with decreasing modulation period and the peak temperature for the formation of a continuous layer of Ni_2Si between the nickel and the amorphous-nickel-silicide layers does not shift with decreasing modulation period. These results are similar to the observations reported in section 4.2 for nickel/amorphous-silicon multilayer films with 2 Ni atoms to 1 Si atom atomic concentration ratios.

Three observations can be drawn from the trace of figure 2 for the 33.0 nm multilayer thin film. First, peak 1 of figure 2 for this thin film occurs at 450 K. This is the same temperature as peak 1 for figure 1 of section 4.2. This fact allows us to identify peak 1 in figure 2 with the growth of amorphous-nickel-silicide from a reaction between nickel and amorphous-silicon. Second, peak 2 of figure 2 is not seen in the 33.0 nm

Figure 2 Constant-heating-rate DSC traces for nickel/amorphous-silicon multilayer films with atomic concentration ratios of 1 Ni atoms to 2 Si atom and modulation periods of 116.2, 95.2, 58.1 and 33.0 nm.



multilayer thin film indicating that in this thin film, the formation of Ni_2Si does not occur. This observation was confirmed with X-ray diffraction.¹ Third, the NiSi formation temperature (peak 4) for the 33.0 nm multilayer thin film is higher than the NiSi formation temperature of the longer modulation period films. This is an unexpected observation which we suspect is due to the fact that for longer modulation period films, NiSi forms via a reaction between Ni_2Si and amorphous-silicon while for the 33 nm film NiSi forms from a reaction between amorphous-nickel-silicide and amorphous-silicon.

A.3 References

1. L.A. Clevenger, C.V. Thompson, A. Judas and K.N. Tu, First MRS International Meeting on Advanced Materials, 10, 431 (1989)

Appendix B. Modeling of the Double Peak Structure in Constant-Scan-Rate Calorimetric Data for the Formation and Growth of a Crystalline Silicide Phase

B.1 Ni₂Si Formation and Growth

In the constant-scan rate calorimetric data of figure 14, section 4.5, peak 1 was due to the formation of a continuous layer of Ni₂Si at the polycrystalline nickel/amorphous-nickel-silicide interface and peak 2 was due to the one-dimensional growth of this continuous layer to completely transform the film into Ni₂Si. Recently Coffey et al.¹ have developed a two step model for the Ni₂Si formation and growth. They model the formation of a continuous layer of Ni₂Si by proposing that nucleation barriers allow growth from only a fixed density, n , of pre-existing nucleation sites in the plane of the interface. For simplicity they chose the shape of the n nuclei to be cylinders of height w_0 , and radius r , with their axes of symmetry oriented perpendicular to the planar interface. The height of the Ni₂Si nuclei is fixed and they grow in the plane of the original interface by increasing in radius. The growth rate of the nuclei can be modeled as being interface limited:

$$\frac{dr}{dt} = K_{io} \exp\left(\frac{-Q_i}{kT}\right) \quad (1)$$

where K_{i0} and Q_i are the interface-limited growth prefactor and activation energy respectively. The growth of the Ni_2Si nuclei occurs two dimensionally, with the growth direction lying in the plane of the original interface. This stage of the reaction is limited by the impingement of one growing island upon another. For random nucleation sites in a plane, impingement effects can be accounted for using the "extended fraction" concept, initially used by Johnson and Mehl² and Avrami³, and applied to two-dimensional grain boundaries by Cahn.⁴ If the extended area fraction which would react if impingement were not considered is $n\pi r^2$, the actual reacted area fraction, X_A , when impingement is taken into account, is given by:

$$X_A = 1 - \exp(-n\pi r^2) \quad (2)$$

Peak 1 of figure 14 (section 4.5) is interpreted as representing the termination of the interfacial reaction as the individual Ni_2Si nuclei coalesce into a continuous layer between the nickel and amorphous-nickel-silicide layers.

Peak 2 is modeled as the one-dimensional thickening of Ni_2Si to consume the entire thin film. Defining the Ni_2Si layer thickness as "w" and assuming diffusion controlled thickening with the interdiffusivity having an Arrhenius temperature dependence, the product layer growth rate is described by:

$$\frac{dw}{dt} = \frac{K_{d0}}{w} \exp\left(\frac{-Q_d}{kT}\right) \quad (3)$$

where K_{d0} and Q_d are the diffusion-limited growth prefactor and activation energy respectively.

The results of these two mechanisms are combined to produce a single model describing the product phase growth. Using equations (1), (2), and (3) this model gives the reaction rate in terms of the rate of volume fraction, X_v , transformed as:

$$\frac{dX_v}{dt} = \left(\frac{dX_A}{dt}\right)\left(\frac{w}{w_{\max}}\right) + X_A \left(\frac{dw}{dt}\right)\left(\frac{1}{w_{\max}}\right) \quad (4)$$

where

$$\frac{dX_A}{dt} = 2 n \pi r \left(\frac{dr}{dt}\right) \exp(-n\pi r^2) \quad (5)$$

and where w starts from the initial nuclei thickness, w_0 , and the reaction proceeds until consumption of one or both reactant layers at thickness w_{\max} . Equation 5 is the same as equation 14 of chapter 4 section 5.

B.2 VSi₂ Formation and Growth

In the constant-heating-rate calorimetric traces for figure 3 chapter 5, peak 1 was due to the formation of a continuous layer of VSi₂ at the amorphous-vanadium-silicide/amorphous-silicon interface and peak 2 was due to the one-dimensional growth of this continuous layer to completely transform the film into VSi₂. The formation and growth of VSi₂ can be modeled with almost the same formalism that was used to model the formation and growth of Ni₂Si at a nickel/amorphous-nickel-silicide

interface present in section B.1. The only difference is that the one-dimensional growth of VSi_2 to consume the entire thin film is interface limited while, by equation 3 section B.2, the one-dimensional growth of Ni_2Si to consume the thin film was diffusion limited. For VSi_2 one-dimensional growth, we can express the growth rate as:

$$\frac{dw}{dt} = K_o \exp\left(\frac{-Q_o}{kT}\right) \quad (1)$$

where K_o is the interface-limited one-dimensional growth prefactor and Q_o is the one-dimensional growth activation energy, When equation 3, section B.1 is replaced by equation 1, the analysis of section B.1 then models the constant-heating-rate calorimetric data of figure 3, section 5.3 for VSi_2 formation and growth.

B.3 References

1. K.R. Coffey, L.A. Clevenger, K. Barmack, D.A. Rudman and C.V. Thompson, to be published
2. W.A. Johnson and R.F. Mehl, Trans. AIME 135, 416, 1939.
3. M. Avrami, J. Chem. Phys. 7, 1103, (1939); 8, 212, (1940); 9, 177, (1941).
4. J.W. Cahn, Acta Met. 4, 499 (1956).

Appendix C Thermodynamic Data

The nickel/amorphous-silicon and vanadium/amorphous-silicon Gibbs free energy versus composition diagrams in chapters 4,5 and 7 were calculated using the following equations. The units for all the Gibbs energies reported in this appendix are J/g-atom.

C.1. Liquid and bcc Vanadium

The lattice stabilities of stable bcc vanadium, fcc nickel and diamond cubic silicon were taken to be $H^{\circ}(0\text{ K}) = 0$ and $S^{\circ}(0\text{ K}) = 0$. The Gibbs energy of bcc vanadium was derived from data given in the JANAF tables:¹

$$G(\text{bcc V}, T) = -4038.8 + 152T - 26.835T\ln T + 8.20 \times 10^{-5}T^2 - 6.08 \times 10^{-7}T^3 + 97360T^{-1}$$

The Gibbs energy of liquid vanadium was obtained from the Gibbs energy difference between bcc vanadium and liquid vanadium proposed by Guillermet and Huang²,

$$G(\text{liquid V}, T) = 18070 + 141.929T - 26.835T\ln T + 8.20 \times 10^{-5}T^2 - 6.08 \times 10^{-7}T^3 - 5.19098 \times 10^{-22}T^{-7} + 97360T^{-1}$$

C.2. Liquid and fcc Nickel and Liquid, fcc, Amorphous and Diamond Cubic Silicon

The Gibbs free energies of fcc nickel, liquid nickel, fcc silicon, diamond silicon and liquid silicon were taken from a thermodynamic evaluation of the nickel/silicon system by Mey.³ However Mey's data was corrected for the convention in the present study with the enthalpies of the pure elements at 298.15 K determined by Hultgreen et al.⁴ The calculated free energies are given below in table C1.

Table C1: Gibbs free energies for fcc nickel, liquid nickel, fcc silicon, diamond silicon and liquid silicon. The general form of the Gibbs free energy is:

$$G(T) = a + bT + cT \ln T + dT^2 + eT^3 + \frac{f}{T} \text{ where the constants } a, b, c, d, e,$$

and f for the different possibilities are listed below.

phase	a	b	c	d/10 ⁻²	e/10 ⁻⁶	f
fcc Ni	-5744.4	192.073	-36.647	1.237645	-7.2583	180977
liq Ni	-4550.2	268.073	-43.095	0	0	0
dia Si	-4946.6	137.185	-22.823	-.192880	0	176983
fcc Si	44843.4	119.319	-22.823	-.192880	0	176983
liq Si	43580.6	137.682	-27.196	0	0	0

The Gibbs energy of amorphous-silicon was estimated from the work of Donovan et al⁵ and the Gibbs energy of bcc silicon from the lattice stabilities proposed by Kaufman.⁶ These values are:

$$G(\text{amorphous Si, T}) = 11950 - 1.66T + G(\text{diamond Si, T})$$

$$G(\text{bcc Si, T}) = -6276 + 10.46T + G(\text{liquid Si, T})$$

C.3 Gibbs and Excess Gibbs Energies of Nickel/Silicon and Vanadium/Silicon Solutions

The Gibbs energies of the fcc and liquid nickel/silicon solutions and the bcc and liquid vanadium/silicon solutions can be described by,

$$G = (X_{\text{metal}}) G_{\text{metal}}^{\circ} + (X_{\text{silicon}}) G_{\text{silicon}}^{\circ} + 8.314 T (X_{\text{metal}} \ln(X_{\text{metal}}) + X_{\text{silicon}} \ln(X_{\text{silicon}})) + G_{\text{sol}}^{\text{xc}}^{\text{ess}}$$

where G_{metal}° and $G_{\text{silicon}}^{\circ}$ are the free energies of the pure elements, X_{metal} and X_{silicon} are the atomic fractions of the metal and silicon in the solution and $G_{\text{sol}}^{\text{xc}}^{\text{ess}}$ is the excess free energies for the solution. The excess energies for liquid and bcc solutions of vanadium and silicon are the values proposed by Kaufman⁶ with corrections in the minus signs. They are:

$$G^{\text{xc}}^{\text{ess}}(\text{liq V+Si, T}) = X_{\text{V}}X_{\text{Si}}((-182422+27.196T) X_{\text{V}} - 83680X_{\text{Si}})$$

$$G^{\text{xc}}^{\text{ess}}(\text{bcc V+Si, T}) = X_{\text{V}}X_{\text{Si}}((-145603+2.092T) X_{\text{V}} + 83680X_{\text{Si}})$$

The excess energies for the fcc and liquid nickel/silicon solutions were the same as those proposed by Mey. For both the vanadium/amorphous-silicon systems and the nickel/amorphous-silicon systems the free energy of the

amorphous-metal-silicides was assumed to be approximated by the free energy of the undercooled liquid solution.

C.4 Gibbs Energies of Crystalline Vanadium Silicides

The Gibbs energies for crystalline vanadium silicides, except for V_5Si_3 , were derived from a thermodynamic assessment done by Smith.⁷ They are listed below in table C2. Smith underestimated the Gibbs energy of V_5Si_3 . The Gibbs energy of this phase was taken as that purposed by Kaufman,⁶ i.e.

$$G(V_5Si_3, T) = .625 (G(\text{bcc V}, T)) + .375 (G(\text{diamond Si}, T)) - 69224 + 10.225 (T)$$

Table C2: Gibbs free energies for the crystalline vanadium silicides. The general form of the Gibbs free energy is:

$$G(T) = a + bT + cT \ln T + dT^2 + eT^3 + f \frac{1}{T} \text{ where the constants } a, b, c, d, e,$$

and f for the different possibilities are listed below.

phase	a	b	c	d/10 ⁻²	e/10 ⁻⁶	f/10 ⁴
V_3Si	-46343	129.13	-22.61	-.2086	0	8.95
V_6Si_5	-54725	151.47	-25.48	-.1265	0	21.0
VSi_2	-44707	134.39	-22.6	-.25	0	11.5

C.5 Gibbs Energies of Crystalline Nickel Silicides

The Gibbs energies for crystalline nickel silicides were obtained from Mey³ and they were corrected for the enthalpy standard state used in this work. These values are listed below in table C3. Ni₅Si₃ is not considered in this work due to a lack of reliable data for its free energy.

Table C3: Gibbs free energies for the crystalline vanadium silicides. The general form of the Gibbs free energy is:

$$G(T) = a + bT + cT \ln T + dT^2 + eT^3 + f \frac{1}{T} \quad \text{where the constants } a, b, c, d, e,$$

and f for the different possibilities are listed below.

phase	a	b	c	d/10 ⁻⁶	e/10 ⁻⁶	f
Ni ₃ Si	-44847.6	151.641	-24.8111	-.3132	0	51777
Ni ₂ Si	-41403.1	146.275	-24.7135	-.2922	0	69036
Ni ₃ Si ₂	-41138.1	146.575	-24.5468	-.2222	0	116001
NiSi	-38440.1	145.951	-24.3802	-.1530	0	162967
NiSi ₂	-32393.2	154.020	-25.0199	-.1845	0	180498

C.6 References

1. JANAF Thermochemical Tables, 3rd edition, J. Phys. Chem. Ref. data, 14, suppl. 1, p. 1818 and 1826 (1985)
2. A.F. Guillermet and W. Haung, Z. Metallkde, 79, 88 (1988)
3. S. Mey, Z. Metallkde, 77, 805 (1986)

4. R. Hultgreen, P.D. Desai, D.T. Hawkins, M. Gleisar, K.K Kelly and D.D. Wagman, Selected Values of the Thermodynamic Properties of the Elements, American Society for Metals, Metals Park Ohio (1973)
5. E.P. Donovan, F. Spaepen, D. Turnbull, J.M. Poate and D.C> Jacobson, J. Appl. Phys., 57, 1795 (1985)
6. L. Kaufman, User Application of Alloy Phase Diagrams, ASM International, Metals Park Ohio, p. 59 (1987)
7. J. Smith, Bull. Alloy Phase Diagr., 2, 42 (1981)

Appendix D Calculation of the Temperature of Explosive Silicidation of Nickel/Amorphous-Silicon Multilayer Thin Films with an Atomic Concentration Ratio of 2 Ni to 1 Si

D.1 Analysis

From chapter 9, the measured temperature of explosive silicidation of a 2 Ni to 1 Si multilayer thin film to form homogeneous Ni₂Si was approximately 1500 K. This temperature can be shown to be in agreement with the calculated temperature in the following manner.

We first assume that Ni₂Si forms at 298 K and that all the heat generated by the formation of Ni₂Si goes into heating Ni₂Si towards its melting point (adiabatic heating).

The sources of heat are the heat of formation of Ni₂Si and the heat of crystallization of amorphous silicon. The heat of formation of Ni₂Si at 298 K has been determined by Mey¹ to be

$$\Delta H_{\text{Ni}_2\text{Si}}^{298} = -37.6 \frac{\text{Kj}}{\text{g-atom}} \quad (1)$$

The heat of crystallization of amorphous-silicon at 960 K was determined by Donovan et al.² to be -11.95 kJ/g-atom. We can calculate the heat of crystallization of amorphous-silicon at 298 K by the following equation

$$\Delta H_{ac}^{298} = \Delta H_{ac}^{900} + \int_{900}^{298} \Delta C_{p,ac} dt \quad (2)$$

where²

$$\Delta C_p = -0.244 + 4.8 \left(\frac{T}{1685} \right) \text{ kJ / g-atom} \quad (3)$$

Combining equations 2 and 3 and integrating, we obtain

$$\Delta H_{ac}^{298} = -14.17 \text{ KJ/g-atom} \quad (4)$$

and combining equations 1 and 4, we obtain -51.7 kJ/g-atom as the heat generated by the explosive reaction.

The two sinks of heat are the heat required to raise Ni₂Si up to its melting point and the heat required to melt Ni₂Si. The heat required to raise Ni₂Si from 298 to 1565 K can be calculated from

$$\Delta H_{Ni_2Si, 298 \text{ to } 1565 \text{ K}} = \int_{298}^{1565} C_p dt \quad (5)$$

where C_p can be expressed as:¹

$$C_p = 24.7135 + (2) \times (0.292185 \times 10^{-2}) T^2 + \frac{69036}{T} \text{ KJ/g-atom K} \quad (6)$$

Combining equations 5 and 6 and integrating, we obtain

$$\Delta H_{\text{Ni}_2\text{Si}, 298 \text{ to } 1565 \text{ K}} = 37.8 \text{ KJ/g-atom} \quad (7)$$

The heat required to melt Ni₂Si into a liquid can be expressed as

$$\Delta H_{\text{melt}} = (H_e - H_s)_{1565 \text{ K}} \quad (8)$$

where H_e is the enthalpy of liquid Ni₂Si at 1565 K and H_s is the enthalpy of solid Ni₂Si at 1565 K. From May,¹ these values are

$$H_{l,1565} = 14.3 \text{ KJ/g-atom} \quad (9)$$

$$H_{s,1565} = 0.3 \text{ KJ/g-atom} \quad (10)$$

and the $\Delta H_{\text{fusion}} = 14 \text{ kJ/g-atom}$ for Ni₂Si. Combining equation 7 with this number, we determine that 51.8 kJ/g-atom of heat is required to raise the temperature of Ni₂Si from 298 K to its melting point and to melt Ni₂Si.

Since this value is the same as the amount of heat generated, it is reasonable to expect that during explosive silicidation, the temperature of the thin film gets near the melting point of Ni₂Si. This is in agreement with the experimental results.

D.2 References

- 1) S. Mey, *Z. Metallkde*, 77, 805 (1986)
- 2) E.P. Donovan, F. Spaepen, D. Turnbull, J.M. Poate and D.C. Jacobson, *J. Appl. Phys.*, 57, 4208 (1984)